Analysing the Interactions between Water-induced Soil Erosion and Shallow Landslides

A thesis

submitted in partial fulfilment

of the requirements for the Degree of

Doctor of Philosophy

in Civil Engineering

in the University of Canterbury

by

Govind Acharya

Department of Civil and Natural Resources Engineering
University of Canterbury

2011

Acknowledgements

I would like to express my sincere gratitude to my supervisor Dr. Tom Cochrane, Senior Lecturer, Department of Civil and Natural Resources Engineering for his extensive help, constant guidance and coherent effort in terms of regular advice and encouragement throughout this research. His excellent ideas helped me formulate the research and carryout the work in a smooth way. Without his critical feedback and review, the quality of this thesis would have suffered. I would also like to recognize other members of my committee Dr. Tim Davies and Dr. Elisabeth Bowman for their valuable suggestions in defining the research and improving the thesis.

It is my great pleasure to extend my special thanks to the technical staff Alan Stokes, Ian Sheppard, Kevin Wines, Peter McGuigan and David MacPherson in the Department of Civil and Natural Resources Engineering. The experimental flume set up would not be possible without Alan, Ian and Kevin. I had excellent technical support from Peter for various lab tests, fieldwork and sensors installation while David was very helpful with all kinds of problems in the Fluids and Environmental Engineering Labs. My sincere thanks also go to the Christchurch City Council (CCC) and Landcare Research. CCC provided soils from the Bowenvale research catchment for the flume experiments, rainfall and climate data, and stream discharge at the outlet of the catchment. Landcare Research provided information on the catchment's soil data.

This research was sponsored by a research grant from the Department of Civil and Natural Resources Engineering, University of Canterbury, which is gratefully acknowledged. I would like to extend my sincere thanks to NZAID (New Zealand Agency for International Development) for providing a New Zealand Development Scholarship (NZDS) scholarship to conduct the research at the University of Canterbury.

Special thanks go to my family members and friends who have significantly contributed to create a family environment in New Zealand that helped me a lot to

pursue the study. Finally, my heartfelt thanks go to my wife Nanu and son Ashish for their understanding, support and help during every moment of the research.

Abstract

Water-induced soil erosion and shallow landslides interact with each other and need to be studied in an integrated approach to understand hillslope sediment yields. The principal aim of this thesis was to study and model soil erosion and shallow landslides in an integrated way. The thesis presents results from laboratory and catchment-scale studies and modelling.

A laboratory flume under a rainfall simulator was used for shallow landslide and soil erosion experiments using sandy and silty loess soils. In the experiments, landslide initiation, retrogressions and slip surface depths were measured and monitored directly or by using video camera recordings. Sediment and runoff were collected from the flume outlet every minute during landslides and every 10 minutes before and after landslides. Changes in the soil slope, after landslides, were recorded. Initially, six experiments including two repetitions were conducted using sandy soils at a 30º and 10º compound slope configuration, but with different soil profile depths. The experimental results showed that total and landslide-driven sediment yields were affected by the original soil profile depth; the greater the depth, the higher the sediment yield. Later, twelve other experiments were conducted on different slopes using silty loess soils. The experimental observations were used to validate an integrated modelling approach which includes WEPP for runoff and soil erosion modelling, a slope stability model for simulating shallow landslides, and a simple soil redistribution model for runout distance prediction. The model predictions were in good alignment with the observations. In all (sandy and silty loess) experiments, peak sediment discharges were related to the landslide events, proximity to the outlet and landslide volume. The post-failure soil erosion rate decreased as a function of changes in the slope profile.

The GeoWEPP-SLIP modelling approach was proposed for catchment-scale modelling. The approach simulates soil erosion using the Hillslope and Flowpath methods in WEPP, predicts shallow landslides using a slope stability model coupled with the WEPP's hillslope hydrology and finally uses a simple rule-based soil redistribution model to predict runout distance and post-failure topography. A case

study application of the model to the Bowenvale research catchment (300 ha) showed that the model predictions were in good agreement with the observed values. However, the Hillslope method over-predicted the outlet sediment yield due to the computational weighting involved in the method. The Hillslope method predicted consistent values of sediment yield and soil erosion regardless to the changes in topography and land-cover in the post-failure scenarios. The Flowpath method, on the other hand, predicted higher values of sediment yield in the post-failure vegetation removal scenario. The effects of DEM resolution on the approach were evaluated using four different resolutions. Statistical analyses for all methods and resolutions were performed by comparing the predicted versus measured runoff and sediment yield from the catchment outlet and the spatial distribution of shallow landslides. Results showed that changes in resolution did not significantly alter the sediment yield and runoff between the pre- and post-failure scenarios at the catchment outlet using the Hillslope method. However, the Flowpath method predicted higher hillslope sediment yields at a coarser resolution level. Similarly, larger landslide areas and volumes were predicted for coarser resolutions whereas deposition volume decreased with the increase in grid-cell size due to changes in slope and flowpath distributions. The research conducted in the laboratory and catchment presented in this thesis helped understand the interactions between shallow landslides and soil erosion in an integrated approach.

Keywords: Soil erosion, Shallow landslides, Soil redistribution, Experimental flume, WEPP, Catchment, Integrated modelling approach

Table of Contents

List of Tables

List of Figures

Chapter 1 Introduction

1.1 General introduction and problem statement

Water-induced soil erosion and shallow landslides are two natural processes occurring in hilly and mountainous areas. Soil erosion by water involves detachment and transport of soils by the erosive forces of rainfall and runoff, and deposition of the transported materials. During rainfall, water infiltrates the ground. The infiltrated water, along with subsurface flow from the upslope contributing areas, increases the pore pressures that reduce the soil's shear strength resulting in slope failures (landslides). The failed materials are then transported to the downslope; this is generally referred to as soil redistribution. Hillslope processes illustrating soil erosion, shallow landslides, and soil redistribution are schematically presented in Figure 1.1.

Water-induced soil erosion and shallow landslides are the main sources of sediment supply in steep hilly catchments. Sediments originate in the form of soil erosion in pre-failure events, landslides or debris flows during failures, and soil erosion in post-failure events. The failure and transport of the soil materials has two major implications. First, the landslide event may significantly increase sediment in nearby stream leading to immediate impacts to the ecosystem. Second, the failures and soil redistribution processes lead to changes in local slope gradient, which will affect subsequent soil erosion.

Past research has resulted in significant understanding of mechanisms and conditions leading to both water-induced soil erosion and shallow landslides. Studies were conducted both in laboratories under controlled conditions and in actual field situations. Soil erosion studies made at plot and laboratory scales have contributed to the current knowledge of erosion processes (Foster et al., 1984; Nearing et al., 1989; Nearing and Parker, 1994; Wendt et al., 1986; Risse et al., 1993; Ruttimann et al., 1995; Zhang et al., 1996; Nearing et al., 1999; Pieri et al., 2007). A considerable amount of research has been conducted on understanding the behaviour of water-induced shallow landslides under controlled laboratory conditions (Iverson et al., 2000; Wang and Sassa, 2003; Lourenco et al., 2006; Olivares and Damiano, 2007) and actual field situations (Anderson and Sitar, 1995; Crosta, 2001; Hunter and Fell,

2003; Malet et al. 2005). However, there have been relatively few investigations that explain actual processes of slope failure initiation and retrogression. Slope failure initiation, retrogression, and spatial distribution can have direct impact on sediment yields during and after shallow landslides. Further studies on initiation and retrogression of landslides are therefore needed to gain a better understanding of slope failures, and variations in sediment yields.

In previous studies of water-induced shallow landslides, some efforts have been made to quantify the influence of landslide-driven sediment yields and to compare these with annual sediment budgets. The landslide-driven sediment yields depend on how the failed material is transported to a stream network. It is generally hypothesized that the sediment yield is significantly high if the material evolves into debris flow after breaking up and mixing with water because it can travel a considerable distance (Corominas, 1996; Iverson et al., 1997; Hunter and Fell, 2003; Malet et al. 2005), and discharge directly into the stream network. In many cases, however, not all sediment dislodged from the landslides reaches the main stream: much of it remains within the hillslope (Johnson et al., 2000; Schuerch et al., 2006; Schwab et al., 2008). If the material deposits immediately downslope area from a landslide scar, then sediment can enter the stream network only if the landslide is adjacent to the stream network or by soil erosion processes. The effects of soil hydrologic properties, slope morphology, and other factors may control the mobilisation of failed materials, and eventually sediment yields to the stream network. Until now, influences of these factors on sediment yields have not been well understood. The magnitude and frequency of landslide-derived sediment yields from the hillslope is of critical importance to the safety of local settlements and infrastructure located downslope areas.

.

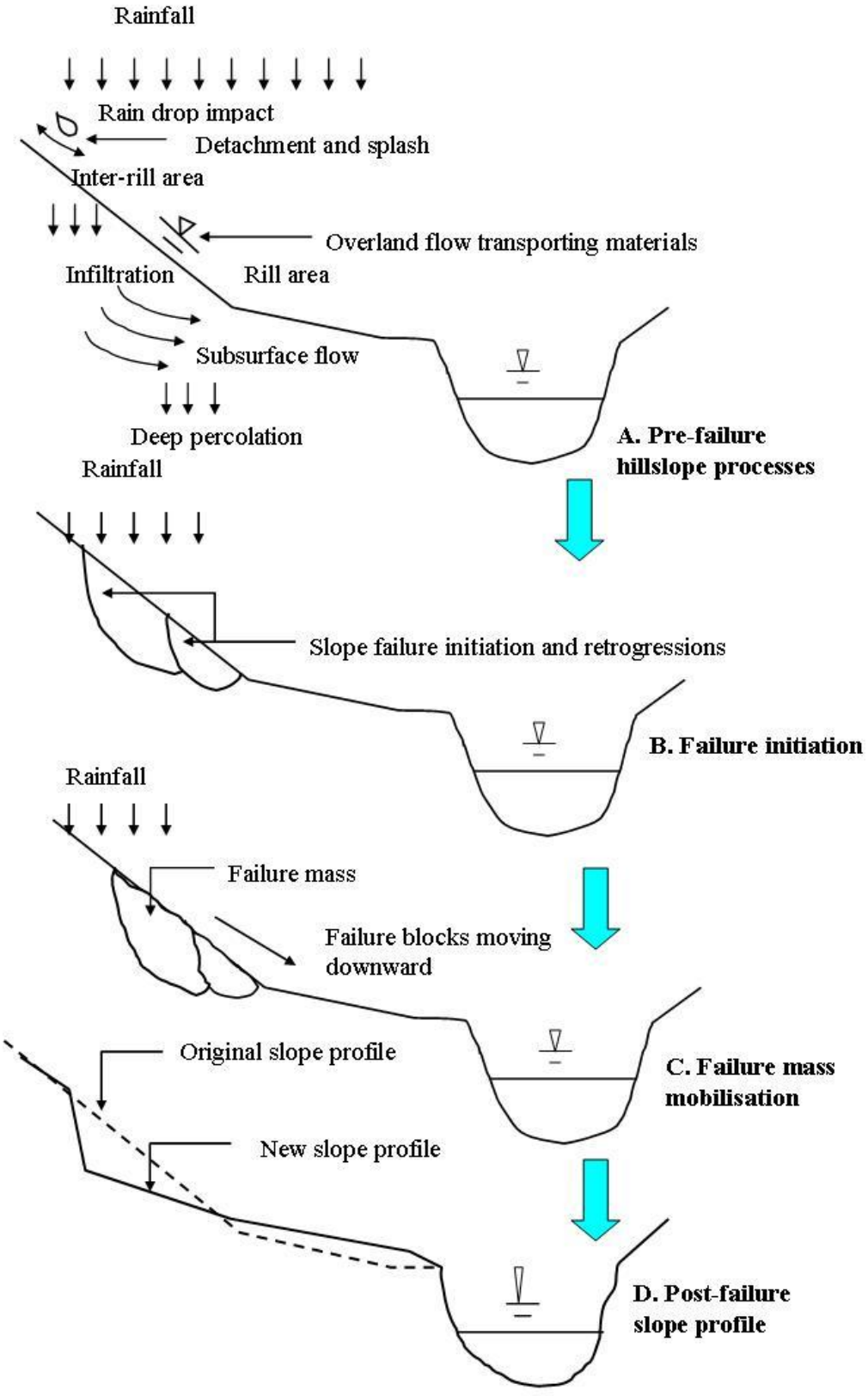

Figure 1.1: Schematic diagram showing different phases of sediment transport in a hillslope: (A) initiation of overland flow and soil erosion, (B) failure initiation and retrogressions, (C) mobilisation of failure materials and (D) changes in hillslope profile following landslides.

Soil redistribution following shallow landslides is generally responsible for changes in hillslope topography and evolution of a new hillslope profile. In general, mobilisation of materials results in a decrease in slope in the failure area and an increase in slope in the deposition area. However, relatively few data are available that explain the changes in topography and evolution of a new hillslope profile after slope failure mobilisation. It is therefore important to study the potential changes in the local topography. Additional research is also required to understand how the changes in local topography alter the soil erosion rates and sediment yields.

To quantify changes in long-term soil erosion rates and sediment yields, it is important to understand shallow landslide initiation, evolution, retrogression, mobilisation, and deposition processes. Changes in sediment yields during and after landslides can be studied by triggering landslides under controlled conditions in laboratory flume experiments.

Monitoring soil erosion and shallow landslides and their mobilisation can be a highly expensive, labour-intensive, and time consuming activity that results in limited data. Models are therefore used to estimate potential soil erosion and shallow landslides and to quantify their influence on sediment yields. Since soil erosion and shallow landslides are two different processes, they are modelled separately: erosion models only predict soil erosion, and landslide models only predict shallow landslides. Integration of shallow landslide and soil erosion models is important to predict hillslope sediment yields. However, there have been relatively few efforts to model shallow landslides and soil erosion in an integrated approach (e.g. Burton and Bathurst, 1998; Bathurst et al., 2010). In these studies, sediment yield before failure, spatial distribution of shallow landslides, and landslide driven sediment yields are modelled. However, an approach has yet to be developed that predicts changes in local topography in response to shallow landslides and the impact of shallow landslides on long-term sediment yields due to changes in topography and land-cover. Such an approach should simulate soil erosion, runoff in pre- and post-failure events; identify the potential landslides; compute the soil mobilisation and runout; and estimate the changes in local slope gradient after slope failures. The approach should also be applicable at both hillslope and catchment scales

For catchment-scale integrated modelling, the use of Geographical Information System (GIS) is desirable because GIS can be used to efficiently organize spatially distributed data allowing rapid assessment of spatial correlations between different data types related to topography, soil, and land-cover. When modelling with GIS, an important issue that needs to be examined is the resolution of input data. The resolution greatly influences the model output. It is generally believed that coarse resolution data would reduce the spatial representation of the landscape. On the other hand, deriving high resolution data may require significant field and laboratory work, model parameterisation, and computation that may increase the modelling costs. It is therefore important to evaluate how sensitive the integrated modelling approach and methods are to input data resolution.

1.2 Research objectives

Main motivation behind the research presented in this thesis was to increase our understanding of the impacts of shallow landslides on soil erosion and sediment yields and to propose a new model to estimate these impacts. The research has four specific interrelated objectives which aim to study the interactions between shallow landslides and soil erosion from a hillslope to a catchment scale:

The first objective is to understand how shallow landslide events alter sediment yields. To quantify variations in sediment yields in response to shallow landslides, it is important to understand conditions leading to landslide initiation, evolution, and retrogression. These variations are studied by triggering shallow landslides in a laboratory flume under controlled conditions.

The second objective is to study changes in long-term soil erosion due to changes in local slope gradient following shallow landslides. These changes are related to the evolution of a new hillslope from shallow landslides, soil redistribution and mobilisation, and post-failure slope stabilization. To meet the objective, changes in post-failure soil erosion are quantified using a laboratory flume under controlled rainfall.

The third objective is to develop an integrated modelling approach for soil erosion, shallow landslides, and soil redistribution. WEPP, a slope stability model, and a

simple rule based soil redistribution model are respectively used to model soil erosion, shallow landslides, and soil redistribution. The approach is applied at both the hillslope and catchment scale. The hillslope model is validated with the laboratory flume experiments and the catchment modelling is validated by comparing simulated versus measured values from a research catchment.

The fourth objective of the research is to evaluate how input grid-cell resolution affects the integrated catchment modelling approach. The objective is met by comparing simulation results from the different resolutions to the measured flow and sediment yields from the research catchment.

1.3 Thesis outline

Following this introductory chapter, this thesis comprises of six more chapters dealing with various aspects of the objectives mentioned in the previous section. In Chapter 2, a comprehensive literature review of soil erosion and shallow landslide processes is presented. It documents past research on triggering factors that control transport and mobilisation of failure mass, and conditions leading to shallow landslides and soil erosion. The chapter covers various modelling approaches with particular emphasis on physically-based models.

Chapter 3 deals with shallow landslide and soil erosion investigations in a flume under simulated rainfall using sandy soils of different depths. In the chapter, the slope failure initiation, evolution, and retrogressions are related to the variations in soil depth. It compares the sediment yields before, during, and after shallow landslides in different depth configurations.

In Chapter 4, experiments with the flume using fine-grained silty soil (loess) are presented. Similar to experiments in sandy soil, it also compares the sediment yields in pre-, during- and post-failure environments. An integrated modelling approach for hillslopes is proposed and validated with the experimental flume results.

An integrated modelling approach for catchments is presented in Chapter 5. The Bowenvale Reserve catchment (3 sq. km.) was chosen for applying and testing the model.

Chapter 6 evaluates digital elevation model (DEM) resolution effects on the catchment model results. The aim is to quantify the influence of grid-cell resolution on pre-failure sediment yields, landslide distribution, soil redistribution, and post-failure sediment yields.

In Chapter 7, a synthesis of the research is presented. The methods developed throughout the thesis and results obtained from experiments and modelling are summarised, and evaluated. Limitations of the methods are presented, together with suggestions for future model improvements and research needs.

1.4 Definition of terms

AGNPS : Agricultural Non-Point Source Pollution Model (Young et al., 1989)

ANSWERS : Areal Nonpoint Source Watershed Environment Response Simulation (Beasley et al., 1989)

ANUDEM : Australian National University DEM

BCDG : Breakpoint Climate Data Generator (Zeleke et al., 1999)

CCC : Christchurch City Council

CEC : Cation Exchange Capacity

CLIGEN : CLImate GENerator (Nicks et al., 1995)

CSA : Critical Source Area (minimum drainage area to define the beginning of a channel)

DEM : Digital Elevation Model

GeoWEPP : WEPP (Water Erosion Prediction Project)-GIS extension

GIS : Geographical Information System

GPS : Global Positioning System

KINEROS : A KINematic Runoff and EROSion Model (Woolhiser et al., 1990)

LAPSUS : LandscApe ProcesS modelling at mUlti-dimensions and Scales (Schoorl et al., 2000)

LiDAR : Light Detection and Ranging (an optical remote sensing technology used to collect highly dense sets of discrete elevation point)

MSCL : Minimum Source Channel Length (Minimum length whose concentrated flow defines the beginning of a channel)

MUSLE : Modified Universal Soil Loss Equation (Williams, 1975)

NTU : Nepthelometric Turbidity Units

OFE : Overland Flow Element

RUSLE : Revised Universal Soil Loss Equation (Renard et al., 1997)

SC : Sediment Concentration

SDR : Sediment Delivery Ratio

SHE : Système Hydrologique Européen (Abbott et al. 1986a, b)

SHETRAN : Système Hydrologique Européen TRANsport (a basin scale physically-based hydrological model) (Bathurst et al., 1995)

TAPES-G : Topographic Analysis Program for Environmental Science-Grid (Wilson et al., 2000)

TOPAZ : TOpographic PArameteriZation, is an automated digital landscape analysis tool for topographic evaluation, drainage identification, watershed segmentation and sub-catchment parameterization (Garbrecht and Martz, 1995)

TSS : Total Suspended Sediment

WEPP : Water Erosion Prediction Project (Flanagan and Nearing, 1995)

USDA-ARS : United States Department of Agriculture, Agricultural Research Service

USLE : Universal Soil Loss Equation (Wischmeier and Smith, 1978)

Chapter 2 Literature Review

2.1 Introduction

A broad understanding of various topics in hydrological and geotechnical science and modelling technology was required to complete the studies presented in this thesis and it is important to review each of them thoroughly. The first part of this chapter gives a brief description of soil erosion processes by water. The description is limited to field scale processes in space and time. Next, common empirical, conceptual and physically-based soil erosion models are reviewed in terms of their scope, rationale, structural framework, computational procedures and data requirements. A large portion of the review focuses specifically on surface and sub-surface hydrology and sediment transport because these are the major topics of this thesis.

The second part of the literature review covers the current understanding of mechanisms behind water-induced shallow landslides by illustrating comprehensive information on laboratory and real field scale landslide studies. Research conducted to demonstrate the evolution of shallow landslides and their mobilisation are presented in this section. The factors influencing transport and deposition of the failure materials are discussed. Subsequently, common approaches of modelling shallow landslides and soil mobilisation are reviewed.

2.2 Water-induced soil erosion processes

The term ‘erosion’ refers to the removal of solid (sediment, soil, rock or other particles) in a natural environment due to the transport by wind, water, snow melting, or by downslope creep of soil or other material under the action of gravity or by living organisms such as burrowing animals, in the case of bio-erosion. Water-induced soil erosion occurs as natural processes from rainfall, snowmelt or artificially by irrigation (Foster, 1982). The erosion involves three main processes: detachment; transport; and deposition of soil particles by the erosive forces of rainfall and runoff. The soil detachment processes start when the raindrops impact on the surface and overcome the interstitial forces holding the soil particles together. This is commonly referred to as ‘rainsplash’ or ‘raindrop splash’.

As the rainfall continues, water infiltrates the soil at a rate controlled by rainfall intensity and infiltration capacity of the soil profile. The infiltration capacity of a soil is the maximum rate that water can infiltrate it in a given condition. The infiltration capacity is a function of several hydraulic characteristics that relate the spacing and bonding of soil particles to each other and the effects of other surface and subsurface characteristics. Water that does not infiltrate begins to pond on the surface. When sufficient depth is achieved on the surface, water will flow in the direction of the steepest unimpeded slope. This initiates the hydrological processes referred to as 'overland flow' or 'runoff'. Soil particles may be dissolved or suspended in the overland flow, causing the process of sediment transport.

Soil erosion occurs in various forms such as splash, sheet, rill or gullies depending on the stage of progress in the erosion cycle and the position in the landscape. Sometimes the term referring to erosion also indicates where it occurs for example, trail erosion, riverbank/riverbed erosion, road slope erosion, cropland erosion. The factors that influence overland flow generation and detachment and transport of materials over the land surface are shown in Figure 2.1. These factors may also be grouped under five major headings: climate, relief, soil and bedrock properties, vegetation cover and human influence.

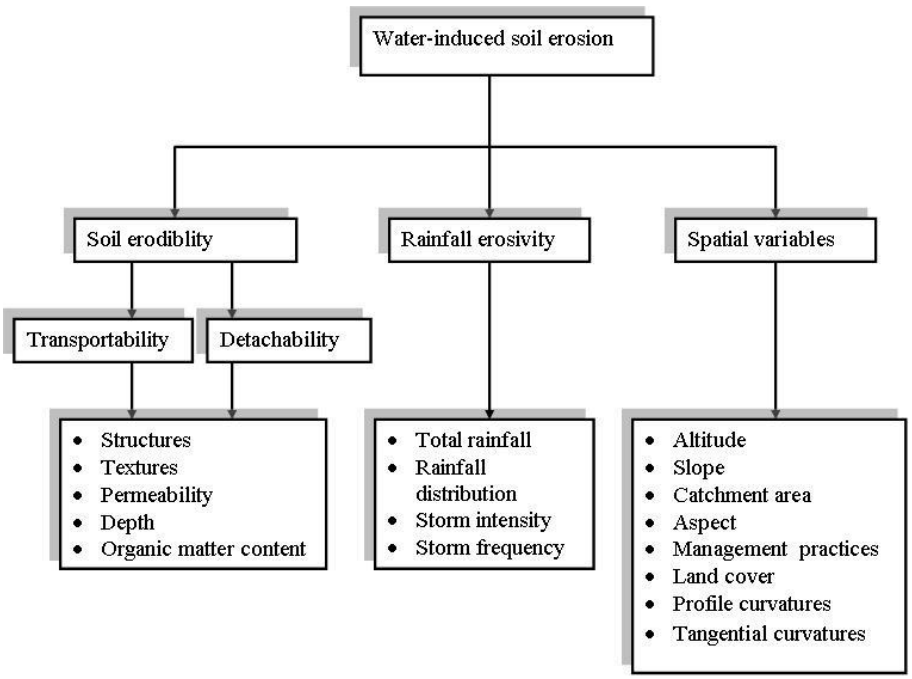

Figure 2.1: The main factors controlling the water-induced soil erosion processes (Source: Saavedra, 2005).

A catchment is usually divided into upland or hillslope areas and the stream network. In the upland areas, the overland flow is conceptually divided into rill and inter-rill flow mechanisms, which occur on the land surfaces. As the overland flow converges from various portions of the upland areas and becomes more concentrated, it becomes sufficiently erosive to form shallow channels, referred to as 'rills'. Additional soil particles may be detached as water flows through these rills. In the inter-rill areas, runoff occurs as thin sheet also termed as a 'sheet flow'. Both detachment and transport may occur in the rill and inter-rill areas. Schematic representation of rill and inter-rill erosion is presented in Figure 2.2. As erosive power increases, small rills may converge to form a large surface channel, called 'gullies'.

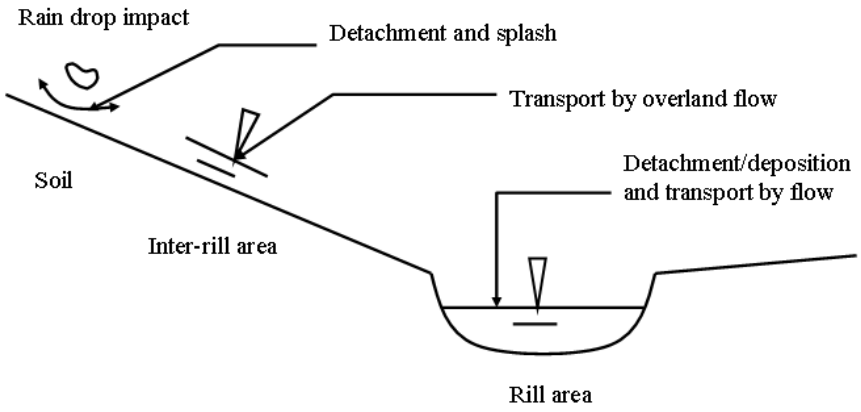

Figure 2.2: Soil erosion and transport on inter-rill and rill areas (Source: Doe and Harmon, 2001).

Inter-rill, rill and gullies are the sources of water-induced soil erosion. If sufficient flow continues to the downslope, it will reach well-defined channels, through which both water and sediment will be carried downstream towards the catchment outlet. If at any point along the water flow path the velocity decreases, for example, due to change in slope or flow, some soil particles may be deposited because the reduced flows cannot carry that much sediment. The transport capacity is the maximum amount of sediment that a given flow can carry without net deposition. The detachment and transport capacities are interrelated and it is their interaction that controls the patterns and magnitude of both erosion and deposition (Foster et al., 1984; Nearing et al., 1989; Ferro, 1998).

Sediment yields are linked to whether transport or detachment capacity is the limiting factor during the erosion process. If the detachment capacity is significantly lower than the transport capacity, the process is referred to as 'detachment-limited erosion' (Van Rompaey et al., 2003). Clayey soils are an example where the inter-particle binding forces (cohesion) are large and resist detachment, but are easily transported once detached. On the other hand, if the detachment capacity is significantly greater than the transport capacity it is referred to as 'transport-limited erosion' (Doe and Harmon, 2001). Sandy or loamy soils, for example, are easily detached, however the amount and magnitude of soil erosion is limited by the sediment transport capacity of runoff.

Another process important to quantifying soil erosion is soil armouring. When a certain type of soil surface is subjected to overland flow, the finer particles are preferentially removed, leaving coarse particles which results in an armoured surface. As the finer, more transportable materials are selectively removed, the remaining materials become more difficult to remove, which leads to the decrease in sediment yield. Soil armouring is defined as the process of surface coarsening where a surface layer becomes coarser than the underlying soil material due to overland flow over time. The rate of soil armouring is dependent on various parameters such as length and slope gradient of hillslope, soil profile properties, rainfall intensity etc. Sharmeen and Willgoose (2007) observe extensive armouring along longer hillslopes and quicker armouring in steeper slopes. Rainfall intensity also influences the armouring rate; higher intensity leads to quicker armouring due to increased runoff (Cochrane et al., 2007b).

The amount of sediment actually leaving a catchment is a function of erosional and depositional processes, both on surfaces and in channels, which occurs upstream of a catchment outlet. The amount of sediment being carried per time unit is called the sediment load. The velocity of the entrained sediment passing a given point is the sediment transport rate. A mass rate of transport 'sediment discharge' can be determined by multiplying the cross sectional area of the channel through which it is passing with the sediment concentration. Sediment yield is the amount of eroded soil that is delivered to an outlet point of the catchment. Figure 2.3 schematically represents soil erosion processes in a catchment.

In a catchment, the sediment yield includes erosion from hillslopes, channels and slope failures minus the sediment that is deposited after it is eroded and before it reaches the point of interest. The sediment yield can be estimated for a given point in a catchment by applying Sediment Delivery Ratio (SDR), which is the fraction or percentage of gross erosion arriving at a given point (Brooks et al., 1991):

$$SDR = \frac{Y_s}{T_e} \qquad \text{Equation 2.1}$$

Where Y_s is the sediment yield at a given point and T_e is the gross erosion from the catchment upstream of the given point.

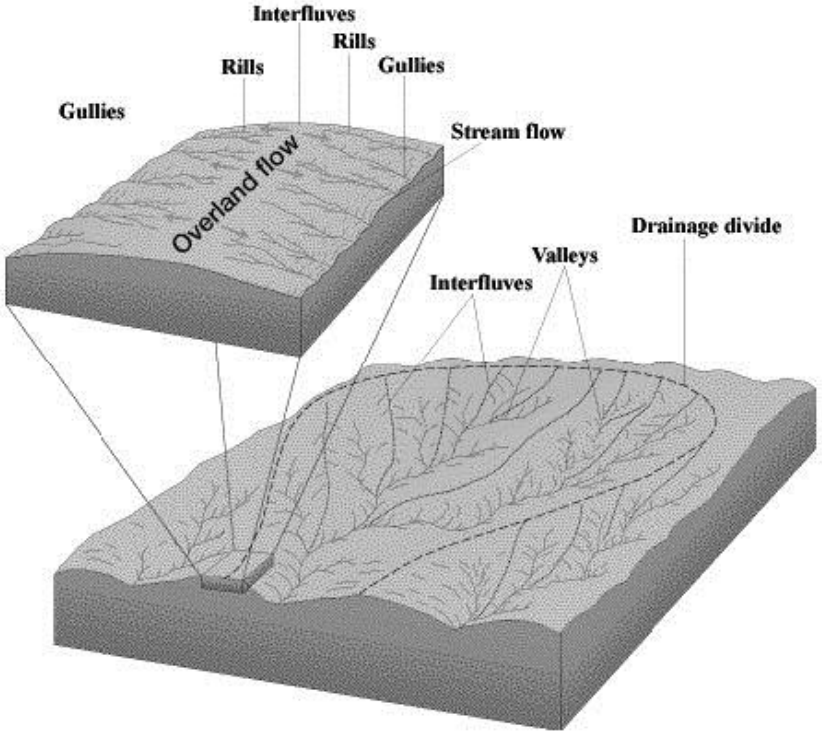

Figure 2.3: Schematic view of rill, inter-rill areas and gulley in a sub-catchment (Source: Saavedra, 2005).

2.3 Erosion models

Erosion modelling is based on an understanding of the physical laws and landscape processes such as runoff, soil mobilisation. Modelling translates these components into mathematical relationships, describing the fundamental water-induced soil erosion processes of detachment, transport and deposition. In general, models fall into three main categories, depending on the physical processes simulated, the model

algorithms describing these processes and the data dependency of the model. These three categories are the empirical, conceptual and physically-based models.

Empirical models are generally the simplest of the three model types. They are primarily based on the analysis of field experiments (plots) and seek to characterise the response from these plots using a statistical interface. The computational and data requirements for such models are usually less than for conceptual and physically-based models (Zhang et al., 1996a). These models usually have a high spatial and temporal aggregation and are based on the analysis of the erosion processes using statistical techniques. They are particularly useful as a first step in identifying the sources of sediments. USLE and RUSLE are commonly used empirical models.

Conceptual models aim at reflecting the physical processes governing the system but describe them with empirical relationships. They are typically based on the representation of a catchment as a series of internal and usually linear storages (Sivapalan et al. 2002). They tend to include a general description of catchment processes without including the specific details occurring in the complex process interactions. This allows these models to provide an indication of the qualitative and quantitative effects of land-use changes, without requiring large amounts of spatially and temporally distributed input data.

Physically-based models are based on an understanding of the physics of the erosion and sediment transport processes and describe the sediment system using equations governing the transfer of mass, momentum and energy (Flanagan and Nearing, 1995; Kandel et al. 2004). In principle, they can be applied outside the range of conditions used for calibration, and as their parameters have a physical meaning, they can be evaluated from direct measurements and without the need for long hydro-meteorological records (Smith et al., 1995). They are limited only by the relevance of the physical laws on which they are based. Physically-based technology computes erosion using a mathematical representation of fundamental hydrological and erosion processes. The fundamental erosion processes are detachment by raindrop impact, detachment of soil particles by overland flow, transport by raindrop impact and transport and deposition by overland flow. The Water Erosion Prediction Project

(WEPP: Flanagan and Nearing, 1995) and SHETRAN (Bathurst et al., 1995) are the two most widely used physically-based soil erosion models.

2.3.1 The USLE erosion model

The USLE has been the most widely used empirical erosion model because of its simplicity and practicality. It was developed for sheet and rill erosion based on a large set of experimental data from agricultural plots and is only valid when applied to a field area up to approximately 1 ha. Although it was developed in USA, it has been widely applied in many parts of the world (Mellerowicz et al., 1994; Kinnell and Risse, 1998; Bartsch et al., 2002). The mean annual erosion rate is expressed as a function of six erosion factors:

$$A = RKLSCP \qquad \text{Equation 2.2}$$

Where A (t ha^{-1} yr^{-1}) is the computed annual average soil loss per unit of area, and R (MJ mm ha^{-1} hr^{-1}) is the rainfall erosivity factor. K (t ha hr ha^{-1} MJ^{-1} mm^{-1}) is the soil erodibility factor representing the soil loss per erosion index unit for a specified soil as measured on a standard plot which is defined as a length of 22.1 m of uniform slope of 9% in a continuous clean tilled fallow. L (-) is the slope length factor, the ratio of soil loss from field slope length to a 22.1 m length plot under identical conditions and is therefore the function of slope. S (-) is the slope steepness factor, the ratio of soil loss from field slope gradient to a 9% slope under identical conditions. C (-) is the vegetation cover and crop management factor or the ratio of soil from an area with specified cover and management to soil loss from an identical area under continuous tilled fallow. P (-) is the erosion control practice or support practice factor. It represents the ratio of soil loss with a support practice such as contouring, strip cropping or terracing to soil loss with straight row farming up and down the slope.

The USLE concept has been modified and adapted during the past 30 years by a number of researchers. The Modified Universal Soil Loss Equation (MUSLE) (Williams, 1975), the Revised Universal Soil Loss Equation (RUSLE) (Renard et al., 1997), ANSWERS (Beasley et al., 1989), and the RUSLE-3D (Mitasova et al., 1996) are all modifications or improvements of the USLE. Use of the USLE and its derivatives is limited to estimating gross erosion. The model, therefore, lacks the

capability to compute deposition along hillslopes, depressions, and valleys or in channels.

2.3.2 SHETRAN model

SHETRAN is a physically-based, distributed, integrated surface and subsurface modelling system, designed to simulate water flow, sediment and contaminant transport at a catchment-scale (Bathurst et al., 1995). The starting point of its development was Système Hydrologique Européen (SHE) (Abbott et al. 1986a, b). In the simulation processes of water flow, soil erosion and transport, SHETRAN uses the partial differential equations of mass, momentum and energy conservation, and empirical equations derived from independent experimental research.

A. Hydrology Component

SHETRAN provides an integrated surface and subsurface representation of water movement in a catchment, incorporating the major factors involved in hydrological cycles such as interceptions, evapo-transpiration, snowmelt, overland and channel flow in unsaturated and saturated zones. In SHETRAN, actual evapo-transpiration is computed using Penman-Monteith (Monteith, 1965) equation. Surface water is routed as overland and channel flow as a function of topography, channel shape and flow resistance, using the diffusion wave approximation of the Saint Venant equation of continuity and momentum. Overland flow, generated by excess of rainfall over infiltration or by upward saturation of the unsaturated zone, is modelled in two dimensions.

The unsaturated zone flow determines the soil moisture content and tension in the zone, infiltration at the ground surface and an exchange with the saturated zone at the phreatic surface. The unsaturated flow is simulated using one-dimensional Richard's equation. The model simulates the flow in the saturated zone by determining the phreatic surface level and flows in the unsaturated zone of an unconfined aquifer, stream/aquifer interactions, groundwater seepage at the ground surface and artificial groundwater extraction using non-linear Boussinesq equation. This combines Darcy's law and mass conservation of two-dimensional laminar flow in an anisotropic heterogeneous aquifer.

B. Erosion Component

In SHETRAN, sediment erosion and transport are modelled using the measured rainfall data and the simulated overland and channel flow data. The SHETRAN model simulates soil erosion by raindrop impact, leaf drip and sheet overland flow and transport of the eroded material by overland flow. Soil detachment by raindrop and leaf drip impact is given by:

$$D_r = k_r F_w (1 - C_g)[(1 - C_c)M_r + M_d] \quad \text{Equation 2.3}$$

The soil detachment by overland flow is computed as:

$$D_f = k_f \left[\frac{\tau}{\tau_c} - 1 \right] \text{ for } \tau > \tau_c \quad \text{Equation 2.4}$$

$$D_f = 0 \text{ for } \tau \leq \tau_c \quad \text{Equation 2.5}$$

Where D_r (kg m^{-2} s^{-1}) and D_f (kg m^{-2} s^{-1}) are the respective rates of detachment of materials per unit area, k_r (J^{-1}) is the raindrop impact soil erodibility coefficient and k_f (kg m^{-2} s^{-1}) is the overland flow erodiblity coefficient. C_g (-) is the proportion of ground protected from drop/drip erosion by near ground cover such as low vegetation (range 0-1) and C_c (-) is the protection of ground against the raindrop impact erosion by canopy cover (range 0-1). M_r (kg^2 m^{-3}) is the momentum-squared for rain falling directly onto the ground and M_d (kg^2 m^{-3}) the momentum squared for leaf drip. Both of the momentum-squared terms are calculated using rainfall rates and canopy drainage rates which are passed from the flow component of SHETRAN to the erosion model. F_w (-) represents the effect of a surface water layer in reducing the energy imparted to the soil by raindrop impact. τ and τ_c (N m^{-2}) are the actual and critical shear stresses respectively. Estimates of values of erodibility coefficients are generally made through model calibration (Wicks et al., 1992; Wicks and Bathurst, 1996).

In sediment routing procedure, the eroded sediment is transported downslope by overland flow. Transport of the eroded material by overland flow is computed using

numerical solutions of the two-dimensional mass conservation equation (Wicks and Bathurst, 1996):

$$\frac{\partial(hc)}{\partial t}+(1-\lambda)\frac{\partial z}{\partial t}+\frac{\partial g_x}{\partial x}+\frac{\partial g_y}{\partial y}=0 \qquad \text{Equation 2.6}$$

Where c ($m^3\ m^{-3}$) is the sediment concentration, h (m) is the depth of water and λ (-) is the soil surface porosity; z (m) is the depth of loose soil, t (s) is the time, g_x and g_y ($m^3\ s^{-1}\ m^{-1}$) are sediment transport rate in x and in y directions respectively. Erosion at a point can continue to take place if there is sufficient transport capacity to carry the suspended sediment load entering from upstream of the point. When the transport capacity of the flow is reached, deposition of the material commences. Transport capacity is calculated using the approach developed by Yalin (1963) for open channel flow, subsequently for overland flow.

2.3.3 The WEPP model

Water Erosion Prediction Project (WEPP) is a physically-based continuous simulation model and is based on fundamentals of stochastic weather generation, infiltration theory, hydrology, soil physics, plant science, hydraulic and erosion mechanics (Flanagan and Nearing, 1995). It is one of the most utilized tools for simulating soil erosion and sediment yields. It is a two-dimensional approach and is able to predict erosion and deposition along the hillslope profile and sediment delivery from the profile.

A. Hydrology Component

Daily or a single-storm climate data may be used in the WEPP. The data can be generated from two different methods: CLIGEN (Nicks et al., 1995) and Breakpoint Climate Data Generator (BCDG) (Zeleke et al., 1999). CLIGEN is used to generate the daily and monthly climate data for the WEPP. It generates mean monthly maximum and minimum temperature (°C), average solar radiation (Langleys day^{-1}) and average precipitation (mm). The daily time series data generated by the CLIGEN include daily precipitation (mm), duration of daily precipitation (h), time to peak (-) (i.e. the ratio of time of peak precipitation to total precipitation duration), intensity to

peak (-) (i.e. the ratio of peak intensity to average intensity of precipitation), daily maximum temperature (°C), daily minimum temperature (°C), daily solar radiation (Langleys day^{-1}), mean daily wind velocity (m s^{-1}), mean daily wind direction (°) and daily dew temperature (°C).

Generation of climate data from the CLIGEN is problematic when the resolution of the observed climate data is poor. Such situations generally happen in developing countries where the time series climate data are poorly recorded. In such cases, computations of various parameters for climate data generation such as time to peak and intensity to peak may be difficult to do with CLIGEN. To overcome the issue, the BCDG has been proposed to generate required continuous climate data for WEPP. Detailed procedures of climate generation in the BCDG are illustrated in Zeleke et al. (1999).

The hydrological simulations in the WEPP model include infiltration, runoff routing, soil evaporation, plant transpiration and seepage. For the simulations, the continuous water balance equation is used:

$$SW = SW_{in} + (P - I) \pm S - Q - ET - D - Q_d \qquad \text{Equation 2.7}$$

Where SW (m) is the total soil water content in any given day; SW_{in} (m) is the initial soil water content i.e. the soil water content of the previous day; P (m) is the cumulative precipitation of the given day and I (m) is the precipitation interception by vegetation in the given day. S (m) is the snow water content which is positive during melt and negative during accumulation; Q (m) is the surface runoff; ET (m) is the cumulative amount of evapo-transpiration; D (m) is the cumulative amount of deep percolation and Q_d (m) is the subsurface lateral flow.

Cumulative infiltration in the model is computed using Green-Ampt Mein Larson (GAML) model (Mein and Larson, 1973) modified by Chu (1978) for unsteady rainfall and multiple time to ponding. Chu (1978) introduces an indicator C_u (m) that determines if ponding occurs within a given interval of rainfall intensity assuming there is no ponding at the beginning of the interval as:

$$C_u = R_i - V_i - \left[\frac{K_e \psi \theta_d}{r_{i-1} - K_e} \right]$$ Equation 2.8

Where R_i (m) is the cumulative rainfall depth and V_i (m) is the cumulative rainfall excess depth. K_e (m s^{-1}) is the effective saturated hydraulic conductivity and Ψ (m) is the average capillary potential. θ_d (-) is the soil moisture deficit and r (m s^{-1}) is the rainfall rate. The soil moisture deficit (-) is computed as:

$$\theta_d = \eta_e - \theta_v$$ Equation 2.9

Where η_e (-) is the effective porosity, and θ_v (-) is the initial volumetric moisture content. The cumulative rainfall excess depth, V_i (m) is computed as difference between cumulative rainfall R_i (m) and cumulative infiltration depth, F_i (m). If C_u is positive, ponding occurs before the end of the interval and no ponding occurs when it is negative.

The depressional storage is related to random roughness and the slope of the flow and is derived using the model proposed by Onstad (1984). When the infiltration and depressional storage are exceeded, a rainfall excess occurs. Once the rainfall excess occurs, peak discharge is computed using the kinematic wave model which can be expressed as:

$$\frac{\partial h}{\partial t} + \frac{\partial q}{\partial x} = v$$ Equation 2.10

Where v (m s^{-1}) is the rainfall excess rate; h (m) is the depth of flow and q (m^3 m^{-1} s^{-1}) is the discharge per unit width of plan; t (s) is the time and x (m) is the distance. The value of q is given by:

$$q = \alpha h^m$$ Equation 2.11

Where α ($m^{0.5}$ s^{-1}) is the depth discharge coefficient ($m^{0.5}$ s^{-1}) and m is the depth discharge exponent (-). The value of α is computed using the Chezy equation.

In shallow soil profiles, the subsurface flow is one of the dominant forms of water yield. The WEPP model simulates the subsurface flow using the equation developed by Sloan and Moore (1984) applying the mass continuity equation within entire hillslope as control volume. The drainable thickness, $H_0(d)$ (m) for any given day in the model is calculated by:

$$H_0(d) = \frac{H_0(d-1)\{L\theta - 8640 K_{e(\theta)} \sin\alpha + 2L(P_e (D + ET))\}}{L\theta_d + 8640 K_{e(\theta)} \sin\alpha} \qquad \text{Equation 2.12}$$

Where $H_0(d-1)$ (m) is the drainable thickness of the previous day; L (m) is the length of the each overland flow element, and θ (m^3 m^{-3}) is the volumetric moisture content. $K_{e(\theta)}$ (m d^{-1}) is the hydraulic conductivity at moisture content θ and α (°) is the average slope of the profile. P_e (m d^{-1}) is the percolated water to the drainable layer; D ((m d^{-1}) is seepage out of the drainable layer, and ET (m d^{-1}) is the actual evapo-transpiration from the drainable layer.

B. Erosion Component

Erosion modelling in the WEPP is based on the continuity equation that describes the movement of sediment in a rill:

$$D_i + D_r = \frac{dG}{dx} \qquad \text{Equation 2.13}$$

Where x (m) is downslope distance; G (kg s^{-1} m^{-1}) is the sediment load and D_i (kg s^{-1} m^{-2}) is the inter-rill sediment delivery. D_r (kg s^{-1} m^{-2}) is the rill erosion rate (+ for detachment and – for deposition). The inter-rill (D_i) and rill (D_r) are computed on the basis of rill area and G is solved per unit rill width basis. The inter-rill component delivers sediment from inter-rill parts of the hillslope to the rills and this component is simulated as:

$$D_i = K_{iadj} I_e \sigma_{ir} SDR_{RR} F_{nozzle} \left[\frac{R_s}{w} \right]$$ Equation 2.14

Where K_{iadj} (kg m^{-4} s^{-1}) is the inter-rill erodibility, I_e (m s^{-1}) is the effective rainfall intensity and σ_{ir} (m s^{-1}) is the inter-rill runoff rate. SDR_{RR} (-) is the sediment delivery ratio which is the function of random roughness, side slope and particle size distribution and F_{nozzle} (-) is the irrigation adjustment factor. R_s (m) is the rill spacing and w (m) is the width of the rill.

Rill erosion is related to the detachment capacity by the rills and sediment transport capacity in the rills. The rill detachment is predicted when the flow shear stress exceeds the critical shear stress of the soil and when the sediment load is below the calculated sediment transport capacity. The rill erosion is thus given by:

$$D_r = D_c \left[\frac{T_c - G}{T_c} \right]$$ Equation 2.15

Where D_c (kg s^{-1} m^{-2}) is the detachment capacity by the rill and T_c (kg s^{-1} m^{-1}) is the sediment transport capacity. The detachment capacity (D_c) by the rill is further estimated as:

$$D_c = K_r (\tau_f - \tau_c)$$ Equation 2.16

Where K_r (s) is the rill erodibility parameter; τ_f (Pa) is the flow shear stress acting on the soil and τ_c (Pa) is the critical shear stress of the soil. Rill detachment is considered to be zero when the shear stress is less than the critical shear stress of the soil.

Net deposition in a rill is predicted when the sediment load (G) is greater than the sediment transport capacity (T_c). The transport capacity is defined by Yalin (1963) after modification by Foster (1982). The deposition is computed as:

$$D_r = \frac{\beta V_f}{q} (T_c - G)$$ Equation 2.17

Where V_f (m s^{-1}) is the effective fall velocity for sediment, q is the flow discharge per width (m^2 s^{-1}) and β is the rainfall turbulence coefficient.

2.3.4 The WEPP catchment model

WEPP can be applied to a hillslope or to a watershed. The WEPP watershed model is an extension of the hillslope model that is applicable to small agricultural watersheds (Ascough et al., 1997). Each watershed has hillslopes i.e. sub-catchments, channels and impoundments. Hillslopes can drain to the left, right and top of individual channels. However, in the case of a secondary channel (i.e. one created by the junction of two other channels) there will be one hillslope to the left and another to the right of the channel but no hillslope draining on the top of the channel. Each hillslope can only contribute sediment and runoff to a single channel. Runoff and sediment yield from adjacent hillslopes is distributed evenly along the channel length. While translating the hillslopes into the WEPP format, hillslopes are represented as rectangular areas with a length and width (Figure 2.4). The topography of each hillslope is represented by a single slope profile with length equal to the length of the representative rectangular hillslope. The hillslopes can further be divided into multiple overland flow elements (OFEs) to incorporate the spatial distribution of soil and vegetation type. Soil and vegetation characteristics in each OFE are unique and uniform. The WEPP watershed model can also simulate various types of impoundments such as farm ponds, culverts, filter fences and check dams. Impoundments can be located between channels or at the bottom of a hillslope.

The application of the WEPP model in a catchment has been made possible by progress in the development of computer tools and technologies such as GIS. GIS is a widely accepted tool used in catchment-scale hydrological modelling. To apply it to a catchment-scale, the catchment is discretised into a number of sub-catchments (i.e. hillslopes) (Cochrane and Flanagan, 2003; Renschler, 2003). Digital elevation models (DEMs) in a grid-based format of certain resolution can be used to extract hillslopes, channels and slope profiles in WEPP (Cochrane and Flanagan, 1999). To do this, flow-routing algorithms that find out the steepest descent direction and gradient between cells are used. Various flow-routing algorithms are presented in the research of O'Callaghan and Mark (1984), Zevenbergen and Thorne (1987), Jenson and

Domingue (1988), Martz and Garbrecht (1992) and Tarboton et al. (1991). Another commonly used tool to analyse the landscape is TOpographic PArameterizZation (TOPAZ) (Garbrecht and Martz, 1995). This is an automated digital landscape analysis tool for topographic evaluation, drainage identification, watershed segmentation and sub-catchment parameterisation. TOPAZ has an advantage over other traditional tools because it has additional ability to overcome their limitations with respect to channel network identification in depression and over flat terrain. TOPAZ requires a critical source area (CSA) and a minimum source channel length (MSCL) to derive channel networks and sub-catchments. The CSA and MSCL represent respectively a drainage area and length whose concentrated flow defines the beginning of a channel (Garbrecht and Martz, 1995).

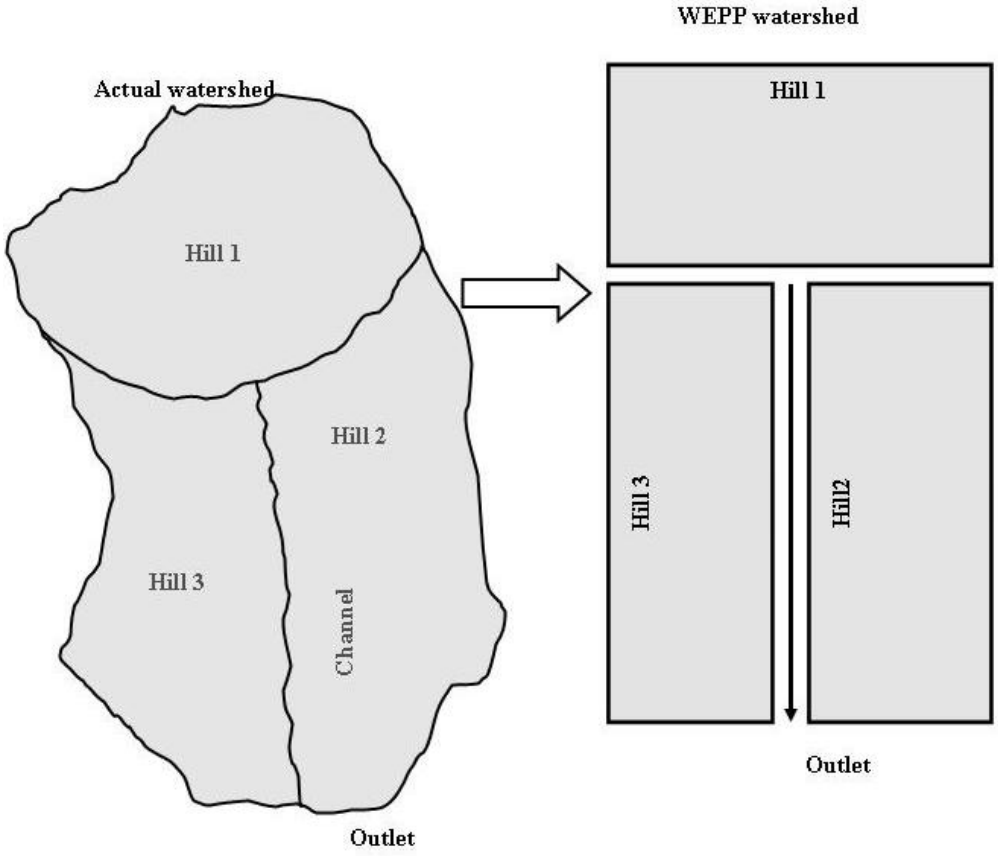

Figure 2.4: Discretisation of watershed into WEPP hillslopes and channels.

The WEPP catchment simulation can be performed with either of two procedures: the Hillslope method; and Flowpath method. The Hillslope method allows simulating sediment and runoff from a single representative profile for each sub-catchment. A representative slope profile (Figure 2.5) is derived from the sub-catchment that

represents the slope profile of all individual flowpaths within the sub-catchment. Cochrane and Flanagan (1999) developed three different methods of creating representative slope profiles using flowpaths derived from DEMs. These methods are linear, weighted and exponentially transformed average methods. Flowpaths are defined as the route water travels when flowing from one area of a catchment to the next, starting from an area having no water inflow and terminating at a channel. Generally, each hillslope may have a large number of flowpaths. The flowpaths may start at the watershed boundary or at points within the watershed. It is worth noting that length of a representative slope profile is an important aspect in the discretisation process used in the Hillslope method. Since a WEPP hillslope is represented as a rectangular surface with a fixed width and length, calculations are greatly simplified for application with GIS. However, this may not produce an adequate representation of the hillslope and results of runoff or sediment yield may be biased (Cochrane and Flanagan, 2003).

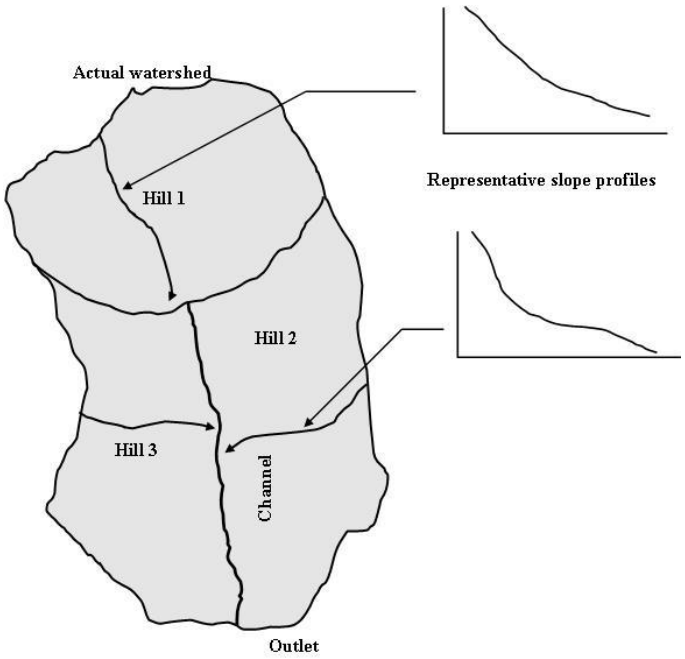

Figure 2.5: Defining representative slope profiles for each hillslope in the catchment.

Another method of applying WEPP to a catchment is the Flowpath method. In this method, WEPP is applied to all possible flowpaths in the catchment. Many flowpaths may eventually intersect (Figure 2.6) as they approach a channel. At locations where flowpaths intersect, erosion is calculated by using a weighted average approach. All the points where flowpaths drain into a channel are also identified. For every one of

these points, an average quantity for sediment and runoff discharging into the channel is calculated (Cochrane and Flanagan, 1999). For example, Figure 2.6 shows three flowpaths (1, 2 and 3); two flowpaths (2 and 3) intersect at point C and all three at point B. Point A represents the location where all runoff and sediment is discharged to the channel from these flowpaths. Initially, WEPP is applied for each flowpath using the actual slope profile of the flowpath. The width used for the WEPP application for individual flowpath is calculated by dividing the total area of all three flowpaths (represented in yellow in Figure 2.6) by the length of individual flowpath. The results of WEPP application to each of three flowpaths are averaged to obtain sediment loss and runoff into the channel at point A.

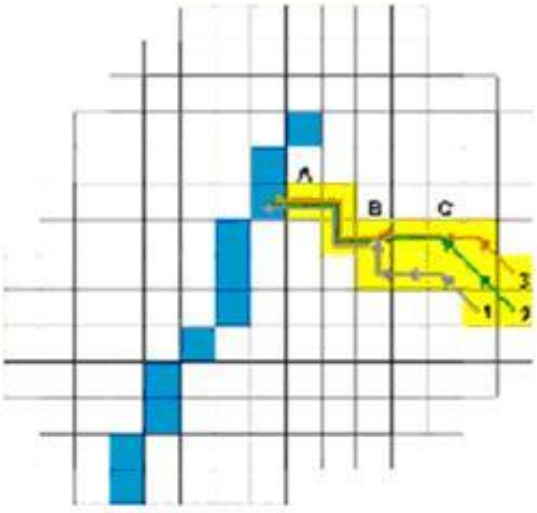

Figure 2.6: Intersecting flowpaths draining into a channel in a catchment (Source: Cochrane, 1999).

2.3.5 Erosion models summary

Erosion on a hillslope profile can be divided into two major components: rill and inter-rill erosion. Inter-rill erosion is assumed to be constant down a profile on uniform slopes, whereas the rill erosion may increase down the slope. The sediment load is a summation of the rill and its constant inter-rill contribution. In empirical models such as USLE, both inter-rill and rill areas are lumped together, but the effects of rill and inter-rill areas are adjusted by changing the equations for slope factor and ratio of inter-rill and rill erosion in the length factor. Application of USLE in the present research is not possible because it does not relate erosion with the actual hydrological process.

SHETRAN is a physically-based spatially-distributed model for runoff, soil erosion and sediment yield and solute transport. It simulates soil erosion by raindrop impact, leaf drip and sheet overland flow, and the transport of eroded materials by overland flow. For channel, the component simulates the soil erosion of the bed material and the downstream transport of this material together with that supplied by overland flow. It is a catchment-scale model and the application of the model to a hillslope profile is not possible.

WEPP simulates the soil loss by adding the sediment loss from the inter-rill areas to the rill areas, which is dependent on detachment capacity by rill flow and sediment transport capacity. In WEPP, an empirical equation is used to estimate the sediment yield from inter-rill areas. Individual processes of the detachment and transport in the inter-rill area are not incorporated. The equations for estimating inter-rill erosion were derived from various studies and are considered simple and stable (Nearing and Parker, 1994). The contribution of inter-rill to rill is considered independent of distance downslope and sediment delivery to rills is adjusted for ground cover, dead and live roots, canopy cover and plant and soil management practices affecting infiltration. Inter-rill process may be dominant in cases where gradients are low, and slope lengths are short. In rangelands and no-till areas, the inter-rill processes prevail. But in the most other cases, rills are the major sediment carriers. Any factor that influences the formation of rills, quantity of rills or transport and detachment in a rill will have a significant effect on the sediment loss; for example, surface cover, management practices and soil factors (textures, structures) affect the hydraulic properties in the rill, and thus may have impact on sediment loss.

For hydrological simulations, WEPP uses a continuous water balance equation. This equation incorporates all possible hydrological features such as evapo-transpiration, infiltration, percolation, precipitation, snow water content, interception by vegetation, subsurface flow etc. Recent studies have shown that WEPP can adequately simulate the water balance and runoff (Yu and Rosewell, 2001; Pieri et al., 2007). These studies have shown that the water balance and runoff simulations are highly sensitive to defining a restrictive layer at the bottom of the soil profile, and model calibration parameters, primarily hydraulic conductivity.

The deep percolation component of WEPP uses storage routing techniques to predict flow through each soil layer in the root zone. In each layer, water content exceeding the corresponding field capacity is subjected to percolation through the succeeding layer. Water moving below the root zone is considered lost and will not be traced. The daily subsurface flow in WEPP is simulated using a simple storage-discharge model (Sloan and Moore, 1984). The model uses a mass continuity equation for the entire hillslope as a control volume. The subsurface flow model incorporates the influence of upslope contributing length to simulate the downslope subsurface flow.

2.4 Landslide processes

2.4.1 General landslide features

The term ‘landslide’ is generally used to denote a downslope movement of mass of earth, debris or rock down a slope due to the action of external forces such as rainfall, snowmelt, volcanic eruption, earthquakes, anthropogenic activities etc. Any landslide is generally classified and described by two nouns: the first describes the materials (e.g. earth, debris or rock); and the second, the type of movement (e.g. falls, topples, slides, flows, spread etc.) (Varnes, 1978). As shown in Table 2.1, a fall starts with detachment of soil or rock from a steep slope along a surface on which little or no shear displacement takes place. The material then descends largely through air by falling or rolling.

A toppling occurs as a result of overturning of blocks rather than sliding or falling. It is a forward rotation, out of the slope, of a mass of soil or rock about a point axis below the gravity of the displaced mass. A slide, on the other hand, is the downslope movement of a soil or rock mass occurring dominantly on the surface of rupture or relatively thin zones of intense shear strain. The term ‘spread’ refers to an extension of cohesive soil or rock mass combined with a general subsidence of the fractured mass of a cohesive material into softer underlying material. The spread may result in from liquefaction or flow of softer materials. In flows, materials move as a coherent but constantly changing mass, involving internal shear or mixing of the mass and even sorting based on particle size and position in the flow. The distribution of velocities in displacing mass resembles that in a viscous fluid.

Table 2.1: Landslide classification (Source: Varnes, 1978).

Type of movement		Type of material		
		Bedrock	Soil	
			Coarse	Fine
Fall		Rock fall	Debris fall	Earth fall
Topple		Rock topple	Debris topple	Earth topple
Slide	Rotational Translation	Rock slide	Debris slide	Earth slide
Spread		Rock spread	Debris spread	Earth spread
Flow		Rock flow	Debris flow	Earth flow
Complex		Combination of two or more		

The landslides occur when stresses acting on soil mass on a hillslope exceed the soil strength. It has generally been recognized that these forces are functions of various parameters relating to bedrock geology, lithology, geotechnical properties, rainfall characteristics and duration, groundwater conditions and land-use patterns. As well as natural factors, in many cases human interferences are also responsible for triggering the landslides and create the same effects on a slope as a range of natural processes. Some of the common examples of human interferences leading to landslides are changes in land-cover, deforestation, cutting of slopes etc.

2.4.2 Water-induced landslide processes

Deep-seated landslides

Storms that produce intense rainfall for periods as short as several hours, or a more moderate and low intensity lasting several days, have triggered abundant landslides in many parts of the world. Water-induced landslides are often grouped as shallow and deep-seated landslides depending on the depth and mode of failures. The frequency and magnitude of rainfall events, together with other factors such as lithology, morphology and land-cover, influence the type of landslide. Landslides in which the sliding surface is mostly deeply located below the maximum rooting depth of trees (typically a depth greater than 10 metres) are called deep-seated landslides. A typical example of a deep-seated landslide is shown in Figure 2.7. It is usually believed that the deep-seated landslides are triggered by moderate rainfall intensity distributed over

long periods. Deep-seated landslides are generally slow moving in nature and rarely claim lives, but may cause high property damage. The failure modes in such cases are generally rotational or complex types.

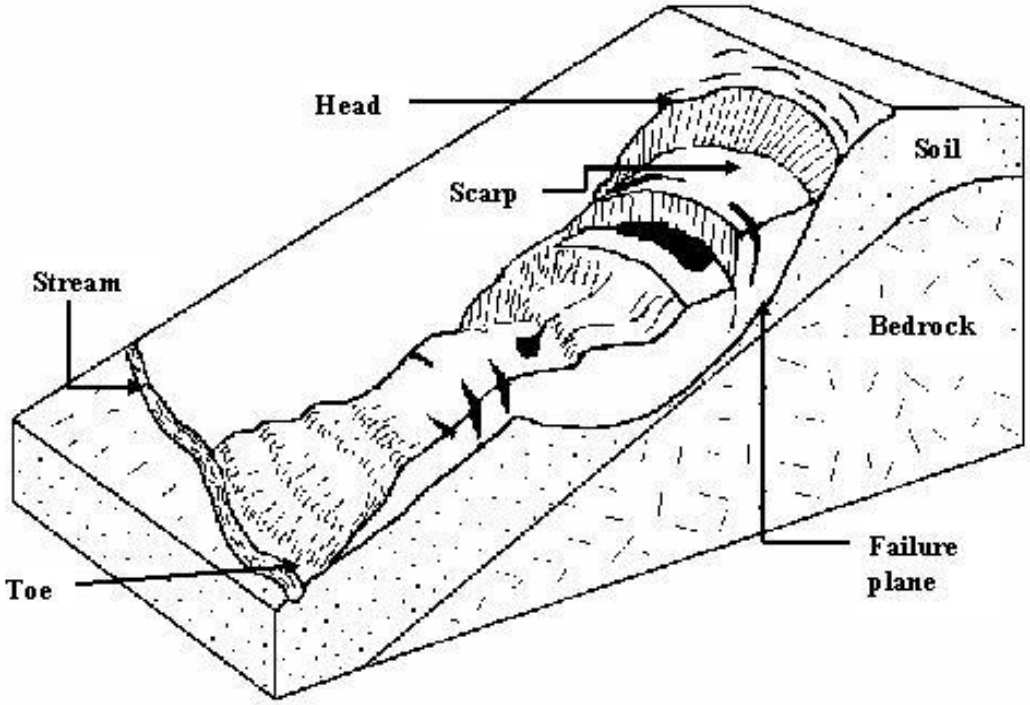

Figure 2.7: Deep-seated landslide characteristics (Source: Cruden and Varnes, 1996).

Shallow landslides

Landslides in which the sliding surface is located within the soil mantle or weathered bedrock (typically to a depth from a few decimetres to several metres) are categorized as shallow landslides. The surface of the slope in steep hilly and mountainous regions is quite often underlain by a plane of weakness lying parallel to it and therefore, shallow landslides are predominant. A schematic diagram of a shallow landslide has been presented in Figure 2.8. In many cases, the shallow landslides are fast-moving and are extremely destructive, causing wide-spread damage and casualties. Shallow landslides can pose grave threat to life and property (Larsen et al., 2000).

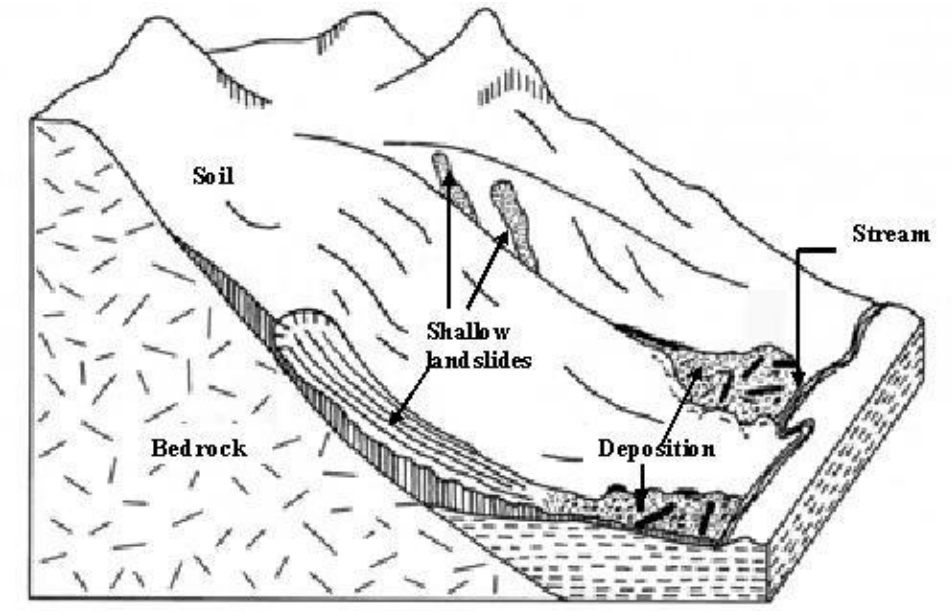

Figure 2.8: Schematic diagram of shallow landslides (Source: Sidle and Ochiai, 2006).

Shallow landslides are often triggered in hilly and mountainous regions in short duration intense rainfall events. Rainfall events increase the pore pressure in the soil. Pore pressure is the amount of force (pressure) exerted by water to the soil. During intense rainfall events, the variations in pore pressures distributed within the soil are highly variable depending on the hydraulic conductivity, topography and other properties of soils. Increase in pore pressure may be directly related to rainfall infiltration and percolation or may be the result of build-up of a perched groundwater table (Terlien, 1998).

It is typically observed that high pore pressures are generated in lower areas of a hillslope (Anderson and Sitar, 1995). Various studies report that the response of the material involved in the pore pressure development is largely dependent on its hydraulic conductivity. In high-permeable soils, generation and dissipation of pore pressures during intense rainfall events can be very rapid (Johnson and Sitar, 1990). In these cases, slope failures are caused by intense rainfall, and antecedent rainfall has little influence on landslide occurrence (Corominas, 2001). On the contrary, in low-permeability soils the reduction in soil suction and the increase in pore pressure are generally caused by long duration-moderate intensity rainfall events. In such soils,

antecedent rainfall is considered a necessary condition for landslide occurrence (Wieczorek, 1987; Sanderson et al., 1996).

Slopes with different permeability have distinct hydraulic and mechanic behaviours during the same rainfall process; for example, Lan et al. (2005) state that in a slope with lower permeability, its shallow portion responds rapidly to the rainfall, where the infiltration capacity is quickly reached, resulting in loss of soil suction and increase of pore pressure. This suggests that a slope with lower permeability might be more prone to shallow slope failure even in moderately intense rainfall events. Its deeper portion responds more slowly. The high pore pressure at a shallow depth tends to be maintained for a longer period even after the rainfall has stopped. In contrast, the shallow portion of highly permeable soils responds more slowly because of high infiltration capacity. The deeper parts of these soils tend to respond simultaneously with the shallower portions.

Pore pressure generation is greatly dependent on the initial density of the soil profiles. Iverson et al. (2000) report that sufficient pore pressures required to trigger landslides can not be generated in dense soil. Wang and Sassa (2001, 2003) relate the pore pressure generation with the relative density. They suggest that with increasing relative density, pore pressure increases up to a certain value, and thereafter the pressure decreases. The relative density is a term that measures the state of compactness of a natural soil and is expressed as $((e_{max} - e)/(e_{max}-e_{min}))$, where e, e_{max} and e_{min} are the void ratio of the soil at natural, loosest and densest state respectively. Soils in loose state (high porosity) have greater water holding capacity and therefore higher pore pressures are usually generated.

Generation of high pore pressure may also result in liquefaction. Liquefaction is a process by which the soil suddenly loses a large proportion of its shear strength and is also a reason for fluidised landslides. Fluidised landslides that travel a long distance at high speed are one of the most dangerous types of landslides, resulting in extensive property damage and loss of lives (Sassa, 2000). Fluidised slope failures are common both in artificial cut slopes and in natural slopes.

Slope failure occurs at a potential slip surface depth which depends on geotechnical properties of the soil and sloping profile characteristics i.e. slope and depth. Terlien (1997) concludes that failure will only take place when the soil becomes saturated from the terrain surface to the depth of the potential slip surface. This saturation depth is a function of the soil profile, initial soil moisture distribution, and rainfall amount and intensity.

As well as soil properties, changes in land-cover due to human interferences also influence the occurrence and distribution of shallow landslides. In particular, forest logging, fire and cultivation on hillslopes are considered the most important in triggering shallow landslides (Cannon, 2000; Squier and Harvey, 2000). For example, change in the forest cover, particularly from clear-cut harvesting affect various hydrological processes such as interception and transpiration. It is well established that forests in sloping ground possess high transpiration and interception rates that increase soil moisture deficit (making the soil drier) allowing reduced pore pressures (Greenway, 1987). The harvesting reduces vegetation surcharge and root cohesion (binding action), resulting in decrease in slope stability and increase in the distribution of shallow landslides (Sidle et al., 1985; Sidle, 1991; Dhakal and Sidle, 2003). Therefore, re-vegetation is often recommended for slope stabilization (Morgan and Rickson, 1995).

2.5 Laboratory scale shallow landslide studies

A deep understanding of landslide triggering factors has been gained from both laboratory experiments under controlled conditions and field observations. Laboratory scale studies are generally carried out to trigger slope failures under simulated rainfall in sloping flumes. Most of the flume-based landslide studies deal with pore pressure generation before, during, and immediately after the slope failure and the influence of soil properties such as grain size on pore pressure generation. For example, Sassa (1984) performed a series of flume test and reported that increasing pore pressure due to un-drained soil layer caused the slope failures during rainfall and the generation of the pore pressure was a result of sudden initiation of subsidence. Iverson and LaHusen (1989) used a rainfall simulator to investigate the distribution of pore pressure near the slip surface. Their landslide experiments showed that a shear rate higher than a certain value led to periodical fluctuation of excess pore pressure near the slip surface.

They inferred that the periodic fluctuation of excess pore pressure occurred when blocks of the failure materials were rearranged and the fluctuation discontinuously reduced the effective stress allowing the landslide mass to travel a long distance.

Eckersely (1990) triggered flowslides in a coal stockpile by raising the water table and showed that the excess pore pressures were generated during rather than before failures. Iverson et al. (1997, 2000) triggered slope failure mobilisation in loose and dense soil in a large experimental flume (95 m long and 2 m wide). In their experiments, rapid increase in pore pressures were observed at the time of failure in loose soil and the soil quickly attained a liquefied appearance. The dense soil on the other hand exhibited slower and more piecemeal initial slope failure and fully mobilised flow did not occur until the moving mass descends some distance in the downslope. In their experiments, the development of pore pressures needed to trigger slope failure in the dense soil was relatively slow and was about twice as large as pore water pressure to trigger the slope failure of loose soil. The average motion of the landslide in dense soil proceeded about 300 times more slowly than the motion of the landslide in loose soil.

In presenting time series pore pressures, Wang and Sassa (2001) observed an abrupt increase in pore pressures immediately after the slope failure initiation. In their flume experiments, they noticed a gradual increase in pore pressure just before slope failure initiation whereas immediately after failure, the pore pressure rose rapidly due to fast shearing rates. Okura et al. (2002) used flume experiments to study the landslide fluidisation processes. In their experiments, they noticed that the landslide fluidisation processes undergo three stages: volumetric compaction with shear, generation of excess pore pressure and induction of fast shearing. These three steps occurred simultaneously.

Wang and Sassa (2003) conducted a series of slope failure experiments in a sloping flume using purely sandy soil and sandy soil with increased finer (loess) contents from 10 to 30% to study the slope failure modes and impact of grain size on pore pressure generation. Their studies revealed that high pore pressures were observed when the fractions of loess were increased. In the failure mode study, they noted retrogressive failure types in the coarser materials and flowslides in the finer ones.

The mobility increased with the increase in finer content of the soil; slow mobilisation rates were observed in coarser grained soils.

Lourenco et al. (2006) studied the pore pressure distribution and failure mode at the interface of two layers of different permeability in an experimental flume. Their experiments were conducted under two hydrologic conditions: downward infiltration with water infiltrating from the top of the upper layer supplied by a rainfall simulator; and upward infiltration with water infiltrating from the bottom of the lower layer. Their results revealed that the failure modes were mostly dependent on the layer position. Seepage erosion was noticed to dominate failure if the lower layer was coarser while retrogressive failure of the upper layer was the most relevant failure mechanism if the lower layer was finer. They noticed that the pore pressure distribution with the two layers was influenced by the infiltration direction: the upward infiltration resulted in a rise in the pore pressure from the bottom to top whereas by downward infiltration perched water tables were formed in the upper finer layer. Olivares and Damiano (2007) used a flume experiment and listed the conditions necessary for the development of a complete landslide fluidisation as susceptibility of the soils to static liquefaction; attainment of fully saturated condition at the start of instability and; slow dissipation of excess pore pressure.

Tohari et al. (2007) conducted flume experiments in wet and dry soils to study the soil moisture regimes during failure. Hydrologic responses during failures of an initially dry and permeable hillslope differed from that of initially wet and less permeable hillslopes. In the former case, the soil moisture content increased in two stages advancing the wetting front from the slope surface and developing the groundwater table at the slope surface. On the other hand, the initially wet and less permeable hillslope exhibited only one stage of increase of moisture content in response to rainfall corresponding to the advancement of saturated wetting front. The commencement of slope failures tended to occur as soil moisture content attained a near saturated value.

2.6 Shallow landslide modelling

Landslide modelling is based on a variety of approaches and models. Statistical and physically-based approaches are widely adopted tools in landslide modelling.

2.6.1 Statistical approach

The statistical methods are based on conceptual models. These models first require identification and mapping of a set of landslide causing (geological and geo-morphological) factors that are directly or indirectly related to slope failures. Then, it involves an estimate of the relative contribution of these factors in generating slope failures, and classification of land surfaces into zones of different hazard or susceptibility degree (Aleotti and Chowdhury, 1999; Süzen and Doyuran, 2004, Pathak and Nilsen, 2004). Bivariate and multivariate statistical methods are the most commonly used for these predictions. The bivariate statistical analysis is a method that describes the relationship between two variables. In landslide modelling, the bivariate method links each landslide causing factor to the landslide distribution map.

On the other hand, in multivariate statistical analysis, the weighted factors controlling the landslide occurrence indicate a relative contribution of each of these factors to the degree of landslide hazard within a defined land unit. The common property of these analyses is their nature of being based on the presence or absence of stability phenomena within these previously defined land units (Van Westen, 2000). The statistical approach can provide an insight into the multifaceted processes involved in shallow landslide occurrence, and useful assessments of susceptibility to shallow landslide hazard in large areas. However, the results are very sensitive to the data set used in the analysis and it is not straightforward to derive the hazard (i.e. probability of occurrence) from the susceptibility.

2.6.2 Physically-based approach

Another approach deals with the spatially-distributed and physically-based models by coupling a slope stability equation with a subsurface hydrological model. The slope stability model obeys the Coulomb failure criterion. The criterion describes the state of stress on surfaces where failure occurs (Lambe and Whiteman, 1979; Cernica, 1995). In its simplest form, the criterion may be expressed as:

$$\tau = c + (\sigma - p)\tan\varphi \qquad \text{Equation 2.18}$$

Where τ (N m^{-2}) is the shear strength, c (N m^{-2}) is the soil cohesion, σ (N m^{-2}) is the normal stress, p (N m^{-2}) is the pore pressure and φ (°) is the angle of internal friction. The Coulomb slope failure model dictates that the failure must occur at a depth where the shear stress equals the strength. As shown in Equation 2.18, Coulomb strength decreases with the increase in pore pressure distribution.

Physically-based landslide models compute a safety factor (Fs) which is the ratio of the Coulomb shear strength, i.e. stabilizing force, to the shear stress, i.e. destabilizing force, occurring in the hillslopes (Graham, 1984). The effect of gravity on the soil mass acts as a destabilizing force. Whenever the safety factor (Fs) is less than 1 for a slope, the slope is predicted to fail. Different approaches have been developed to compute the safety factor (Fs). These include: circular arc analysis; method of slices; infinite slope method, etc.

Circular arc analysis and method of slices

The circular arc analysis and method of slices are mainly based on the principal assumption that a landslide occurs in a curved failure plane. All the acting forces in the potential failure plane are computed and then the safety factor for the slope is calculated. A major distinction between the circular arc analysis and the method of slices is that the method of slices further divides the slope profiles into different vertical sections to incorporate the spatial variability of soil properties within the profile. These two approaches are commonly used to analyse deep-seated landslides (Xie et al., 2003; Chen et al., 2006; Wang et al., 2006). An example illustrating the method of slices is shown in Figure 2.9. In the figure, R (m) is the radius of the failure plane, α_n (°) is the positive or negative dip angle of the tangent line at the centre of the n^{th} slice base, σ_n (N m^{-2}) is the effective stress at the n^{th} slice base, L_n (m) is the base length of the n^{th} slice, and W_n (N) is the weight of the n^{th} slice.

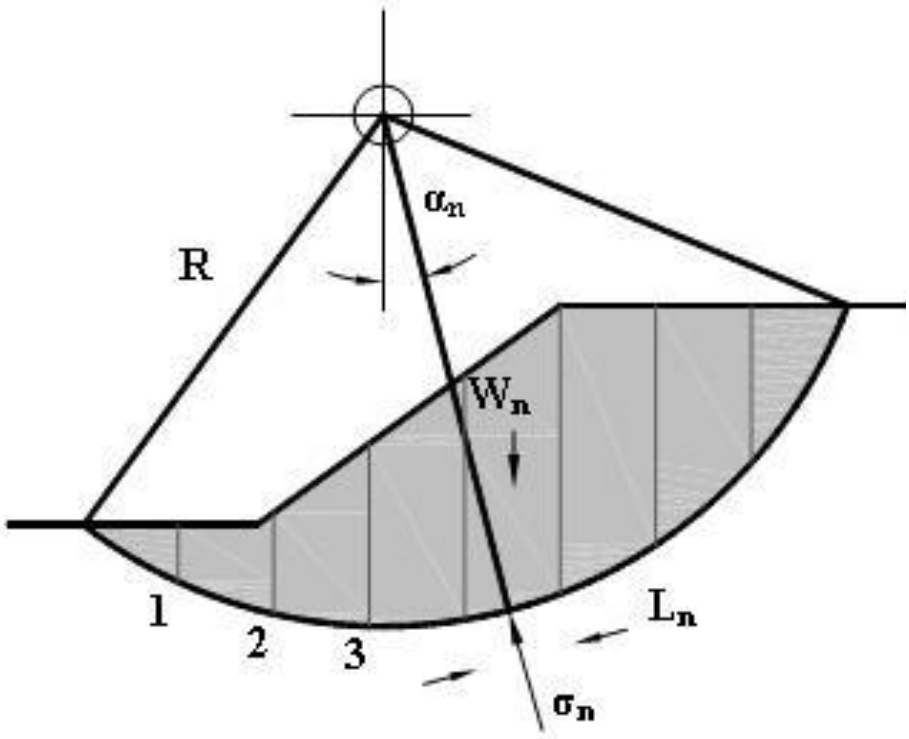

Figure 2.9: Dividing failure mass into different slices in the method of slices (Source: Shahgholi et al., 2001). Symbols are explained in text.

Infinite slope method

In the infinite slope method, the soil slope is assumed to slide on a slip surface parallel to the ground surface, and the slope is assumed to be infinite in extent at an inclination. When the thickness of the soil is much less than the length of the slope, the edging effects are negligible and the infinite slope method is assumed to be valid (Skempton and DeLory, 1957). This method is widely used in modelling shallow landslides in hilly and mountainous catchments (Montgomery and Dietrich, 1994; Pack et al., 2001; Acharya et al., 2006; Rosso et al., 2006). The geometry of the slope, failure plane and other variables assumed in the method are shown in Figure 2.10. In this method, the safety factor is generally computed using the equation proposed by Van Westen and Terlien (1996) as:

$$Fs = \frac{C_s + C_r}{D\gamma_e \sin\theta} + \left[1 - m\frac{\gamma_w}{\gamma_e}\right]\frac{\tan\varphi}{\tan\theta} \qquad \text{Equation 2.19}$$

Where Fs (-) is the safety factor, C_s and C_r (Nm^{-2}) are the soil and root cohesion related to the soil and the vegetation types; D (m) is the depth of the overlying soil. φ (°) is the angle of internal friction; θ (°) is the local slope angle, γ_w (Nm^{-3}) is the unit weight of water and γ_e (Nm^{-3}) is the effective unit weight of the soil, and is given by:

$$\gamma_e = \frac{q\cos\theta}{D} + m\gamma_s + (1-m)\gamma_d \qquad \text{Equation 2.20}$$

Where γ_d (Nm^{-3}) is the dry unit weight; γ_s (Nm^{-3}) is the saturated unit weight; q is the surcharge (Nm^{-2}) on the soil surface. The term, m (-) in Equations 2.19 and 2.20, is the wetness index that expresses the relative water table height (i.e. h_w/D), where h_w (m) is the water table height above the underlying bedrock. Every term except, 'm', in Equations 2.19 and 2.20 is variable in space. In shallow landslide modelling, these parameters are determined from laboratory tests, field investigation, and literature and look-up tables. The 'm' is a hydrological term and is a measure of relative water table height thus varies both in space and time.

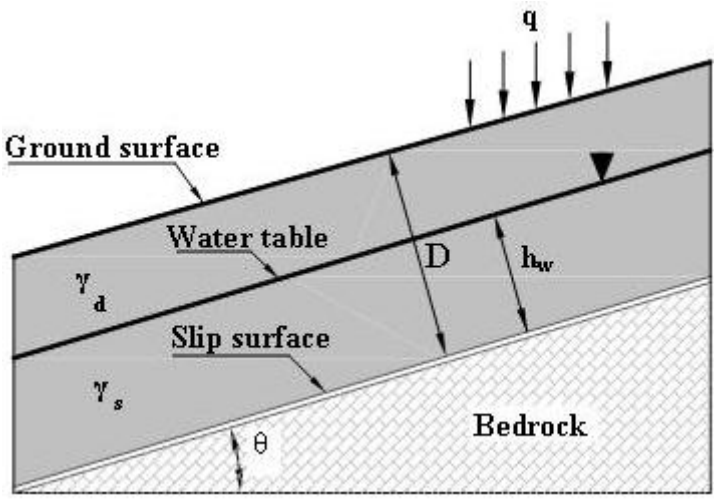

Figure 2.10: Schematic representation of the infinite slope method depicting various parameters and variables (Source: Skempton and DeLory, 1957). Symbols are explained in text.

Different methodologies have been developed to quantify the wetness index. In an initial approach to compute the index, Beven and Kirkby (1979) propose a simple topographic index, (ln(a/tanθ)) where a (m^2 m^{-1}) is the specific upslope contributing

area, and θ (°) is the local slope. The model assumes the contributing area as a surrogate for the local subsurface flow rate. The upslope contributing area of a point of interest is the area draining to the point from its upstream.

Subsurface hydrological simulations for shallow landslide modelling

One of the most commonly employed subsurface hydrological models for shallow landslide modelling is based on assumptions of a quasi-steady water table and that groundwater flows parallel to the hillslope (Barling et al., 1994; Montgomery and Dietrich, 1994; Borga et al., 1998; Acharya et al., 2006). The model assumes that the recharge rate is uniformly distributed and subsurface flow is routed under a uniform recharge rate using a spatially variable velocity. In the model, the wetness index is dependent on the local slope, upslope contributing area and soil profile properties such as hydraulic conductivity, depth etc. and is given by $m = \frac{i\,a}{K\,D\sin\theta}$, where i ($m\ s^{-1}$) is the recharge rate; a ($m^2\ m^{-1}$) is the specific upslope contributing area; K ($m\ s^{-1}$) is the hydraulic conductivity. D (m) and θ (°) are defined in Equations 2.19 and 2.20.

The Green-Ampt infiltration model (Green and Ampt, 1911) has also been used to derive the wetness index in landslide modelling (Fuchu et al., 1999; Delmonaco et al., 2003; Tofani et al., 2005 and Casagli et al., 2006). In this approach, the cumulative infiltration amount is first computed and is then uniformly distributed over the soil profile depth. This model, however, ignores the subsurface flow from the upslope contributing area. Some dynamic subsurface flow models are also used to compute the soil wetness index for shallow landslide modelling (Casadei et al., 2003; Gorsevski et al., 2006). Various hydrological components, such as precipitation (rainfall and snow melt), evapo-transpiration, surface runoff, and upslope subsurface flow, are incorporated in the models.

2.7 Shallow landslide mobilisation and sediment yield

Failed soil materials mobilise to the downslope. The materials may deposit immediately downslope from the landslide scar or may travel a considerable distance. If the failed materials travel down a steep hillslope in hilly and mountainous regions with high pore pressures, the materials release such energy that debris flows nearly always develop. In the mobilisation processes, the region affected between the

landslide initiation and the final deposition is generally referred to as runout or travel distance. The material continues to move downslope until the slope gradient falls below that needed to maintain the flow (Burton and Bathurst, 1998). The continued mobilisation of materials therefore, requires: sufficient water to saturate (or nearly saturate) the soil; high pore pressure; and a sufficiently steep downslope region for gravity effects (Corominas, 1996; Iverson et al., 1997; Dai and Lee, 2002; Hunter and Fell, 2003; Malet et al. 2005). The volume of landslides also influences the runout distance; the runout distances are higher in larger failure examples (Korup et al., 2004; Malet et al., 2005).

Failure of hillslope materials, and the consequent transportation of the failed materials, is one of the principal processes of soil redistribution and the evolution of new hillslope profiles. Conservation of mass dictates that continued surface displacement must eventually decrease the surface elevation and the slope gradient in an active landslide, whereas the surface elevation and the slope gradient should increase in the deposition areas. Soil redistribution processes are responsible for localized changes in hillslope topography. The changes are related to landslide characteristics such as quantity and location, runout distance, and other properties relating to soil profiles.

It is generally accepted that water-induced shallow landslides can be significant sources of sediment supply in hilly and mountainous catchments (Benda and Dunne, 1997; Korup et al., 2004). The materials from the landslides can usually be transported to a channel network if the landslides are connected with the channels, and the failure materials evolve into debris flows after breaking and mixing up with water, travel considerable distance and then discharge directly into the channel networks. These situations are frequently observed in headwaters of a drainage system (Benda et al., 2005). Alternatively, in many cases, much of the failure material remains within the hillslope (Dai and Lee, 2002; Johnson et al., 2000; Schuerch et al., 2006; Schwab et al., 2008). Johnson et al. (2000), for example illustrate the initiation, runout and deposition patterns of more than 300 landslides occurring in natural landscapes. Their findings show that major portion of these failures deposited within the catchment instead of reaching the main stream. If the material is deposited immediately downslope from the landslide scar, the sediment can enter the channel

network only if the landslide is adjacent to the channel network or by subsequent soil erosion processes.

2.8 Landslide induced soil redistribution modelling

Travel distance prediction is useful to delineate potential hazard areas and also to estimate the landslide-driven sediment yields. At present, relatively few attempts have been made to model the effects of shallow landslides on landscape development. There are no rigorous methods which would allow a strict assessment to determine the trajectories of the failure materials. Difficulties in soil redistribution modelling are associated with the complexities of landslide dynamics; for example forecasting of destinations of the slides is very inexact even for an individual slide. Another important issue lies in aggregating data from the individual slide to the assemblage of the slides over a long period. In addition to these aspects, detailed meteorological records and data from the individual slide are rarely available. However, there are a few models proposed to compute landslide motion and runout distance. These include physically-based and empirical models.

Physically-based models

Various theoretical approaches to simulate the runout distance and landslide motion are presented in the research of Takahashi et al. (1991), O'Brien et al. (1993), Iverson (1997), Iverson et al. (1997), Revellino et al. (2004), Iverson (2005). The formulation of the models is complex and the models are more appropriate to examine the detailed behaviour of an individual landslide and debris flow for which flow material composition and hillslope characteristics are well defined (e.g. Hungr, 1995; Iverson, 1997).

Empirical models

Empirical models have been independently developed by different researchers. The models may therefore be generally expected to conform to local conditions and debris flow characteristics (size and composition). They may not necessarily yield the same results when applied to a common data set. The empirical models are also used to predict the impact of landslides on sediment yields at a catchment-scale (Bathurst et al., 1997).

Empirical models generally relate the runout distance with the elevation difference between the starting point and the lowest point of deposition of the mass movement. For example, Vandre (1985) suggests the runout distance is approximately 35-45% of the elevation difference. Various researchers (e.g. Burton and Bathurst, 1998; Bathurst et al., 2006; Claessens et al., 2007) applied those values to estimate the landslide-driven sediment yield assuming the following conditions:

- The debris flow continues unconditionally for a slope steeper than 10°; all the soil along the tracks is scoured and added to the eroded material from the initial landslide site.
- When the slope is between 4° and 10°, the debris flow comes to a halt either over the runout trajectories or on reaching 4°, whichever condition is first met.
- For the slopes less than 4°, the debris flow halts unconditionally and deposits all remaining material.

Some empirical models attempt to relate runout distance on a physical basis to the energy or momentum, as indicated by flow gradient or elevation drop and volume, an indication of momentum. Corominas (1996) proposed a model where runout distance is given as:

$$R = 1.03\, V^{0.105}\, h \qquad \text{Equation 2.21}$$

where V (m^3) is the volume of mass movement, h (m) is the elevation difference between the starting point and the lowest point of deposition of the mass movement. Similar approach has been proposed by Rickenmann (1999) from a regression analysis using debris flow data from the Swiss Alps to predict runout distance as:

$$R = 1.9\, V^{0.16}\, h^{0.83} \qquad \text{Equation 2.22}$$

The unstable soil material is transported following the steepest descent gradient. Estimation of potential failure depth is required to derive the landslide volume. The failure location is a function of the geotechnical properties of the soils and slope gradient. Typically, a shallow soil profile has a planar failure plane along an interface dividing a shallow upper soil layer from an underlying stronger and often less

permeable underlying soil or bedrock (Burton and Bathurst, 1998). Up to now, very few attempts have been made to predict the potential failure depth. Johnson and Rodine (1984), for example, express the critical thickness of the debris flow material, z (m), beginning to flow or stop flowage on an infinite slope depending on the local slope and the soil geotechnical properties according to:

$$z = \frac{C_s}{\gamma \cos\theta (\tan\theta - \tan\varphi)} \qquad \text{Equation 2.23}$$

where φ (°) is the angle of internal friction, and θ (°) is the local slope. C_s (N m^{-2}) is the soil cohesion and γ (N m^{-3}) is the unit weight of soil material.

The model is not able to compute the critical thickness if the bulk friction angle is equal to or greater than the slope angle. To simplify it, approximations of a minimum slope gradient for maintaining transport are used (Benda and Cundy, 1990; Wu and Sidle, 1995; Burton and Bathurst, 1998). Claessens et al. (2007) modified the model by inversing Equation 2.23 and substituting apparent angle of internal friction by a slope angle limit for debris flow movement to estimate the thickness of the eroded material, z (m) depending on soil geotechnical properties and local slope gradient as:

$$z = \frac{\gamma \cos\theta (\tan\theta - \tan\alpha) a}{C_s} \qquad \text{Equation 2.24}$$

where z (m) is the thickness of the eroded material; γ (N m^{-3}) is the unit weight of the soil material. θ (°) is the slope of the profile; α (°) is the minimum local slope to initiate debris flow; a (m^2) is a correction factor for dimension.

2.9 Input data resolution for hydrological and landslide modelling

Catchment-scale modelling has become very popular in recent environmental research, primarily due to advances in availability and quality of digital elevation models (DEMs) (Moore et al., 1991; Goodchild et al., 1993; Wise, 2000). In hydrological modelling, DEMs are most often used in algorithms to derive slopes, aspects, flow direction, upstream contributing area, flowpaths etc. Catchment boundary and stream drainage network can also be obtained from those topographic attributes. The results of these DEM analyses are used in many environmental studies

such as hydrological modelling (Beven and Moore, 1993), soil saturation prediction (O'Loughlin, 1986; Barling et al., 1994), landslide hazard modelling (Montgomery and Dietrich, 1994; Pack et al., 2001; Acharya et al., 2006), soil mapping (Skidmore et al., 1991; Thompson et al., 2001; Scull et al., 2003), land-use change modelling (Verburg et al., 2002; Vanacker et al., 2003), erosion modelling (Mitasova et al., 1996; Cochrane and Flanagan, 1999; Amore et al., 2004)

Generally, topographic information in a DEM can be represented and stored as: Triangular Irregular Network (TIN); Vector or contour lines (vector-based GIS); and Grid (raster-based GIS). Triangular irregular networks are used primarily to represent terrain surfaces or landscapes. In some cases, TINs are used to model the hydrological processes; for example, Vieux (1991) used the TIN facets to provide land surface slope in a finite element solution of overland flow. However, analyses with TIN format data are complex and dependent on the triangle size used to represent a certain region.

Vector DEMs are based on contour topographic maps. The information on elevation is stored as contour lines having a series of x and y coordinates. Analysis using vector-based DEM demands high level of computational framework but one of the advantages of this system is that better accuracy of topography can be achieved at larger scales, very complex and dissected terrain. The grid-based DEMs are most commonly used data source for digital terrain analysis because of its simple structures and compatibility with other digitally produced data (Wise, 2000). In the DEM, the catchment-scale modelling is easy because all spatial entities have a simple, regular and square shape and various types of spatial analysis are possible.

Some of the drawbacks of the raster-based system have been overcome by advances in computing abilities of today's computers. For example, one of the disadvantages of the gird-based systems in the past was large data volume, which now is not a big issue because storage and computational capacity is no longer a major concern. However, one limitation in using grid-cell DEMs is that each grid-cell represents a single data value and the accuracy is therefore defined by the size of the cell when representing 'real-world' topography, aspect, slope, etc.

An important factor in the analysis of DEMs is, therefore, the influence of its grid-cell size i.e. DEM resolution on modelling results. The resolution of DEM greatly affects the prediction of flow characteristics, surface runoff and erosion. It is therefore difficult to suggest an appropriate DEM grid-cell size. An increase in size of the grid-cell would reduce the spatial representation of the landscape. On the other hand, selecting to use high resolution data may require significant field surveys, model parameterisation and computation time which may increase the modelling costs. Although the increasing availability of DEM grid-cell resolutions and computational capacity allows a rapid topographical analysis of a catchment, the degree to which DEM resolution affects the representation of the land surface has not been examined systematically (Zhang and Montgomery, 1994).

2.9.1 Influence of DEM resolution on topographic index

There are significant numbers of studies published in the literature on the influence of DEM resolution on the distribution of topographic index used in TOPMODEL (Beven and Kirkby, 1979). The index is expressed as $\ln(a/\tan\theta)$ where a (m^2 m^{-1}) is the specific catchment area and θ (°) is the local slope. The index measures the tendency of water to accumulate at one point on a slope. When coarsening the resolution, the value of 'θ' tends to drop down because local variation in terrain is smoothened whereas the distribution of 'a' tends to shift to larger values (Wilson et al., 2000). Several studies compare the distributions or mean values of the topographic index computed with DEMs with differing resolution (Zhang and Montgomery, 1994; Saulnier et al., 1997). Wolock and Price (1994) pointed out that in the simulation of topographic index of the TOPMODEL, coarse resolution is not necessarily inappropriate probably because water table configuration mimics surface topography and may be smoother and better represented by a coarse resolution. Becker and Braun, (1999) also proposed that an acceptable approximation of the distribution of the topographic index in a catchment can be obtained from a coarse resolution DEM.

2.9.2 Influence of DEM resolution on hydrological modelling results

There are some studies which demonstrate the influence of grid-cell resolution on hydrological modelling results. For example, by extracting watershed geometry from a DEM and using it in KINEROS (Woolhiser et al., 1990), Thieken et al. (1999) found that drainage length, density and time to peak flow decreased whereas peak

flow rate, maximum total flow length and runoff volume increased with coarsening the DEM grid-cell. The modelling results did not have a systematic trend with the DEM grid-cell size. Wilson et al. (2000) used 30, 100 and 200 m grid-cell size in TAPES-G to derive the primary topographic attributes. They found that slope gradients and drainage lengths were decreasing but specific catchment areas were increasing with increasing grid-cell size. Schoorl et al. (2000) applied a simple single process model (LAPSUS) in artificial DEMs of five different resolutions (1, 3, 9, 27 and 81 m) and noted overestimation of erosion and underestimation of re-sedimentation with coarsening the resolution. Zhang and Montgomery (1994) found that runoff processes in their area were controlled by physical properties of the landscape and suggested that a 10 m grid-cell resolution as a rational compromise between increasing resolution and data volume for geomorphic and hydrologic processes.

Thompson et al. (2001) statistically and visually compare terrain attributes and quantitative soil-landscape models derived from DEMs with different horizontal resolution and vertical precision. They suggest that the vertical precision must increase with increasing horizontal resolution so that it remains greater than the average difference in elevation between grid points in the DEM. They also report that higher resolution of the DEMs may not be necessary for generating useful soil-landscape models. Vázquez et al. (2002) used three grid-cell resolutions (300, 600 and 1200) in a physically-based model in a large catchment of about 600 sq. km. area and observed that most appropriate grid-cell size for achieving reasonably accurate prediction was 600 m in terms of river discharge.

Cochrane and Flanagan (2005) used different grid-cell resolutions to study the variation in erosion and surface runoff using the Hillslope and Flowpath methods in the WEPP model. They noted that using fine resolution DEMs did not predict runoff or soil loss significantly better than using coarser resolutions meaning that a wide range of DEM resolutions could be used for runoff and sediment yield simulations from a watershed outlet. However, resolution played a major role in the WEPP models ability to predict erosion from hillslope or in a distributed manner using flowpaths. Within a single hillslope, fine resolutions increase the prediction of

deposition and reduced overall predictions of sediment yield. Coarse resolution DEMs reduced slope gradients but limited the occurrence of deposition areas.

Shrestha et al. (2006) defined the term "IC ratio" as the ratio between the model input spatial resolution and the catchment area to set a criteria for the selection of an appropriate input data resolution in a distributed hydrological modelling of three large catchments (132,350, 29,844 and 2,093 km^2 area). They used different grid-cell resolutions ranging from 10' to 2.5° and noticed that improvement in the model performance is more pronounced when the IC ratio was below 1:10 and the rate of improvement was negligible if the ratio was above 1:20. They concluded that the IC ratio ranging between 1:10 and 1:20 can be taken as the optimum model performance range considering the data handling and the cost effectiveness.

2.9.3 DEM resolution in landslide modelling

Models used to delineate the location and calculate the potential for shallow landsliding in a grid-based DEM environment are being used with a variety of grid-cell sizes. In general, grid-cell size is selected by the user and should depend on quality and density of the input data, size of the area to be modelled and accuracy required for the output data (Ward et al., 1981). Borga et al. (1998) used a quasi-steady subsurface hydrological model for landslide modelling in a 5 km^2 catchment. In the same catchment, Borga et al. (2002) applied a quasi-dynamic hydrological model to predict spatial distribution of soil saturation and shallow landslides in response to a rainfall of specified duration. In the both studies, they used a 10 m grid-cell resolution DEM. Burton and Bathurst (1998) used a dual resolution approach; modelling basin hydrology at a 200 m resolution and predicting landslide hazard and landslide induced sediment yield at 20 m resolution, which they consider to be appropriate for landslide simulation. Vanacker et al. (2003) used a 5 m grid-cell size DEM to investigate the effect of past and future land-use change on landslide susceptibility in a 2.5 km^2 basin.

Some studies have been done to identify and quantify the influence of DEM resolution on landslide hazard assessment and the resulting soil redistribution. Dietrich and Montgomery (1998) compare the shallow landslide modelling in two cases. In the first case, they use a 30 m and a 6 m DEM and 10 m and 2 m in the

second case. For both cases, they observe total landslide distribution areas are similar for coarse and fine resolutions but the spatial distribution patterns of landslides differ in important ways. In the finer resolution cases, pattern of relative stability are much more strongly defined by local ridge and valley topography. Landslide distributions are more concentrated in steep valleys rather than spread out across the landscape. They conclude that the unstable areas increase with finer resolution topography.

Claessens et al. (2005) compare the critical rainfall required to initiate the landslides, shallow landslide distribution and soil redistribution in a catchment of 12 sq. km. area with four different DEM resolutions of 10, 25, 50 and 100 m. For a given critical rainfall, less unstable areas were observed when using the coarse grid-cell resolution. They report that maximum possible unstable areas are attained for lower critical rainfall scenarios when the resolution is coarsened. They also report higher unit of areas for coarser resolutions do relatively raise the extent of deposition areas.

2.10 Summary of literature review

The current knowledge on hillslope processes such as soil erosion, shallow landslide and soil redistribution was presented in this chapter. The literature review depicted that there have significant studies and research conducted to understand the triggering conditions of shallow landslides, soil erosion and soil redistribution. However, additional research is required to quantify short- and long-term soil erosion rate and sediment yields due to occurrences of shallow landslides. Experimental results presented in Chapter 3 and 4 will provide additional data on landslide initiation, retrogression, evolution of new hillslope profile and impact of shallow landslides on short- and long-term soil erosion rate and sediment yields.

A brief description of various approaches employed to model soil erosion, deposition, and shallow landslide and soil redistribution was also presented in this chapter. Various subsurface hydrological models used to assess the landslide hazard were also presented. Understanding of these models is fundamental to study the soil erosion, shallow landslides and soil redistribution in an integrated approach. An integrated modelling approach is necessary to quantify pre-failure soil erosion, identify potential slope failures and soil redistribution and estimate post-failure sediment yields in a changed topography.

SHETRAN is a model that simulates soil erosion, shallow landslides and sediment delivery to channels and is possibly the first integrated modelling approach to predict sediment yields from soil erosion and shallow landslides (Burton and Bathurst, 1998). However, the ability of the model is strictly affected by the use of fine and coarse grid-cell resolutions for predicting spatial distribution of shallow landslides (Burton and Bathurst, 1998; Bathurst et al., 2006); changes in grid-cell resolution affect both soil erosion and shallow landslide prediction due to variations in representation of local slope gradient (Cochrane and Flanagan, 2005; Claessens et al., 2005). An advantage of WEPP over SHETRAN is that WEPP is applicable to both hillslopes and catchment. Additionally, continuous runoff, soil water content, and subsurface flow are predicted, allowing detailed temporal analyses.

The geotechnical infinite slope method (Skempton and DeLory, 1957) of slope stability analysis is a widely used physically-based approach to model shallow landslides in mountainous and hilly regions (Montgomery and Dietrich, 1994; Pack et al., 2001; Borga et al., 2002; Casadei et al., 2003; Acharya et al., 2006; Claessens et al., 2007). This model provides an insight into shallow landslide triggering processes. The landslide model couples the slope stability model with hillslope hydrological model.

Both physically-based (e.g. Iverson et al., 1997; Revellino et al., 2004; Bertolo and Wieczorek, 2005; Iverson, 2005) and simple empirical methods (e.g. Vandre, 1985; Corominas, 1996; Burton and Bathurst, 1998; Rickenmann, 1999; Claessens et al., 2007) are found in literature to enumerate soil mobilisation, runout, and soil redistribution after shallow landslides. Physically-based models require a large amount of data along with numerous assumptions about the characteristics of failures. For soil redistribution modelling, a simpler, rule-based approach may be used which can be applied to multiple landslides occurring in a hillslope over periods of time ranging from a single rainstorm's duration to several years (Burton and Bathurst, 1998; Doten et al., 2006; Claessens et al., 2007).

In the integrated modelling approach, the main question is how two (soil erosion and shallow landslide) independent models are integrated. To integrate the models, it is

necessary to share the same hydrology particularly sub-surface hydrology. Integration of soil redistribution model in the approach is also critical to predict runout distance, spatial variation of failure and deposition depths. The detail processes explaining the integrated approach will be presented in Chapters 4 and 5.

In catchment-scale modelling with GIS, influence of DEM grid-cell resolution has been critical to model simulations. Main question is how the grid-cell resolution improves the simulations of the integrated landslide soil erosion model. Chapter 6 will address the resolution issue.

Chapter 3 Laboratory Scale Shallow Landslide and Soil Erosion Study in Sandy Soil

3.1 Introduction

Previous studies conducted by different researchers (e.g. Burton and Bathurst, 1998; Ries, 2000; Schuerch et al., 2006, Schwab et al., 2008) have made attempts to quantify the impact of shallow landslides on sediment yield. These studies mainly estimate annual landslide-driven sediment yield patterns from a basin. However, little work has been done to study the potential changes in topography and evolution of a hillslope following landslides.

The main purpose of this chapter is to report the results of a flume-based investigation of water-induced shallow landslides and sediment discharge using sandy soils of different depths. The chapter presents experimental results of water-induced shallow landslides and soil erosion in a flume. The objectives of the study were to determine:

- how the depth of the soil profile affects shallow landslide initiation and its retrogression in the upslope direction under controlled rainfall
- how slope failure events affect sediment discharge from the flume
- the changes in slope profile, composition (e.g. soil armouring) and physical properties as a function of continued rainfall and original soil depth

3.2 Materials and methods

3.2.1 Experimental flume

Soil erosion and shallow landslide experiments were conducted in a two-section experimental flume (Figure 3.1). The flume measured 3.94 m long, 0.30 m wide and 0.80 m deep. The upper part of the flume was 2.44 m long and lower portion 1.50 m long. The upper and lower sections were fixed at their interface, and the inclination of the flume could be changed by using a chain pulley at the end of steeper flume section. The two sides and base of the flume were made of 15 mm thick impervious acrylic sheeting so that failure processes could be readily observed. To provide realistic friction between the material and the bed of the flume, silica-sand was glued to the flume base. Galvanized structural steel was used to support the flume.

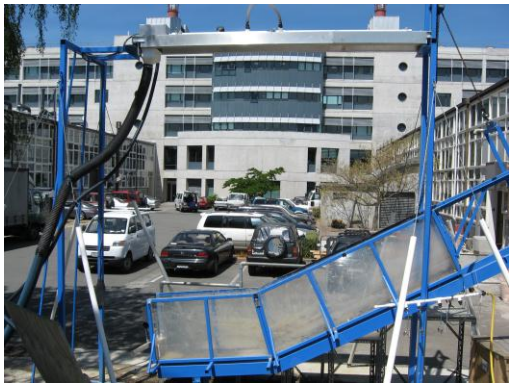

A

B

C

D

Figure 3.1: Overall view of experimental flume setup and rainfall simulator (A), close view of the flume (B), rainfall simulator (C), and flume outlet (D).

A two nozzle (Veerjet 80100) Norton type rainfall simulator (Norton and Brown, 1992), built at the University of Canterbury, was mounted on the flume. The height of the nozzles was enough for raindrops to reach terminal velocity upon soil impact. The simulator provided rainfall coverage of the entire flume over an area of approximately 4 m x 2 m.

Calibration of the simulator was done using an OTT Parsival laser optical disdrometer (Löffler-Mang and Joss, 2000), which measured raindrop particle size and velocity distributions. The calibration results revealed that the simulator could provide a range of rainfall intensities from 15 to 80 mm h^{-1}. The size of the raindrop ranged from 0.5 to 1.5 mm with a mean size of 1 mm. The speed of the drops varied from 3 to 5 m s^{-1} with mean velocity about 4 m s^{-1}. Six cylindrical rain gauges were distributed along the sides of the upper section of the flume to monitor the rainfall intensity and its spatial distribution over time during experimental simulations.

A highly sensitive pore pressure transducer (KYOWA PGM-02 kg) with maximum capacity of 20 kPa was installed at the interface of the two sloping sections of the flume to measure pore pressure during experiments (Lourenco et al. 2006). The transducer measured pore pressures at various time intervals ranging from 0.25 seconds to 24 hours. A soil moisture sensor was also placed along the same transverse line of the pore pressure transducer; the distance between them was approximately 150 mm. The sensor could be set to measure soil moisture at varying time intervals ranging from 1 minute to 24 hours. These two devices were directly connected to a computer for data logging. A video camera was used to monitor failure initiation time, location, and subsequent retrogression of failures.

3.2.2 Experimental method

Four experiments were carried out with soil depths of 200, 300, 400 and 500 mm (Figure 3.2). A sandy type soil was chosen in these experiments because it is a cohesionless soil that easily leads to trigger shallow landslides in the deeper soil profile within experimental timeframe. The inclination of the upper section was set to 30° to facilitate slope failures in the cohesionless granular soil material. The lower section was set to 10° to cause the deposition of failure material and investigate erosional processes after the slope failure events.

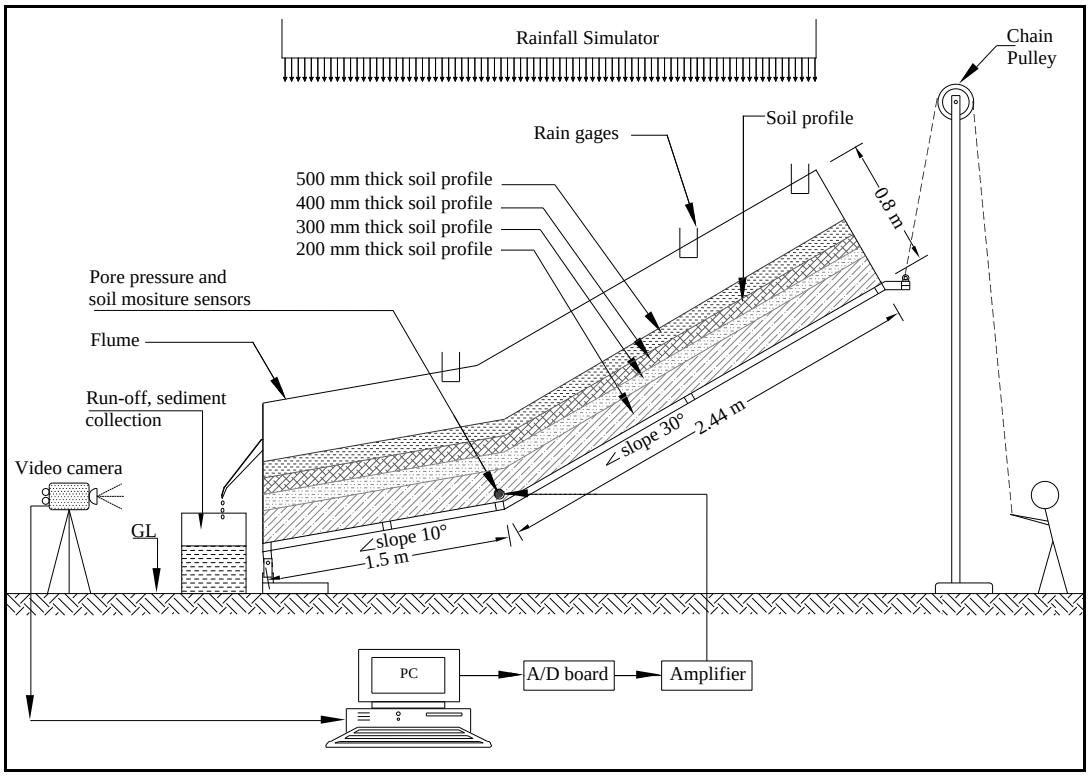

Figure 3.2: Schematic diagram illustrating experimental set up with different soil profile depths.

Experiments were run for total durations of 240, 300, 360 and 390 minutes respectively in 200, 300, 400 and 500 mm depth soil profiles (Table 3.1). The duration of each experiment was determined by the timing and occurrence of failure events, and the need to quantify post-failure sediment yield. Experiments continued for about 60 to 90 minutes past the last observed slope failure. Consistency of data was verified by repeating the experiments with soil depths of 200 and 300 mm. Similarly consistent results were assumed for 400 and 500 mm depth soil profiles, and therefore the experiments for them were not repeated.

Table 3.1: Summary of experimental duration, rainfall, and time of initial slope failure.

Exp. No.	Soil depth (mm)	Time to initial slope failure (min)	Total experiment run time (min)	Total rainfall required to initiate slope failure (mm)	Cumulative rainfall (mm) throughout experiment
1	200	60	240	50	210
2	300	106	300	88	260
3	400	123	360	103	300
4	500	148	390	123	360

In order to maintain uniform soil characteristics spatially and between experiments, soil was placed in the flume in layers of 40 to 50 mm depth and compacted uniformly using a mechanical mallet under about 40 kPa pressure as in Iverson et al. (2000). The soil's relative density, I_d, ranged from 0.76 to 0.82, which ensured dense sandy soil characteristics according to the relative density as adopted in Spence and Guymer (1997), i.e. $0.65 \leq I_d \leq 0.85$.

The soil material used in the experiments was sand with mean particle size (D_{50}) of 0.57 mm containing more than 90% angular silica grains and less than 1% fines ($\leq$ 0.075 mm). Particle size distribution was obtained through dry sample sieving (Figure 3.3). Initial moisture content was determined by collecting and drying the soil sample prior to the experiment runs. In all experiments, the initial moisture content of the soil was measured to be about 7.20 %.

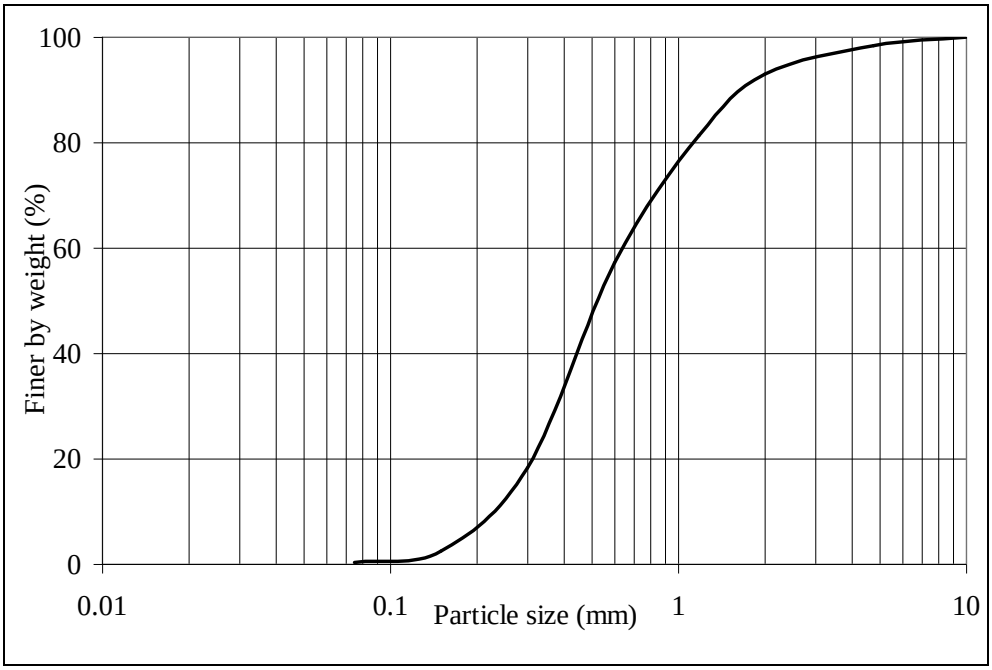

Figure 3.3: Particle size distribution of the sandy soil.

Angle of internal friction (φ) and cohesion (C) were derived from four direct shear tests (e.g. Cernica, 1995) prior to the flume experiment runs (Figure 3.4). Specimens for the tests were prepared by compaction at a dry density of 1.52 kN m^{-3}. To determine saturated hydraulic conductivity and bulk density, soil samples were prepared in the same manner as in the flume experimental runs, that is, applying 40 kPa pressure in 40 to 50 mm layers.

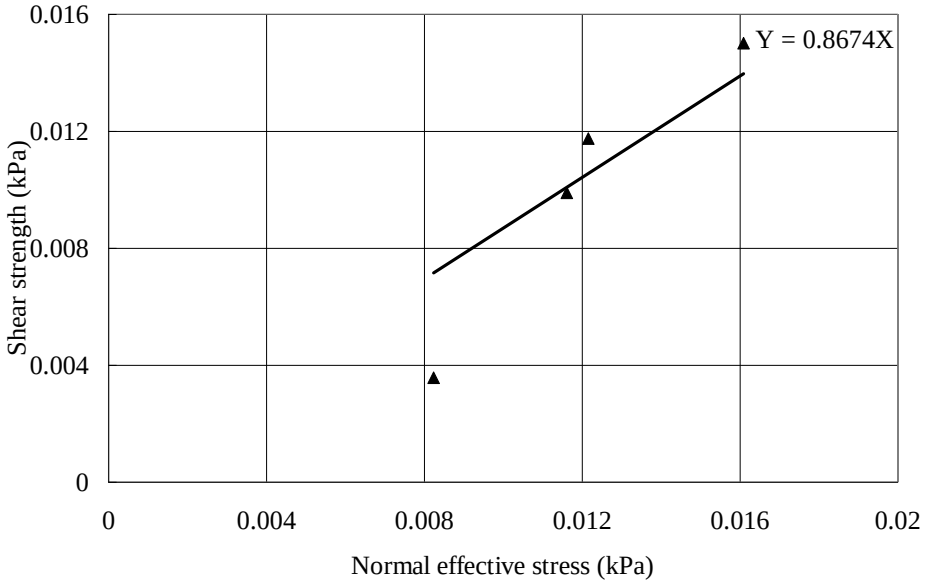

Figure 3.4: Shear strength envelopes for the sandy soil. Measured values are represented by dots and a linear trend line is fitted to values.

The saturated hydraulic conductivity was determined by the constant head method (e.g. Cernica, 1995). The organic matter was determined by incinerating the oven dried soil sample in a muffle furnace at 550°C for 6 hours (Goldin, 1987). Measured soil parameters and profile properties are listed in Table 3.2.

Table 3.2: Physical properties of the sandy soil

SN	Properties	Unit	Mean or range of value
	Properties of soil		
1.	Cohesion (C)	kPa	0
2.	Angle of internal friction (φ)	˚	41
3.	Organic matter content (OM)	%	0.70
4.	Initial moisture content (w)	%	7.20
5.	Uniformity coefficient (UC)	-	3.82
6.	Coefficient of curvature (CC)	-	0.76
7	Mean grain size (D_{50})	mm	0.57
8	Effective grain size (D_{10})	mm	0.20
9	Specific gravity (G)	kN m^{-3}	26.30
10	Bulk unit weight (γ)	kN m^{-3}	16.20-16.80
11	Dry unit weight (γ_s)	kN m^{-3}	15.20 – 15.50
12	Saturated unit weight (γ_{sat})	kN m^{-3}	19.50 – 19.40
13	Porosity (n)	-	0.41 – 0.40
14	Permeability (k_{sat}) at initial porosity 0.40	m s^{-1}	$7.4x10^{-4}$

Rainfall intensity from the simulator was set at about 50 mm h^{-1} in all experiments. The rainfall intensity and its spatial distribution were monitored every 30 minutes in all experiments to verify consistency between experiments. There was little variation in rainfall distribution as measured from the upper four rain gauges during experiments; however the lower two had consistently 20% less rainfall.

Slope failure occurrence time, slip surface depth, location, and slope failure retrogression behaviour were recorded by direct observations and video camera recordings. One minute runoff samples were collected from the end of the flume immediately after runoff reached the outlet, and at 15 minute intervals thereafter.

Sediment discharges and runoff rates were calculated after oven drying the collected runoff samples. Soil samples from the top 10 mm of the soil were collected immediately after each experiment from close to the outlet of the flume, the intersection of the two sloping sections, and from the most upslope point of the flume. These soil samples were analysed to determine the occurrence of soil armouring following each experiment. Soil moisture was measured every minute using the soil moisture sensor. The sensor was linearly calibrated before the experiments using calibration constants derived from sampling the same soil at different soil moisture contents. Pore pressure was measured every second using a pre-calibrated pore pressure transducer.

3.3. Results and discussion

3.3.1 Landslide initiation and evolution

The soil moisture measurements for all experiments at the interface of the upper and lower sloping sections of the flume are presented in Figure 3.5. For the experiment using the 200 mm deep soil, soil moisture started to increase after about 10 minutes of rain, whereas for the 500 mm soil it started after 18 minutes. Moisture content for each of the four soil depths increased linearly towards saturation at different rates according to the depth of soil. The moisture content at the toe of the upper sloping section at the time of slope failure initiation was about 26%, which is near its saturated value. Correspondingly, the calculated saturation ratio based on the soil's initial porosity ranged from about 85 to 90%. The difference of 10 to 15% to reach its complete saturation level was probably due to entrapped air within the wet soil.

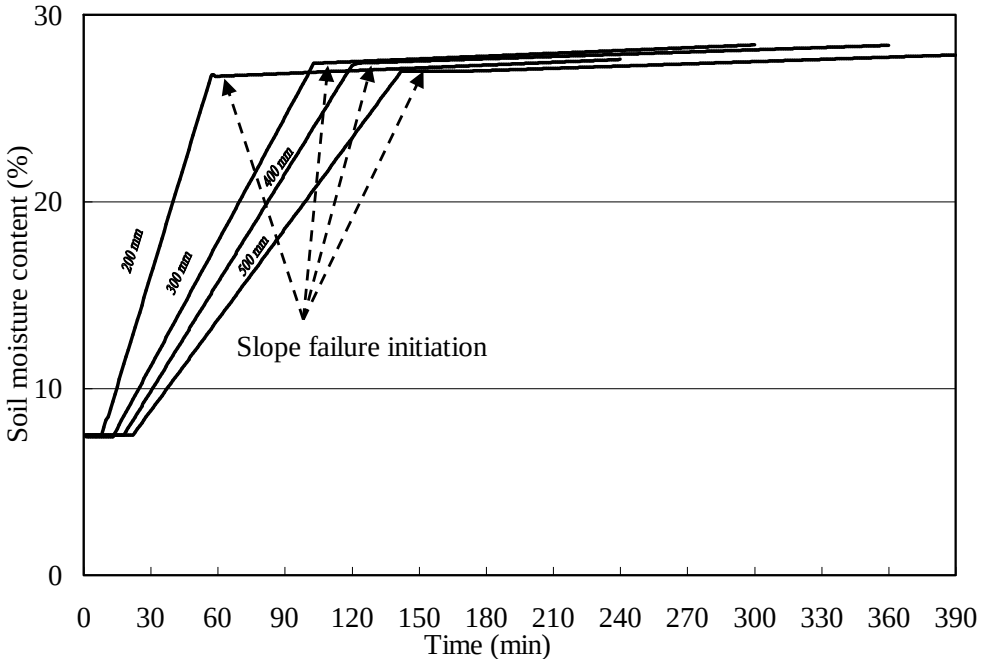

Figure 3.5: Soil moisture content distribution in time series in the flume bed at the toe of two sloping section for 200, 300, 400 and 500 mm deep soil. Rainfall initiated at the start of each experiment.

The initial slope failures occurred in response to the soil saturation process occurring at the toe of the upper slope for each experiment. The process occurred by direct rainfall and by water infiltrating in the upper areas of the slope and gradually flowing towards the base of the flume. As soon as the bottom of the upper slope reached a level close to saturation, localized subsidence occurred, and subsequently slope failures were triggered. Subsidence in the vicinity of the intersection of the two slopes was therefore the direct result of soil saturation processes as voids were gradually occupied by water. The soil moisture observations were consistent with other reported studies which indicate that for homogeneous soil slopes, saturation tends to develop in the lower parts of hillslopes (Weyman, 1973; Tohari et al., 2007). Others show that saturation can be localized and occur in other parts of a hillslope as a result of, for example, perched water tables (Gasmo et al., 1999; Deutscher et al., 2000).

Measurements from the pore pressure sensor for the 300 mm deep soil profile experiment are presented in Figure 3.6. In this experiment, and all others, an abrupt increase in pore pressure following a failure was not observed. The experimental results also show that there was a positive correlation between the pore pressure and

the thickness of the overlying soil. The absence of an abrupt increase in pore pressure following a failure in the experiments may be attributed to one or more of the following causes: hydrological response dominated by infiltration through highly permeable soil material; slow shearing rate; high bulk density and low initial soil porosity; and moderate rainfall intensity. Abrupt increases in pore pressure are generally related to the development of rapid shearing generally associated with intense rainfall (Okura et al., 2002, Wang and Sassa, 2003; Moriwaki et al. 2004). Recent studies have shown that the pore pressure development during landsliding is greatly dependent on initial density of soil as well as thickness of the soil layer (Iverson and LaHusen, 1989, Iverson, 1997; Iverson et al., 2000; Wang and Sassa, 2001, 2003). The permeability of the soil also influences the pore pressure generation (Wang and Sassa, 2003); soils with higher permeability will have quicker dissipation and thus smaller pore pressures are generated.

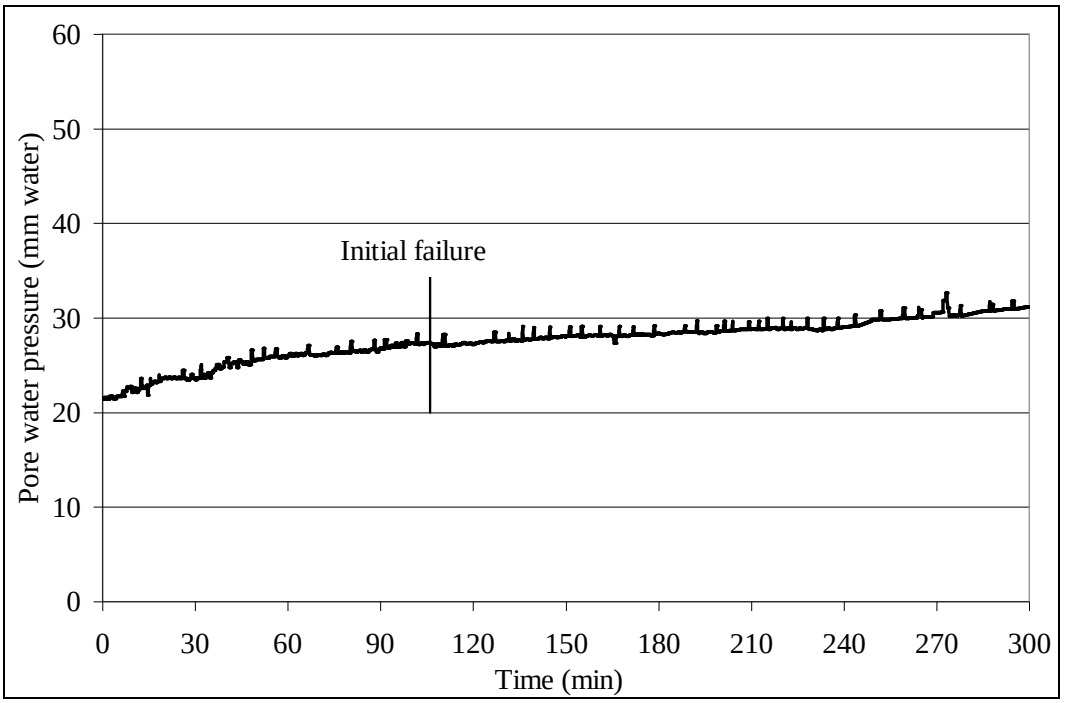

Figure 3.6: Typical pore pressure sensor measurements at the toe of upper sloping section for 300 mm deep soil. Rainfall initiated at the beginning of the experiment.

In all experiments, the slope failures initiated with small slip surface depths. The initial depths of the slip surface were related to the depth of the soil profile. Initial slip surface depths were about 90, 60, 40 and 30 mm for the 200, 300, 400 and 500 mm

deep soil profiles respectively. As depicted in Figure 3.7 and Figure 3.8, the failure block size increased after each new failure, and a longer time interval was required before a new failure occurred. Each newly-failed block moved downward pushing the previously failed mass in front of it. For example, the slope failure in the 200 mm deep soil under continuous rainfall initiated with the depth of failure of 90 mm and increased to 200 mm (i.e. full soil depth) as the failure locations moved upslope. The depth of potential slip surface depends on the geotechnical properties of the soil and sloping profile characteristics i.e. slope and depth. Slope failures take place when the soils become saturated at the potential slip surface depth (Terlien, 1997). This depth of saturation is a function of various parameters such as soil profile, initial soil moisture distribution, infiltration capacity, rainfall amount and intensity. In the experiments, at the time of slope failure initiation the total volume of subsurface flow contributions were higher for deeper soils. This resulted in a higher saturated depth leading to smaller depths of failure for the experiments with deeper soils.

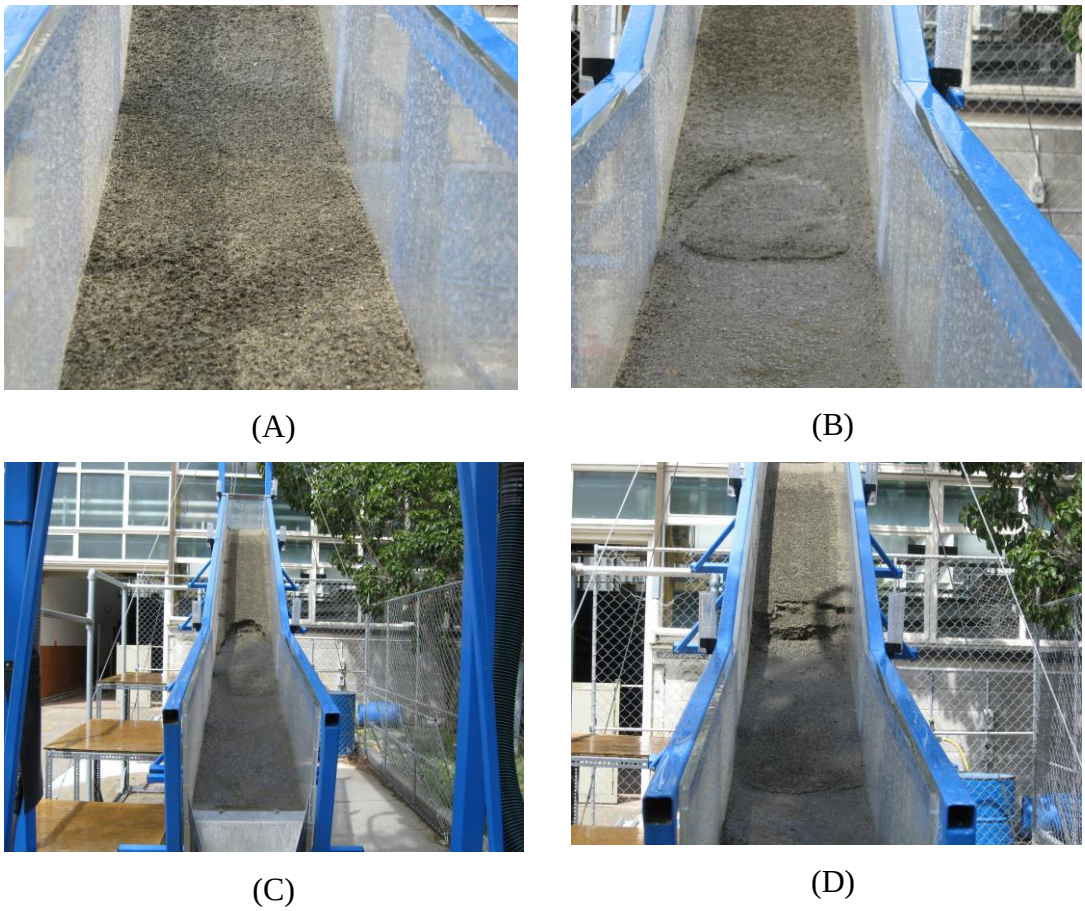

(A) (B)

(C) (D)

Figure 3.7: Images showing development and growth of seepage area (A), slope failure initiation (B), evolution of slope failure (C), and slope failure retrogression with increased failure block size (D).

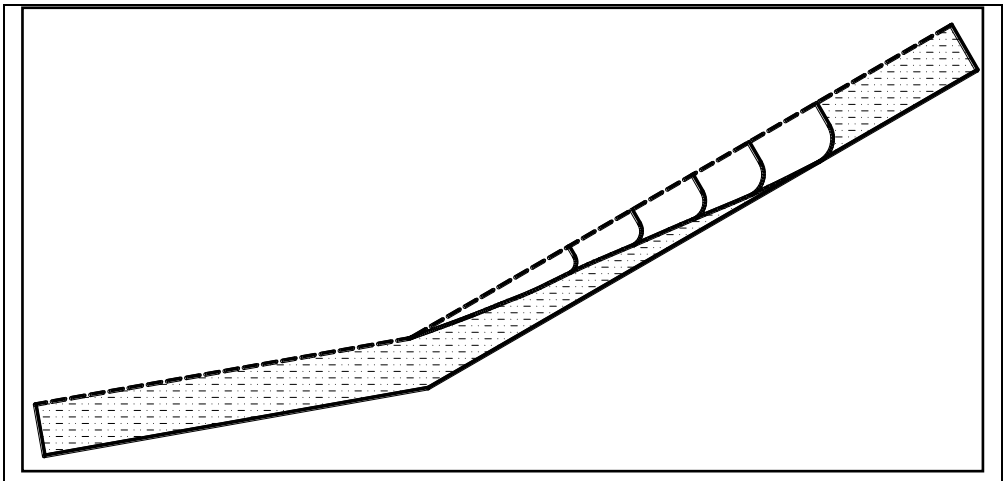

A

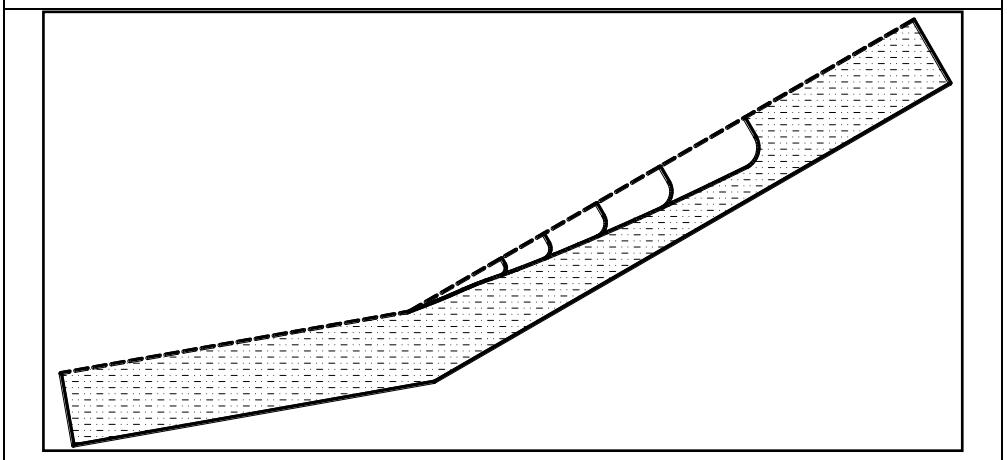

B

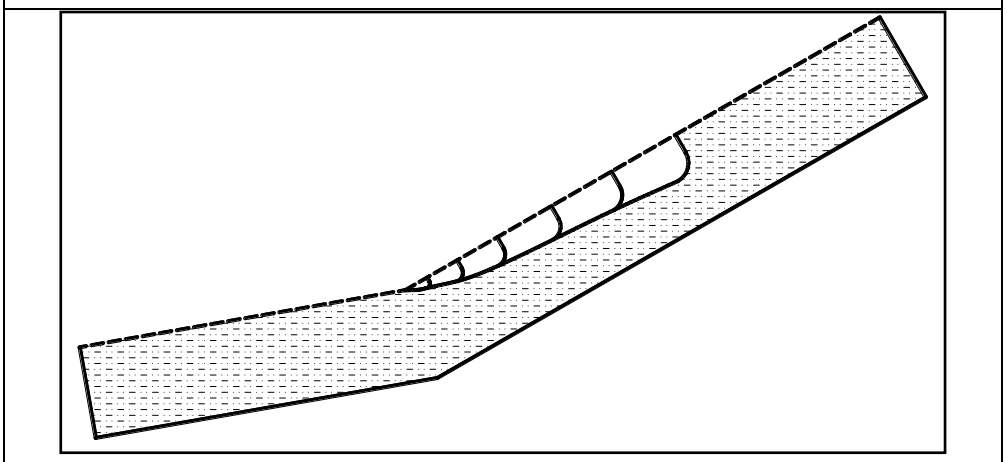

C

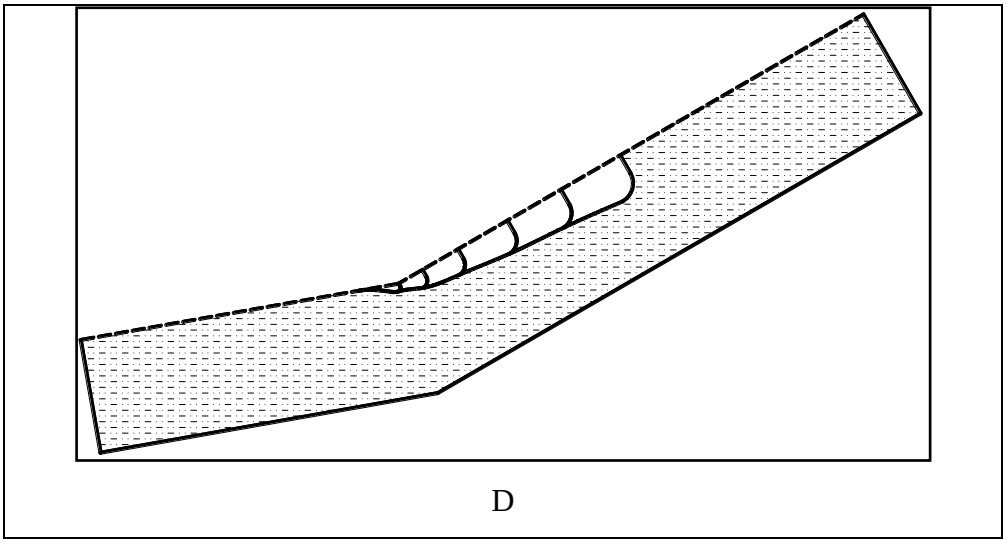

Figure 3.8: Illustrative diagram of failure locations and retrogressions in 200 mm deep soil after 240 minutes rainfall (A), 300 deep soil after 300 minutes rainfall (B), 400 mm deep soil after 360 minutes rainfall (C), and 500 mm deep soil profile after 390 minutes rainfall (D).

Figure 3.8 and Table 3.3 show the retrogressive slope failure behaviour. Initially, the slope failure frequencies were high, but as failures retrogressed upward the frequencies decreased significantly. In other words, landslides were triggered more frequently when they occurred closer to the toe than in the upper slopes of the flume. For instance, the time interval between the first two major failures was only about 12 minutes, whereas that between the last two was nearly 46 minutes for the 200 mm deep profile (Table 3.3). Upslope contributing area (Montgomery and Dietrich, 1994; Pack et al., 2001; Acharya et al., 2006; Claessens et al., 2007) is believed to be one of the key factors contributing to the initiation and retrogression of landslide events. As the slope failures retrogressed upward, the upslope contributing area diminished. This can be noticed in Table 3.3, showing that about 96% of the total contributing area was responsible for triggering the second slope failure, whereas this value was nearly 63% for the last (i.e. 6^{th}) slope failure in the 500 mm deep soil. The reduction of the area is more pronounced in the shallower profiles. For instance, the calculated areas to trigger the 5^{th} slope failure event was 37% of the total contributing area for the 200 mm deep soil, whereas it was 74% of the total contributing area in the 500 mm deep soil.

Table 3.3: Major failure events and measured upslope contributing areas

Major slope failure events	Time of occurrence of slope failures (min) for different soil depths (mm)				Upslope contributing area from failure point (%) for different soil depths (mm)			
	200	300	400	500	200	300	400	500
1	60	106	123	148	100	100	100	100
2	72	118	136	161	70	80	93	96
3	91	138	156	184	58	72	87	92
4	112	163	183	215	47	61	78	84
5	158	214	234	270	37	49	67	74
6	NA	NA	295	325	NA	NA	55	63

NA = Not applicable

3.3.2 Sediment yields in pre- and post-failure events

Seepage was observed to be a primary contributor to the runoff from the upper part of the flume and this runoff produced soil erosion. A seepage area was observed in the vicinity of the toe of the upper slope prior to slope failure initiation (Figure 3.7(A)). This compares with the field observation that seepage areas, where springs exist, are prone to slope failure (Lacerda, 2007). The results showed that the seepage initiated after about 58 minutes in the experiment with 200 mm deep soil and 148 minutes for the 500 mm deep soil profile. The seepage areas grew progressively upslope as the slope failure retrogressed. The growth of seepage area contributed to the development of runoff. No seepage was ever observed on the upper slope above the last failure location because of the high infiltration capacity of the soil.

Sediment yield results for all experiments are presented in Figure 3.9. Low sediment yields were observed during pre-failure rainfall, high during landslide events, and again low under post-failure rainfall. The magnitude of pre-failure sediment yields, during landslide events, and post-failure sediment yields was related to the depth of soil profile. During pre-failure rainfall, only fine sediments were transported by the runoff to the outlet. Interrill soil erosion was low because there was a limited supply (less than 1% by weight) of erodible fine (< 0.075 mm) soil material. Furthermore,

given the high permeability of the soil, overland flow and associated erosion was not observed in the upper sloping section of the flume.

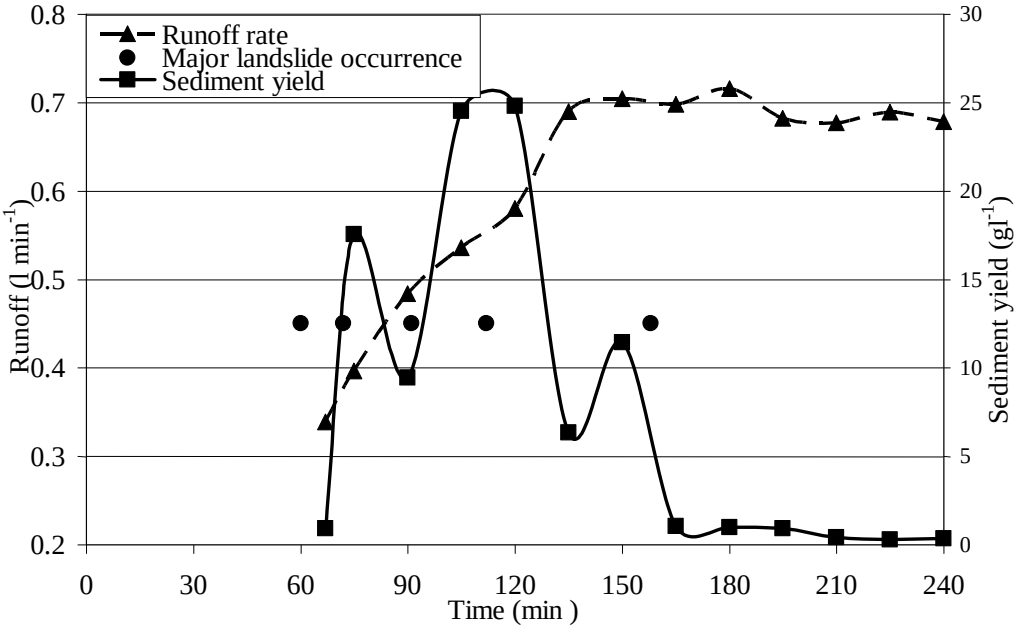

A

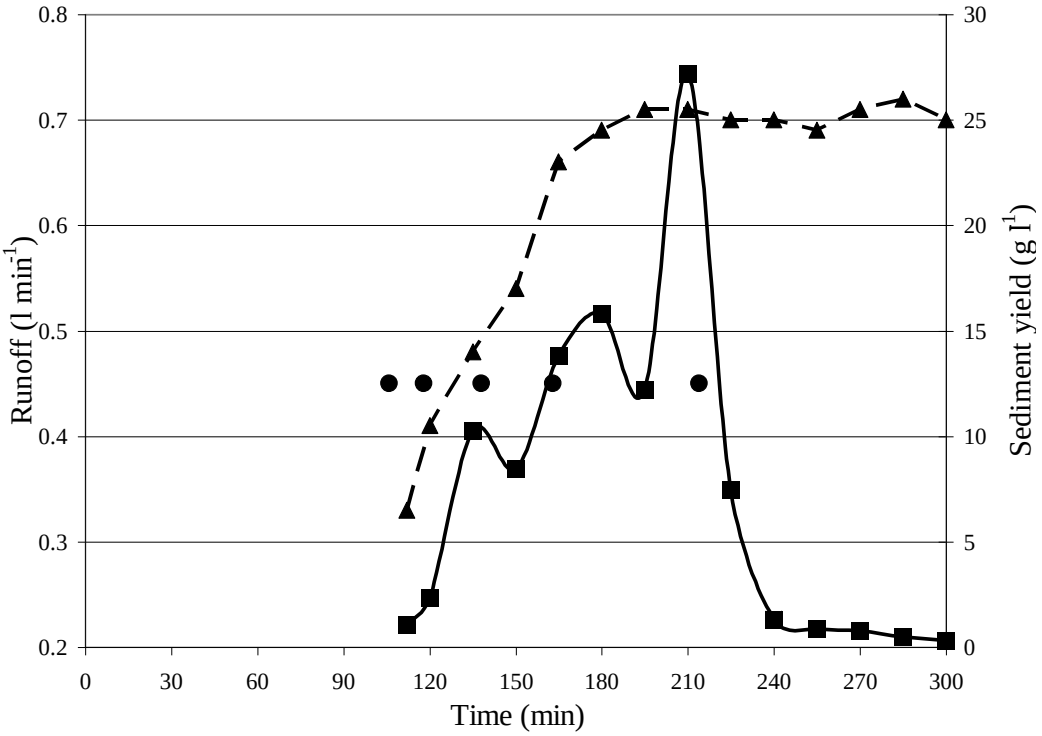

B

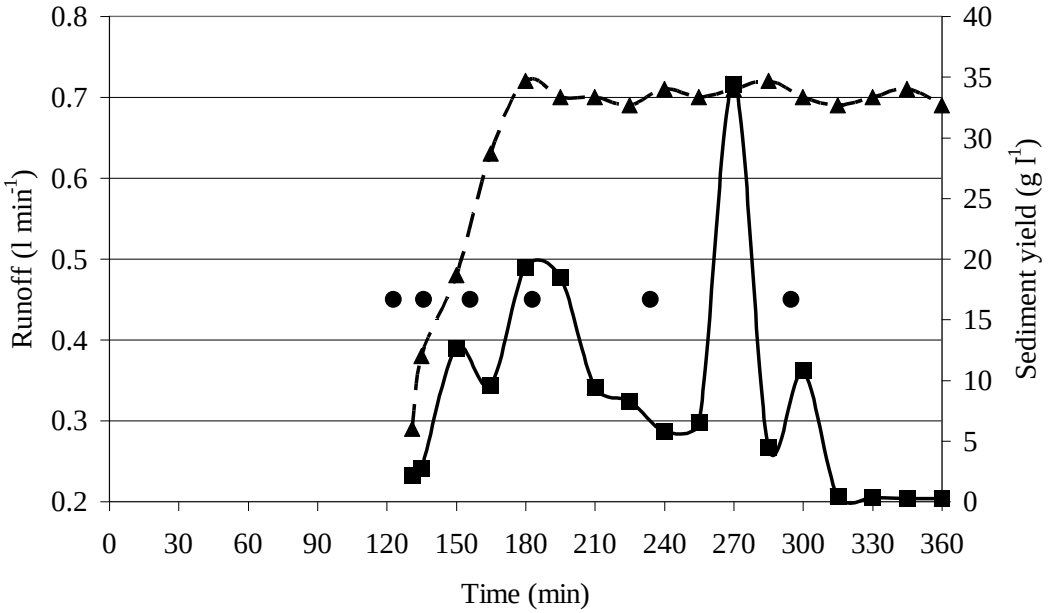

C

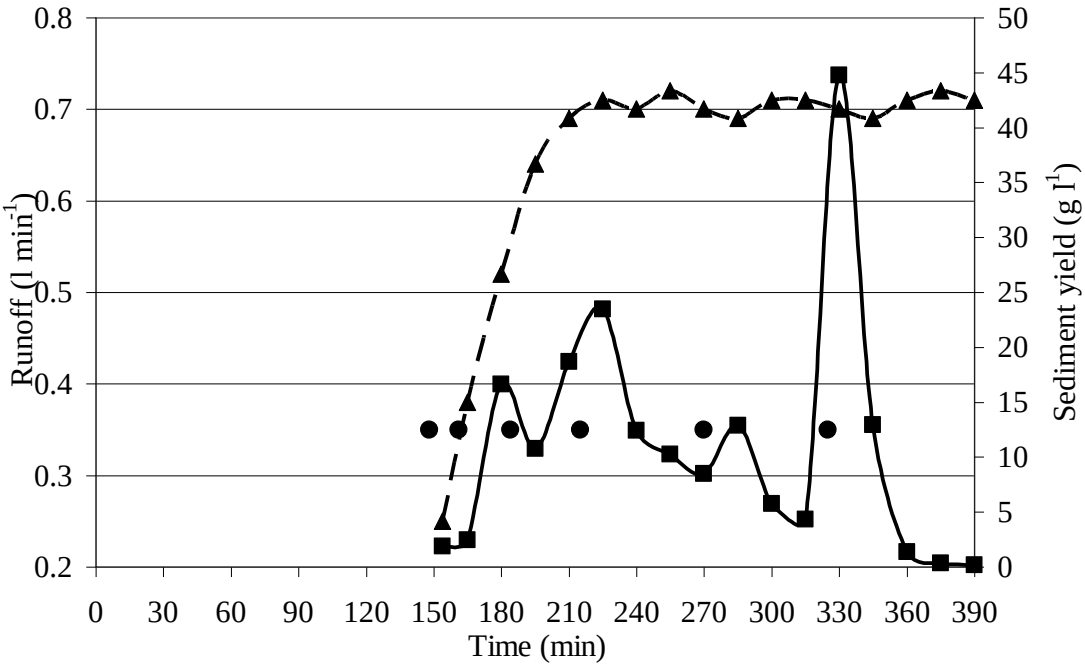

D

Figure 3.9: Runoff and sediment yields over time for 200 mm deep soil in 240 minutes rainfall (A), 300 mm deep soil in 300 minutes rainfall (B), 400 mm deep soil in 360 minutes rainfall (C), and 500 mm deep soil in 390 minutes rainfall (D). Dots represent major slope failure events. Rainfall initiated at the beginning of each experiment.

Shallow rills, which developed to route the surface runoff, were responsible for transporting sediment. Sediment yields increased significantly when the failed mass

reached rills following failure events. Sediment yields during continuous rainfall were highly related to the occurrence of the slope failure events. For instance, in the 200 mm depth soil profile, after two major failures at around 72 minutes of rainfall, shallow rills developed and failed eroded material gradually moved towards the outlet transported by concentrated flows in the shallow rills (Figure 3.9 (A)). When this material reached the outlet (after about 75 minutes of rainfall), the sediment yield suddenly increased to about 16 g l^{-1} of runoff (Figure 3.9 (A)). This value decreased and remained at about 10 g l^{-1} while a subsequent failure occurred. Again, when the subsequent failed material reached the outlet, the sediment discharge increased to a maximum value of approximately 25 g l^{-1}. Concentrations of coarser materials were significantly higher during these peaks, but for the most part, transported sediments were limited to finer particles. Similar results were obtained for the other soil profiles, but the value and time of peaks differed. For example, the peak sediment discharge for the 500 mm deep soil was about 45 g l^{-1}, attained after about 330 minutes of rainfall (Figure 3.9 (D)). These results explain the temporal variation of sediment yields. The temporal variations of landslide-driven sediment yields are generally related to location (i.e. distance from the drainage network) and quantity of landslides, rainfall duration and intensity, and steepness of the downslope profile (Schuerch et al., 2006; Schwab et al., 2008).

Slopes along the sliding sections in the upper flume stabilized at around 23º whereas those in the deposition sections stabilized at about 13º. As shown in Table 3.4, the deposition sections were steeper in deeper soils. Final slope profiles at the end of the experiments are presented in Figure 3.10. Conservation of mass dictates that continued surface displacement must eventually decrease the surface elevation and slope gradient in an active landslide, whereas surface elevation and slope gradient should increase in the deposition area. The experimental results compare with actual observations in catchment-scale studies. Johnson et al. (2000), for example, report the average gradient of landslide deposits to be about 10°. During the retrogression processes of in these experiments, as shown in Figure 3.8 the longitudinal distances between two subsequent failures were shorter for deeper soils. The shorter failed blocks redistributed along a shorter distance making the local topography steeper in the deposited section.

Table 3.4: Minimum and maximum slope angle at the end of experiment measured in failure and deposition zones.

Soil depth (mm)	Range of slope (°)	
	Minimum	Maximum
200	12.3	22.7
300	12.8	22.9
400	13.1	23.0
500	13.7	23.3

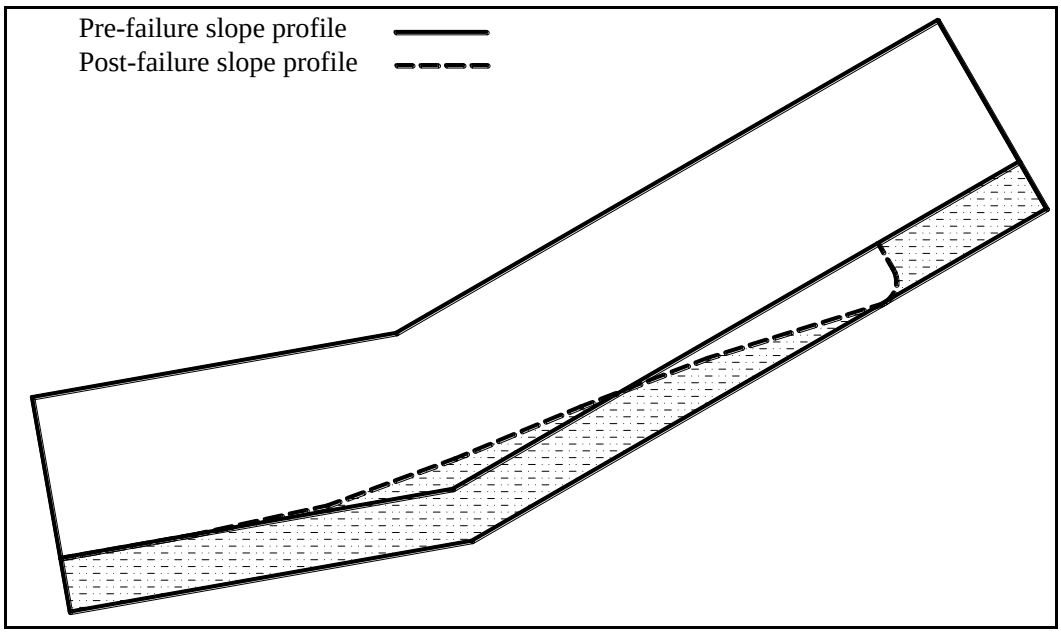

A

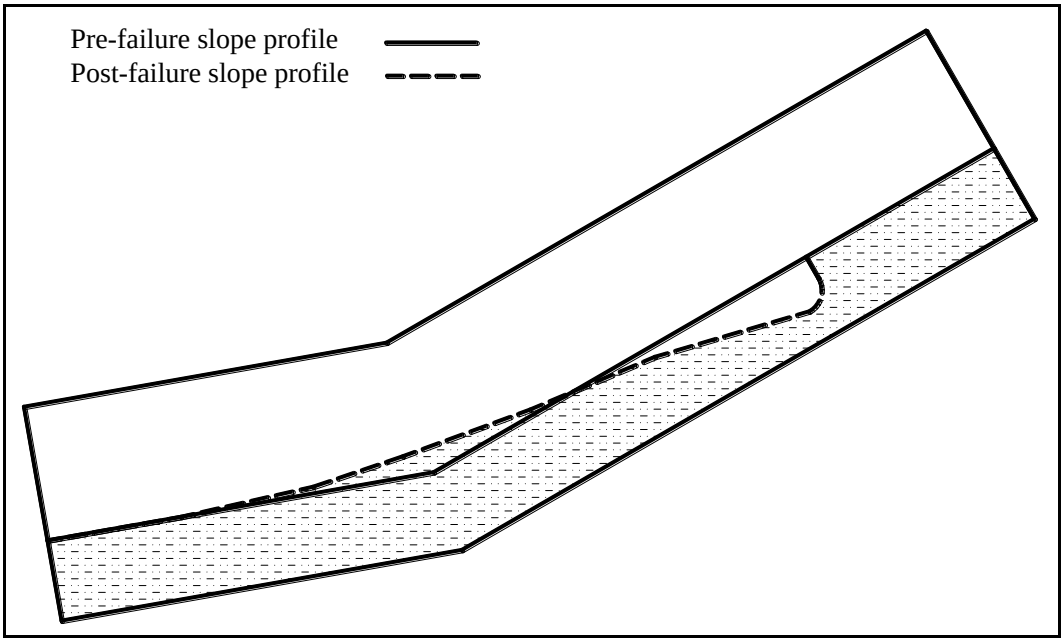
Pre-failure slope profile
Post-failure slope profile

B

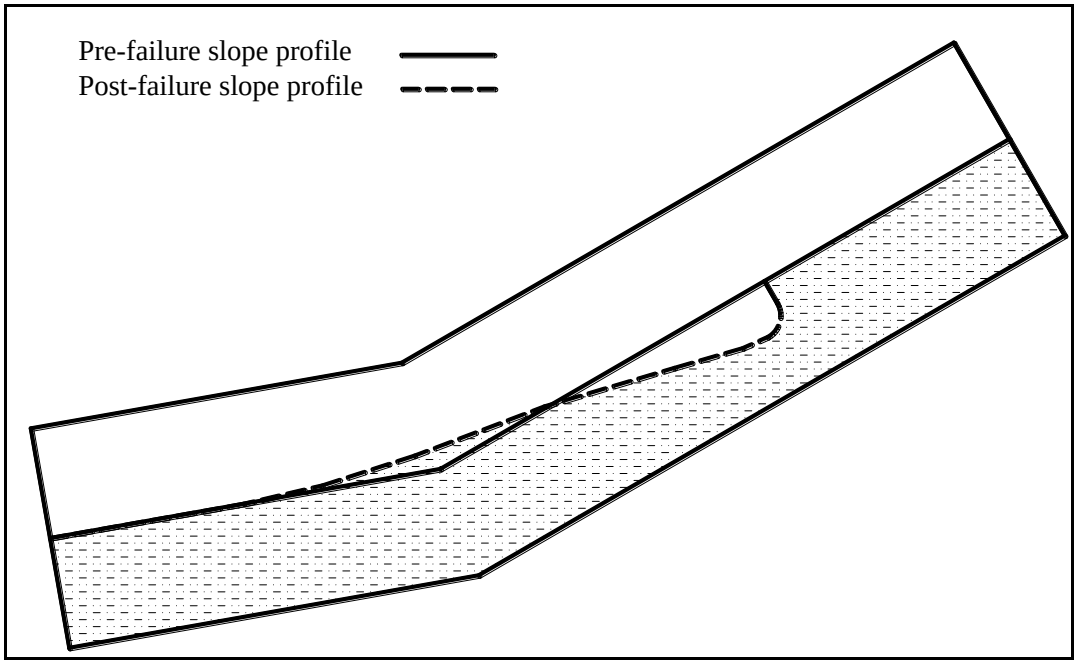
Pre-failure slope profile
Post-failure slope profile

C

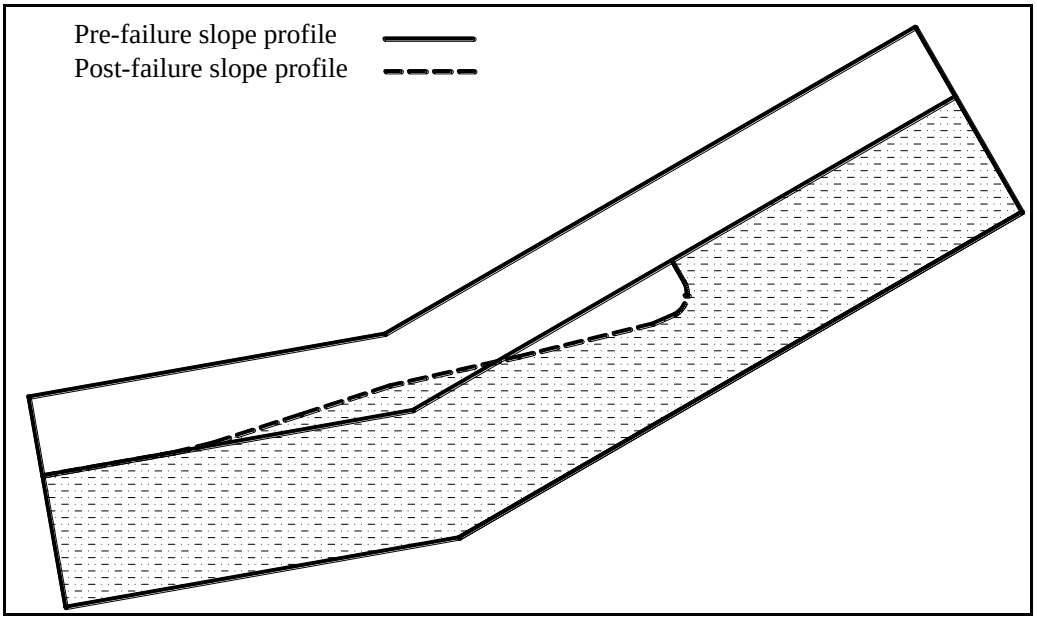

D

Figure 3.10: Initial pre- and post-failure soil profile configurations for 200 mm deep soil after 240 minutes rainfall (A), 300 mm deep soil after 300 minutes rainfall (B), 400 mm deep soil after 360 minutes rainfall (C), and 500 mm deep soil after 390 minutes rainfall.

Maximum and average sediment discharges according to the profile depths are presented in Figure 3.11. With an increase in soil depth from 200 to 500 mm, peak sediment yields increased from 25 to 45 g l^{-1} of runoff, while the average sediment yields increased from 7 to 10 g l^{-1} of the runoff. These peak sediment yields were about 100-115 times higher than pre-failure sediment yields. Results showed that maximum and average sediment discharges were higher in deeper soil profiles than in shallow ones. This phenomenon is related to the sloping profile configuration developed in the deposition section of the flume; steeper profiles developed in the deposition section of the experiments with deeper soil profiles.

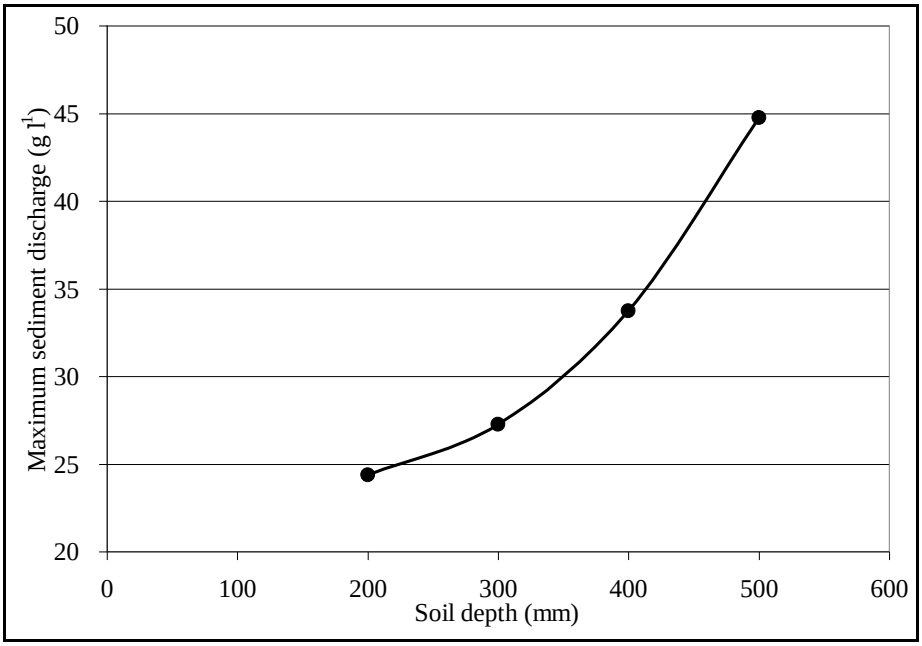

A

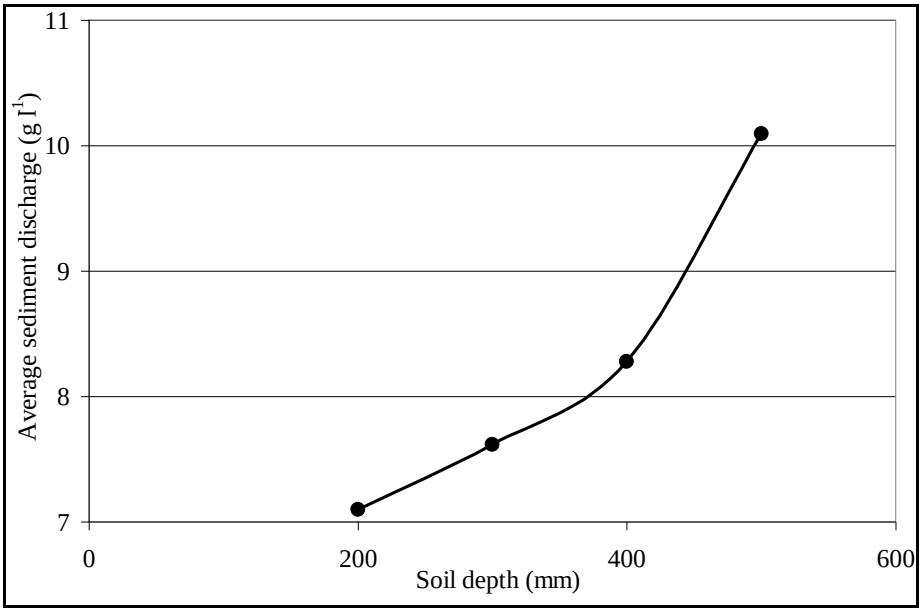

B

Figure 3.11: Plot of maximum (A) and average (B) sediment yield (g l^{-1}) for different soil depths.

Fluvial reworking of sediment derived from shallow landslides also involves soil armouring that leads to surface coarsening because of the selective removal of the finer transportable materials from the soil surface by rainfall and overland flow. Soil armouring can be quantified in laboratory experiments by sampling the runoff and determining the particle size distribution of the top soil layer after the experiments. An investigation of soil armouring, carried out by sieving samples of soil collected

from the top 10 mm in the deposition section, showed that the mean particle size (D_{50}) of the armoured soil material was 0.98 mm compared to 0.57 mm for the original soil (Figure 3.12). It is important to note that the rate of armouring is dependent on the intensity of rainfall; higher intensity would lead to quicker armouring due to increased runoff (Cochrane et al., 2007b).

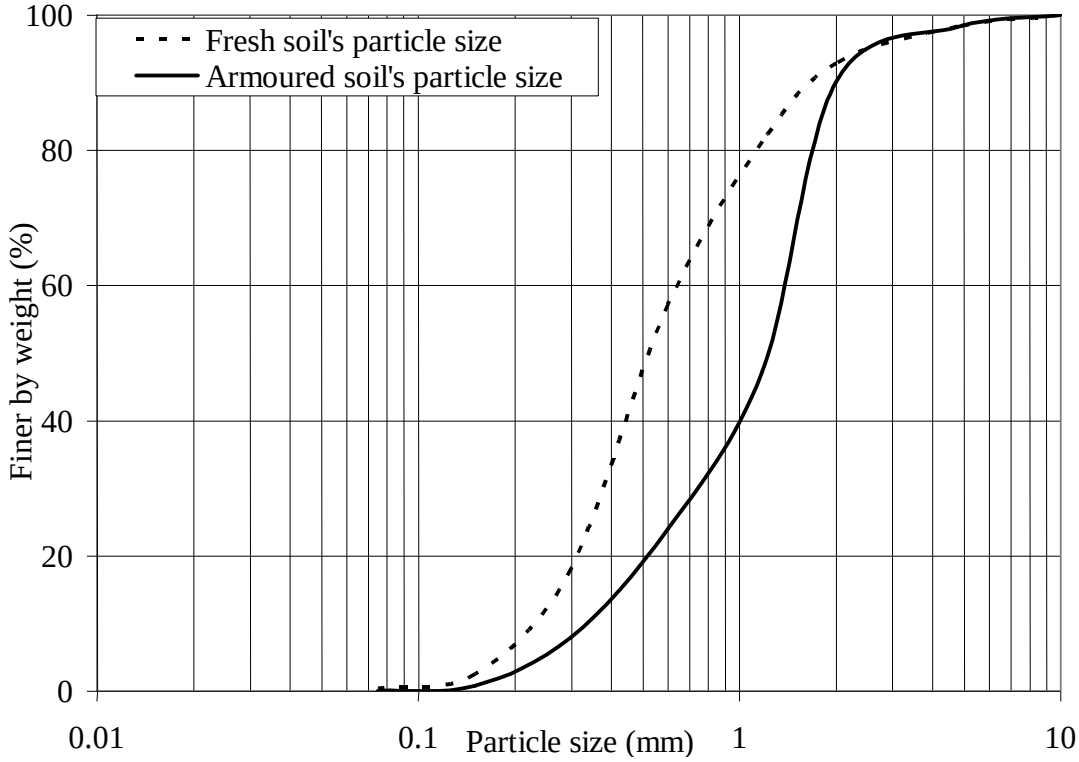

Figure 3.12: Particle size distribution before and after an experimental run showing the soil armouring phenomenon. Armoured soils were sampled from the 500 mm deep soil profile after the experiment.

Up to six times lower sediment yields were observed in post-failure events compared to initial conditions. This reduction in sediment yields can be attributed to (a) change in local topography of the soil profile in which there was a significant decrease in slope gradient in the failed zone and only a slight increase in slope gradient in the deposition section, and (b) soil armouring which occurred in the deposition zone, reducing erosion further. The reduction in long-term sediment yields due to changes in local topography brought about by shallow landslides has also been observed in field studies. Korup et al. (2004), for example, report that post-failure sediment yield

rate decreased by about 20 fold following changes in topography in a catchment over a period of about two years. The experimental results demonstrate the mechanics of changes in sediment yields under continuous rainfall and also suggest that armouring can be partially responsible for those changes.

3.4 Summary and conclusions

Water-induced shallow landslides and soil erosion were investigated using a two sloping flume in granular sandy soil. Sediment yield behaviour before, during and after slope failure events were studied. Experiments were conducted with varying depths of sandy soil.

Water-induced shallow landslides initiated in response to soil saturation process. The soil was close to saturation with moisture content of about 26%. The time of highest soil moisture content varied in time according to the soil profile depth. The slope failure initiation, evolution, and retrogression were related to the soil profile depth. Slope failure retrogressions were more frequent in shallower soils and frequency decreased as the failures extended upward which was attributed to the gradual reduction in upslope contributing area. The reduction was pronounced in the shallower profile. Initial slope failure depth was related to the soil profile depths; the failure depth decreased with increase in depth of profile.

Pre-failure sediment yields were quite low and dominated by fine grains. After slope failures occurred failed materials moved downward, which increased sediment yields. Rill formation also helped to transport coarser materials. Peak sediment discharges in the failure events ranged from 100 to 115 times higher than pre-failure erosion rates. However, when the landslides retrogressed farther from the outlet, the effects of landslide on sediment discharge decreased.

Soil redistribution after shallow landslides made the deposition profile steeper in the experiments with deeper soil. Higher peak sediment discharges were therefore observed with the deeper soil profiles compared to the shallower soil. Soil mass redistribution and soil armouring were responsible for reducing soil erosion of fine grained material by approximately 6 times compared with the initial conditions.

Chapter 4 Laboratory Scale Shallow Landslide and Soil Erosion Study in Silty Soil

4.1 Introduction

Sediment yield patterns before, during and after shallow landslides from depth varying sandy soil profiles were presented in Chapter 3. The chapter reported the impacts of shallow landslides on sediment yields from only granular sandy soils, but it is also important to study those impacts using fine grained soils which react differently than sandy soils. In this chapter, the evolution of shallow landslides and sediment yields using fine grained silty soil will be presented.

The main objective of this chapter is to quantify sediment yield patterns before, during and after water-induced shallow landslides from soil profiles on fine silty soil. To understand the changes in sediment yields, an understanding and simulation of landslide initiation, evolution, retrogression and deposition processes is required. Although these processes are readily observed along natural hillslopes, studying and monitoring these processes in a natural environment is significantly challenging given the extended timeframe between occurrences of these processes, variability in rainfall, soils, and other factors. These specific processes are therefore best studied and quantified in a flume using a rainfall simulator under controlled laboratory conditions. Through a flume scale landslide study, it is possible to accurately quantify the changes in sediment yields before, during, and after shallow landslides in a reasonable time period. It is important, however, to note that although flume experiments are possibly the best approach to simulate natural slope failures, translating these results to natural conditions requires caution because natural soil variability and initial stress conditions are difficult to reproduce in a flume study (Lourenco et al., 2006).

Another aim of this study is to develop a framework for an integrated approach to modelling sediment yields in landslide prone landscapes by combining a landslide model, a soil redistribution model and an erosion/runoff model. The infinite slope method (Skempton and DeLory, 1957) of slope stability analysis is chosen to predict landslides and a simple rule based soil redistribution model is validated using the

experimental results. The Water Erosion Prediction Project (WEPP) model (Flanagan and Nearing, 1995) is chosen for modelling pre- and post-failure soil erosion and runoff. Physically-based models such as WEPP, with an explicit attempt to describe runoff and soil erosion process, are better equipped to evaluate the impact of management intervention and environmental change at a range of temporal and spatial scales than other empirically-based models (Yu and Rosewell, 2001). Testing of the WEPP model in non-failure conditions is well reported in literature both at plot (e.g. Yu and Rosewell, 2001; Pieri et al., 2007) and watershed/catchment scales (e.g. Cochrane and Flanagan, 1999; Amore et al., 2004; Pandey et al., 2009), but further validation is necessary for loess soil conditions.

4.2 Experimental procedures

Shallow landslides were triggered in fine grained silty loess soils using an experimental flume with different sloping configurations. The experimental results were used to test the landslide, soil redistribution, and soil erosion models.

4.2.1 Experimental flume

The same flume and rainfall simulator used in the sandy soil experiments illustrated in Chapter 3 were used for loess soils. However, some modifications were made in the flume set up to facilitate shallow landslide processes during the experimental timeframe in the fine grained low permeable silty loess soil. In these experiments, eight cylindrical rain gauges were placed along the two sides of the flume to monitor the rainfall intensity (Figure 4.1) and its spatial distribution over time during experimental simulations. Three 2 m long and 12 mm diameter low pressure (0.5 kPa) porous pipes were interconnected and placed along the flume bed longitudinally downward from uppermost part of the upper flume section (Table 4.1). The transverse distance between each pipe was 100 mm. The pipes were externally connected to a precisely regulated water supply system from immediately outside of the upper flume section to introduce desired levels of groundwater.

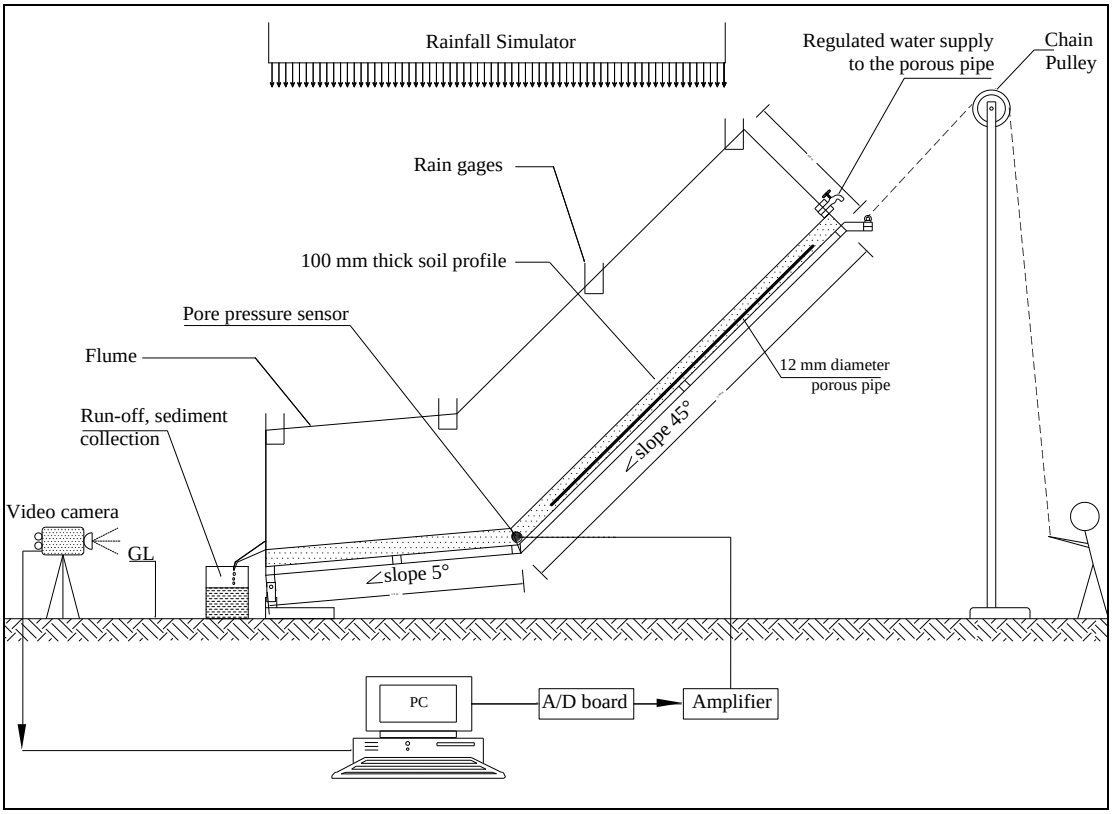

Figure 4.1: Schematic diagram illustrating a typical experimental set up.

Table 4.1: Experimental summary, sloping configuration, rainfall, and soil initial porosity.

Exp	Upper (°)	Lower (°)	Soil depth (mm)	Total rainfall (mm)	Porosity
1	35	10	100	158	0.41-0.42
2	40	10	100	158	
3	45	5	100	154	
4	47	7	100	161	
5	35	10	100	312	0.41-0.42
6	40	10	100	317	
7	45	5	100	317	
8	47	7	100	320	
9	35	10	100	315	0.46-0.48
10	40	10	100	318	
11	45	5	100	316	
12	47	7	100	332	

4.2.2 Experimental method

Twelve experiments were conducted in the loess soils (Table 4.1). The soils' physical and chemical properties were derived from various tests, for example, particle size distribution was determined jointly by sieving the coarser fraction (>75 micron) and by using the hydrometer method (Day, 1965) for the finer fraction (<75 μm) of the soil. The saturated hydraulic conductivity was determined by the falling head method (e.g. Cernica, 1995). The Cation Exchange Capacity (CEC) of the soil was measured using the method defined by Sumner and Miller (1996). Other geotechnical properties such as angle of internal friction (φ), cohesion (C) and organic matter content were determined as in sandy soil described in Chapter 3. The results of soil tests are listed in Table 4.2.

As in the sandy soil experiments, the rainfall and its spatial distribution were monitored every 30 minutes to verify consistency among the experiments. Total rainfall volume from the simulator was obtained by adding together the hourly averages of rain falling in the rain gauges. There was little variation in rainfall distribution, as measured by the upper rain gauges during the experiments; however because of the angle and elevation difference the lower four consistently had about 30% less rainfall. Similar to the sandy soil experiments, slope failure occurrence time, slip surface depth, location, and slope failure retrogression behaviour were recorded by direct observations and video camera recordings. One minute runoff samples were collected from the end of the flume immediately after runoff reached the outlet and at 10 minute intervals thereafter. Runoff samples were collected at a 1 minute interval during slope failures. Sediment discharges and runoff rates were calculated from the collected runoff samples after oven drying. For each experiment, the particle sizes of the runoff samples were analysed by sieving for particles greater than 1 mm, and by using a high definition digital particle size analyser (Micrometrics Saturn Digisizer 5200) (e.g. Meadows et al., 2005) for particles finer than 1 mm. Pore pressure was measured every second using the same pore pressure transducer in sandy soil experiment. Post-failure topography was measured using an instantaneous-profile laser scanner (Darbourx and Huang, 2003). Post-failure slope profiles were obtained for WEPP modelling purpose from the scanned topography using a GIS based tool as described in Cochrane and Flanagan (2003).

Table 4.2: Soil physical properties and properties of the soil profiles.

SN	Properties	Unit	Mean or range of value
	Soil properties		
1	Cohesion (C)	kPa	1.04
2	Angle of internal friction (φ)	°	31
3	Organic matter content (OM)	%	3.40
4	Moisture content at the time of soil placement (w)	%	12
5	Moisture content at the time of experiment	%	~30
6	Mean grain size (D_{50})	mm	0.075
7	Effective grain size (D_{10})	mm	0.010
8	Specific gravity (G)	-	2.60
9	Cation exchange capacity	meq $100g^{-1}$	14
	Properties of soil profiles		
1	Bulk unit weight (γ)	kN m^{-3}	13.80-16.10
2	Dry unit weight (γ_d)	kN m^{-3}	11.60-13.20
3	Saturated unit weight (γ_{sat})	kN m^{-3}	17.32-17.80
4	Porosity (n)	-	0.41-0.48
5	Coefficient of permeability (k_{sat})	m s^{-1}	$1.7x10^{-6}$– $2.5x10^{-6}$ in experiments 1-8 & $3.9x10^{-6}$ – $4.4x10^{-6}$ in experiments 9-12

Soil profile depth in all experiments was set to 100 mm to trigger shallow landslides within the experimental timeframe. To achieve soil saturation levels required to trigger slope failures in low permeable silty soil profiles, the soil moisture was increased by upward infiltration at a total steady rate of 10 ml min^{-1} from the 3 porous pipes at the base of the flume for about 96 h prior to the experiments. The experiments were grouped into three sets according to differences in rainfall and soil

placement technique (i.e. compaction level) in the flume. Each set of four experiments was completed using sloping configurations of 35°, 40°, 45° and 47° in the upper flume section, and the respective inclinations in the lower flume were fixed at 10°, 10°, 5° and 7° (Table 4.1). In the first set of four experiments, soils were uniformly placed and compacted in layers of 40 to 50 mm depth using a 40 kPa pressure mechanical mallet that resulted in a densely compacted profile with porosity ranging from 0.41-0.42 and unit weight between 15.9 and 16.1 kN m^{-3}. The first set of four experiments was run under a lower rainfall rate of approximately 20 mm h^{-1}. A similar soil placement technique was adopted in the second set of experiments but the rainfall rate was increased to about 40 mm h^{-1}. Lastly, four more experiments were completed under rainfall rates of approximately 40 mm h^{-1} but the soil placement technique differed. In this third set, soils were uniformly placed in a layer 100 mm thick and compacted using the mallet. The prepared soil was in a loose state (e.g. Iverson et al., 2000) with porosity ranging from 0.46 - 0.48 and unit weights between 13.8 and 14.1 kN m^{-3}. Although most of the first two sets of experiments (1-8) did not trigger shallow landslides, they are included in this study as their results were useful in modelling erosion and to compare with the results from the third set (9-12).

4.3 Modelling approach

The modelling approach consists of three components: soil erosion, landslide prediction, and soil redistribution models. WEPP provides spatial distribution of soil erosion and deposition along a hillslope in a single storm event or during a long-term time series of climatic conditions ranging from a single year to hundreds of years. The landslide prediction model is based on slope stability analysis using time varying pore pressure distributions. A simple ruled based soil redistribution model is used to predict failure depth and runout distance.

4.3.1 Soil erosion model: WEPP

In this study, WEPP was tested using a single storm event to model surface runoff and soil erosion in pre- and post-failure events. A detailed description of the model has been given in Chapter 2. The model was tested for two main conditions: (a) pre-failure for 8 h (total experimental period) (experiments 1-8); and (b) post-failure for the final 6 h in the landslide modified sloping profiles (experiments 9-12). The measured runoff and sediment yields were used to test the model. The model inputs

describing the soil's physical properties are presented in Table 4.3. The values of critical shear stress, inter-rill and rill erodibility, and effective hydraulic conductivity were adjusted while calibrating the model for the silty loess soil (Table 4.3). However, other model input parameters related to the soil's physical properties were obtained from laboratory tests. For climate input, the measured precipitation (amount, duration, time to peak, and peak intensity) was calculated for the model from the measured rainfall. Temperature (maximum, minimum, dew point) and solar radiation data, for each experimental day were gathered from an automated climate station located at the University of Canterbury. In all experiments, the WEPP management practice was set to fallow management and the acrylic flume base was defined as a highly impermeable restricting layer.

If the failures retrogressed further upslope and resulted in exposed flume bed in some portion of the flume, a separate WEPP overland flow element (OFE) was assigned to that portion of the flume. The OFE was characterised as highly impermeable rocky materials with extremely low erodibility and with the properties illustrated in Table 4.3. Values of soil properties used for the OFE were adjusted during calibration.

Three performance indices, (a) the Nash-Sutcliffe coefficient of efficiency (NSI) (Nash and Sutcliffe, 1970), (b) the index of agreement (IOA) (Willmott, 1981) and (c) the root mean square error (RMSE), were used to evaluate the model performances by comparing the simulated and observed runoff. Equations 4.1 to 4.3 describe the evaluation criteria

$$NSI = 1 - \frac{\sum_{i=1}^{n} (O_i - P_i)^2}{\sum_{i=1}^{n} (O_i - \overline{O})^2} \qquad \text{Equation 4.1}$$

$$IOA = 1 - \frac{\sum_{i=1}^{n} (O_i - P_i)^2}{\sum_{i=1}^{n} (\left|P_i - \overline{O}\right| + \left|O_i - \overline{O}\right|)^2} \qquad \text{Equation 4.2}$$

$$RMSE = \sqrt{\frac{\sum_{i=1}^{n} (O_i - P)^2}{N}} \qquad \text{Equation 4.3}$$

Where O_i and P_i represent the measured and predicted values respectively at the i^{th} time; N is the total number of measurements. $\overline{O}$ is the mean value of O_i. The ideal condition is that Equations 4.1 and 4.2 yield a value of unity, and RMSE is zero.

Table 4.3: Soil properties used for the WEPP simulations.

Soil properties	Values for	
	Soil	Exposed flume bed
Rock, % weight		100
Sand, % weight	64	
Clay, % weight	2.8	
Organic matter, % weight	3.4	NA
CEC meq $100g^{-1}$	14	NA
Albedo	0.23	0.5
Initial soil saturation, %	100	100
Interrill erodibility, kg s m^{-4}	3×10^{6}	2×10^{4}
Rill erodibility, s m^{-1}	2×10^{-3}	0.06
Critical shear stress, N m^{-2}	2.3	100
Effective hydraulic conductivity for soil, m s^{-1}	9.58×10^{-7}	2.22×10^{-10}
Effective hydraulic conductivity for restrictive layer, m s^{-1}	2.7×10^{-20}	2.7×10^{-20}
Soil depth	100	0

NA: Not Applicable

4.3.2 Landslide model

The infinite slope method (Skempton and DeLory, 1957) of slope stability analysis is a widely accepted tool to assess shallow landslides in mountainous and hilly regions. This is because the topographic surface is quite often underlain by a bedrock plane lying parallel to the slope, and the potential failure plane generally lies at a depth below the surface which is small compared to the profile length. In this study, the landslide model was validated against where slope failure occurred in the experiments. The criterion to decide whether a slope is stable or unstable depends upon the value of Fs (Equation 2.19 - Chapter 2) being larger or smaller than 1.

Montgomery and Dietrich (1994) define four stability classes depending upon the value of the safety factor. The slope is considered *unconditionally unstable* if the slope is unstable, even when dry or when the safety factor is less than 1, and *stable* if Fs is greater than 1.5, even when the soil is fully saturated. Table 4.4 defines two other classes between Fs = 1 and 1.5.

Table 4.4: Slope stability classes according to the safety factor value.

Safety factor	Slope stability	Remarks
Fs > 1.5	Stable	Only major destabilizing factors lead to instability
1.25 < Fs < 1.5	Moderately-stable	Moderate destabilizing factors lead to instability
1 < Fs < 1.25	Quasi-stable	Minor destabilizing factors can lead to instability
Fs < 1	Unstable	Stabilizing factors are needed for stability

4.3.3 Soil redistribution model

A simpler rule-based empirical model (Corominas, 1996) as expressed in Equation 2.21 was used to predict the runout distance. The model can be applied to multiple landslides occurring on a hillslope over periods of time ranging from a single rainstorm to several years.

Estimation of potential failure depth is required to derive the landslide volume in Equation 2.21. Few studies have been published to predict the potential failure plane (depth). The failure depth prediction model proposed by Claessens et al. (2007) as expressed in Equation 2.24 is simple to use and incorporates the geotechnical properties (cohesion, angle of internal friction and density) of the soil and the local slope topography. However, the model has two noticeable deficiencies: (a) the model does not take into account the original soil profile depth, and (b) the model is not valid for cohesionless granular soil due to presence of soil cohesion parameter in the denominator of the model. As a result, the model may grossly overestimate the landslide induced materials (Claessens et al., 2007). In general, the location of a failure plane may lie within the soil, at an interface between soils of different packing densities, at the bedrock interface, or at an interface corresponding to a decrease in hydraulic conductivity from the overlying soil to the lower layer. The failure plane location is a function of the geotechnical properties of the soils and slope gradient.

Typically, a shallow soil profile has a planar failure plane along an interface dividing a shallow upper soil layer from an underlying stronger and often less permeable underlying soil layer or bedrock (Burton and Bathurst, 1998). In hilly and mountainous areas where soils are shallow, landslides generally occur along the underlying bedrock contact (e.g. Dai et al., 1999). Failure will only take place when the soil becomes saturated from the terrain surface to the depth of potential failure plane. The saturated zone usually defines the potential failure zone (Terlien, 1997). Here, a simple failure depth prediction approach was applied which is similar to the approach used by Doten et al. (2006) who used the original soil profile depth as the failure depth in their study. Hence in this study, the failure depth in an unstable area equates to the saturated soil profile depth.

4.4 Results and discussion

4.4.1 Landslide evolution and mobilisation processes

Slope failures could not be induced in experiments 1-6. Minor slope failures were triggered in the vicinity of the interface of the two sloping sections in experiments 7 and 8; however, these failures occurred in the initial period of experiments. The mobilisation of the failure material was not significant and thus the processes did not noticeably alter the slope gradient of the profiles. Therefore, experiments 1-8 were grouped as non-failure experiments. The compaction techniques adopted in these experiments yielded low porosity (Table 4.1) and, as a result, sufficient pore pressures could not be imparted to trigger the slope failures. However, experiments 9-12 exhibited high pore pressure generation as measured by the pore pressure transducer located in the interface of the two slopes. Measurements from the pore pressure sensor for experiment 10 are presented in Figure 4.2. The peak pore pressure tended to be maintained for a relatively long time period (about 30 minutes) after the initial slope failures. The results are consistent with previous studies; for example, Iverson et al. (2000) did not record slope failures in their experiments when the porosity of soil was as low as 0.42. Soil porosity has an important role in infiltration rate and amount. Soils in loose state (i.e. high porosity) have greater water holding capacity and therefore higher pore pressures are usually generated upon compression and shearing (Iverson and LaHusen, 1989; Iverson, 1997; Iverson et al., 2000; Mukhlisin et al., 2006). Generation of excess pore pressure is also related to the development of rapid

shearing (Iverson and LaHusen, 1989, Iverson, 1997; Okura et al., 2002; Wang and Sassa, 2001, 2003; Moriwaki et al., 2004).

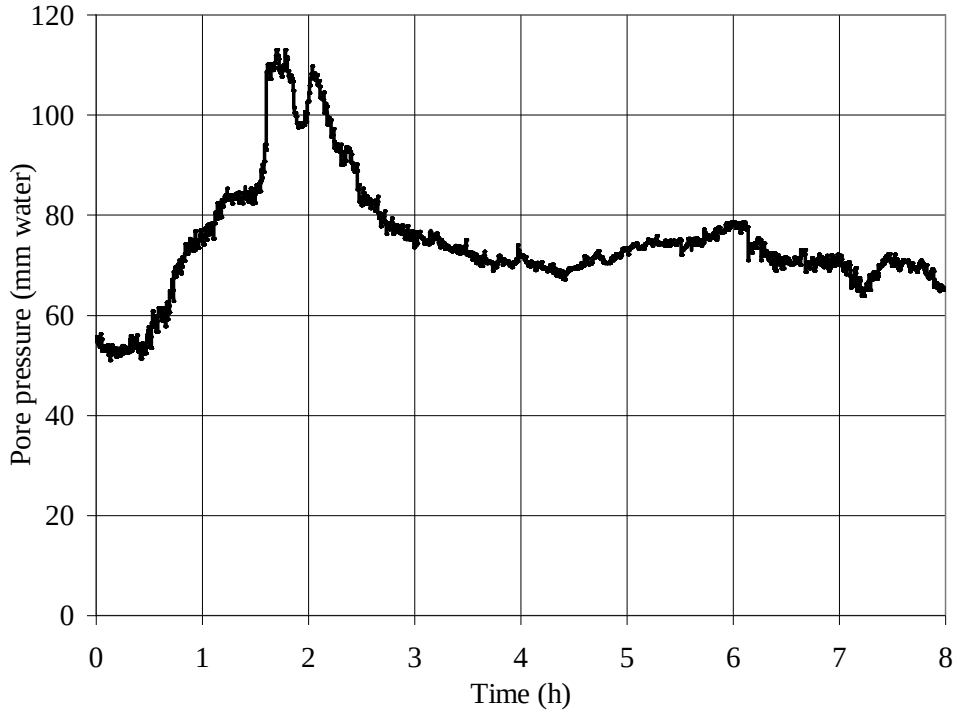

Figure 4.2: Measured pore pressures at the interface of upper slope of the flume in experiment 10. Rainfall initiated at the start of the experiment.

Flowslide failures occurred in experiments 9-12. Flowslides are shallow slope failures triggered by ground saturation and groundwater seepage. Flowslides involve full or partial soil liquefaction due to high pore-pressures and may trigger highly mobile landslides (Hungr et al., 2001). In these experiments under continuous rainfall, slope failures initiated in the vicinity of the interface of the two sloping section of the flume and then retrogressed upslope, pushing the previously failed mass in front of it.. The depths of the blocks were limited to the full depth of the soil due to the shallow profile (100 mm deep). The number of retrogressions was higher in steeper profiles; three in experiments 11 and 12 and two in experiments 9 and 10. All failures retrogressions occurred in the initial two hours of the experiments. Timing of all major failure events for each experiment are summarised in Table 4.5. The observed failure modes are presented in Figure 4.3.

Table 4.5: Timing of major slope failure events for experiments 9-12.

Major slope failure events	Time of occurrence of slope failures (min) for different experiments			
	9	10	11	12
1	48	37	32	30
2	83	81	61	58
3	-	-	86	76

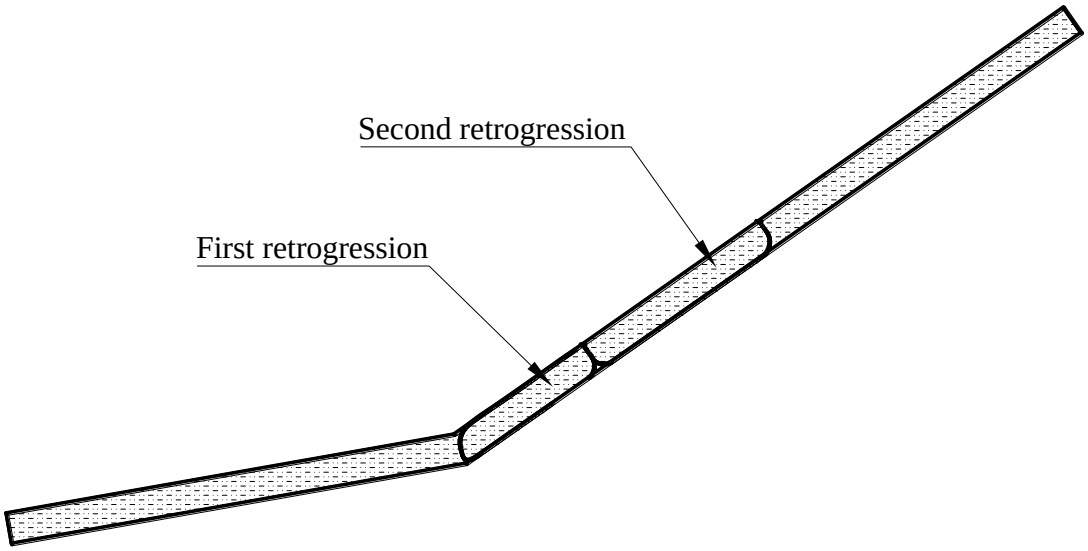

A

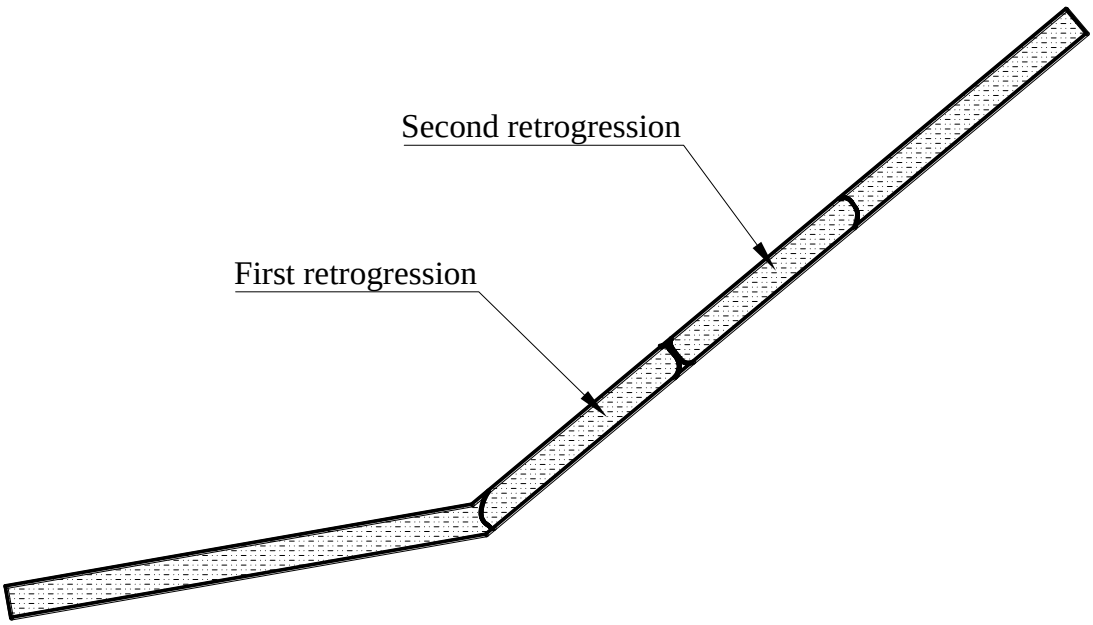

B

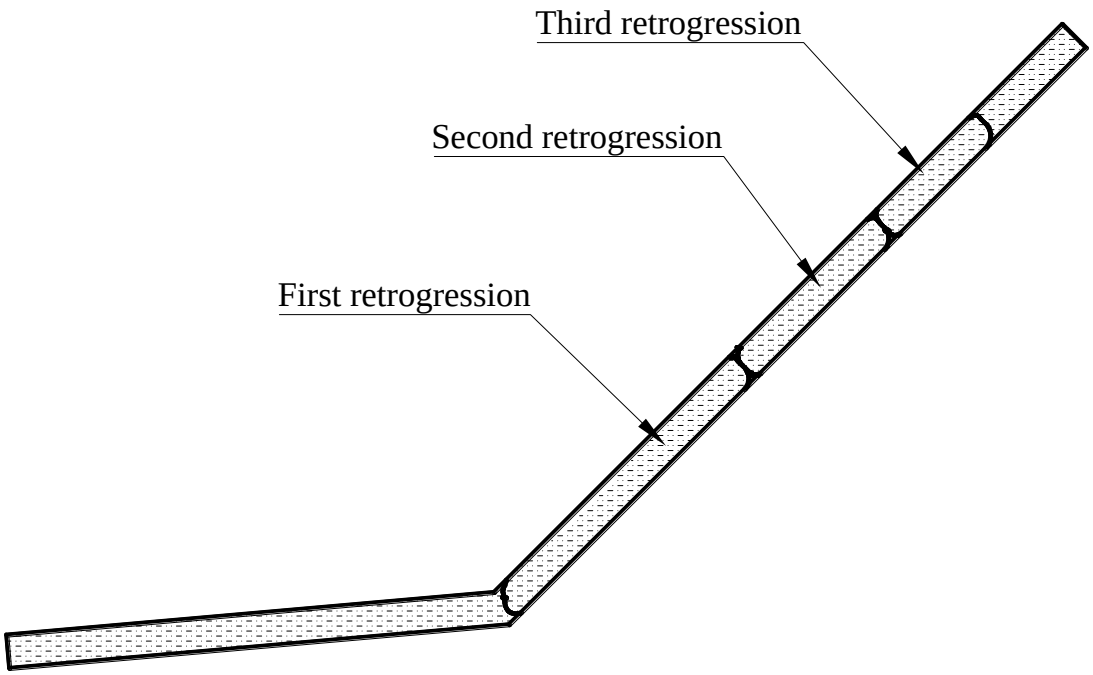

C

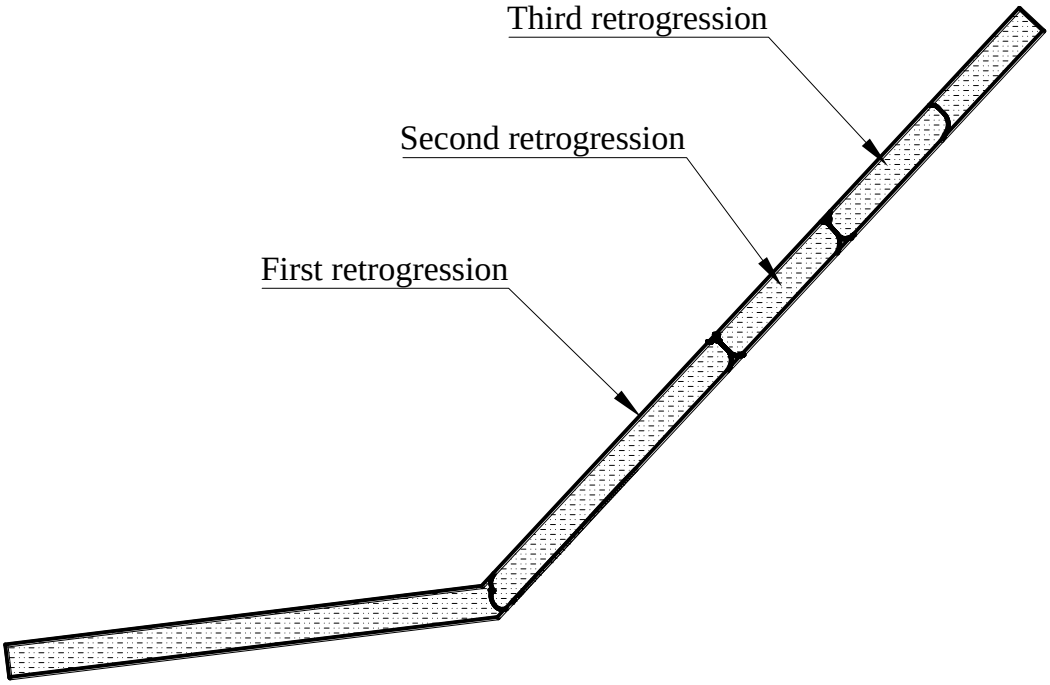

D

Figure 4.3: Summary of failure mode in loess soils in experiments 9 to 12 represented respectively by A, B, C, and D.

The failed and moved soil altered the slope gradient of the soil profiles on fine silty soil in both lower and upper flume sections (Figure 4.4). The slope gradient decreased in the failure section and increased in the deposition zone. The final slope profile was

measured to be between 23° to 25° in the upper section and 7° to 13° in the lower section. This led to the evolution of the new hillslope profile which can lead to subsequent changes in potential soil erosion and sediment yields. The new hillslope is characterised by an upslope and a downslope which are respectively refer to as erosional and depositional slopes. The change in topography is a function of various factors such as occurrence of landslides and runout (travel) distance. The runout distance is related to the development of pore pressures in the mobilized materials and other various properties relating to the soil profile and rheological properties (Corominas, 1996; Iverson et al., 1997; Dai and Lee, 2002; Hunter and Fell, 2003; Malet et al. 2005). Higher pore pressures and material in loose state can trigger a longer runout event.

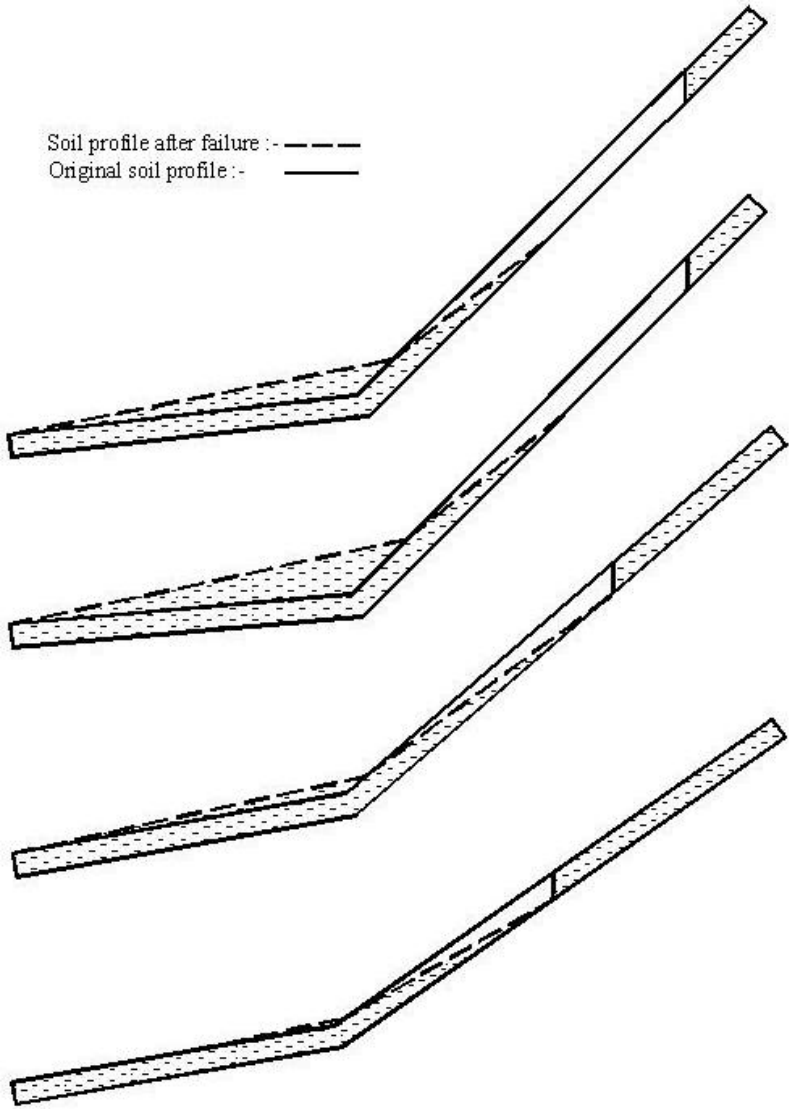

Figure 4.4: Pre- and post-failure slope profile configurations in experiments 9 to 12 represented from bottom to top respectively.

4.4.2 Runoff and sediment yields

Observed surface runoff and sediment yields in experiments 1-8 are presented in Figure 4.5. The results showed steady runoff rates in experiments 1-6. The peak runoff and sediment yields (Figure 4.5 (B)) observed in the initial period of experiments 7 and 8 were the results of minor slope failure events. In all experiments, the sediment yield rates decreased gradually. The average decrease rates were about 0.004 and 0.025 kg m^{-2} h^{-1} in experiments 1 to 4 and 5 to 8, respectively. The decrease rates were more pronounced in the steeper profiles. The diminishing trends of sediment yield rates are characterized by the soil armouring process that leads to the surface coarsening because of the selective removal of finer transportable materials from the soil surface by rainsplash and overland flow. The reduction of sediment yield rates was likely caused by armouring of the soil surface because of the selective removal of finer transportable materials by rainsplash and overland flow. This is clearly shown in Figure 4.6 where the particle size distribution of the eroded material (determined for experiment 5) is plotted against the particle size distribution of the original material. Although the mean particle size of the eroded materials (d_{50} = 0.082 mm) did not significantly differ from the original soil (d_{50} = 0.075 mm), the range of eroded particle sizes was different and the largest particle in the runoff was about 0.8 mm which is significantly smaller than that of the original material. Soil armouring can be quantified in laboratory experiments by sampling the runoff and determining the particle size distribution of the top soil layer after the experiments. Since the soil used was fine grain silty loess, armouring was measured by sampling the runoff. The soil armouring rate is related to parameters such as slope gradient, length of hillslope and rainfall intensity. Extensive armouring is usually observed along longer hillslopes and it develops more quickly on steeper slopes (Sharmeen and Willgoose, 2007). As discussed in Chapter 3, rainfall intensity also has a strong influence on the armouring rate; higher intensity leads to quicker armouring due to increased runoff (Cochrane et al., 2007b).

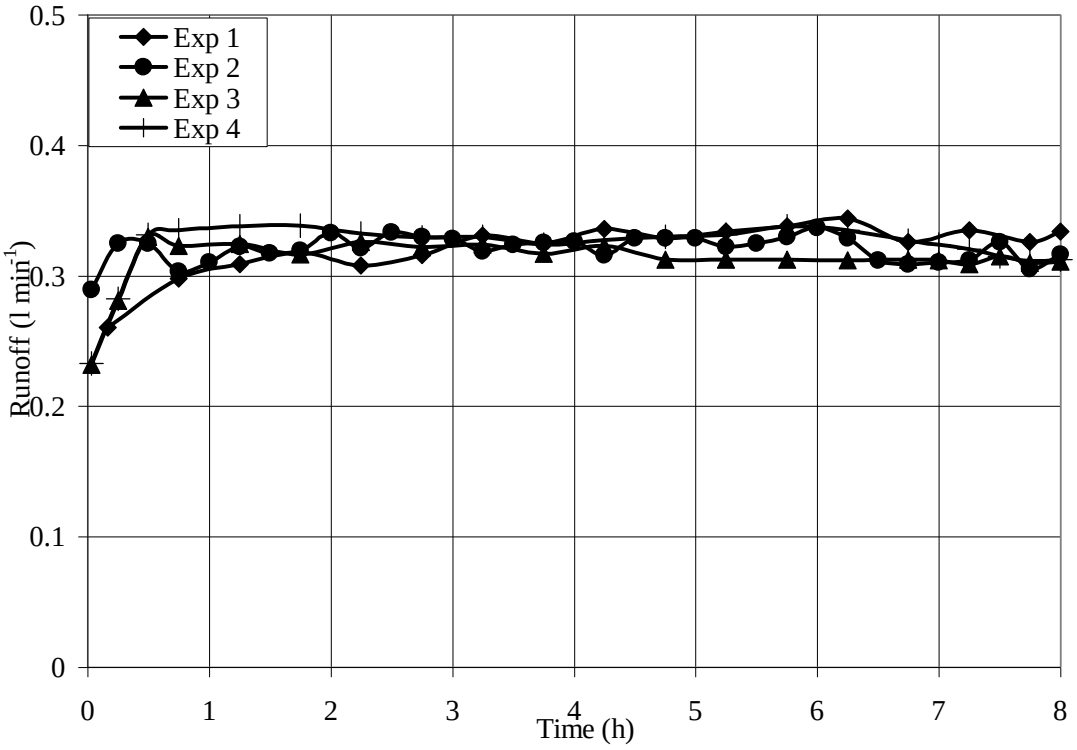
Exp 1
Exp 2
Exp 3
Exp 4
Runoff (l min-1)
0.5
0.4
0.3
0.2
0.1
0
0
1
2
3
4
5
6
7
8
Time (h)

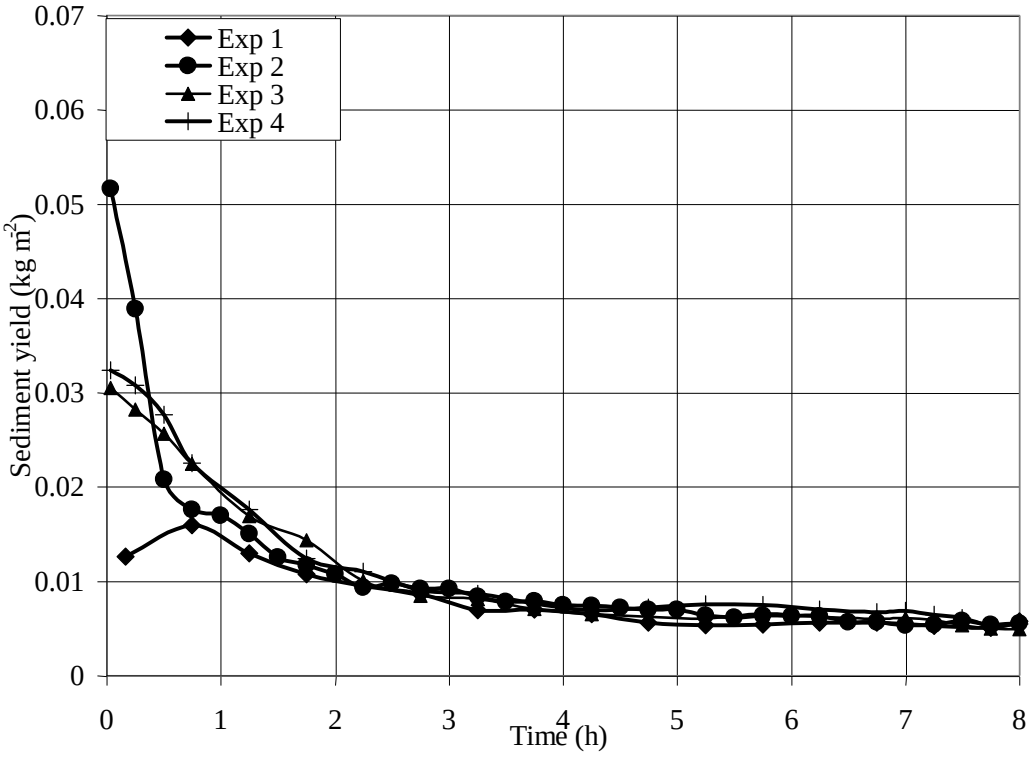
Exp 1
Exp 2
Exp 3
Exp 4
Sediment yield (kg m-2)
0.07
0.06
0.05
0.04
0.03
0.02
0.01
0
0
1
2
3
4
5
6
7
8
Time (h)

A

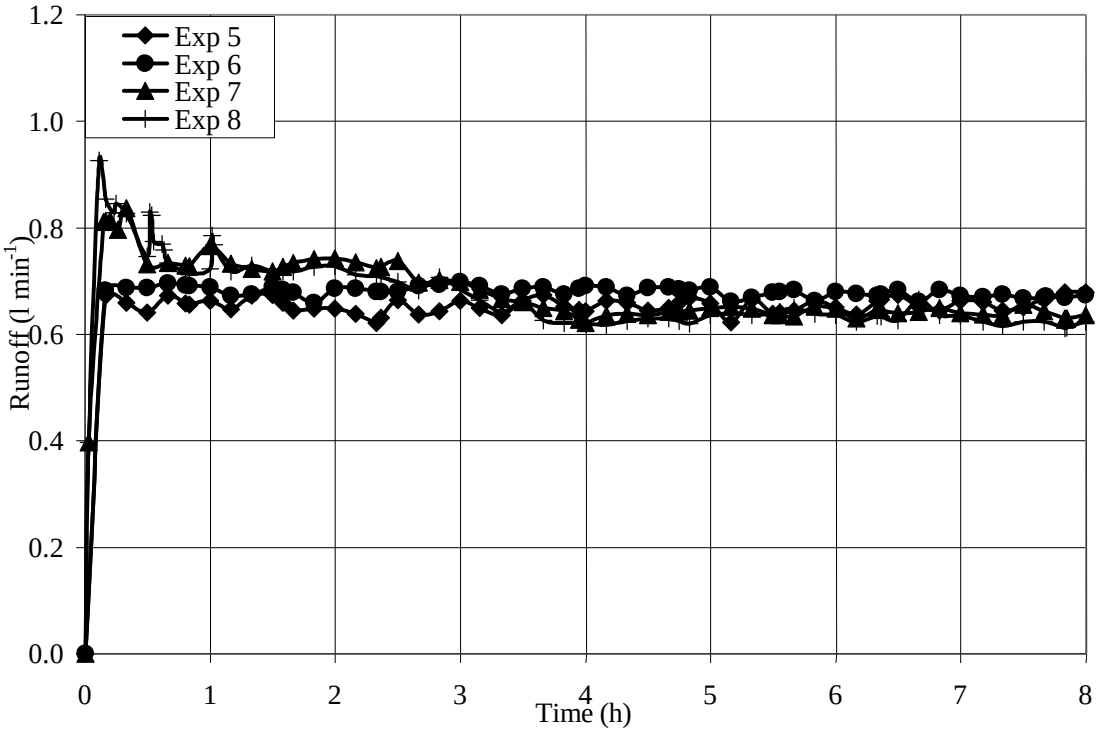

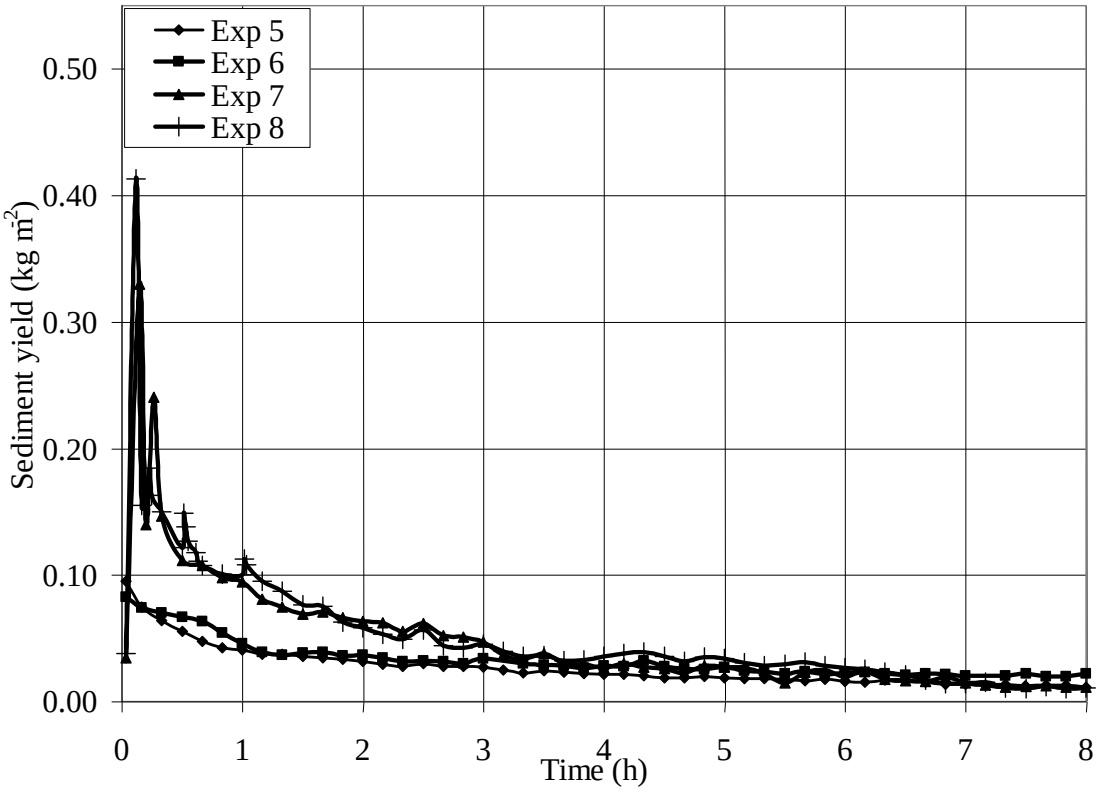

B

Figure 4.5: Measured runoff and sediment yields in non-failure experiments 1 to 4 (A) and 5-8 (B) under low and high total rainfall respectively. Rainfall initiated at the start of each experiment.

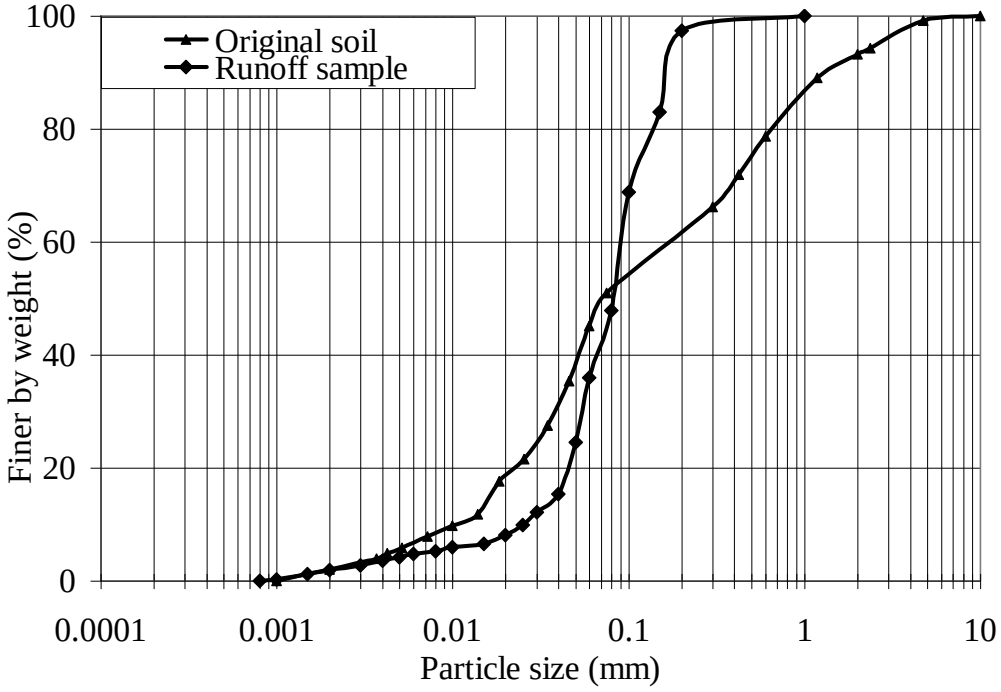

Figure 4.6: Particle size distribution of original soil material versus typical runoff sample collected after 8 hours of rainfall during experiment 5.

As shown in Table 4.6, sediment yield rates were high during failure and low during post-failure events in experiments 9 to 12. In these experiments, the peak sediment yield rates were about 10 to 50 times higher than the post-failure rates. These results compatible with the sandy soil results reported in the previous chapter. For example, peak sediment yields during failure events in sandy soil experiments ranged from 100 to 115 higher than post-failure erosion rates. Similar differences are reported from field observations of landslides. Ries (2000), for example, describes a three day long landslide event in a river basin of Central Nepal where sediment yield rates increased to 4 kg m^{-2} which was twice the normal total annual sediment yield.

Table 4.6: Average sediment yield rates during failure and post-failure periods.

Exp.	Average sediment yields (kg m^{-2} h^{-1})	
	during failures (first two hours)	In post-failures (last six hours)
9	4.662	1.43
10	4.995	1.64
11	8.665	1.59
12	10.295	1.64

Runoff and sediment yield rates from experiment 9 are presented in Figure 4.7. Measured peaks of sediment yield were a direct result of slope failure events. The magnitude of subsequent peaks that resulted from the slope failure retrogressions decreased gradually, meaning that landslide driven sediments were related to the proximity of slope failures from the outlet. This can clearly be seen in Figure 4.7 where the peak sediment yield, at the time of first failure, was about 0.245 kg m^{-2}, but then decreased to 0.113 kg m^{-2} in the second retrogression. Comparable results were observed in other failure experiments (10, 11, and 12) where the differing magnitude and frequency of the peaks was related to the number and location of the slope failure retrogressions. These results explain the temporal variation of sediment yields in response to slope failure events. The temporal variation of the landslide-driven sediment yields in the field, reported by different researchers (e.g. Martin et al., 2002; Schuerch et al., 2006; Schwab et al., 2008), are usually the function of location of landslides with reference to drainage network, and the quantity of landslides, rainfall characteristics (i.e. intensity and duration), and the steepness of the downslope area.

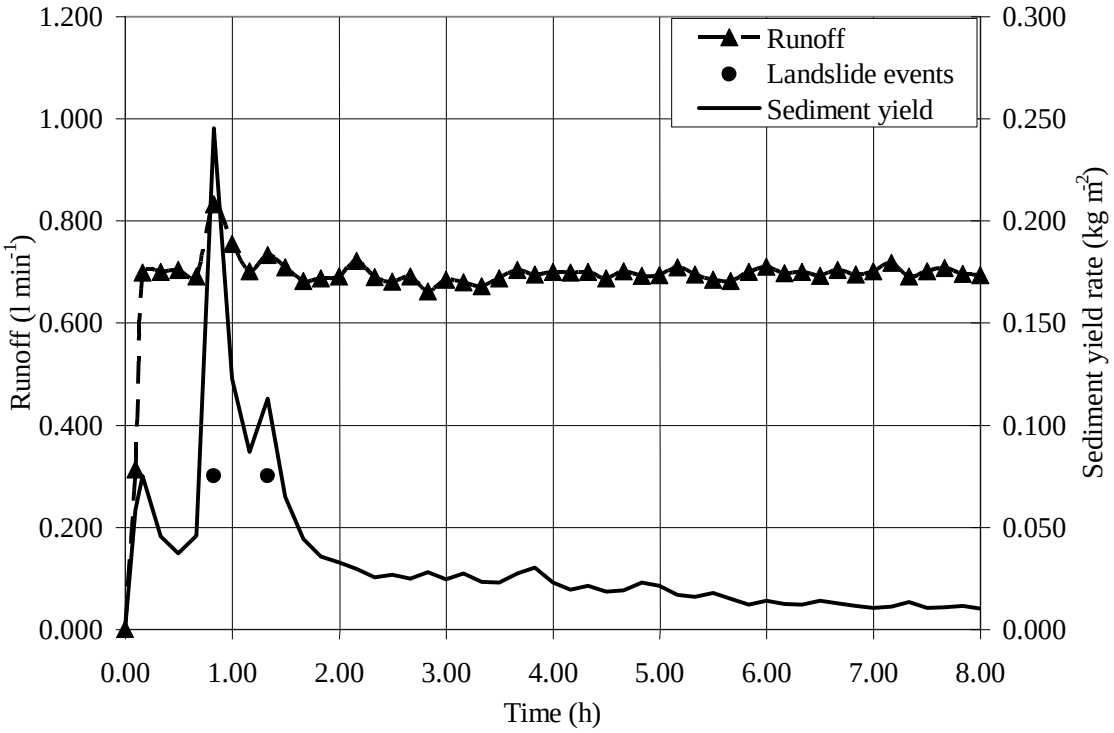

Figure 4.7: Runoff and sediment yields from experiment 9 showing peak sediment yields triggered by slope failure events. Rainfall initiated at the start of the experiment.

Post-failure sediment yields were low in the active landsliding experiments (9-12). This can be seen in Table 4.7 where sediment yields were compared between experiments of similar slope profiles and applied rainfall. The results revealed that the sediment yields in the failure experiments were between 6 to 12% (10% on average) less than non-failure experiments. The sediment yield reductions were due to modification of the original hillslope topography by slope failures. Undoubtedly, these geomorphic changes will have a long-term impact on sediment yields. It is also noted that there may be a decrease in soil surface area due to slope failures retrogressions exposing the flume bed as was observed in experiments 11 and 12, which may influence the inter-rill component of the soil erosion. The reduction in long-term sediment yields has been observed in many field studies (e.g. Korup et al., 2004; Schwab et al., 2008). These results demonstrate the mechanics of changes in sediment yields under continuous rainfall and suggest that evolution of a new hillslope topographic profile is mainly responsible for those changes.

Table 4.7: Comparison of total sediment yields during last six hours from non-failure experiments (5-8) versus failure experiments (9-12).

Non failure experiment		Failure experiment	
Exp	Total sediment yield (kg m^{-2})	Exp	Total sediment yield (kg m^{-2})
5	9.43	9	8.59
6	10.46	10	9.81
7	10.84	11	9.55
8	11.01	12	9.81

4.3 Validation of numerical models

A. Slope stability, runout and soil redistribution model

Slope stability and soil redistribution models were tested against the results of experiments 9-12. A safety factor was calculated for each experiment in response to the time varying pore pressure distribution. As shown in Table 4.8, the safety factors in all cases were between 1 and 1.5. The safety factor is a function of pore pressure, porosity, slope gradient and soil shear strength. In all cases, the predicted runout distances were lower than the respective measured distances (Table 4.8); the predicted distances were in average 14% (ranging from 6 to 23%) lower than the measured values. This depicts that the model worked reasonably well for the given experimental conditions.

Table 4.8: Observed vs. predicted landslides and runout distance.

Exp.	Landslides		Runout (m)	
	Safety factor	Retrogressions	Observed	Predicted
9	1.47	Two	0.76	0.59
10	1.36	Two	0.82	0.77
11	1.31	Three	1.36	1.20
12	1.29	Three	1.45	1.24

B. Erosion and runoff model

Observed and modelled runoff rates and sediment yield results and three performance indices for first two set of experiments (1-8) are presented in Table 4.9 . The soil input

parameters used in the model simulations are listed in Table 4.3. Results show that mean measured runoff rates were consistently lower than the predicted model simulation runoff rates in all cases. The model performance indices (Nash-Sutcliffe coefficient of efficiency, Index of agreement and Root mean square error) were quite favourable except for experiments 7 and 8 where total measured sediment yields exceed (by about 1.5 times) the predicted sediment yields. The slightly lower values of the NSI, and higher values of RMSE, in these two experiments were related to peak runoff observed during the minor slope failure events. The slight over-prediction of runoff in all cases may be attributed to the calibration of effective hydraulic conductivity. In the calibration process the value of hydraulic conductivity of the soil was set to 9.58×10^{-7} m s^{-1} which is about 2.5 times less than the measured saturated hydraulic conductivity. Increasing the value of hydraulic conductivity could marginally narrow the difference between the measured and predicted runoff, but this would reduce the predicted sediment yields and thus widen the difference between measured and predicted sediment yields. In general, however, the model performance indices in these experiments were comparable with similar previous plot scale studies (e.g. Yu and Rosewell, 2001; Oropeza-Mota et al., 2004; Adams and Elliott, 2006; Pieri, et al., 2007). In a single storm event WEPP does not simulate the subsurface flow and total soil water content; therefore model testing of these parameters was not undertaken.

Table 4.9: Comparison between observed and predicted runoff and sediment yields, and performance indices for runoff in non-failure experiments.

Exp	Mean runoff (l min^{-1})		Performance indices for runoff			Total sediment yield (kg m^{-2})	
	Observed	Predicted	NSI	IOA	RMSE	Observed	Predicted
1	0.279	0.303	0.66	0.93	0.0326	4.68	4.70
2	0.311	0.332	0.78	0.95	0.0279	5.03	4.92
3	0.308	0.322	0.73	0.93	0.0309	5.02	4.83
4	0.316	0.340	0.75	0.95	0.0307	5.24	5.13
5	0.630	0.699	0.62	0.92	0.0751	12.57	14.94
6	0.657	0.711	0.77	0.95	0.0601	15.47	15.84
7	0.658	0.696	0.53	0.89	0.0943	22.26	14.77
8	0.665	0.697	0.34	0.84	0.1139	23.81	15.45

NSI : Nash-Sutcliffe coefficient of efficiency

IOA : Index of agreement

RMSE : Root mean square error

Measured and predicted runoff rates and sediment yields were also in good agreement in the post-failure period (Table 4.10). Predicted sediment yields were slightly higher than the measured ones for experiments 9 and 10, but lower for experiments 11 and 12 (Table 4.10). Lower predictions in experiments 11 and 12 were believed to be governed by the decrease in soil surface areas as a result of slope failures and their retrogressions. However, higher measured values imply that sediment yields were not influenced by the decrease in surface area in these experiments. This indicates that the erosion processes were dominated by the concentrated overland flow transport capacity.

Table 4.10: Comparison between observed and predicted runoff and sediment yields, and performance indices for runoff in post-failure duration of failure experiments.

Exp	Mean runoff (l min^{-1})		Performance indices for runoff			Total sediment yield ($kg\ m^{-2}$)	
	Observed	Predicted	NSI	IOA	RMSE	Observed	Predicted
9	0.667	0.675	0.77	0.93	0.064	8.59	10.01
10	0.684	0.702	0.89	0.97	0.037	9.81	10.23
11	0.645	0.698	0.68	0.92	0.068	9.55	7.49
12	0.690	0.717	0.83	0.96	0.049	9.81	7.69

4.5 Summary and conclusions

No failures occurred in 8 of the 12 experiments, because low porosity probably prohibited the development of higher pore pressures capable of triggering slope failures. Overall, 4 shallow slope failures were triggered out of a total of 12 experiments in fine grained silty soils. In the four experiments where shallow landslides were triggered, failure and transport of the materials significantly altered the original slope profiles. The slope gradient decreased in the failure section and increased in the deposition zone. The final slopes in the upper flume section of the experiments ranged from 23° to 25°, and in the lower deposition section ranged from 7° to 13°, resulting in a new profile with lower soil erosion susceptibility.

Landslide-driven sediment yields were related to the slope failure retrogressions, landslide volumes, and the gradient of both flume sections. Peak sediment yields at the time of slope failures were related to the location of slope failure; higher peaks were observed if the slope failures occurred close to the outlet. In active landsliding experiments, post-failure erosion rates decreased as a function of changes in the slope profile.

Prediction from the physically-based soil erosion and landslide models were compared against the results from the flume experiments. WEPP model predictions were compared to sediment yields in experiments where failures did not occur, and in the post-failure period when landslides occurred. The predictions were consistent with observed results in all cases. A landslide model using the factor of safety approach

also worked well for predicting the occurrence of landslides with silty soils. Runout predictions using the simple soil redistribution model were in good agreement with experimental values.

The three models presented in this chapter form part of an integrated soil erosion and shallow landslide modelling approach to (a) predict runoff and soil erosion during the pre-failure period, (b) predict landslides, (c) estimate the changes in local slope gradient after landslides, and (d) predict post-failure, long-term sediment yields from the modified slope profile. Although the integrated modelling approach needs further validation with other types of soils and under a range of landslide scenarios, the applications with silty soils indicate that it can be a useful tool for studying the impact of landslides on long-term sediment yields in hilly and mountainous slopes.

Chapter 5 Catchment-scale Shallow Landslide and Soil Erosion Modelling

5.1 Introduction

Results of surface runoff and sediment yields before, during, and after shallow landslides from a hillslope, represented by a two-slope flume under controlled laboratory conditions, were presented in Chapters 3 and 4 for sandy and silty soils respectively. It was demonstrated that for a 2D hillslope, model simulations of soil erosion in pre- and post-failure conditions, shallow landslides, and soil redistribution were in good agreement with experimental observations. In this chapter, the 2D hillslope integrated modelling is extended to a catchment-scale 3D application.

Catchment-scale hydrological models generally require a large number of input data related to land-cover, management, climate, soils and topography. This information is usually managed as spatial information with Geographical Information Systems (GIS) which allows for simpler and faster data management than conventional maps and databases. Therefore, modelling of soil erosion, shallow landslides, and soil redistribution at a catchment-scale is best done with GIS tools.

There have been a few efforts to develop and apply integrated modelling approaches for predicting soil erosion, runoff and landslides at a catchment-scale (e.g. Bathurst et al., 2005; Doten et al., 2006). In these studies, a hydrological model is used to predict pre-failure soil erosion and runoff. Spatial distribution of shallow landslides is predicted by coupling a geotechnical stability model with the hydrological model. However, no approach yet predicts changes in the local topography in response to shallow landslides at a catchment-scale.

The main objective of this chapter is to predict how landslides and their runout alter the local topography at a catchment-scale. To accurately model the changes in the topography, the spatial distributions of shallow landslides and their runout need to be predicted accurately. However, modelling shallow landslides and their runout in a catchment is subject to a number of uncertainties associated with the evaluation of

model parameters. The uncertainty in the model parameterisation and its impacts for model output should therefore be explicitly recognized in the modelling.

A further objective of this chapter is to investigate catchment-scale long-term soil erosion and sediment yields in response to changes in local topography and land-cover following shallow landslides. Long-term soil erosion and sediment yields are modelled for two scenarios following changes in topography: (a) vegetation not re-established (long-term fallow), and (b) re-establishment of vegetation in the failure and deposition areas. The modelling and comparison of these scenarios are intended to help managers and others determine the value or need for post-failure management.

5.2 GeoWEPP-SLIP model

The integrated catchment-scale soil erosion, shallow landslide, and soil redistribution modelling approach developed is referred to as the GeoWEPP-SLIP model (**S**hallow **L**andslide **I**ntegrated **P**rediction model). This approach (Figure 5.1) is similar to the one described in Chapter 4, but extended to catchment-scale using GIS. The GeoWEPP (Renschler, 2003), which is the WEPP-GIS extension, was chosen for modelling the pre- and post-failure soil erosion and runoff. The infinite slope method (Skempton and DeLory, 1957) of slope stability analysis was used to predict shallow landslides, and a simple rule-based soil redistribution model to predict the runout of landslide-driven materials. The integrated modelling used a raster-based GIS in which a catchment is divided into regular squares of pre-defined size (i.e. grid-cell size) which become the mapping units of reference. Each grid-cell is assigned a value for each model input factor such as elevation (DEM), slope, land-use, soil, and other properties that need to be taken into consideration. Computer implementation is simple and processing is fast in raster-based GIS because the data are stored in a matrix form. Each component of the proposed model is described below.

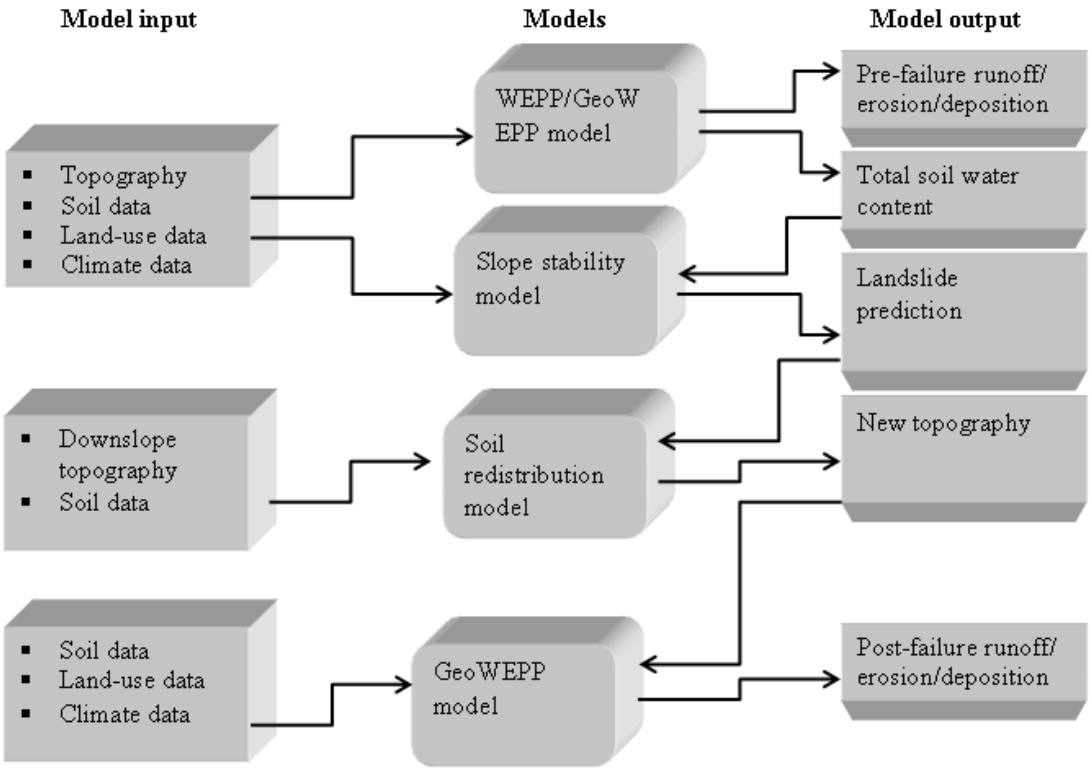

Figure 5.1: Flow chart depicting the proposed methodology to model soil erosion, shallow landslides, and soil redistribution in the GeoWEPP-SLIP modelling framework

5.2.1 Soil erosion modelling using GeoWEPP

A detailed description of the application of WEPP to predict soil erosion, and runoff has been given in Chapter 2. GeoWEPP combines WEPP (Flanagan and Nearing, 1995) with the TOpographic PArameteriZation (TOPAZ) model (Garbrecht and Martz, 1995) within ArcGIS 9.x to predict runoff and soil erosion at a catchment-scale. Topography as DEMs, land-cover, soils, and climate data are used to model soil erosion and runoff. The outputs can be viewed and analysed in a GIS environment. Spatial distribution of soil erosion and deposition can be obtained from both the Hillslope and Flowpath methods (Cochrane and Flanagan, 2003; Renschler, 2003). Modelling soil erosion using the Hillslope and Flowpath methods has been illustrated in Chapter 2. Three performance indices (a) the Nash-Sutcliffe coefficient of efficiency (NSI) (Nash and Sutcliffe, 1970), (b) the index of agreement (IOA) (Willmott,, 1981) and (c) the root mean square error (RMSE) were used to evaluate the predictive ability of the model by comparing predicted and observed runoff and

sediment yields from the outlet of the catchment. Equations 4.1 to 4.3 in Chapter 4 describe these indices.

5.2.2 Landslide prediction

Landslide predictions are based on the concept that hydrological triggering of a landslide occurs when the local pore pressure reduces soil shear strength below the imposed stresses. An infinite slope method of slope stability analysis was used to predict the landslides. The model assumes the slip surface to be the soil-bedrock interface as shown in Figure 2.10 (Chapter 2), and the subsurface water flow is assumed to be parallel to the ground surface. The model runs only for a single time step with the greatest basin saturation happening during the largest storm of a year or a simulation period which predicts the spatial distribution patterns of landslides for the period. This approach is similar to that used by Benda and Dunne (1997) and Doten et al. (2006). As discussed in Chapter 2, the slope is predicted to be stable or unstable according to the value of safety factor (Fs) computed using Equations 2.19 and 2.20 and criteria defined in Table 4.4.

The soil wetness index in the landslide model (Equations 2.19 and 2.20) is a measure of relative water table height and is an important parameter to compute safety factor (Fs) because it varies both in space and time. To determine the water table height at each grid-cell for computing the safety factor (Fs), the WEPP hillslope version was applied to each flowpath of the catchment. The spatial distribution of flowpaths can be obtained from a Digital Elevation Model (DEM) of a catchment. The WEPP model simulates daily total soil water content based on the daily water balance equation (Equation 2.7). Computation of the total soil water content in each cell of a flowpath was handled in a unique way because soil water content is only calculated for a single OFE (overland flow element). OFE's are segments of the hillsllope (or flowpath) with unique management and soil combinations and only 10 of these are allowed in WEPP for a hillslope profile (flowpath in this case). In a shorter flowpath ($\leq$ 10 times grid-cell size), the flowpath was divided into multiple segments where the length of an individual segment was set to match the grid-cell size. Each segment was characterised by a unique combination of soil and vegetation properties (individual OFE's). The maximum values of the simulated soil water content of each segment of the flowpath were then directly attributed to the respective grid-cells of the flowpath.

On the other hand, in a longer (>10 times the grid-cell size) flowpath, the maximum values of total soil water content in each grid-cell were computed by linearly interpolating the WEPP simulated total soil water content between the 10 permissible OFE's. If multiple flowpaths merged in a grid-cell as shown in Figure 2.6 while approaching a channel, the maximum value of the total soil water of those flowpaths for the grid-cell was attributed to that cell. The maximum value of the total soil water content was used to compute soil wetness index. Procedures used to obtain the soil wetness index raster map are schematically presented in Figure 5.2.

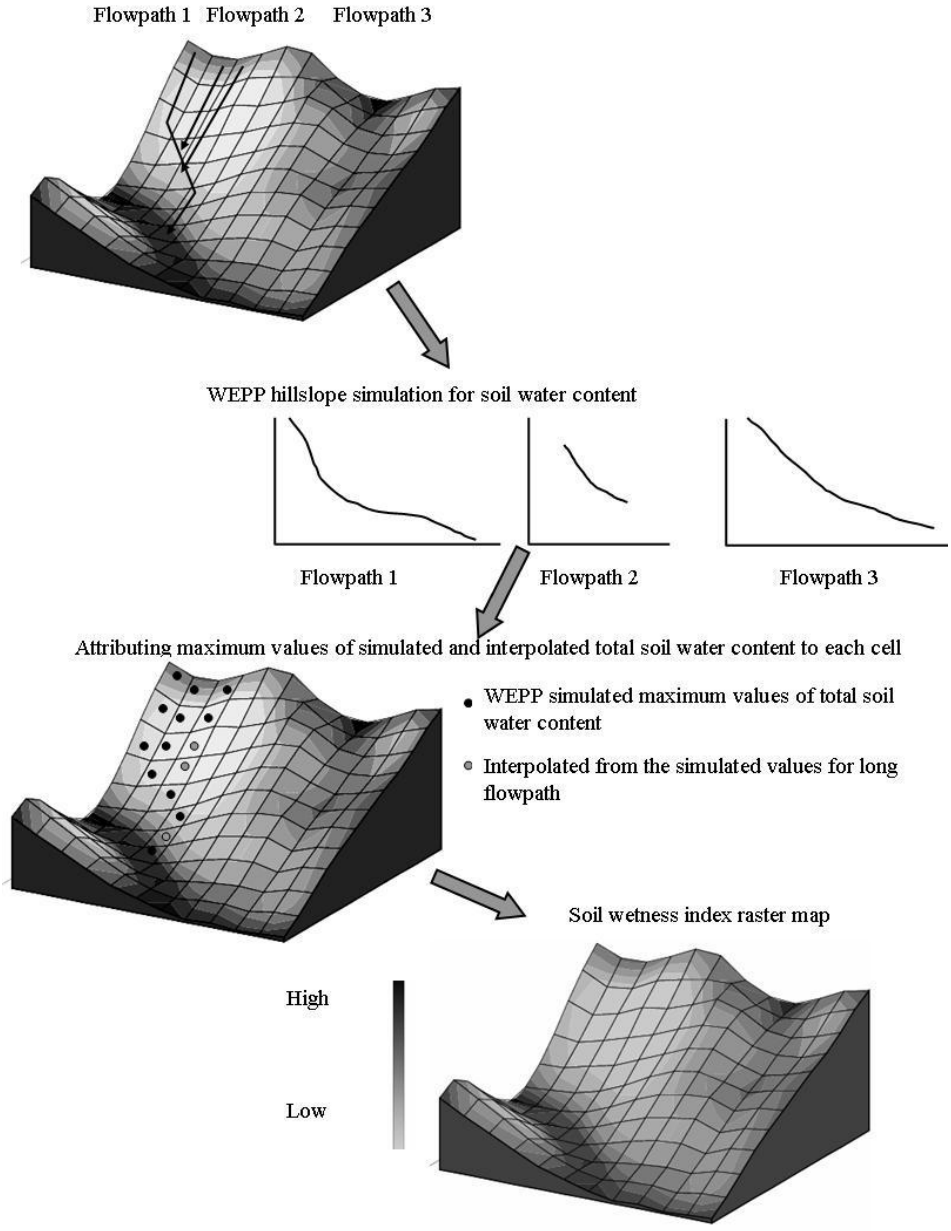

Figure 5.2: Schematic diagram showing the development of soil wetness index map from the WEPP simulated total soil water content using flowpaths.

The spatial distribution of shallow landslides can be predicted from topography, land-cover, soil types and soil wetness index by using the landslide model and raster map calculator in ESRI ArcGIS. The procedure adopted to predict landslides at a catchment-scale is presented in Figure 5.3. In the figure, θ (°) is the local slope angle, m (-) is the soil wetness index i.e. relative water table height, q (N m^{-2}) is the vegetation surcharge, C_s and C_r (N m^{-2}) are respectively the soil and root cohesion related to the soil and vegetation types, γ and γ_e (N m^{-3}) are the unit weight and the effective unit weight of the soil respectively, D (m) is the thickness of the overlying soil and φ (°) is the soil angle of internal friction.

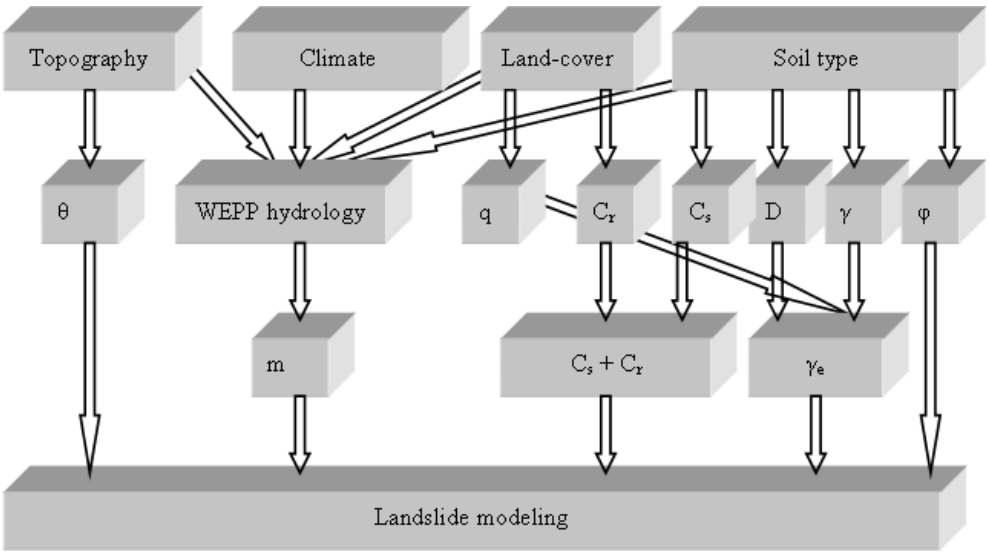

Figure 5.3: Flowchart showing the proposed methodology to derive the GIS based landslide map from topography (DEM), land-cover, soil types and the WEPP water balance simulation.

5.2.3 Soil redistribution model

Modelling landslide volume and runout distance is important because it may directly impact stream sediment yields. However, there are no rigorous methods which allow a strict assessment to determine the trajectories of the failure materials. Difficulties in the soil redistribution modelling are associated with the complexities of landslide dynamics. The complexities are due to various factors such as downslope topography, soil types, rainfall characteristics and pore pressure distribution that lead to a wide range of variations in runout distance, velocity, the motion mechanics and the thickness of the mobilised materials.

Given difficulties in physically-based soil redistribution modelling at a catchment-scale, a simple rule-based model was used to predict the trajectories of the failure materials and to quantify the failure and deposition volumes. The failure volume was computed as the product of landslide delineated area and the failure depths; the saturated soil depths in the area were assumed to be equal to the failure depths. In the model, the failure materials were routed downslope until the materials encountered a grid-cell having a local slope gradient less than a critical threshold slope (Doten et al., 2006). The critical threshold slope was set to 10° (e.g. Burton and Bathurst, 1998; Claessens et al., 2007); the threshold slope was consistent with the experimental observations using loess soils as illustrated in Chapter 4. The deposition depth usually decreases with an increase in runout distance for a given volume (Legros, 2002). A shallow deposition depth does not significantly alter the post-failure topography. Here, in order to avoid very long runout simulations, a critical threshold deposition depth was set to 0.03 m; further routing of landslide materials stopped at the critical deposition depth. If the failure and the redistribution encountered a stream network, the failure material entered the stream implying that the material entering the stream network directly contributed to the total sediment yields.

In soil redistribution modelling, the failure materials (LV) were categorised as: (a) landslide-driven sediment yields (SV) i.e. the materials reaching stream network, and (b) the materials that deposit in a catchment/hillslope (DV). The distribution of the failure materials in each grid-cell of the downslope topography was simulated using multiple flow direction principles as shown in Figure 5.4.

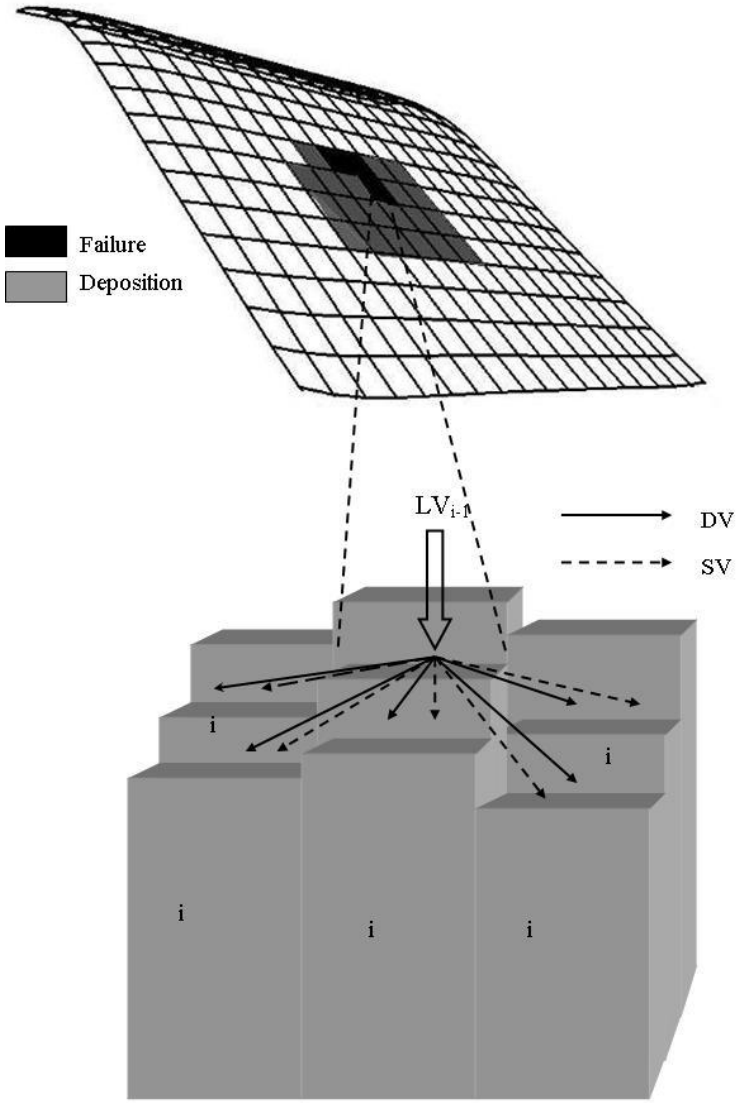

Figure 5.4: Schematic representation of adopted methodology for soil redistribution in each grid-cell.

In order to predict the deposition volume (DV) and the landslide-derived sediment volume (SV) in the downslope grid-cells, it was first necessary to compute the number of downslope grid-cells involved in the soil redistribution, Grid-cell Number (GN) (-) which is expressed as:

$$GN = \frac{R}{W} \qquad \text{Equation 5.1}$$

where R (m) is the runout distance; W (m) is the grid-cell resolution. The accumulated landslide materials were routed downslope with the multiple flow

direction principles (Quinn et al., 1991) using the method described by Claessens et al. (2007). The deposition material DV_i (m) in the grid-cell (i) was simulated as:

$$DV_i = \left(\frac{LV_{i-1}}{GN_{i-1}} \right) f_i \qquad \text{Equation 5.2}$$

where LV_{i-1} (m) is the accumulated amount of the landslide materials coming from the upslope. In each downslope grid-cell, the number of the grid-cell (GN_{i-1}) is reduced by one and when $GN_{i-1}<1$, the remaining material is deposited. The landslide-driven sediment reaching the stream network (SV) was computed as the difference of volume between failure (LV) and deposition (DV) materials:

$$SV = LV - DV \qquad \text{Equation 5.3}$$

In Equation 5.2, f_i is the fraction of the deposition volume (DV) allocated to each downslope neighbouring cell and determined by the multiple flow direction principles (Quinn et al., 1991) and is expressed as:

$$f_i = \frac{\tan\theta_i}{\sum_{j=1}^{\max 8} \tan\theta_j} \qquad \text{Equation 5.4}$$

Where θ_i (°) is the local slope gradient at the i^{th} grid-cell and the denominator in Equation 5.3 represents the summation of the local slope for all downslope neighbours of the i^{th} grid-cell.

5.3 Case study application

The GeoWEPP-SLIP model was applied to the Bowenvale research catchment (43°34´58"S and 172°38´27"E to 43°36´20"S and 172°39´45"E) located in the Port Hills, Banks Peninsula in Christchurch, New Zealand (Figure 5.5 (A)).

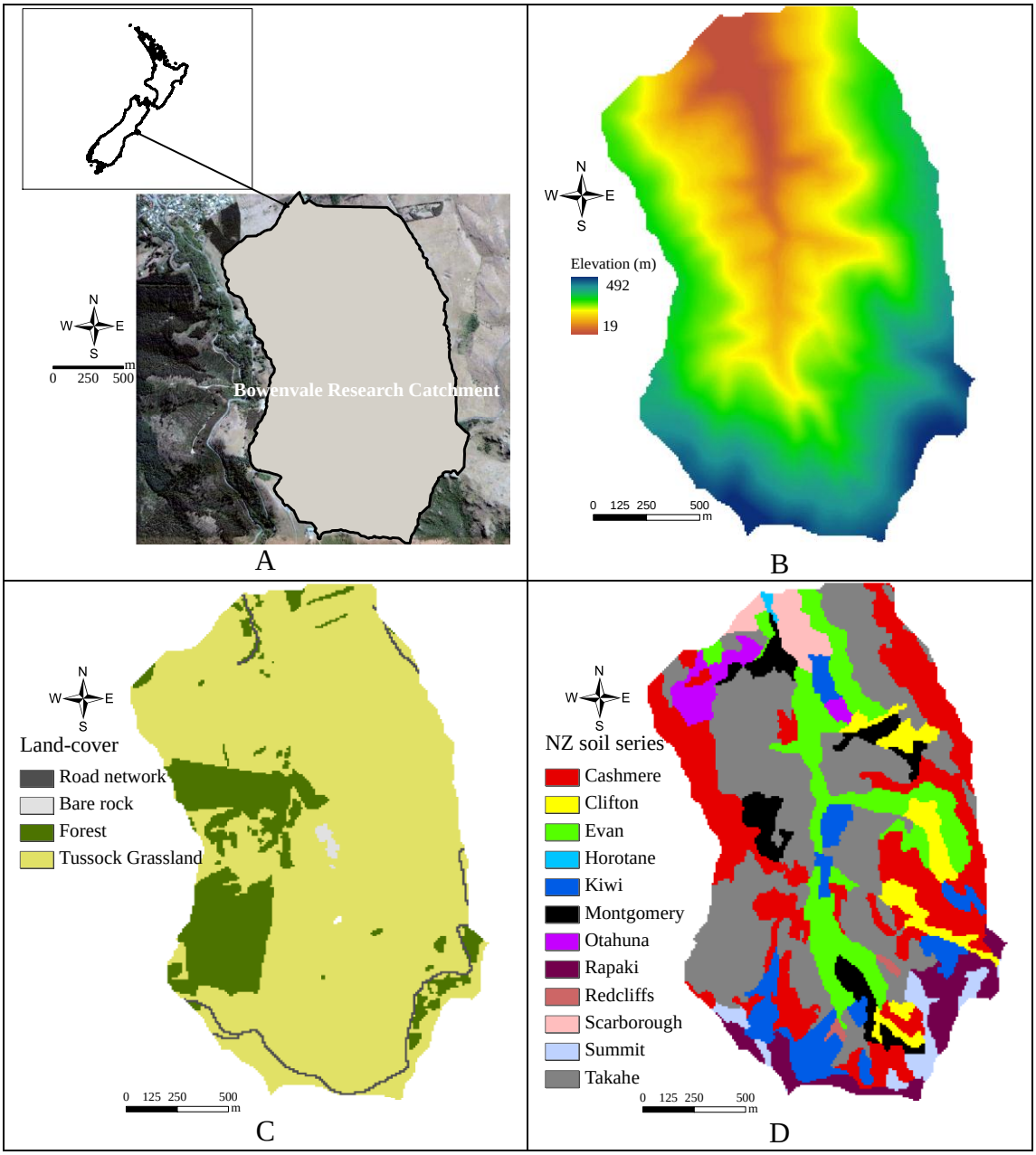

Figure 5.5: The Bowenvale research catchment in Christchurch, New Zealand (A) location map, (B) topography, (C) land-cover classifications, and (D) soil types according to the New Zealand Soil Series

5.3.1 Topography

A Digital Elevation Model (DEM) was developed from a Light Detection and Ranging (LiDAR) survey conducted by Christchurch City Council (CCC) in July 2003. The LiDAR survey measured surface elevation at 1.3 m average intervals (i.e. average distance between two nearest data points) in and round the Bowenvale; the LiDAR datasets provided high resolution topography. The standard error of accuracy of the elevation data at 68% confidence interval was estimated to be less than 0.07 m

based on 155 test points, and the error of accuracy in the horizontal data was less than 0.55 m (1/2000 flying height). The errors may be higher in vegetated steep slopes. Since tens or hundred of thousands of laser pulses per second are made during a LiDAR survey, LiDAR can potentially provide the DEMs with much more accurate depiction of the topographic surface than the DEMs derived from other sources such as photogrammetrically mapped contours, even in heavily vegetated areas.

Physically-based modelling requires DEMs of adequate resolution to predict the spatial distribution of erosion and deposition (e.g. Cochrane and Flanagan, 2005), to capture the landslide features, and to model the soil redistribution (e.g. Claessens et al., 2005). The LiDAR elevation point datasets of the Bowenvale were interpolated to a 10 m grid-cell resolution DEM using the 'Topo to Raster' function in ESRI ArcGIS 9.1. 'Topo to Raster' uses an interpolation method specifically developed to generate hydrologically correct DEMs using the Australian National University DEM (ANUDEM) program (Hutchinson, 1989).

Topographic attributes computed from the DEM were the local (grid-cell to grid-cell) slope angle (θ), stream networks, hillslopes (sub-catchments), spatial distribution of flowpaths, and upslope contributing area. The elevation of the 300 ha Bowenvale catchment ranges from about 20 m to 490 m (Figure 5.5 (B)) and the slope angle from 0.5° to 40° averaging about 22°. A total of 2481 flowpaths were generated from 33 hillslopes (sub-catchments) which were created using 6 ha for the critical source area (CSA) and 300 m for the minimum source channel length (MSCL) in the GeoWEPP. The areas of the sub-catchments (hillslopes) ranged from 1.9 ha to 25 ha and flowpaths lengths from 10 m to 803 m. The upslope contributing area was derived using both the steepest descent algorithm (Fairfield and Leymarie, 1991) and the algorithm of the multiple flow direction principles (Quinn et al., 1991) using the 'Flow Accumulation' function in the ESRI ArcGIS 9.1.

Changes in topography in post-failure scenario

The deposition (+) and failure (-) depths were algebraically added to the present DEM to create a new post-failure DEM of the catchment. The new DEM was then used to derive various topographic attributes such as local slope angle, flow direction, flow

accumulation, and to predict runoff, soil erosion and sediment yields in post-failure scenarios.

5.3.2 Land-cover

A land-cover map of the Bowenvale catchment was produced by digitising land-cover features from a high resolution aerial photograph and field verified by surveying with a Trimble Global Positioning System (GPS). Four land-cover types were observed: tussock grassland, forest, road network, and bare rock (Figure 5.5 (C)). Forest and tussock grassland were the main land-cover types as they occupy more than 98% of the total study area. Vegetation provides both mechanical and hydrological effects that are important in reducing soil erosion and in stabilising the slopes. It is well-established that forests in sloping ground possess high transpiration and interception rates that increase the soil moisture deficit (making the soil drier) causing reduced pore pressures (Greenway, 1987). In an undisturbed forest, soil erosion is generally negligible. Vegetation also provides root cohesion (binding action) which is favourable for slope stabilisation (Sidle, 1991; Dhakal and Sidle, 2003).

Tussock grassland (pasture) is the dominant land-cover in the area, occupying more than 82% of the study area. Forest covers about 16% of the total area, which mainly includes plantations of mostly conifers and some eucalypts. The vegetation property data required for the GeoWEPP-SLIP simulations were obtained from literature or from the WEPP database; for example, an existing WEPP management file for pasture land-cover was used for the tussock grassland because it has similar cover and management factors. For forest, an input file was built using information for pine forests from literature (Elliot and Hall, 1997). For landslide modelling, the root cohesion parameter was based on literature data (Sidle et al., 1985; Preston and Crozier, 1999; Abernethy and Rutherfurd, 2001) and the vegetation surcharge was assumed to be negligible because the vegetation surcharge has low impact on slope stability analysis (Van De Wiel and Darby, 2007).

Changes in land-cover in post-failure scenario

The existing land-cover map was modified to predict soil erosion and deposition in post-failure scenarios. Bare soil was incorporated in the pre-failure (i.e. existing) land-cover map to mimic the changes in land-cover in the failure and deposition areas due

to landslides and soil redistribution prediction. An existing WEPP fallow management file was used for these areas.

5.3.3 Soils

Soil data required to run the GeoWEPP-SLIP model were obtained from laboratory tests, field investigations, and literature. The spatial distribution of soils for the study area was generated from a 1:15,000 regional soils map (Trangmar, 1998). The soil map of the Bowenvale catchment is shown in Figure 5.5 (D). The soil map database provided information on soil types, textures, parent materials, drainage condition for all mapped soil types. In the catchment, there were 12 well-defined soil types consisting primarily of loess soils. The dominant soils were Udic Ustochrept, Typic fragiochrept according to USDA Soil Taxonomy (Soil Survey Staff, 1998) (Table 5.1). These two soils cover respectively about 40% and 35% of the total catchment.

The soils' properties were obtained from laboratory tests conducted on 30 different samples collected across the catchment (2 to 5 samples per mapped soil type). Twelve WEPP soil input files were created for the 12 mapped soils. Each input file had soils data for two soil layers obtained from the laboratory tests on the samples collected from about 10 cm and 40-50 cm below the surface. The deeper (40-50 cm) samples were additionally tested to obtain geotechnical properties such as angle of internal friction (φ) and cohesion (C) to be used in the landslide modelling. The measured soil properties included particle size distribution, organic matter (OM), cation exchange capacity (CEC), saturated hydraulic conductivity (K_{sat}), angle of internal friction (φ) and cohesion (C) using the methods illustrated in Chapter 4. Properties were assumed to be uniform within each soil type. The measured soil properties are summarised in Table 5.1. The values of critical shear stress, inter-rill and rill erodibility were obtained from the calibration and the validation of the WEPP model using the flume experiments in Chapter 4, as these experiments were conducted using the soils obtained from the Bowenvale catchment. These values were lumped for the entire catchment.

Table 5.1: WEPP and landslide models parameters for mapped soil types obtained from laboratory tests and field observations

New Zealand soil series	USDA Soil taxonomy	Fraction (%)			CEC, cmol kg^{-1}	K_{sat}, mm h^{-1}	Unit weight, kN m^{-3}		C, kN m^{-2}	Φ, °	D, m
		Rock	Sand	Clay			γ	γ_{Sat}			
Cashmere	Udic Ustochrept	0.6	42.6	1.6	13	7.8	11.8	18.6	3.2	33	0.60
Clifton	Udic Ustochrept	1.2	44.1	1.4	14	4.2	11.6	18.8	4.7	32	0.60
Evan	Lithic Ustochrept	0.8	55.7	2.1	12	8.3	13.2	18.6	4.2	37	0.45
Horotane	Typic Haplaquept	0.1	38.2	1.9	12	4.4	11.8	18.3	4.2	34	1.20
Kiwi	Udic Ustochrept	0.5	39.5	1.8	15	7.7	12.4	18.3	2.7	37	0.45
Montgomery	Udic Ustochrept	1.1	54.6	1.2	13	9.1	13.9	18.5	3.4	37	0.40
Otahuna	Aquic Fragiochrept	0.8	38.7	1.1	11	4.4	11.6	18.4	5.5	36	0.60
Rapaki	Lithic Hapludoll	1.4	43.6	1.5	12	8.5	12.8	18.6	4.0	36	0.50
Redcliffs	Mollic Haplaquept	2.3	39.3	2.8	14	4.3	11.3	18.5	3.8	35	0.55
Scarborough	Typic fragiochrept	3.1	47.6	1.5	16	4.2	12.7	18.1	6.8	35	1.20
Summit	Umbric Dystrochrept	1.2	47.8	1.0	14	8.7	12.5	18.5	3.3	35	0.55
Takahe	Typic fragiochrept	0.8	58.7	1.8	15	3.8	12.2	18.6	3.1	36	0.45

Soil depth (D) is one of the most important parameters in the GeoWEPP-SLIP model because it affects the soil infiltration and soil moisture distribution. The depth also affects the landslide prediction due to its presence in the denominator of the landslide modelling component. However, soil depth is rarely mapped. Physically-based landslide modelling has usually relied on either empirical or theoretical models to develop soil depth maps (e.g. Dietrich et al., 1995; Casadei et al., 2003; Lee and Ho, 2007; Godt et al., 2008), or lumped soil depth mapping approaches according to soil or vegetation types (e.g. Bathurst et al., 2005; Acharya et al., 2006; Doten et al., 2006; Claessens et al., 2007; Bathurst et al., 2010). The soils in the Bowenvale catchment are shallow with frequent minor exposed bedrock outcrops. The soil depth was measured either in pre-exposed soil profiles or by screwing a solid steel auger vertically into the ground until it would go no further assuming that it had reached the

base of the soil layer (i.e. underlying bedrock). Several measurements were made for each soil type to account for local variability and the mean of the measured depths were attributed to each soil type. The soil depth in the catchment varies from about 0.4 to 1.2 m; deeper soils occur in areas of topographic convergence (i.e. valley), while shallower soils occur in more exposed areas such as ridges and along steep slopes.

5.3.4 Climate

Fifteen minute interval rainfall data were collected from an automated rain gauge station located at the outlet of the catchment (Figure 5.6 (B)). The data were then used to compute the total daily rainfall, daily rainfall duration, time and intensity to peak required for the WEPP. The collected historical (1989-2009) rainfall data showed that the annual rainfall ranged from about 435 mm in 2001 to 1040 mm in 2006, averaging about 750 mm yr^{-1}. Other climate data such as radiation, temperature and wind direction were collected from a station located at the Hagley Park Botanical Gardens, approximately 6 km north-east from the outlet of the study catchment. The north-western slopes of the catchment are exposed to the dry north-west winds in summer, while the eastern slopes are exposed to the cooler drying north-easterly winds. Temperature reductions with increase in altitude are not significant.

5.3.4 Other temporal data

An automated stream gauging station was located at a permanent concrete flume built at the outlet of the catchment (Figure 5.6 (B)). The daily stream flow at the outlet was compiled from the 15 minute interval stream flow measurements using the gauge height readings at the station. The daily stream flow measurements were used to calibrate and validate the model.

The time series soil moisture data were obtained using linearly calibrated soil moisture probes (Charlesworth, 2000) for the period between June 10 and December 31, 2009. The sensors were gravimetrically (g g^{-1}) calibrated in the laboratory using the catchment's loess soils. The moisture sensor consists of a string of capacitance sensors housed in a waterproof container. It measures the dielectric constant of the soil to determine the soil moisture content. Ten sensors (Figure 5.6 (C)) were installed approximately 40 cm below the surface along two hillslopes (sensors 1-5 in tussock grassland and 6-10 in forest area) to measure the potential changes in soil moisture (g

g^{-1} %) over time and in response to location and land-cover. The sensors were set to record every 10 minutes.

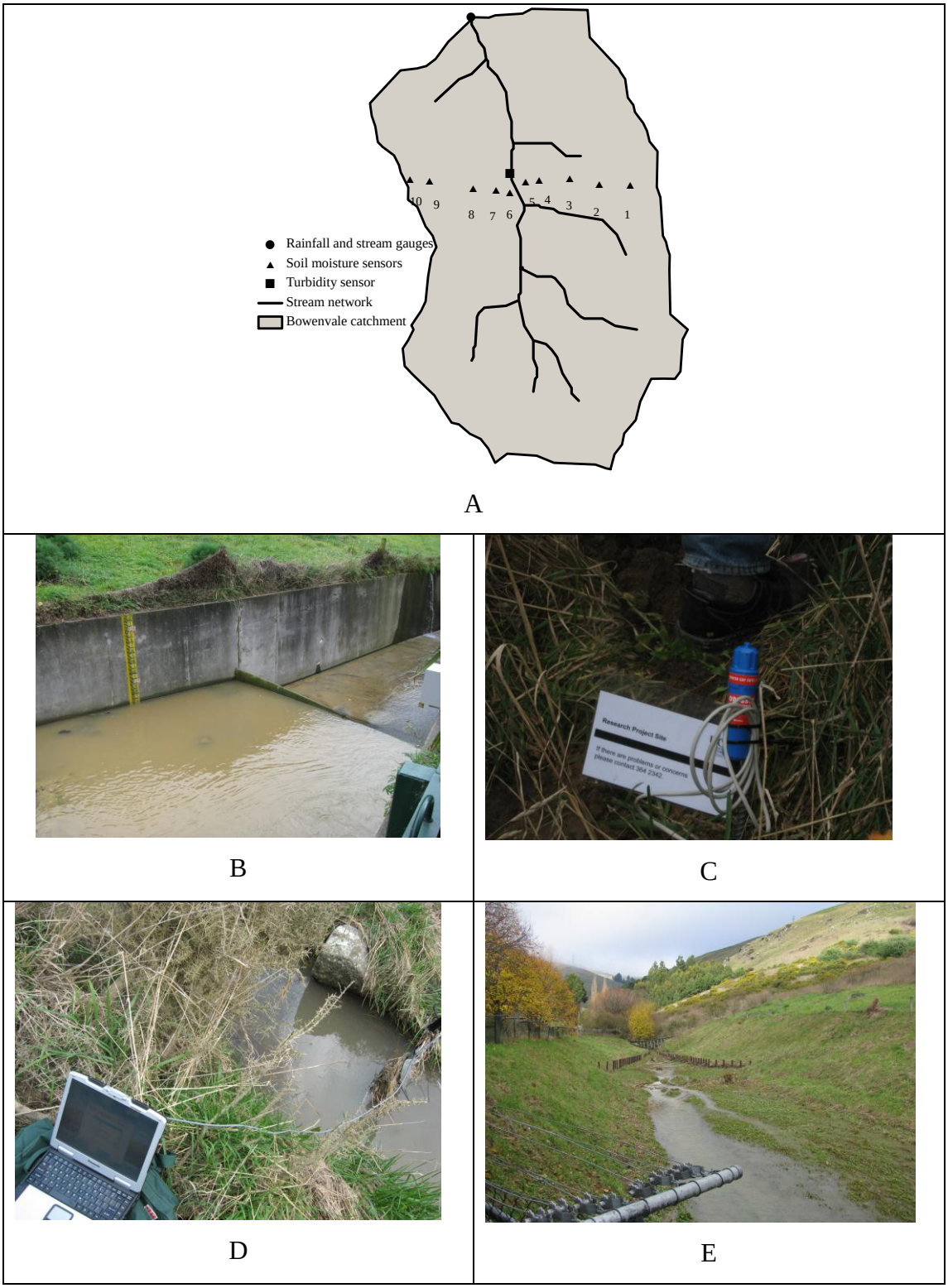

Figure 5.6: Monitoring stations: (A) location, (B) stream outlet and rain gauges, (C) a typical soil moisture probe, (D) a turbidity sensor, and (E) overall view of the catchment from the stream outlet.

There were no historic sediment yield records for the Bowenvale catchment. However, a Greenspan Turbidity Sensor was installed about 700 m upstream of the catchment outlet (Figure 5.6 (D)). Turbidity was measured at 10 minute intervals from October 1 to December 31, 2009. Calibration of the sensor was done using runoff samples collected from the Bowenvale stream during different storm events. The calibration results showed that readings of up to 1000 nepthelometric turbidity units (NTU) could be recorded, which is equivalent to 1.4 g l^{-1} of sediment concentration (SC). The daily average total suspended sediments (TSS) were computed from the relationship established between SC and NTU (Figure 5.7). Bed load sediment from a catchment dominated by fine-grained silty soils is usually low (Lenzi and Marchi, 2000). It was, therefore, assumed that most sediment was transported as TSS and very little as bed load. The TSS was computed at the outlet. Runoff samples were collected in various storm events from the catchment outlet and the turbidity location to compare the variations of the TSS between these locations. Results showed that the variations of TSS are negligible. Spatial variation of TSS in a catchment is more likely dependent on variations in land-cover and stream morphology (Vanacker et al., 2007). For this study, it was assumed that the sediment concentration would remain consistent between the turbidity sensor station and the catchment outlet.

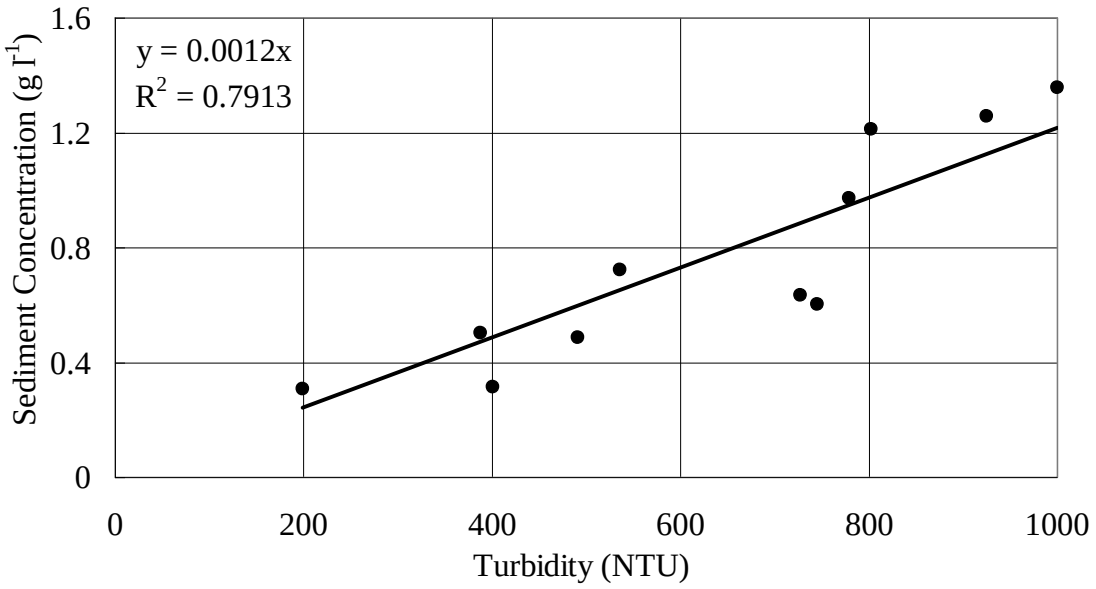

Figure 5.7: Turbidity sensor calibration showing the relationship between turbidity and sediment concentration. Observations are represented by dots and fitted values by the solid line.

There were no historic data on the relationship between shallow landslide occurrence and triggering conditions in the Bowenvale catchment. A landslide inventory was therefore prepared during 2008-2010 field surveys using a Trimble Global Positioning System (GPS) unit and aerial photography. Images of typical landslides are presented in Figure 5.8. A total of 39 landslide scars were mapped which were mostly found on the steeper foot slopes, and the downstream ends of steep and un-channelled valleys. The landslides were shallow translational failures. The landslides were observed to trigger along a wide range of local slopes (22 to 38°). Fourteen of the 39 observed landslides were located along slopes steeper than 30°. The landslide source lengths varied between 1 and 32 m with a mean value of about 7.6 m. The landslides generally had a failure depth varying between about 0.20 to 1.1 m with a mean value of about 0.46 m. The observed landslides were compared with the 2009 landslide modelling results.

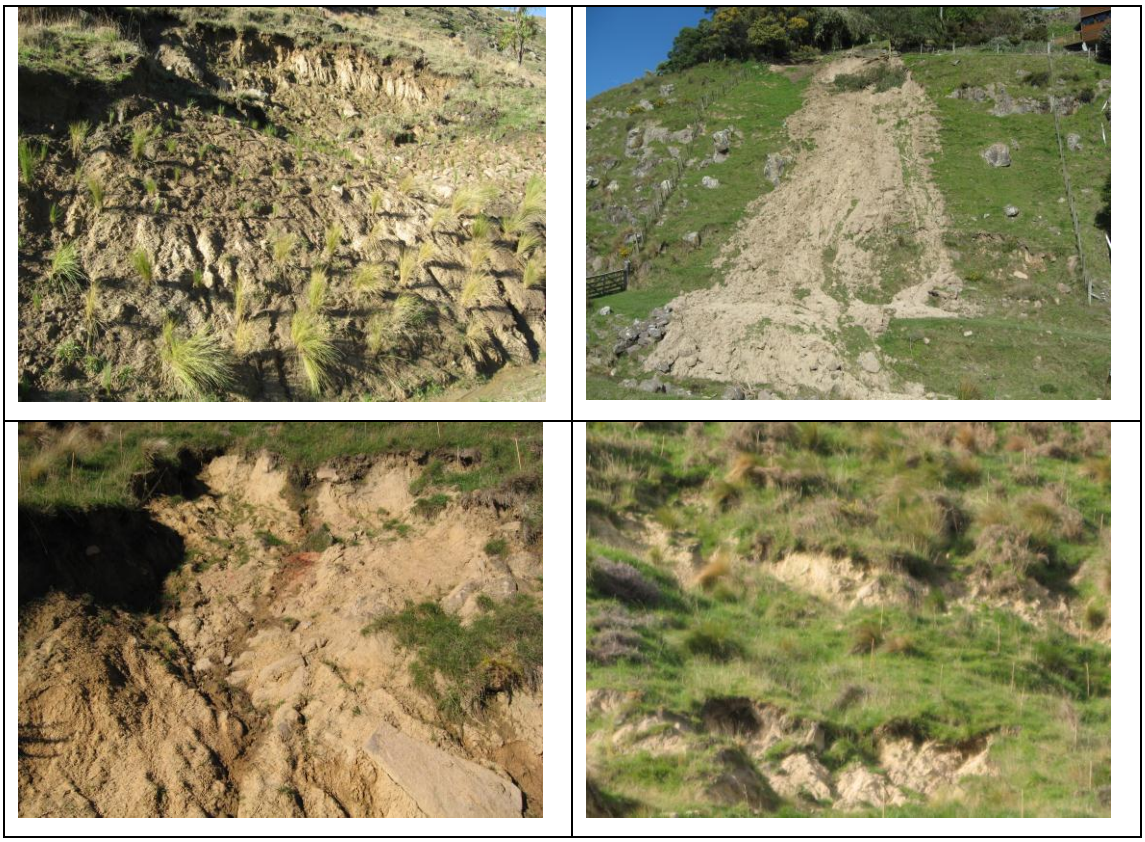

Figure 5.8: Images of typical shallow landslides in the Bowenvale catchment.

5.4 Results and discussion

5.4.1 Runoff and soil erosion modelling

GeoWEPP was initially run using daily climate data for each year between 2000 and 2002 to calibrate the hydrological component of the GeoWEPP-SLIP model. Figure 5.9 (A) and (B) present graphical comparison between the observed and the simulated runoff at the Bowenvale catchment outlet for the calibration (2002) and validation (2009) years respectively using the Hillslope method (Cochrane and Flanagan, 2003; Renschler, 2003). For the model validation, the calibrated parameters were used to simulate the runoff. The model performance indices (NSI, IOA and RMSE) for both calibration and validation periods were quite favourable (Table 5.2). Figure 5.9 (A) and (B) show that the daily runoff during the winter/rainy season was predicted well by the model. However, some storm events that occurred in the dry season, such as 29 April (i.e. 119th day), 2002 and 8-11 May (i.e. 128th-131st day), 2009 (Figure 5.9 (A) and (B)) events, were not simulated well by the model. The under-prediction in larger events and over-prediction in smaller events can be better seen in Figure 5.10 which shows the observed and predicted runoff (m^3/s) as a scatter plot for the model calibration and validation periods. The under-prediction of storm event peak-flows from the WEPP model has been reported in other studies (e.g. Oropeza-Mota et al., 2004; Covert et al., 2005; Pieri et al., 2007). The slight under-prediction in large events and over-prediction in small events is inherent to WEPP due to the complexity of the model and model input parameters (Nearing, 1998; Tiwari et al., 2000); however, the model performed well overall. Since runoff during the wet/rainy season was predicted well, it implies that soil moisture was also being predicted well. The prediction of soil moisture is important in this study for landslide modelling.

Table 5.2: Evaluation criteria for the assessment of the model performances for runoff. Calibration period was for 2000-2002 and the validation for 2009.

Year	NSI (%)	IOA (%)	RMSE (m^3/s)
2000	89.51	97.15	0.03163
2001	58.80	80.59	0.00197
2002	79.02	93.53	0.0254
2009	58.99	87.94	0.04208

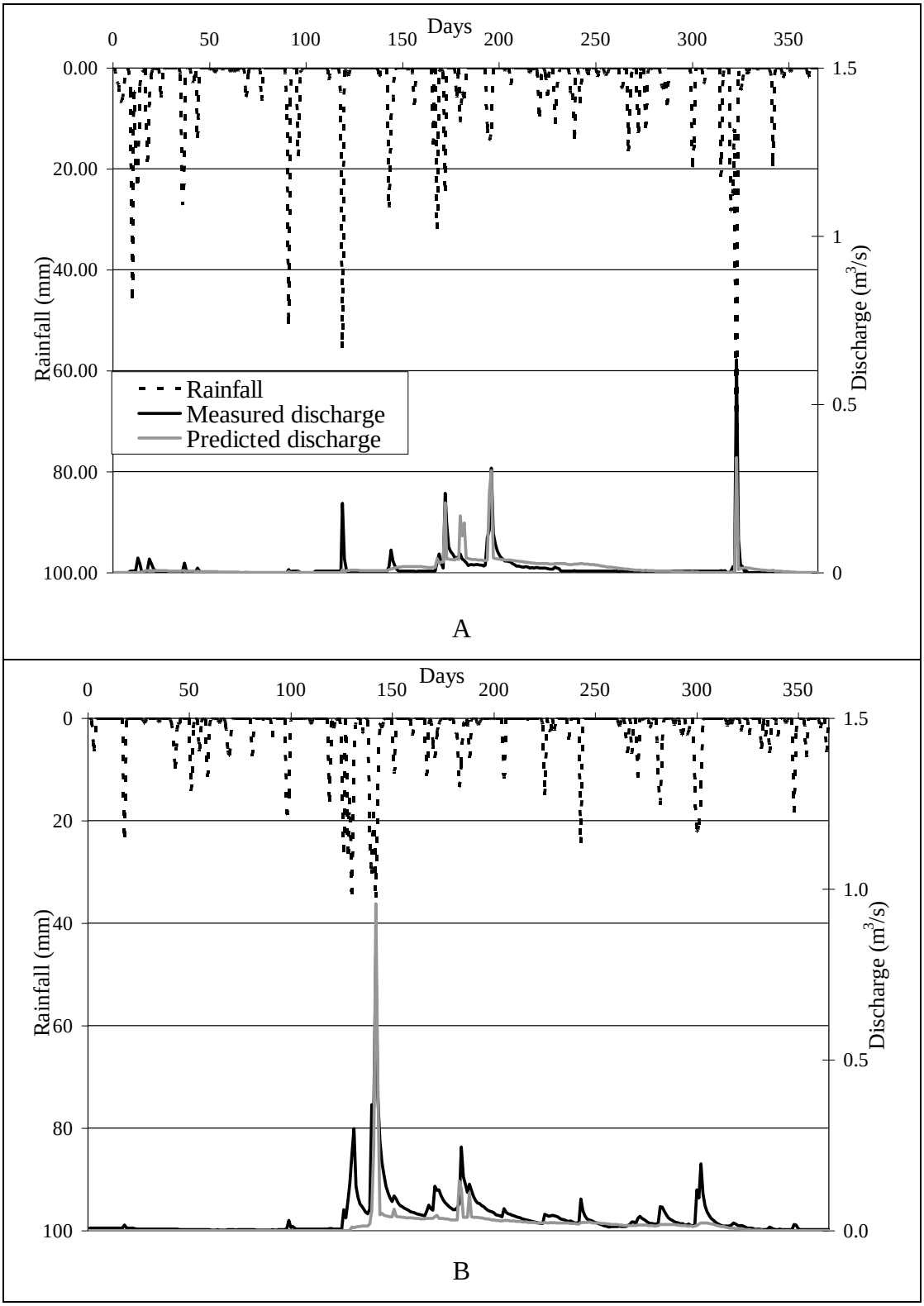

Figure 5.9: Comparison between daily observed and modelled runoff at the outlet of the Bowenvale catchment (A) for the year 2002 of the calibration period, and (B) for the year 2009, the validation period using the Hillslope method

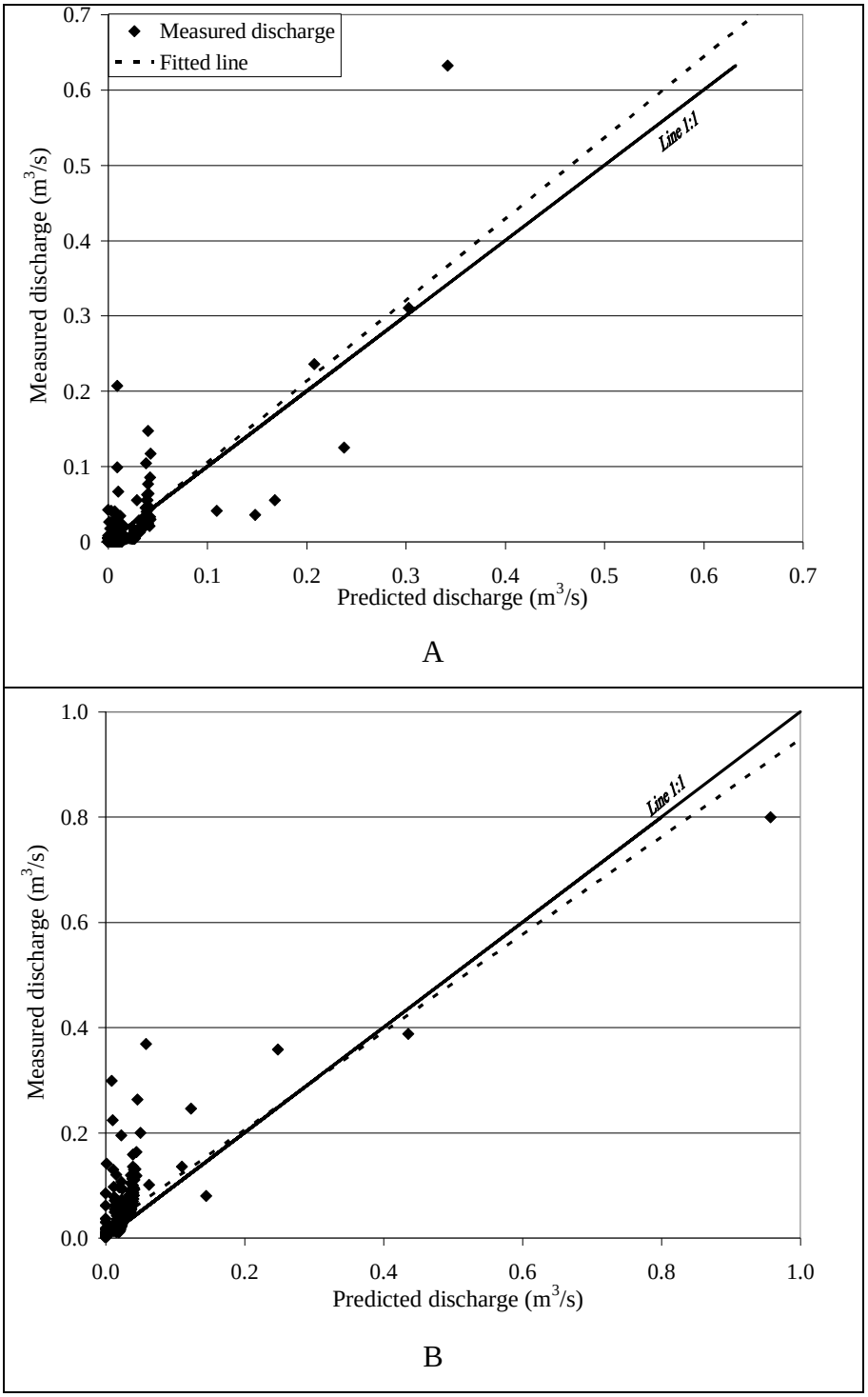

Figure 5.10: Scatter plot of observed versus simulated flows (A) for the year 2002 of the calibration period and (B) for the year 2009, the validation period using the Hillslope method

Comparison between the measured and the predicted sediment yields at the catchment outlet was not done for the calibration period (2000-2002) due to lack of sediment data for the period. The daily sediment yields computed from the turbidity

observations were compared with the model predicted values using the Hillslope method for the period October to December 2009 (Figure 5.11). In general, the predicted sediment yields were lower than the measured ones; the total sediment yield for the period (October to December 2009) was about 16 T and the model simulated value was about 10.8 T. The model under-predictions of sediment yields were significant during the October 9, 27 and 28 storm events.

The lower predicted values may be due to a number of reasons. First, it is related to the under-prediction of the runoff in the storm events of the period (Figure 5.9 (B)). Second, the difference could be due to the facts that the model only predicts sediment yields from hillslopes of the catchment and not from other sources such as road erosion. Contributions from both the cut slope and road surface of hilly roads on sediment yields are generally high (e.g. Doten et al., 2006). Third, model prediction of runoff and sediment yield is also related to the soil parameterisation, particularly effective hydraulic conductivity and soil erodibility factors. In this study, saturated hydraulic conductivity measured in the laboratory for each soil type was used as the effective hydraulic conductivity for catchment modelling. WEPP uses the effective hydraulic conductivity to internally compute infiltration rate and amount and small variation can lead to prediction errors. Studies indicate that runoff prediction is sensitive to the values of effective hydraulic conductivity (e.g. Pieri et al., 2007). Soil erodibility parameters such as soil rill and inter-rill may also have influenced the low sediment yield prediction. Potential spatial variability of these parameters was not taken into account. One value of rill erodibility and one value of interrill erodibility was used for the entire catchment. Fourth, it is also worth noting that the catchment erosion observations using turbidity involve reliability of relationships established between turbidity reading and sediment concentration. It requires an intensive sampling to develop a reliable turbidity and sediment concentration relationship. The sensor was calibrated from 11 runoff samplings. However, the sampling should have covered a variety of storms in duration and magnitude. Furthermore, previous studies have demonstrated sediment load estimation depends on how the data is fitted such as linear, power, polynomial (Sun et al., 2001). In this study, a simple linear relationship was established between the turbidity and sediment concentration. A linear relationship between the daily runoff and sediment yield was developed using the observed values of daily runoff and sediment yield for the October to December 2009

(Figure 5.12). The data produced a reasonably good linear regression having the value of R^2 equal to 0.96.

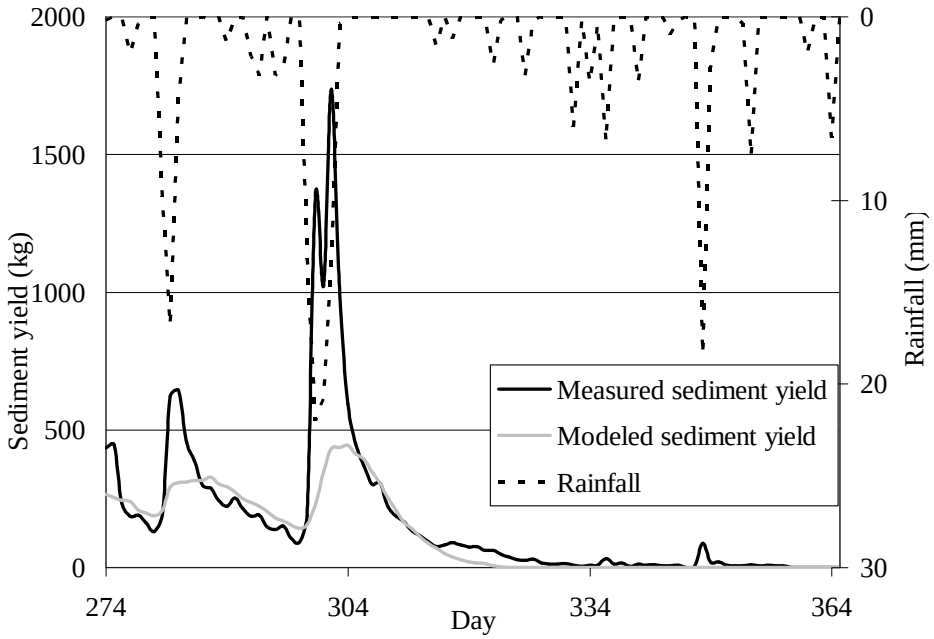

Figure 5.11: Comparison between the computed daily average sediment yields from the Greenspan turbidity sensor and the model predicted average sediment yields using the Hillslope method for the observed period (October to December 2009).

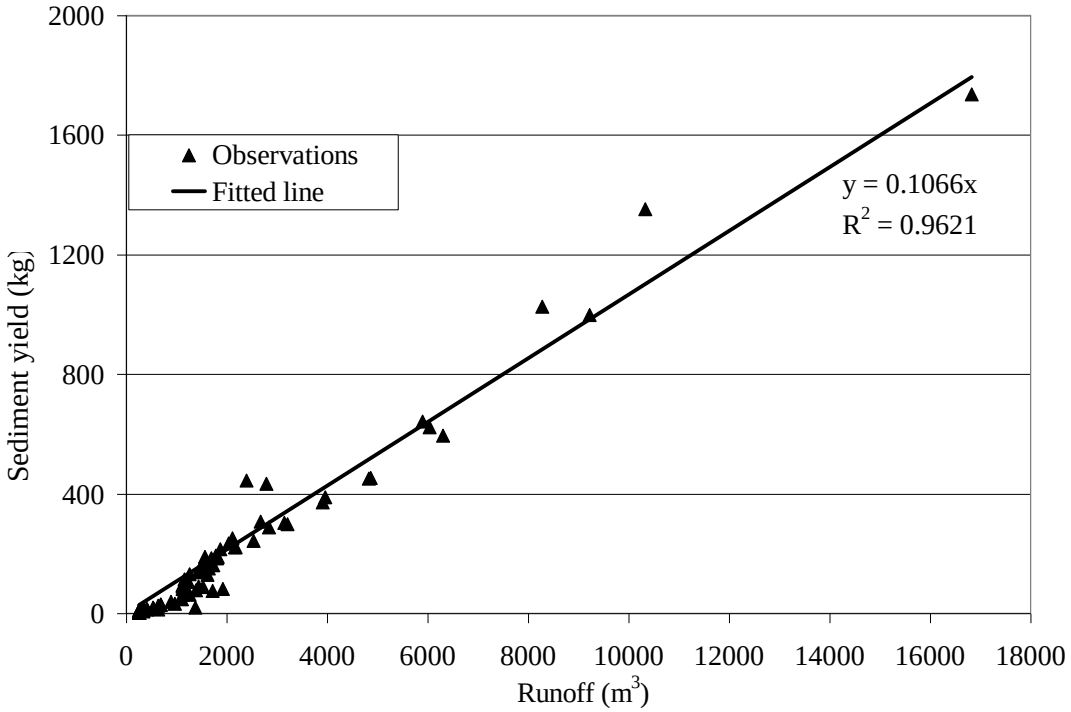

Figure 5.12: Relationship between the measured values of daily runoff and sediment yield for the period October to December 2009.

Table 5.3 summarises soil erosion and deposition simulated using the two (i.e. Hillslope and Flowpath) methods for the year 2009. The Flowpath method simulates the hillslope sediment yields but not the channel and outlet ones. Therefore, no comparison was possible between the methods for the outlet sediment yields. However, a comparison of hillslope sediment yields showed that the Hillslope method predicted about 19 times higher values than the Flowpath method. The higher values of the sediment yield predicted by the Hillslope method may be related to the computational weighting involved in the method. The Hillslope method computes the sediment yield using a representative slope profile for a sub-catchment. In the representative slope profile, the length and slope of the profile are weighted from all flowpaths in the sub-catchment (Cochrane and Flanagan, 1999). The dominating soil and management of the sub-catchment are lumped in the entire profile; this does not take into account the spatial variation of the soil and management data and may lead to higher sediment yield prediction. An advantage of the Flowpath method over the Hillslope method is that the Flowpath method can compute the spatial variation of erosion and deposition in a catchment. Table 5.3 shows that the Flowpath method predicted about 50 T of sediment deposition which occurs in 5% of the catchment area.

Table 5.3: Comparison of simulated soil erosion and deposition using two different methods for 2009.

Method	Sediment yield (T)			Area (%)		Hillslope sediment (T)	
	At the outlet	From hillslope	From channel	Erosion	Deposition	Erosion	Deposition
Hillslope	2863.4	2316.2	547.2	74.9	-	2316.2	-
Flowpath	NA	119.5	NA	43.9	4.9	169.6	50.1

*NA Not Applicable

5.4.2 Landslide modelling

Figure 5.13 shows the time series soil moisture measurements (g g^{-1} %) from the soil moisture sensors along the two hillslopes. The temporal variations in the soil moisture were observed in response to rainfall events as recorded in the sensors 1-5, 9 and 10. In all these sensors, the peak measurements were observed on October 28 from the

rainfall events spanning between October 26 and 29, 2009. Soil moisture values generally stayed elevated for a few days even after the rainfall stopped on October 29. The antecedent rainfall of previous days (October 26-27) along with rainfall occurring on October 28 contributed to attain the peak soil moisture measurements. Among these sensors, the highest peak was observed from sensor 5 which gave a value of about 26% soil moisture. The value may be attributed to the influence of upslope contributing area because the sensor is located at the lowest spot in the hillslope (Figure 5.6). According to Beven and Kirkby (1979), higher soil moisture is generally expected in the downslope area due to increase in upslope contributing area.

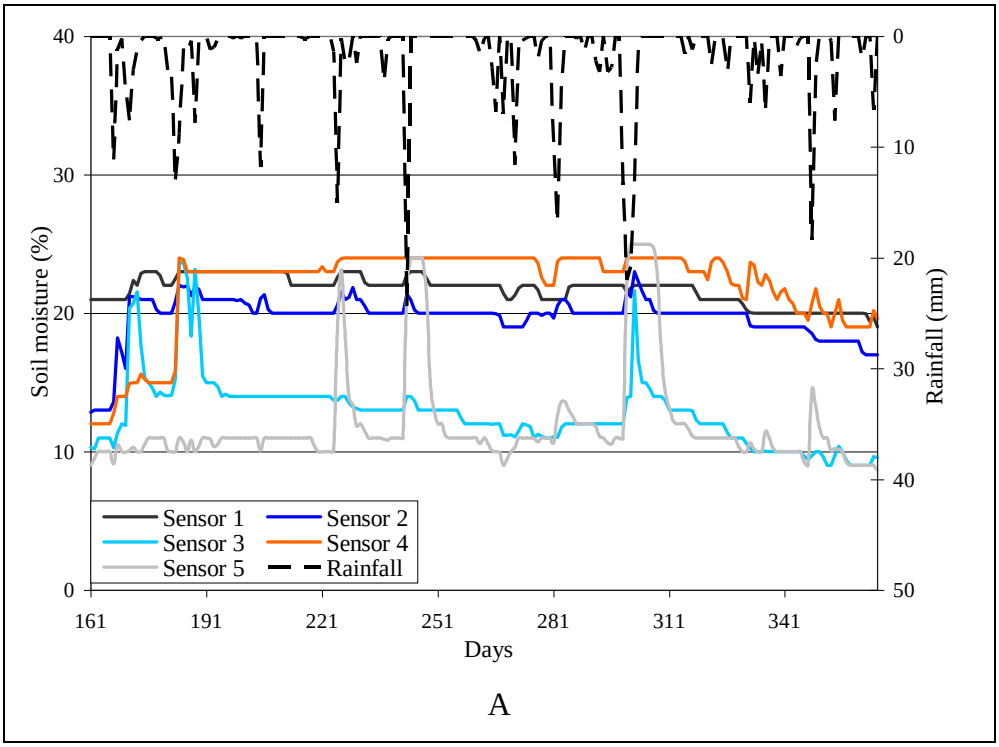

A

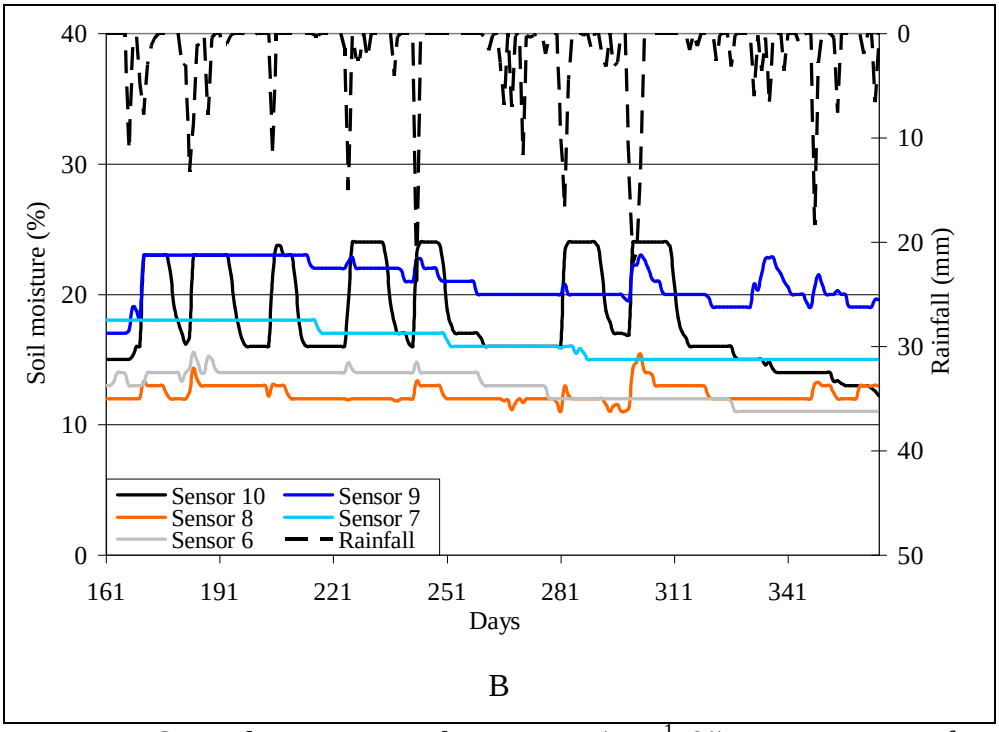

Figure 5.13: Daily average soil moisture (g g^{-1} %) measurements from the soil moisture sensors in tussock grassland (A) and forest area (B). The sensors are labelled according to their location shown in Figure 5.6 (A).

In general, soil moisture at a point is related to the upslope contributing area draining to that point i.e. soil moisture increases with increase in the upslope area. However, this kind of relationship is not always true in a hilly region with dense vegetation. In such case, the relation between the soil moisture and topographic index is overlain by a much stronger relationship between the soil moisture and the vegetation type and canopy properties. This is specifically observed in Figure 5.13 (B) where sensors 6-8, which were under dense forest cover, exhibited uniform soil moisture without significant changes in response to rainfall events during the entire observation period. Furthermore, these sensors recorded lower soil moisture than the sensors located upslope (e.g. 9 and 10).

Vegetation-cover can have complex and contrasting impacts on soil moisture which are strongly dependent on vegetation type, its density and age. On the one hand, dense vegetation cover decreases the soil moisture due to greater transpiration and less rainfall falling on the ground because of larger interception by plant leaves (Ran et al., 2002; Chen et al., 2009). On the other hand, the canopy shades the soil and consequently prevents the direct radiation absorption, resulting in lower soil

temperature and soil evaporation rates, and eventually higher soil moistures (Belsky et al., 1989).

In addition to vegetation, some site-specific properties such as local topography and landform, soil depth and type may have an impact on the soil moisture distribution. Ridge type landforms common in the upper section of the study hillslope may retain soil moisture longer, delaying topographically-driven drainage. Local topography is the dominant control in soil moisture distribution; soil moisture at a point is inversely proportional to the local slope gradient (Yeakley et al., 1998) indicating that lower soil moistures should occur along steeper slopes. The spatial variability of the soil moisture is also related to soil infiltration capacity. Soils along the lower areas of the study hillslopes are less permeable (Table 5.1 and Figure 5.5 (D)) delaying water infiltration.

From the soil moisture observations and modelling, October 28 was determined to be the wettest day of 2009 and a large portion of the catchment was saturated. The total soil water content on October 28 was obtained from the daily WEPP simulations of water balance for each of 2481 flowpaths simulated in the catchment for the 2009. The reason for running the full year simulation with the WEPP to obtain peak soil water content was to account for the antecedent soil moisture condition. The soil water content simulation in the catchment estimated about 29% of the catchment to be completely saturated on the day. The soil wetness index (i.e. relative water table height) in the catchment area ranged from about 0.25 to 1 (i.e. completely saturated condition).

Figure 5.14 shows the relative hazard for shallow landsliding based on spatial distributions of the factor of safety (Fs) according to the criteria given in Table 4.4; for simplification and soil redistribution modelling purpose; Fs greater than 1.5 was categorised as safe and stable. More than 98% of the slopes were predicted to be unconditionally stable (i.e. factor of safety greater than 1.5), and none of the catchment as unconditionally unstable (i.e. factor of safety less than 1). Approximately 1.4% of the catchment area falls into a quasi- and moderately-stable classification which should be considered as sites for possible landslides as these

areas are located on steep slopes between about 24° and 40° with pasture land-cover type.

Local slope gradient has a great influence on the susceptibility of a slope to landsliding. The landslides in the Bowenvale catchment were probably triggered by a transient water table above the interface between the soil surface and impermeable underlying bedrock, resulting from infiltration and subsurface seepage. An analysis was carried out to assess the relationship between the stream network and landslide occurrence. About 80% of the landslides were within 100 m of the nearest stream. As the distance from the stream network increased, landslide probability generally decreased. This may be attributed to the hydrological triggering of landslides due to increased soil moisture closer to streams.

The success of landslide modelling is typically evaluated by comparing the location of the known landslides with the simulated ones (e.g. Montgomery et al., 1998; Lee and Ho., 2007; Godt et al., 2008). An ideal landslide susceptibility map maximizes the agreement between the known and the predicted landslide locations. Although the present landslide simulation does not cover the full period represented by landslide inventory, simulated landslides were compared with the landslide inventory assuming that the mapped landslides would have been triggered by the rainfall storm events similar to that occurred in the year 2009.

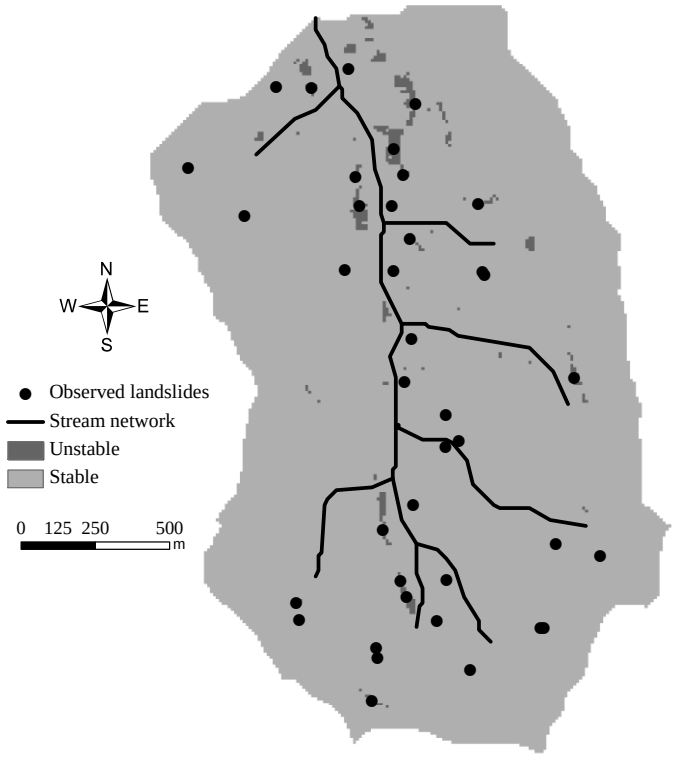

Figure 5.14: Locations of the observed landslides indicated as black dots overlain on the classified landslide hazard areas generated from the integrated modelling approach.

Figure 5.14 shows 39 observed landslides displayed over the classified landslide hazards map obtained from the GeoWEPP-SLIP for 2009. The map of the simulated landslides shows that in general, slopes are much more prone to landsliding in the east and north catchment than in the west. The model captured eight landslides in the east, five in the south, and three in the west. These result in approximately 40% of the observed slide locations coinciding with the simulated failures. Most of the coinciding landslides were found along the steep foot slopes corridor running parallel to the stream network. The model over-predicted the landslides near the outlet in the east of the catchment (Figure 5.14), which probably indicates an under-estimation of the soil strength and root cohesion in these areas.

The model was not able to predict most of the observed landslides in the upper catchment. The under-prediction is probably related to over-estimation of the soil strength and depth. The observed landslides in these high areas are very shallow (typically less than 0.30 m) and characterised by a smaller size (typically less than 10

m^2 area) than the grid-cell resolution used for modelling (i.e.100 m^2 in this study). The grid-cell resolution also clearly influences the landslide prediction because the spatial variability of the local slope alters with changes in resolution (Claessens et al., 2005). For shallow soils, the model under-predicts landslides because the landslide model computes higher values of safety factor for the shallow soils due to the presence of the depth parameter in the denominator of the model (Equation 2.19).

5.4.3 Soil redistribution modelling

The total displaced soil volume from the 39 observed landslides was estimated to be about 2100 m^3. The volume was computed from the landslide database documented by the repeated field surveys during the period 2008-2010. The model predicted volume of the failure material was approximately 7,900 m^3 from approximately 4.34 ha (i.e. about 1.4% of the total catchment area) of potential landslide prone areas (Figure 5.15). The estimated volume of the 16 coinciding landslide scars was computed to be about 1,400 m^3 and the model predicted volume was about 4,800 m^3 in the same areas. This indicates that the total predicted volume of the eroded materials by shallow landslides was about 4 times higher than the total observed volume. The over-prediction of landslide materials was directly associated with the over-prediction of the landslide-delineated area. The failure volume over-prediction was also attributed to the assumption that the failure depth coincides with the saturated depth. In many cases, however, a failure plane is shallow and may not necessarily coincide with the saturated soil depth. The failure plane location is a function of the geotechnical properties of the soils, local slope gradient and soil depth (Terlien, 1997). Typically, a shallow soil profile has a planar failure plane along an interface dividing a shallow upper soil layer from an underlying stronger and often less permeable underlying soil layer or bedrock (Burton and Bathurst, 1998).

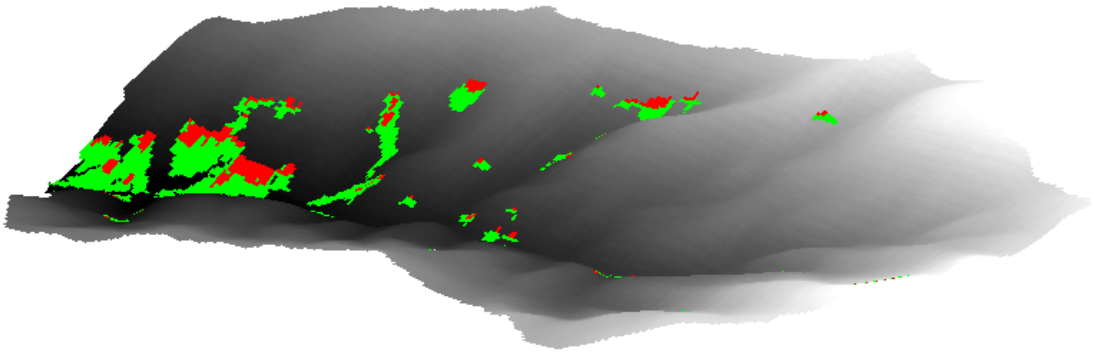

Figure 5.15: Topography of the catchment overlain with the predicted landslide and soil redistribution patterns from the GeoWEPP-SLIP modelling approach. Red and green patches represent failure and deposition areas respectively

The failure materials were routed to downslope grid-cells using Equations 5.1-5.3 and the assumptions illustrated in section 5.2.3. About 80% of the landslide materials were predicted to deposit inside the catchment and the remaining 20% to reach the channel network. In many cases, the failure and runout of the failure materials alter the elevation and slope gradient in the failure and deposition areas. In the Bowenvale catchment, the decrease in surface elevation was predicted to be from 0.29 m to 1.13 m due to failure, whereas the soil depths increased from 0.03 m to 1.50 m in the deposition area. The results are comparable with previously reported results (e.g. Doten et al., 2006). This caused a decrease of up to 6.4° and an increase of up to 2.5° in failure and deposition areas respectively. The results show that spatially variable sediments derived from landsliding leave a long-term imprint on the hillslope morphology. Similar observations were reported in previous laboratory scale landslide studies (Chapters 3 and 4); for example, there were approximately 7° decrease and 3° increase in slope in the failure and the deposition area respectively in sandy soil experiments illustrated in Chapter 3.

5.5 Post-failure scenarios due to land management and topography changes

Because the proposed model was developed to predict the effects of hillslope evolution on long-term soil erosion, the model was evaluated under two scenarios: (a) vegetation not re-established (long-term fallow), and (b) re-establishment of vegetation in failure and deposition areas. The post-failure soil erosion and runoff

were evaluated for the same simulation year 2009 to compare them against the results of simulations with the original topography and land-cover, which is termed as the 'base case' condition.

Approximately 17.9 ha (i.e. 5.9%) of the total catchment was predicted to alter its topography and land-cover due to failure and soil redistribution. The predicted failure and deposition area was assumed to remain as bare soil until the vegetation was fully re-established. Table 5.4 presents the post-failure soil erosion and deposition predicted using the Hillslope and Flowpath methods in the two scenarios and the results were compared with 'base case' results. Among these three cases, 'case a' predicted the highest hillslope and outlet sediment yields for the Hillslope method and the highest hillslope sediment yields for the Flowpath method. The difference in the value of hillslope sediment yield between the 'case a' and 'base case' for the Flowpath method was significantly higher than the difference for the Hillslope method. The difference was about 522 T for the Flowpath method whereas it was approximately 50 T for the Hillslope method. The significant differences in results between the Flowpath and Hillslope methods are due to how land-cover is simulated in each method for computing soil erosion. For the Hillslope method, a representative profile is used for each sub-catchment. Most of the representative profiles in the Bowenvale catchment did not capture the bare soil (fallow conditions) following the landslide and soil redistribution modelling because the soil and management data are lumped for each hillslope and profile in the Hillslope method. This only led to a slight increase in the value of hillslope sediment yield in the 'case a' compared to the 'base case'. The Flowpath method, on the other hand, captures spatial variations better because each flowpath is simulated and thus changes from vegetation cover to bare soil are readily captured. This significantly increased the hillslope sediment yields in 'case a' compared to the 'base case'.

In the Flowpath method, the value of the hillslope sediment yield in 'case b' was slightly higher than in 'base case' despite decrease of slope gradient in the failure predicted areas. The result may be attributed to two main reasons. First, it was related to the prediction of increase in local slope in the deposition area. The deposition area was over 3 times larger than the failure area. Second, the changes in elevation and local slope gradient due to landslide and soil redistribution modelling altered the

flowpaths' distribution in the catchment, for example, the number of flowpaths increased from 2481 in the 'base case' to 2523 in the 'case a' and 'case b'. The higher number of flowpaths might also be responsible for the increase in hillslope sediment yield for the Flowpath method.

Table 5.4: Comparison of the predicted annual post-failure soil erosion and deposition between 'case a' and 'case b' for the two methods for the 2009 simulation year.

Case	Method	Sediment yield (T)		Hillslope sediment (T)	
		Outlet	Hillslope	Erosion *	Deposition *
Base		2863.4	2316.2	2316.2 (74.9)	- (-)
a	Hillslope	2916.5	2366.3	2366.3 (74.9)	- (-)
b		2902.2	2306.0	2306.0 (74.9)	- (-)
Base		NA	119.5	169.6 (43.9)	50.1 (4.9)
a	Flowpath	NA	641.5	1533.9 (46.1)	892.4 (6.5)
b		NA	121.0	172.2 (44.0)	51.2 (4.9)

* Results in parenthesis represent % of the catchment area involved in soil erosion and deposition.

In the post-failure scenarios ('case a' and 'case b'), it was hypothesised that post-failure topography and land-cover would alter the predicted soil erosion and deposition only inside the area affected by landslide and soil redistribution prediction, and other areas would remain unchanged. In order to test the hypothesis, the difference in spatial distribution of soil erosion and deposition between 'case a' and 'base case', and 'case b' and 'base case' for the Flowpath method was calculated. The results presented in Figure 5.16 show that the changes in topography altered the soil erosion and deposition not only inside the affected area but also up and downslope of the area. This was probably related to the changes in the flowpath distribution, length and number in the post-failure topography.

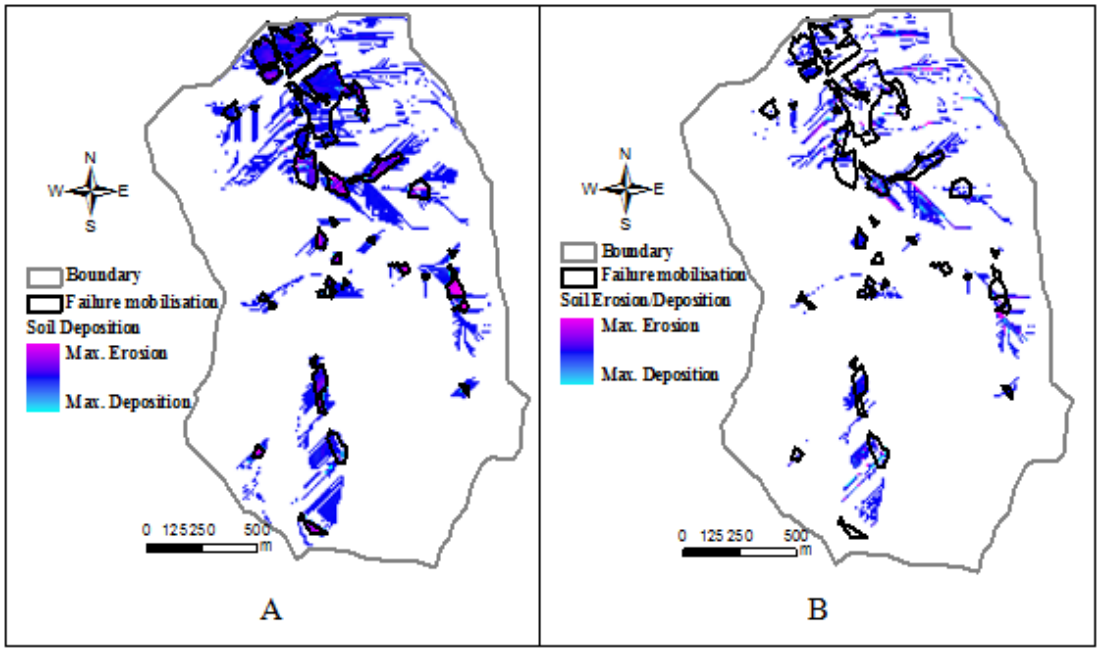

Figure 5.16: Differences of spatial distribution of soil erosion and deposition between (A) 'case a' and 'base case', and (B) 'case b' and 'base case' for the Flowpath method for the 2009 simulation period.

Figure 5.17 compares the simulated daily sediment yields at the catchment outlet between 'base case', 'case a' and 'case b' in various storm events detected in the simulation year 2009 using the Hillslope method. The model summed the outlet sediment yields from the 198 events of the year in all three cases. In the event-wise distribution, there was no difference in sediment yields between the 'base case' and the 'case b'. However the results showed that there were slight differences in sediment yields between 'base case' and 'case a' scenarios particularly in larger events. Therefore, further statistical analyses such as Student T-test and P-value (at significance level of 0.01) were used to compare event results between the 'case a' and 'base case' scenarios. A T-value of 1.59 which was less than the critical T value (2.59) indicates that there was not significant difference between the mean sediment yields between the scenarios. Similarly, the P value was 0.97; values greater than 0.05 indicate no significant difference between the sediment yields. Therefore in the present study, the outlet and hillslope sediment yields were not significantly affected by the changes in topography and land-cover when using the Hillslope method.

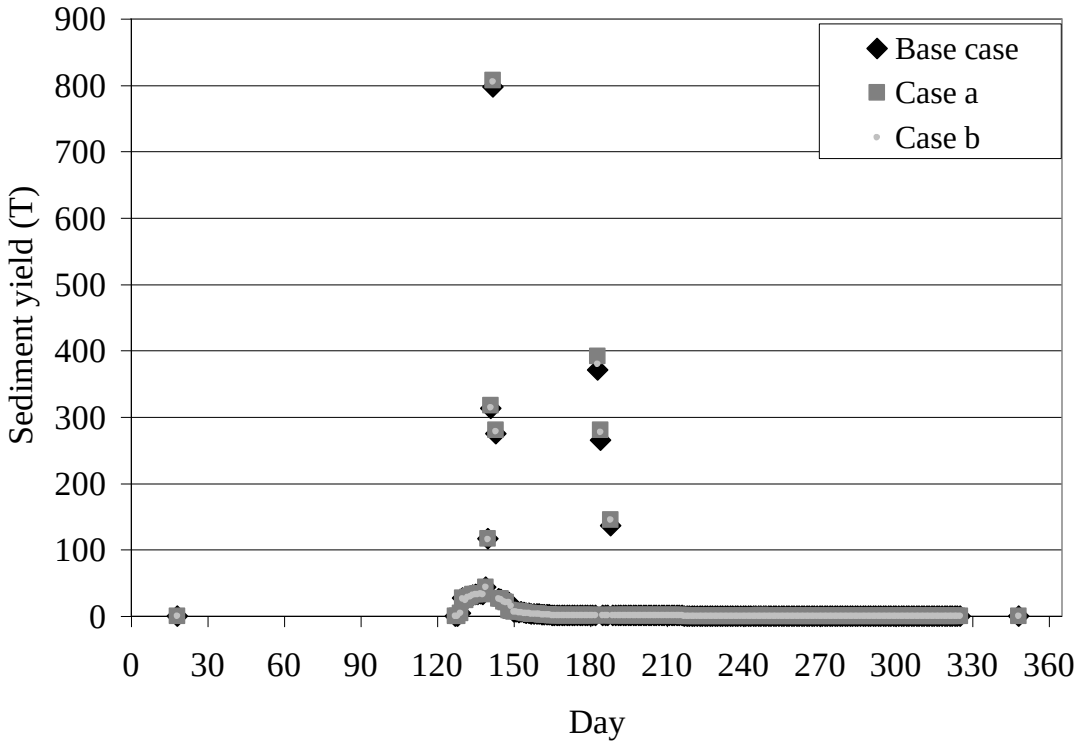

Figure 5.17: Comparison of predicted daily outlet sediment yields between the 'base case', 'case a' and 'case b' scenarios for the Hillslope method for the simulation year 2009.

Figure 5.18 presents daily hillslope sediment yields for the 'base case', 'case a' and 'case b' in various storm events detected using the Flowpath method for the 2009 simulation year. The method simulated the sediment yields from 24 events for the 'base case' and 'case b' for the year, and the number of events increased to 46 for the 'case a'. The events are significantly lower in the Flowpath method than in the Hillslope method. In the Hillslope method, contribution of seepage to stream flow is significantly high due to higher amount of infiltration. The higher infiltration amount is characterised by smoothening effect in the representative profile due to aggregation processes. On the other hand, in the Flowpath method particularly in a finer grid-cell resolution, the flowpath can have abrupt changes in slopes which can cause lower water infiltration and subsequently lower seepage contribution to the stream flow reducing the number of events. A first visual interpretation indicates that the values of sediment yield in the 24 events did not significantly differ between the 'base case' and 'case b', whereas some distinct higher values of the sediment yield were clearly observed for the 'case a'. Statistical analyses (T tests) were therefore used to show whether there was significant differences of mean sediment yields between the 'base

case' and 'case a' and between the 'base case' and 'case b'. An alpha level of 0.01 (confidence interval of 99%) was used for the T tests to determine whether the difference between the means of one of the data events and another was equal to zero or not. The analyses showed that there was no significant difference of mean values of the sediment yield between the 'base case' and 'case b'; the T value was 1.54 less than critical T value (2.69). However, there was significant difference of the mean sediment yields between the 'base case' and 'case a'; the T value was 4.1 greater than critical T value (2.69). This implies that the hillslope sediment yield prediction with the Flowpath method was significantly affected by the changes in land-cover due to shallow landslides and soil redistribution modelling.

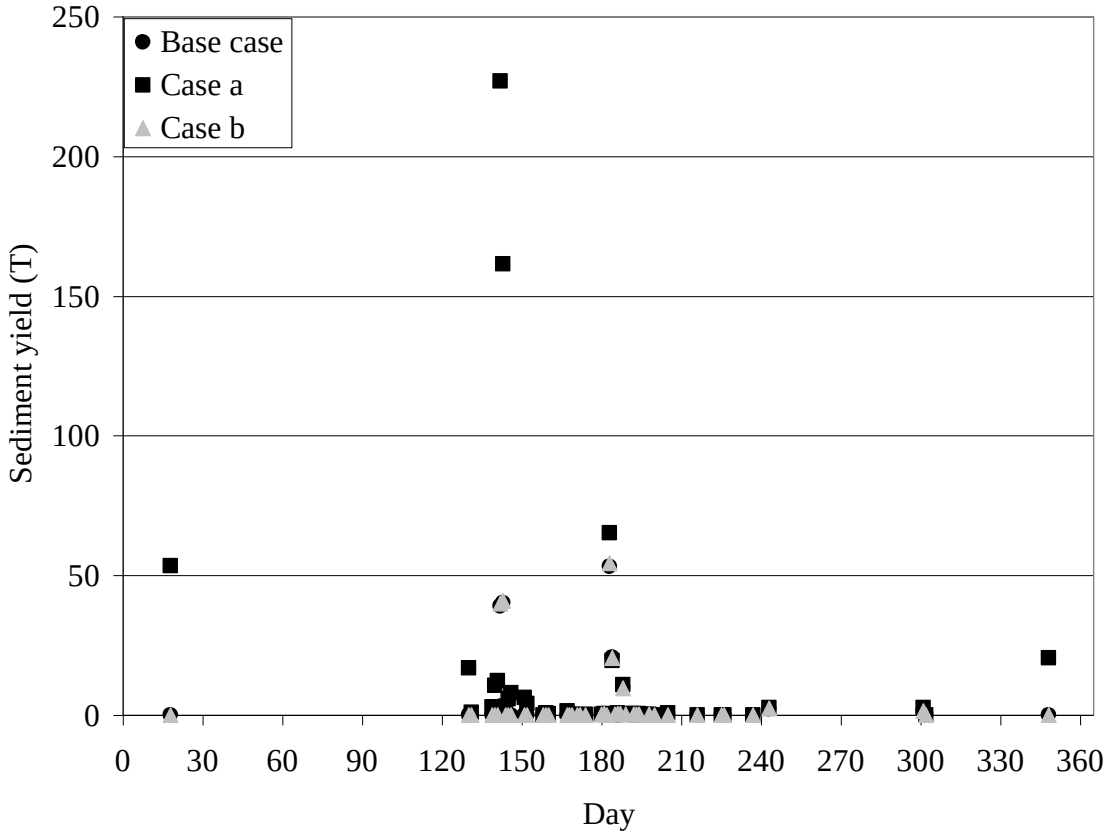

Figure 5.18: Comparison of predicted daily hillslope sediment yields between the 'base case', 'case a' and 'case b' scenarios for the Flowpath method for the simulation year 2009.

5.6 Extreme landslide scenarios

Effects of shallow landslides on landslide materials and changes in post-failure topography and land-cover were further studied for five extreme landslide modelling scenarios. The first four of the five scenarios were done using the peak values of the total soil water content simulated from the four different WEPP simulation periods;

2005-2009, 2000-2009; 1995-2009 and 1989-2009. The last one was performed in a completely saturated scenario i.e. the entire catchment's soils were assumed to be completely saturated. The landslide-delineated areas, landslide volumes and soil redistribution and post-failure sediment yields were computed for each scenario and compared with the landslide and soil redistribution modelling results presented in section 5.4.2-5.4.3 (i.e. landslide and soil redistribution modelling using the 2009 soil moisture simulations) which is termed as the '2009 modelling case'. Table 5.5 shows a gradual increase in the landslide prone areas and the areas covered by the soil redistribution (i.e. deposition area) from the '2009 modelling case' to 'case 4'. About 16% more of the catchment area was predicted to be completely saturated in 'case 4' than in the '2009 modelling case' which resulted in about 1% more catchment area classified as unstable in 'case 4' than in the '2009 modelling case'. The unstable area elevated to 4.1% of the catchment area when the entire catchment was completely saturated (i.e. 'case 5') which represents the worst case scenario. In all these cases (1-5), the model could not capture all the observed landslides which may be due to the under-estimation of the soil input parameters in the landslide areas (Figure 5.19).

There was a gradual increase in deposition area from the '2009 modelling case' to 'case 5'. However, the ratio of the deposition to failure areas decreased significantly from the '2009 modelling case' to 'case 5'; the deposition area in the '2009 modelling case' was about 3.1 times larger than the failure area whereas the deposition area exceeded the failure by only 1.8 times for 'case 5'. The predicted deposition volumes were also comparable between these scenarios; about 80% of the failure volume was predicted to deposit within the catchment in the '2009 modelling case'. In contrast, more than 75% of the failure volume would reach the stream network in 'case 5'. This indicates that the portion of the failure materials encountering the stream network increased significantly from the '2009 modelling case' to 'case 5'. The results are directly related to the spatial distribution of the predicted landslides, their location from the drainage network and steepness of the downslope topography. Most of the predicted landslides in these cases were spatially distributed along the corridor running parallel to the stream network (Figure 5.19).

Table 5.5: Failure and soil redistribution modelling in extreme landslide cases

Case	Soil moisture simulation period	Landslides captured by model	Failure area (ha)	Deposition area (ha)	Failure volume (m^3)	Deposit volume (m^3)
2009 modelling	2009	16	4.34	13.52	7,900	6,300
1	2005-2009	16	5.30	14.37	12,000	7,700
2	2000-2009	16	5.88	15.27	14,200	8,500
3	1995-2009	16	6.97	16.49	18,600	10,600
4	1989-2009	17	7.34	16.59	20,100	10,700
5	Completely saturated	20	12.42	22.81	54,900	13,300

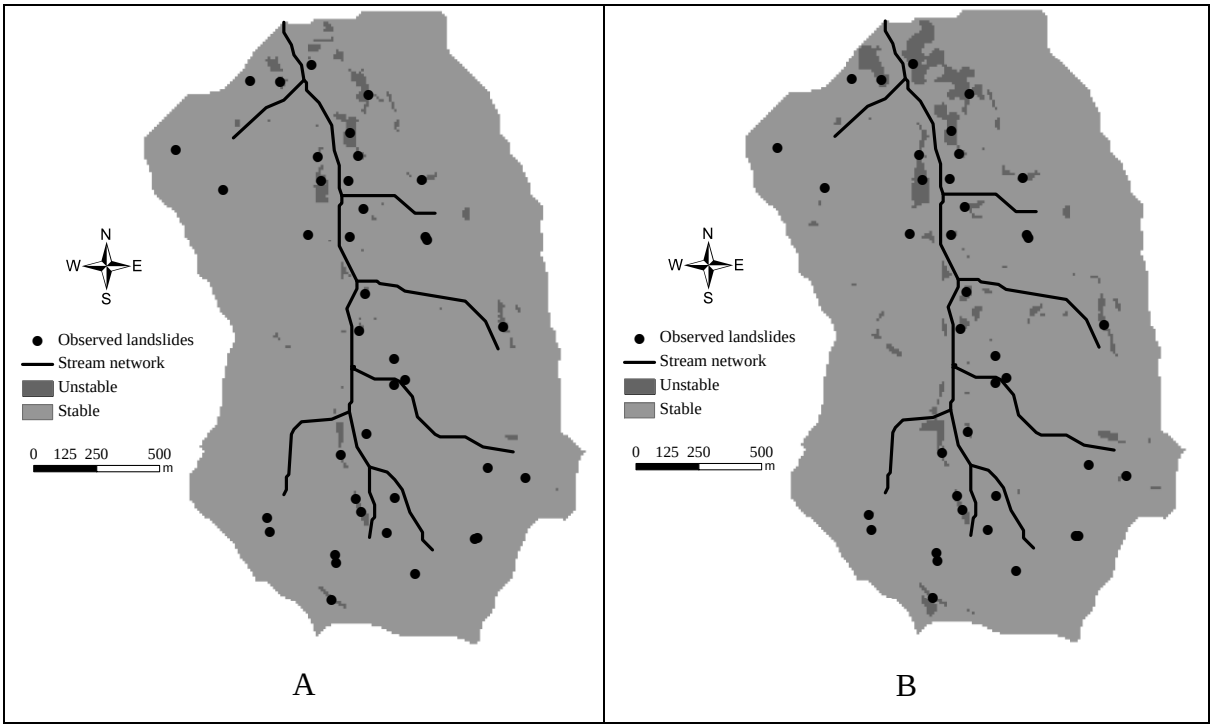

Figure 5.19: Location of observed landslides indicated as black dots overlain on the classified landslide hazards areas for (A) case 1, and (B) case 5.

Figure 5.20 (A) and (B) show how the shallow landslide and soil redistribution area affect the long-term hillslope sediment yields for the Hillslope and Flowpath methods. The area was simulated in various extreme landslide modelling cases (Table 5.5); the failure and the soil redistribution would change the existing topography and land-cover (until the existing vegetation is re-established) from about 5.9% of the total catchment area in the '2009 modelling case' to 11.7% in 'case 5'. In all of these cases,

the post-failure sediment yields were modelled using 2009 simulation period rainfall data. For both methods in the vegetation re-establishment scenario, there was a gradual decreasing trend of hillslope sediment yields with increase in the area affected. In the scenario where vegetation is not re-established, the Hillslope method showed a gradual increase in sediment yield with increase in the area affected. However for the Flowpath method, sediment yields increased significantly with increase in the area affected (Figure 5.20 (B)). The value of the hillslope sediment yield increased from about 640 T to 1075 T with an increase in the affected area from 5.9 to 11.7% of the catchment when vegetation was not re-established. These results were also directly related to the computational methods used in the Flowpath and Hillslope methods.

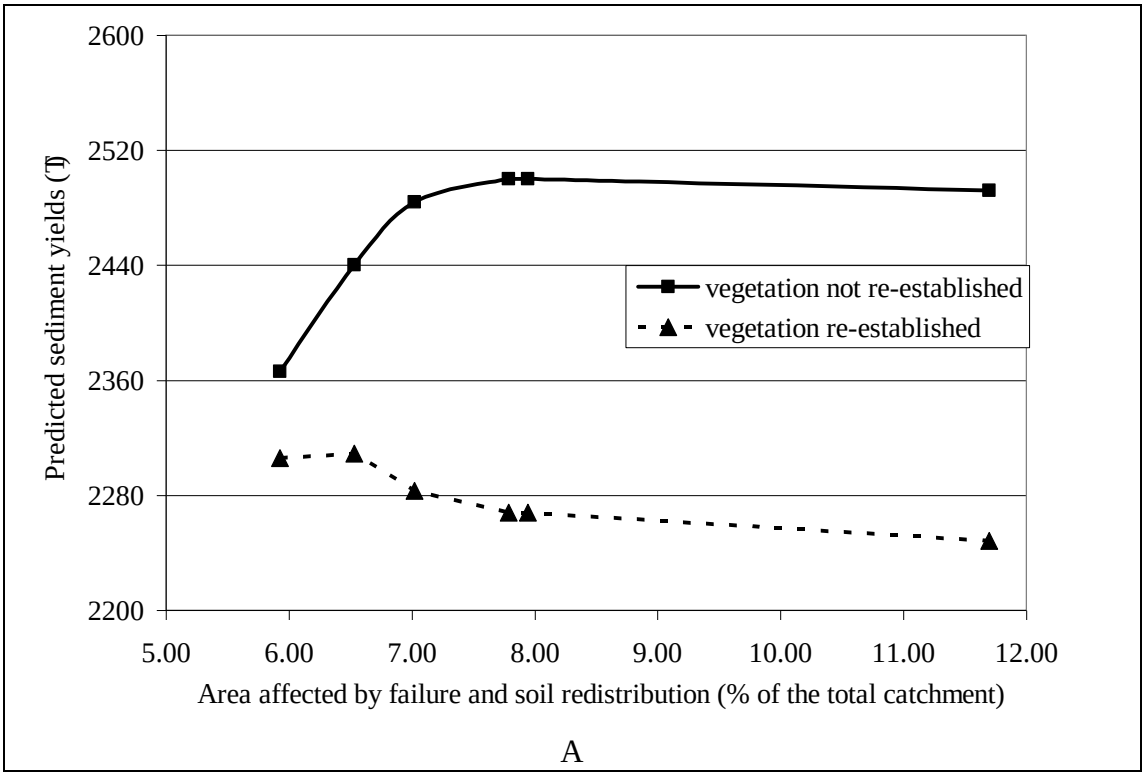

A

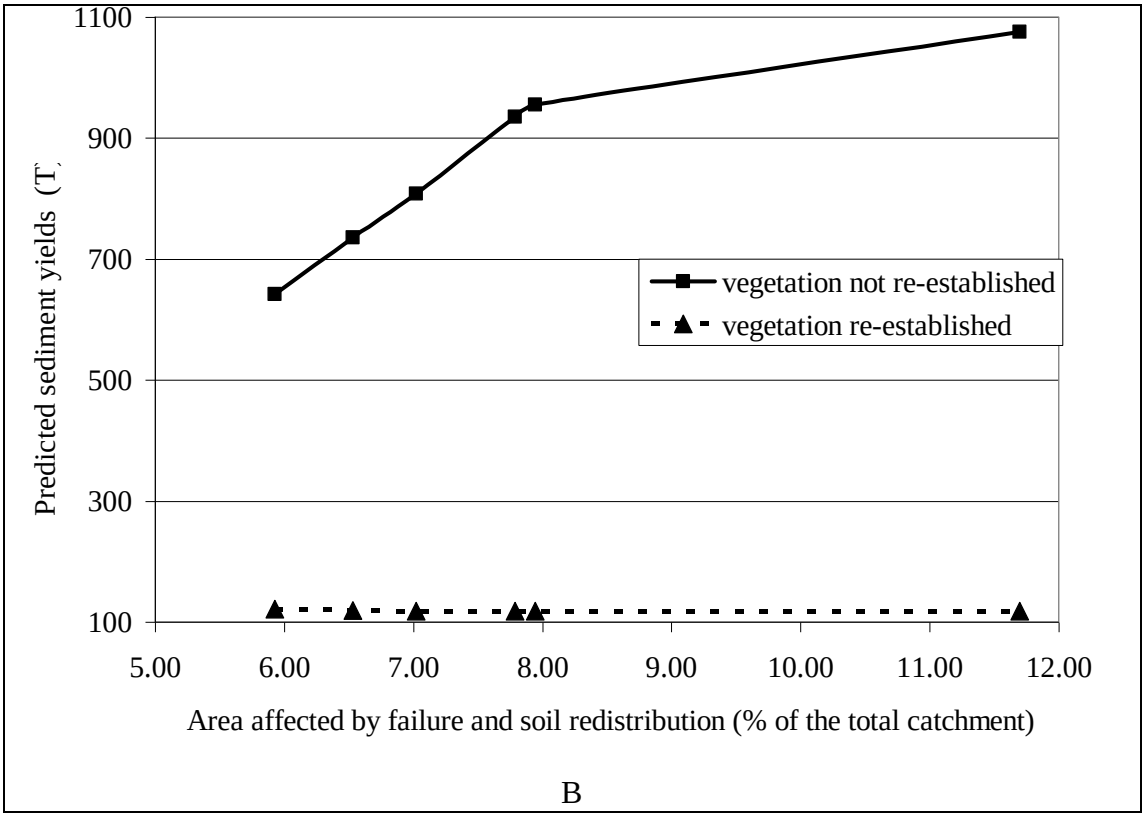

Figure 5.20: Post-failure hillslope sediment yields after changes in the area affected by shallow landslides and soil redistribution due to extreme landslide cases (A) for the Hillslope method, and (B) for the Flowpath method for the 2009 simulation year.

5.7 Model limitations

The overall aim of the integrated modelling was to assess the impacts of shallow landsliding on longer-term landscape dynamics at a catchment-scale. However, validation of soil redistribution and post-failure soil erosion was not possible in the present study. Validation of soil redistribution model requires data sets linking landslide events with rainfall condition. Given the relative short time period of this research project, it was not feasible to do and no historical data sets were available.

The model has some limitations and therefore needs further improvement. As there was no automated tool developed to simulate the total soil water content at a catchment-scale using the WEPP, simulation of the water content was a time consuming activity for this case study application. Therefore, a user friendly automated tool needs to be developed. The tool has to integrate GIS and WEPP to simulate peak values of the total soil water content for a simulation period. The tool further needs to integrate the landslide and soil redistribution. Second, further

research is required to expand the modelling framework to integrate other sediment supply components such as road and channel erosion specifically for the Flowpath method because these components significantly contribute to basin sediment yields.

5.8 Summary and conclusions

In this chapter the GeoWEPP-SLIP modelling framework was proposed to predict pre- and post-failure runoff and soil erosion, landsliding and soil redistribution. The approach estimates the main sources of sediment supply in hilly and mountainous catchments: shallow landslides and soil erosion. It also includes sediment distribution and routing from these sources to downslope areas and/or to the catchment channel network. A case study application of the GeoWEPP-SLIP approach to the Bowenvale research catchment showed that the model produced plausible stream discharge and sediment yields in comparison with the observed values obtained from the monitoring stations. The landslide model coupled with the soil moisture routing from the WEPP model performed well in predicting locations of landslide failure potential. The model was able to capture approximately 40% of the observed landslides with respect to location. For the determination of failure material trajectories, a simple rule-based approach was adopted.

Simulations showed that the occurrences of landslides and their subsequent mobilisations could lead to changes to the existing land-cover and topography in about 5.9% of the catchment. The area could increase to 11.7% if the entire catchment becomes completely saturated. The predicted changes in local slope could range from -6.4° to +2.5° in failure and deposition areas respectively. These values are similar to the values obtained from the landslide erosion flume experiments presented in the previous chapters. Influence of the area affected by shallow landslides and soil redistribution on long-term soil erosion and sediment yield was evaluated by modelling the shallow landslides and soil redistribution for different soil moisture simulation periods. The Flowpath method was sensitive to changes in vegetation in the affected landslide areas; higher soil erosion and hillslope sediment yields were also predicted when the affected area increased significantly. However, consistent soil erosion and sediment yields were predicted for the Hillslope method in both land-cover scenarios (vegetation re-established and not re-established) after shallow landslides and soil redistribution.

The GeoWEPP-SLIP model is sensitive to the model parameterisation related to topography, land-cover and soil. For example in catchment-scale modelling, the topographic parameterisation is related to the grid-cell resolution. Changes in the resolution may alter the prediction of runoff, soil erosion and sediment yields, spatial distribution of landslides and soil redistribution. Therefore, the next chapter will deal with the influence of input grid-cell resolution in the integrated approach.

Chapter 6 Effects of Input Grid Resolution

6.1 Introduction

In the previous chapter, the GeoWEPP-SLIP modelling approach was proposed and applied to the Bowenvale research catchment in Christchurch, New Zealand using a 10 m DEM resolution. Modelling results were presented for: (a) runoff and soil erosion during pre-failure scenarios, (b) spatial distribution of shallow landslides and their runout, (c) changes in local topography due to shallow landslides and their runout, and (d) post-failure runoff and soil erosion due to changes in the topography and land-cover. It was observed that the model predictions were in good alignment with the observed values when using the 10 m DEM. However, hydrological modelling is directly influenced by the spatial parameterisation related to soil, vegetation and topography (grid-cell resolution of the DEM). In this present chapter, the influence of the grid-cell resolution on the GeoWEPP-SLIP model is examined.

DEMs can be developed from a variety of data such as field surveys, contour maps, global positioning systems (GPS), laser surveys, and aerial and satellite surveys. The selection of a DEM resolution in a hydrological model is generally governed by the economical aspect of the DEM creation. The cost of creating very accurate finer resolution DEMs can be significantly high because it may require extensive field work or expensive surveying technology. On the other hand, too fine grid-cell resolution does not necessarily produce better results (Saulnier et. al., 1997). It is therefore very difficult to choose an appropriate grid-cell resolution for modelling because the resolution and size of the catchment both affect the simulation results (Shrestha et al., 2006).

Changes in DEM resolution may impact the GeoWEPP-SLIP model results. Changing resolution will alter the local slopes, which will subsequently affect the simulation of soil erosion and sediment yields. Changes in flowpath distribution and length can also alter the spatial distribution of soil erosion and deposition. The changes are also expected to have an effect on the soil moisture prediction which eventually alters the spatial distribution of predicted landslides and soil redistribution. Therefore, it is

important to assess how the model predictions align with the observed values when using different DEM resolutions.

6.2 Model description

A detailed description of the GeoWEPP-SLIP model used for this analysis has been provided in the previous chapter (Figure 5.1). In this study, runoff and soil erosion simulations in pre- and post-failure scenarios were carried out using both the Hillslope and Flowpath methods. The landslide modelling was done using slope stability analysis coupled with the dynamic simulation of the total soil water content from the Hillslope version of the WEPP model; and a simple rule-based model for the soil redistribution modelling. Soil erosion and runoff simulation, prediction of landslide distribution and quantity were compared with the observed values for all results using various grid-cell resolutions.

6.3 Case study application

The model was applied to the Bowenvale research catchment (43°34´58"S and 172°38´27"E to 43°36´20"S and 172°39´45"E) located in the Port Hills, Banks Peninsula in Christchurch, New Zealand (Figure 5.5). To investigate the effect of the DEM resolution, four different resolutions (10 m, 20 m, 30 m and 50 m) DEMs were derived using the 'Topo to Raster' function in ESRI ArcGIS 9.1 from the point data obtained from a LiDAR survey conducted in July 2003. The resolution sizes were chosen to offer a wide range between the finest DEM and the coarsest DEM possible for the catchment. A DEM grid-cell resolution coarser than 50 m caused significant changes to the catchment's shape and size and therefore would not have been representative of the original catchment. A resolution finer than 10 m was not used because the number of flowpaths became exceedingly large for the GeoWEPP-SLIP application to the Bowenvale catchment. For all grid-cell resolutions, delineating catchment and sub-catchments, defining flowpaths, and deriving other topographic attributes such as slope, flow accumulation, upslope contributing area were carried out using the methods and the model input parameters described in the previous chapter. The same soil, vegetation and climate input data used for the 10 m grid-cell resolution (Chapter 5) were used for other grid-cell resolutions.

6.4 Results and discussion

6.4.1 Changes in DEM grid-cell resolution

The catchment area changed slightly as a function of input grid-cell DEM resolution (Table 6.1). Total catchment area decreased as the DEM grid-cell resolution was degraded. The average and maximum elevation as well as the standard deviation of the elevation decreased, while the minimum elevation value increased as the resolution became coarser. Figure 6.1 shows slope calculated from different resolution DEMs. Similar trends were observed for slope values in the catchment, i.e., the average slope, standard deviation, and maximum slope values decreased, whereas the minimum values increased with a decrease in resolution. The results are consistent with previous findings (e.g. Claessens et al., 2005; Cochrane and Flanagan, 2005) and attributed to the slope computation method used in GIS. Slope is calculated over a 'slope distance' equal to the DEM resolution or the diagonal distance between grid cells. The changes in topographic attributes such as catchment area, elevation values, and slope are associated with the smoothening effect that occurs when using progressively coarser DEM resolution data in GIS (Wolock and Price, 1994; Zhang and Montgomery, 1994).

Table 6.1: Area, elevation and slope values of the study catchment calculated using different grid-cell resolution DEMs.

Parameter	Resolution			
	10 m	20 m	30 m	50 m
Catchment area, ha	301.20	297.08	295.47	287.00
Maximum elevation, m	492.31	489.07	482.24	481.64
Minimum elevation, m	19.33	18.53	18.68	21.70
Average elevation, m	251.22	249.36	248.46	248.42
Standard deviation of elevation, m	96.87	97.53	97.75	97.11
Maximum slope, °	39.74	35.01	32.46	32.32
Minimum slope, °	0.44	0.26	0.26	0.24
Average slope, °	21.54	20.64	19.83	18.23
Standard deviation (slope), °	6.57	5.92	5.66	5.56

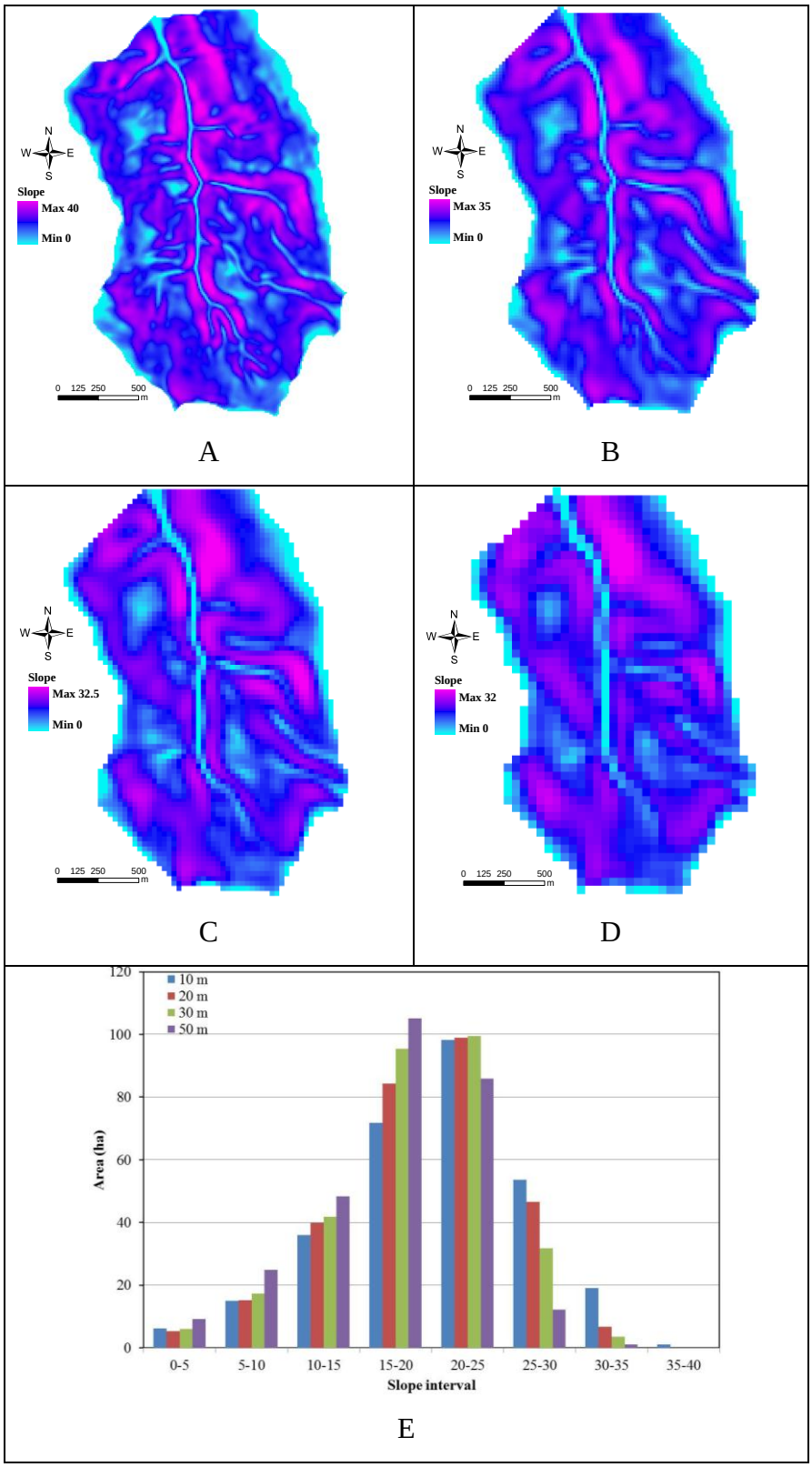

Figure 6.1: Slope values of the Bowenvale catchment for (A) 10, (B) 20, (C) 30, (D) 50 m grid-cell resolutions and (E) slope distribution comparison for these grid-cell resolutions.

The number of flowpaths derived from a finer resolution DEM is higher than for a coarser one because the flowpath width is analogous to the grid-cell size. The average length of the flowpaths increased as the resolution became coarser. Similarly, the length of the largest flowpath also increased but the standard deviation of the flowpath length decreased with coarser resolution DEMs (Figure 6.2). The changes in the lengths of the flowpaths may affect the simulation of hillslope sediment yields when using both the Hillslope and Flowpath methods. Longer flowpaths produced more runoff and consequently more sediment is delivered to the channels. The effect should be more pronounced when using the Flowpath method because erosion simulations are conducted for each individual flowpath in contrast to the Hillslope method where a single representative profile is used to simulate erosion. The following sections will illustrate the effects in detail.

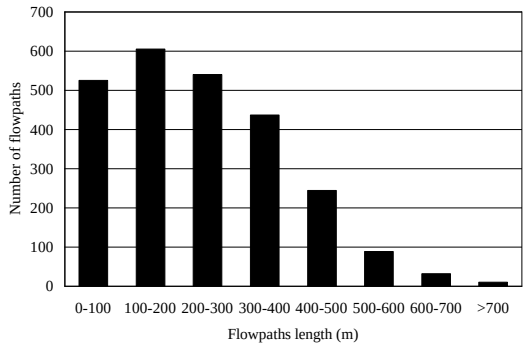

DEM resolution 10 m

Total flowpath number 2481

Largest flowpath length 803 m

Smallest flowpath length 10m

Average flowpath length 243 m

Standard deviation 147 m

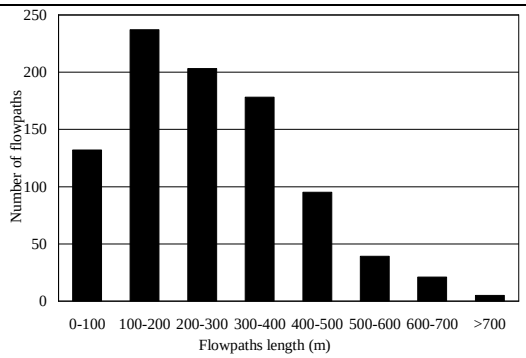

DEM resolution 20 m

Total flowpath number 910

Largest flowpath length 814 m

Smallest flowpath length 20m

Average flowpath length 270 m

Standard deviation 146 m

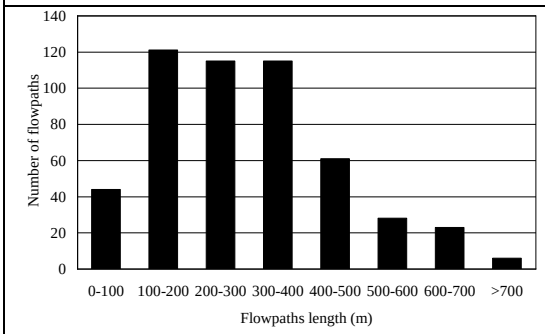

DEM resolution 30 m

Total flowpath number 513

Largest flowpath length 837 m

Smallest flowpath length 30m

Average flowpath length 282 m

Standard deviation 145 m

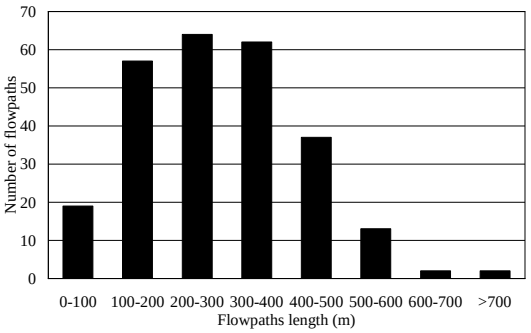

DEM resolution 50 m

Total flowpath number 256

Largest flowpath length 833 m

Smallest flowpath length 50m

Averageflowpath length 313 m

Standard deviation 139 m

Figure 6.2: Distribution of flowpaths lengths using different DEM resolutions for the Bowenvale catchment.

6.4.2 Pre-failure runoff and soil erosion modelling

The Hillslope method was used to simulate the runoff at the catchment outlet for all grid-cell resolutions for the calibration and validation periods. For all simulations, the model's predictive ability was evaluated by comparing the simulated and the observed values of the runoff using three performance indices: (a) the Nash-Sutcliffe coefficient of efficiency (NSI), (b) the index of agreement (IOA), and (c) the root

mean square error (RMSE). Consistent model performance indices for runoff were obtained for all resolutions in the calibration as well as validation periods (Table 6.2); the NSI, IOA and RMSE were quite favourable. The results depict that the grid-cell resolution did not have a significant effect on runoff predictions. Previous studies (e.g. Cochrane and Flanagan, 2005; Zhang et al., 2009) also suggested that using finer DEM resolution did not improve runoff predictions. However, among the four grid-cell resolutions, the 10 m resolution had marginally the overall best model performance indices for both the calibration and validation periods. The 10 m grid-cell resolution results were, therefore, used as baseline for comparison with results using the other grid-cell resolutions.

Table 6.2: Comparison of model performance indices for runoff using different grid-cell resolutions for the calibration (year 2002) and the validation (year 2009) period.

Year	Grid-cell (m)	NIS (%)	IOA(%)	RMSE(m^3/s)
2002	10	79.02	93.53	0.0254
	20	78.35	93.27	0.0259
	30	79.41	93.69	0.0252
	50	77.84	93.28	0.0262
2009	10	58.99	87.94	0.0421
	20	57.46	86.56	0.0439
	30	58.27	87.01	0.0424
	50	56.31	86.77	0.0434

The effects of DEM resolution on runoff from the catchment outlet predicted using the Hillslope method are shown in Figure 6.3, in which the values of runoff simulated by the 10 m grid-cell resolution were compared to predicted runoff using the other grid-cell resolutions. Consistent values of the simulated runoff were noticed when the flows were low. However, some peak flows were slightly affected by the changes in grid-cell size. This means that the resolution issue needs to be more carefully addressed during high flows.

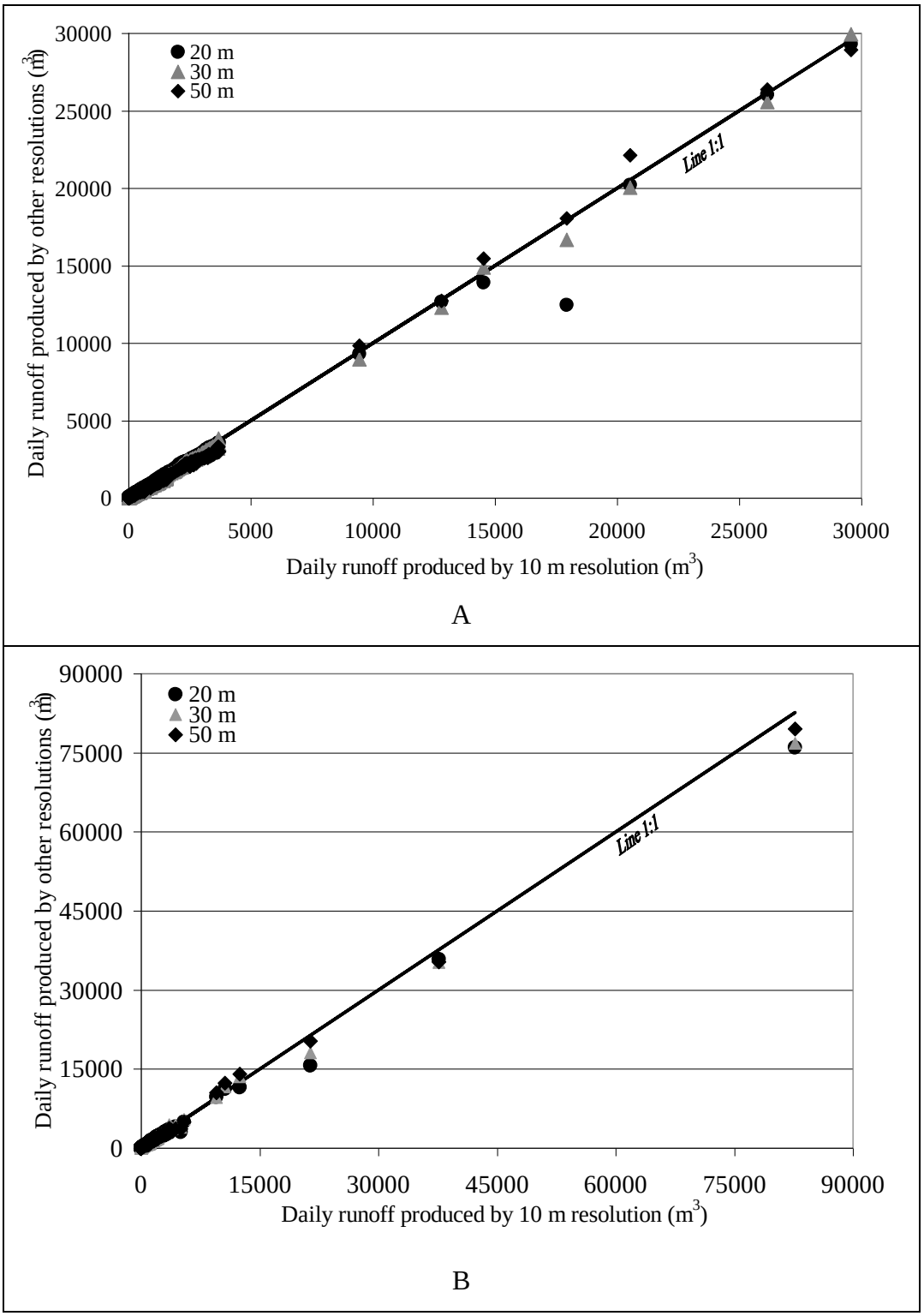

Figure 6.3: Deviation of the simulated runoff due to changes in grid-cell resolution for (A) the calibration period (year 2002), and (B) the validation period (year 2009).

Figure 6.4 shows the cumulative values of the simulated runoff using the Hillslope method for the different grid-cell resolutions compared with the observed cumulative

runoff for the calibration and validation periods at the catchment outlet. The cumulative values of runoff decreased as the DEM resolution became coarser for both calibration and validation periods. This is solely due to the changes in values of slopes and flowpaths as influenced by grid-cell resolution. Slopes were steeper with finer resolution DEMs which resulted in lower amounts of subsurface flows and an increase in runoff. Differences between the cumulative values of the simulated and the observed runoff in the calibration period were minimal; however the differences were significant in the validation period. The significant differences were related to the model under-predicting runoff in various storm events for the validation period. The likely reasons for these under-predictions for the 10 m grid-cell resolution were listed in the previous chapter and the same reasons are expected to cause the under-prediction for the other grid-cells.

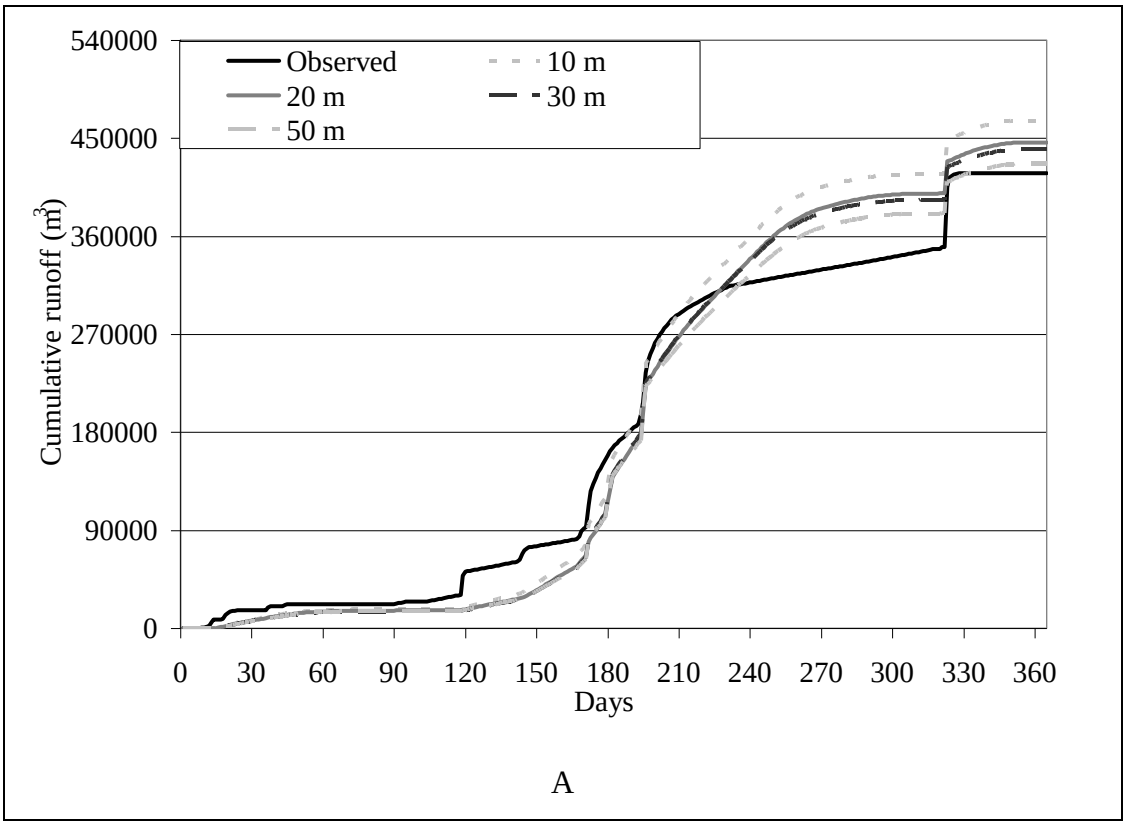

A

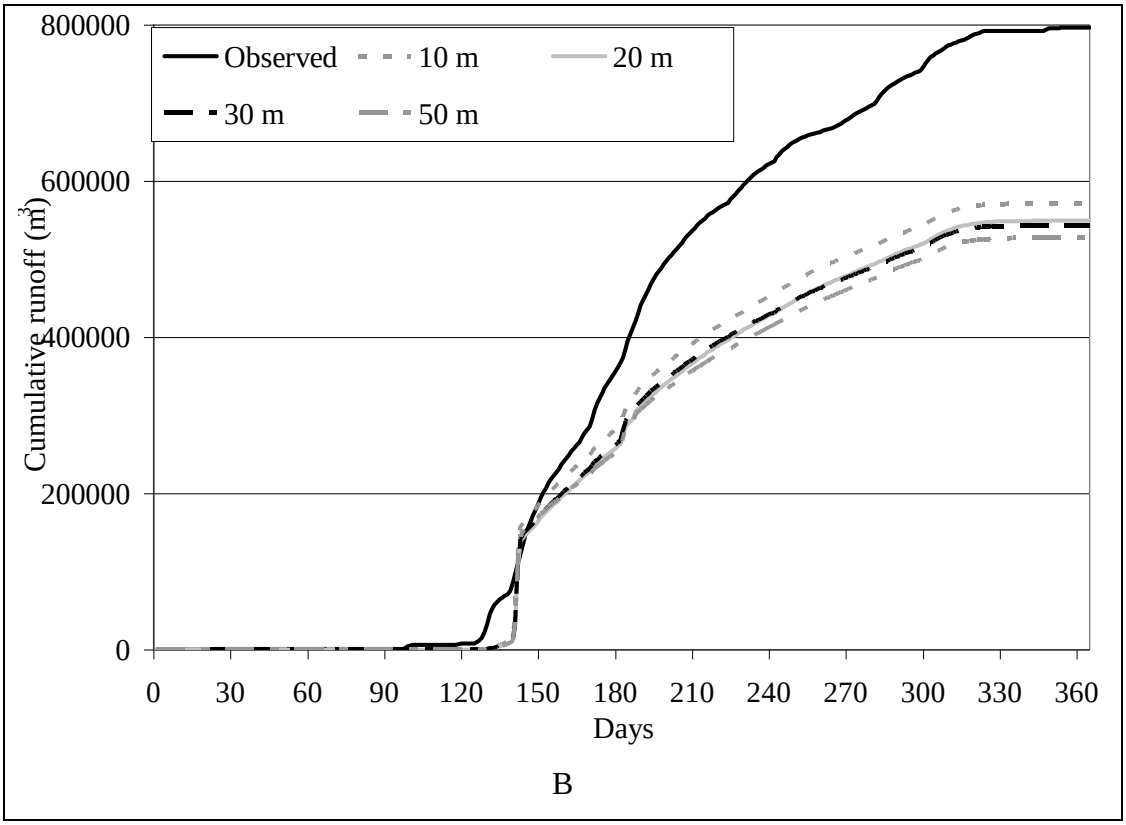

Figure 6.4: Cumulative runoff simulated using different DEM resolutions compared with the observed cumulative runoff at the catchment outlet: (A) for the calibration period (year 2002), and (B) for the validation period (year 2009).

Statistical analyses (T tests) were used to show whether there was a significant difference between the observed and simulated means of runoff. An alpha level of 0.01 (confidence interval of 99%) was used for all T tests to determine whether the difference between the means of one of data events and another was equal to zero or not. Figure 6.5 shows that the T values were smaller than the critical T value for all resolutions in the calibration period implying that there was no significant difference between the observed and the simulated means of the runoff at the 0.01 alpha. However, higher (than the critical) T values in the validation period depict that there was a significant difference between the means. In the calibration period, the T values decreased gradually with an increase in grid-cell size which indicates that the difference of the mean values between the observed and the simulated runoff were lower for simulations with the coarser DEMs. This is additionally supported by Figure 6.4 (A), which shows that the observed cumulative runoff was closer when using the 50 m DEM than to simulations with the other resolution DEMs. On the other hand, the T values increased steadily in the validation period with an increase in grid-cell

size, implying that the difference of the mean values between the observed and the simulated runoff were higher for a coarser than a finer DEM.

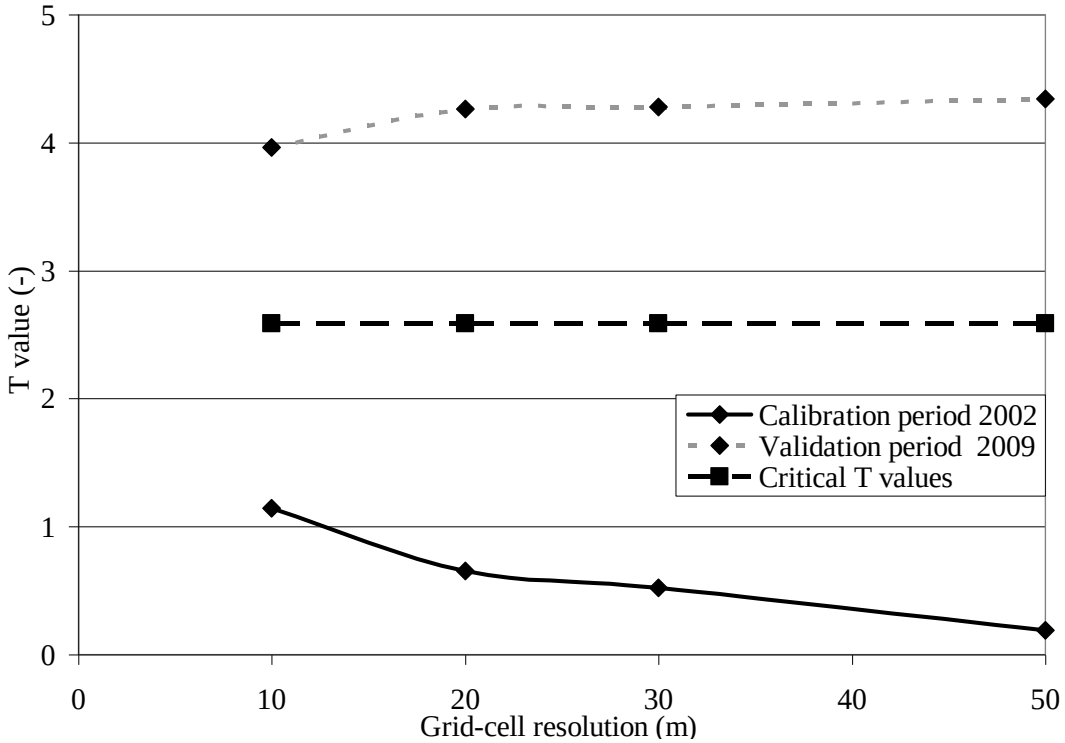

Figure 6.5: Comparison of the T values between the measured and simulated runoff for the different DEM resolutions.

Simulated sediment yields from the catchment outlet with the Hillslope method using each DEM resolution were compared to sediment yields derived from the turbidity observations for the period October-December 2009. Simulated sediment yields for all DEM resolutions were significantly lower than the observed value for the period. The total simulated sediment yields for the period were approximately 10.8, 11.9, 11.8 and 10.7 T using 10, 20, 30 and 50 m DEM resolutions respectively compared to the observed 16 T. Further statistical (T tests) analyses were done to compare sediment yields between simulations using the 10 m DEM and the other DEM resolutions. The results of the T tests showed that there was no significant difference of the mean values of the simulated sediment yield between the 10 m and 50 m DEM resolutions which had a T-value of 0.18 at a 0.01 alpha level. However, there were significant differences in the mean values between the 10 m and 20 m, and the 10 m and 30 m resolutions; the respective T-values were 7.55 and 7.68. The critical T value for these analyses was 2.63.

In contrast with runoff, the DEM resolution affected the sediment yield predictions from the outlet. Figure 6.6 shows a plot of cumulative values of the sediment yield at the catchment outlet using the Hillslope method for the different DEM resolutions for the 2009 simulation year. The shape of the plot for simulations using all DEM resolutions was consistent throughout the year and the values of the cumulative sediment yield were also consistent until the 183rd day (i.e. July 2) of the year. However, the values changed after July 2 with changes in the DEM resolutions. The peak runoff predicted on July 3 and 4 produced different values of sediment yield resulting in distinct changes in the cumulative sediment yield. Using the 30 m DEM produced the highest sediment yields. These results are consistent with the results reported in previous studies (e.g. Cochrane and Flanagan, 2005) which report that simulations with a coarser DEM resolution are more likely to predict higher sediment yields than simulations with finer DEMs. Finer DEM resolutions result in a larger likelihood of deposition areas in the topography whereas coarser DEMs result in smoother topography and thus higher sediment yields. Further statistical analyses were carried out to find out whether there were significant differences in sediment yields between simulations using the 10 m DEM and other resolutions at a 0.01 alpha level. The analyses showed that there were no significant differences of the mean values of the simulated sediment yield between the 10 m and the other resolutions. The T values of these analyses were 0.73, 0.48 and 1.05 respectively while the critical T value which was computed to be 2.60. Consistent soil erosion and runoff prediction using these grid-cell resolutions depicts that grid-cell resolutions have little effect on the calculation of the representative slope profile.

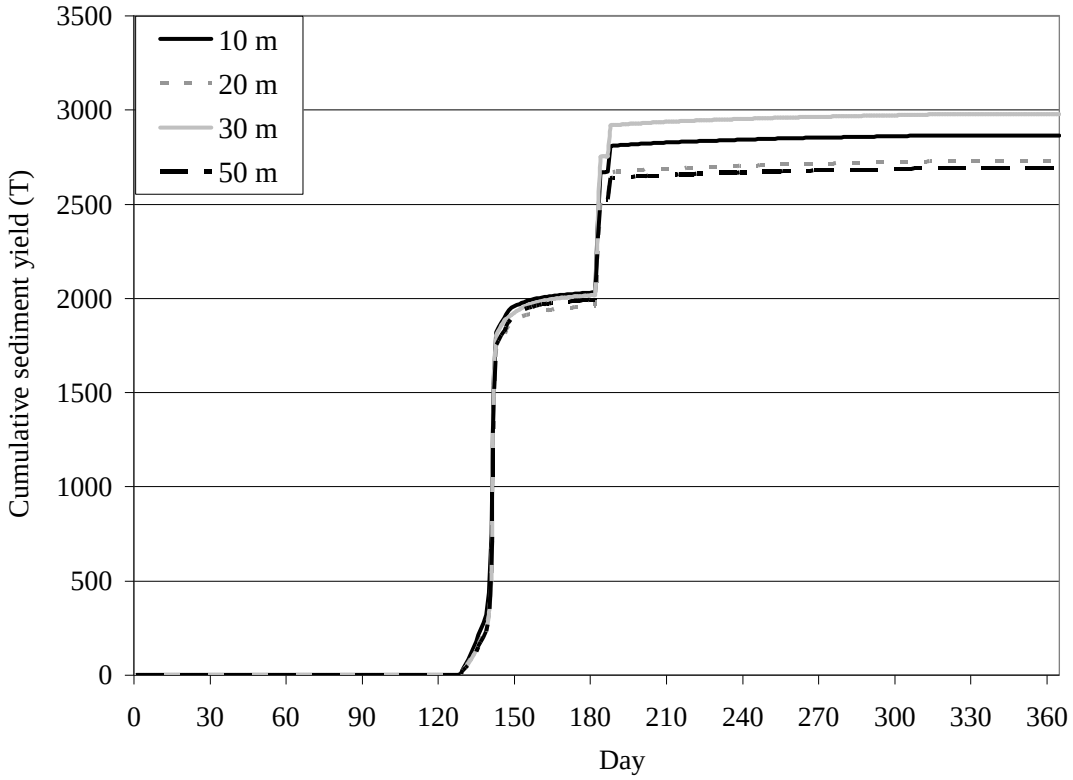

Figure 6.6: Cumulative sediment yield using different DEM resolutions for the 2009 simulation year.

The DEM resolution had various levels of impact on sediment yield predictions from the catchment outlet, hillslope and channels when using the Hillslope method. DEM resolution also affected sediment yields from the hillslope when using the Flowpath method. It is important to note that the Flowpath method does not simulate sediment yields from channels and outlet of the catchment. The Hillslope method produced similar sediment yields at the outlet of the catchment for all DEM resolutions with variation of between 4 and 5% (Table 6.3 and Figure 6.6). The Hillslope method uses a representative slope profile for each sub-catchment and therefore sediment yield prediction is not affected as much as the Flowpath method because an averaging of slopes and lengths occurs to create the representative slope profile. However, contrasting results were obtained for predictions of channel erosion from the Hillslope method. Simulation results showed a decreasing trend in erosion with an increase in grid-cell size; however, simulations with the 30 m DEM resolution resulted in the channel being in deposition mode. The changes in resolutions have an effect on channel lengths and thus sediment yields at the catchment outlet when using the

Hillslope method. At fine resolutions, channels may meander more thus changing the length. This change may also affect the calculation of sub-catchment width and thus length of the representative profile in the Hillslope method. For the Flowpath method, however, there was significant increase in hillslope sediment yield as the grid-cell size was increased. The increase in predicted sediment yields when using coarser grid-cell resolutions may be related to two main reasons. First, this may be due to the process of aggregation; the slope values are averaged out creating a smoother profile. For fine grid-cell resolutions, the topography can have many small changes in slope, which can cause simulated deposition along the flowpaths resulting in lower sediment yield values. Abrupt changes in elevation and slope are reduced at the coarser grid-cell resolution which in turn creates smoother flowpaths and less deposition. End slope conditions of flowpaths are also averaged out and facilitate a smoother delivery to the channel when using coarser grid-cell resolutions. Second, the distribution of flowpath length can have an effect on simulations. With finer DEM resolutions, larger numbers of flowpaths are created and the average length of them is shorter than with coarser resolutions (Cochrane, 1999).

Table 6.3: Sediment yields using different grid-cell resolutions for simulations with the Hillslope and Flowpath methods for the 2009 simulation year.

Method	Grid-cell (m)	Sediment yield (T)			% of catchment area	
		Outlet	Hillslope	Channel	Erosion	Deposition
Hillslope	10	2863.4	2316.2	547.2	74.8	-
	20	2727.2	2354.0	373.2	71.9	-
	30	2974.9	3140.1	-165.2*	63.1	-
	50	2689.4	2594.0	95.4	83.6	-
Flowpath	10	NA	119.5	NA	43.9	4.9
	20	NA	544.3	NA	48.8	3.5
	30	NA	1184.5	NA	55.4	2.6
	50	NA	1647.4	NA	62.4	2.7

NA Not Applicable

* The negative sign represents depositional mode

6.4.3 Landslide and soil redistribution modelling

As illustrated in the previous chapter, the spatial distribution of soil wetness index (i.e. relative water table height) in the catchment for October 28, 2009 was predicted for each grid-cell using the WEPP simulated total soil water content for all flowpaths. Table 6.4 shows the saturated area, maximum, minimum and mean values of the wetness index in the catchment predicted to happen on the day using each of the DEM resolutions. The saturated (i.e. the soil wetness index equating to 1) area was low for a finer resolution and the area increased with the increase in grid-cell size. About 30% of the catchment area was predicted to be completely saturated for the 10 m which increased to about 55% for the 50 m resolution. The minimum and mean values of the soil wetness index in the catchment were significantly higher when using a coarser resolution. A possible explanation for the increase in saturated area using the coarser resolution is that slope and length of flowpaths are affected by resolution. The slopes are steeper in a finer grid-cell resolution DEM. The local topography is one of the main controlling factors in soil moisture distribution; the soil moisture generally decreases with the increase in local slope gradient (Yeakley et al., 1998).

Table 6.4: Variation of soil wetness index in the catchment for the 2009 modelling for different grid-cell resolutions.

Grid-cell	Saturated area (%)	Wetness index (-)		Mean wetness index
		Minimum	Maximum	
10 m	29.16	0.26	1.00	0.85
20 m	40.53	0.52	1.00	0.88
30 m	43.59	0.55	1.00	0.90
50 m	54.38	0.59	1.00	0.93

The changes in the simulated soil wetness index and local slope gradient with changes in grid-cell resolutions had an effect on landslide predictions. The landslide potential area increased from about 1.42 to 1.83% (Table 6.5) of the total catchment area with the increase in the grid-cell size from 10 to 30 m and then decreased to 0.97% at the 50 m resolution level. A smaller landslide area was predicted even though the simulated slopes were steeper for a finer resolution. This may be due to lower values of the simulated soil wetness index (Table 6.4) for the finer resolution. Slopes at the

50 m resolution decreased significantly compared to the other resolutions; the average slope was over 1.5° less in the 50 m than in 30 m resolution. This led to a significant reduction in the shallow landslide potential area even though the 50 m resolution produced the largest saturated area. Table 6.5 and Figure 6.7 compare the observed and the simulated shallow landslides for all the grid-cell resolutions. Smaller numbers of the observed shallow landslides was captured by the model when using the coarser DEM. For example, the model was able to capture 16 observed shallow landslide scars at the 10 m, and the number decreased to 2 when the grid-cell was 50 m (Table 6.5 and Figure 6.7). The results were related to the spatial distribution pattern of the predicted shallow landslides. In a coarser resolution, lower numbers of shallow landslide blocks were predicted which were most commonly delineated near the catchment's outlet and no unstable areas were predicted in the upper catchment where shallow landslide scars are frequently seen (Figure 6.7).

Table 6.5: Predicted landslide distribution and the comparison between observed and the predicted landslides using different grid-cell resolutions from the 2009 modelling

Grid-cell	Stable area (%)	Unstable area (%)	Captured landslides by model
10 m	98.58	1.42	16
20 m	98.29	1.71	9
30 m	98.17	1.83	5
50 m	99.23	0.97	2

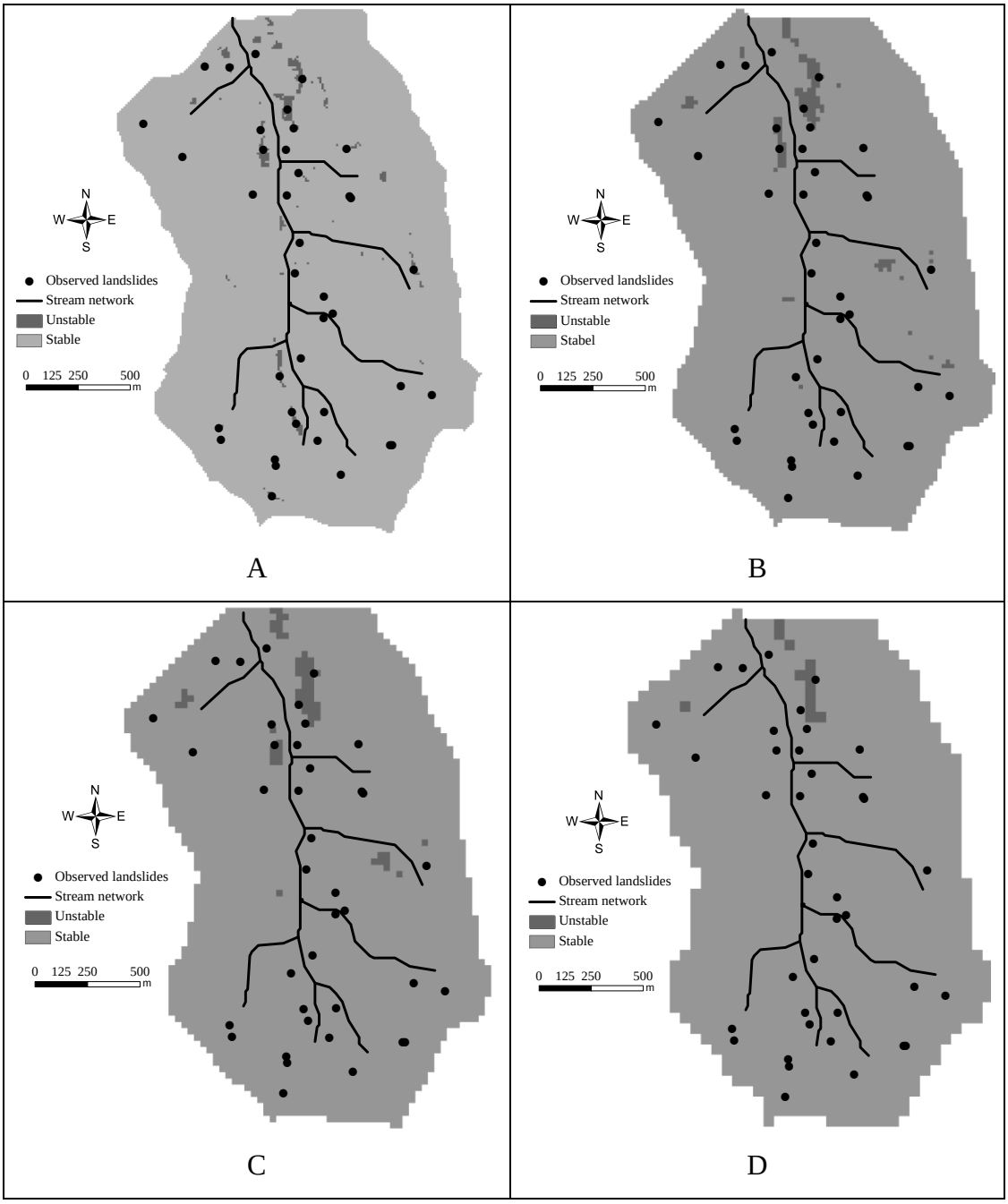

Figure 6.7: Spatial distribution of predicted landslides for (A) 10 , (B) 20, (C) 30 and (D) 50 m grid-cell resolutions overlain with the observed landslide scars.

After modelling the shallow landslide delineated areas in the Bowenvale catchment for the different grid-cell resolutions, the landslide-driven materials and their redistribution were assessed for each resolution using the methods and procedures explained in the previous chapter. The failure and deposition depth, and the increase and decrease in slopes due to landslides and soil redistribution were computed in the catchment for all grid-cell resolutions.

Table 6.6 depicts that the values of predicted maximum failure and minimum deposition depths respectively in failure and deposition areas were not altered by using varying DEM resolutions. However, the DEM resolution significantly affected the minimum failure and maximum deposition depths. The minimum failure depth was higher when using coarser resolutions. These results were due to the influence of grid-cell size on the spatial distribution of shallow landslides and soil wetness index. Higher values of predicted soil wetness index resulted in higher saturated soil and consequently failure depths when using coarser resolutions. The DEM resolution had an opposite effect on the maximum value of deposition depth; the depth decreased with the increase in the grid-cell size.

The changes in the local slopes due to shallow landslides and soil redistribution were low when using a coarser resolution. The changes in the local slopes were computed as the difference in local slopes derived from the existing and the predicted post-failure DEM. The post-failure topography was derived from the algebraic summation of the existing DEM and the failure (-) and the deposition (+) depths. The maximum values of the slope decrease in the failure and increase in the deposition were predicted to be 0.48° and 0.39° respectively for the 50 m while the respective values were 2.53° and 6.41° for the 10 m DEM resolution. The prediction of lower values of the slope change in a coarser resolution is directly related to the GIS procedures to compute the slope. In GIS, local slope is computed over a 'slope distance' equal to the grid-cell size. The shallow landslide and soil redistribution area decreased with the increase in the grid-cell size, for example, about 6% catchment area was predicted to be affected by shallow landslide and soil redistribution for the 10 m which decreased to about 3% for the 50 m resolution. Variations in the spatial distribution pattern of the predicted shallow landslide with the changes in the DEM resolution affected the shallow landslide and soil redistribution area.

Table 6.6: Prediction of failure and deposition depths, changes in slopes in failure and soil redistribution for different grid-cell resolutions.

Parameter	Resolution			
	10 m	20 m	30 m	50 m
Maximum failure depth (m)	1.13	1.13	1.13	1.13
Minimum failure depth (m)	0.29	0.34	0.41	0.45
Maximum deposit depth (m)	1.50	0.48	0.47	0.29
Minimum deposit depth (m)	0.03	0.03	0.03	0.03
Maximum slope decrease in failure zone (°)	2.53	1.22	1.13	0.48
Maximum slope increase in deposition zone (°)	6.41	1.54	0.81	0.39
Area affected by landslide and redistribution (%)	5.84	5.76	5.69	3.16

Figure 6.8 presents a comparison between the predicted failure and deposition volume for the different DEM resolutions. The failure volume increased with an increase in the grid-cell size. This is because higher landslide potential areas and failure depths (Table 6.6) were predicted due to higher soil saturation prediction with coarser resolutions. The deposition volume, on the other hand, decreased with an increase in grid-cell size indicating that a greater portion of the failure volumes could be transported to the nearest stream network. The results may be inferred to the spatial distribution pattern of the predicted shallow landslides. As stated earlier, more landslide areas were spatially distributed in the lower catchment for the coarser resolution which could be easily routed to the stream network.

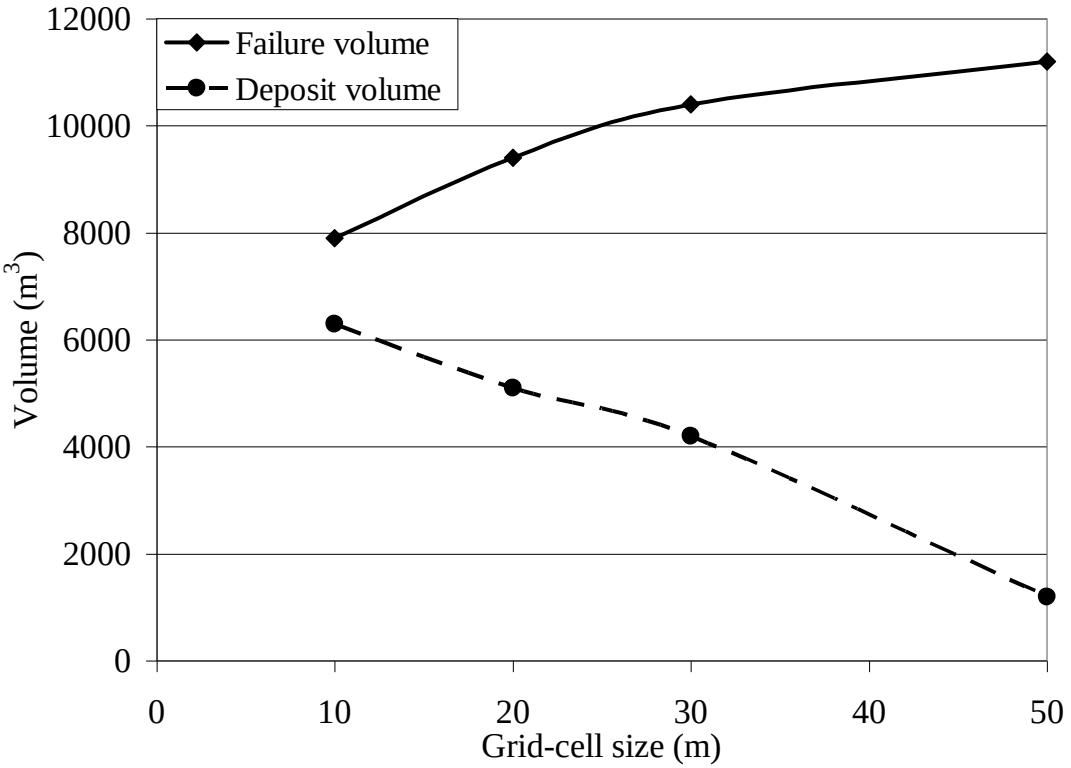

Figure 6.8: Total failure and deposition volumes predicted in the catchment for the different grid-cell resolutions with the GeoWEPP-SLIP modelling approach for the 2009 simulation year.

6.4.4 Post-failure scenario due to land management and topography changes

Post-failure changes in soil erosion were evaluated using all DEM resolutions for two scenarios: (a) 'case a': vegetation not re-established (long-term fallow), and (b) 'case b': re-establishment of vegetation in the failure and deposition areas. The post-failure soil erosion and runoff were evaluated for the same simulation year 2009 to compare them against the simulation results for the original topography and land-cover, which is termed as the 'base case' condition. Values of the predicted runoff at the catchment outlet using the Hillslope method in 'case a' and 'case b' scenarios for all the grid-cell resolutions were compared with the 'base case' runoff for the 10 m DEM resolution (Figure 6.9). A first visual interpretation of the comparison shows that there were no significant differences in runoff between the post-failure (i.e. 'case a' and 'case b') scenarios for different resolutions and the 'base case' scenario for the 10 m grid-cell when the flows were low. However, peak flows for 'case a' and 'case b' using the coarser grid-cell resolutions were lower than the 'base case' peak flows calculated

using the 10 m DEM resolution. These results were comparable with the runoff predictions from the coarser resolutions in the pre-failure (i.e. 'base case') scenarios for the different DEM resolutions as illustrated in Figure 6.3.

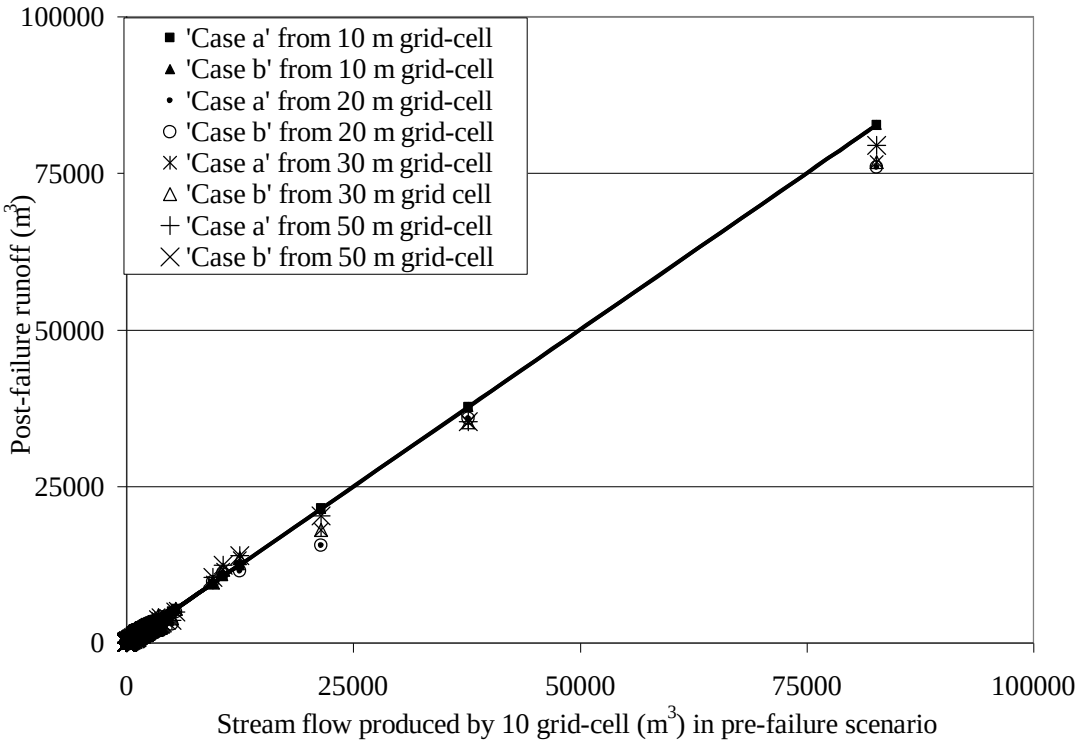

Figure 6.9: Deviation of the simulated post-failure runoff due to changes in grid-cell resolutions.

Statistical analyses (T tests) were done to find out whether there was a significant difference of simulated runoff between the 'base case' for the 10 m and the post-failure ('case a' and 'case b') scenarios for all the grid-cell resolutions at the catchment outlet with the Hillslope method. An alpha level of 0.01 (confidence interval of 99%) was used for all the T tests to determine whether the difference between means was equal to zero or not. The T values were smaller than the critical T values for finer grid-cell resolutions (Figure 6.10). The smaller T values in the finer (than 20 m) DEM resolutions indicate that there was no significant difference between the means of the simulated runoff for the10 m grid-cell size in the 'base case' scenario and for the 10 and 20 m grid-cell resolutions in 'case a' and 'case b' (i.e. post-failure) scenarios. However, the values were higher than the critical T value for the coarser grid-cell resolutions which indicate that the mean values of runoff for 'case a' and

'case b' (post-failure) scenarios for the coarser (than 30 m) grid-cell resolutions were significantly deviated from the 'base case' runoff for the 10 m grid-cell resolution.

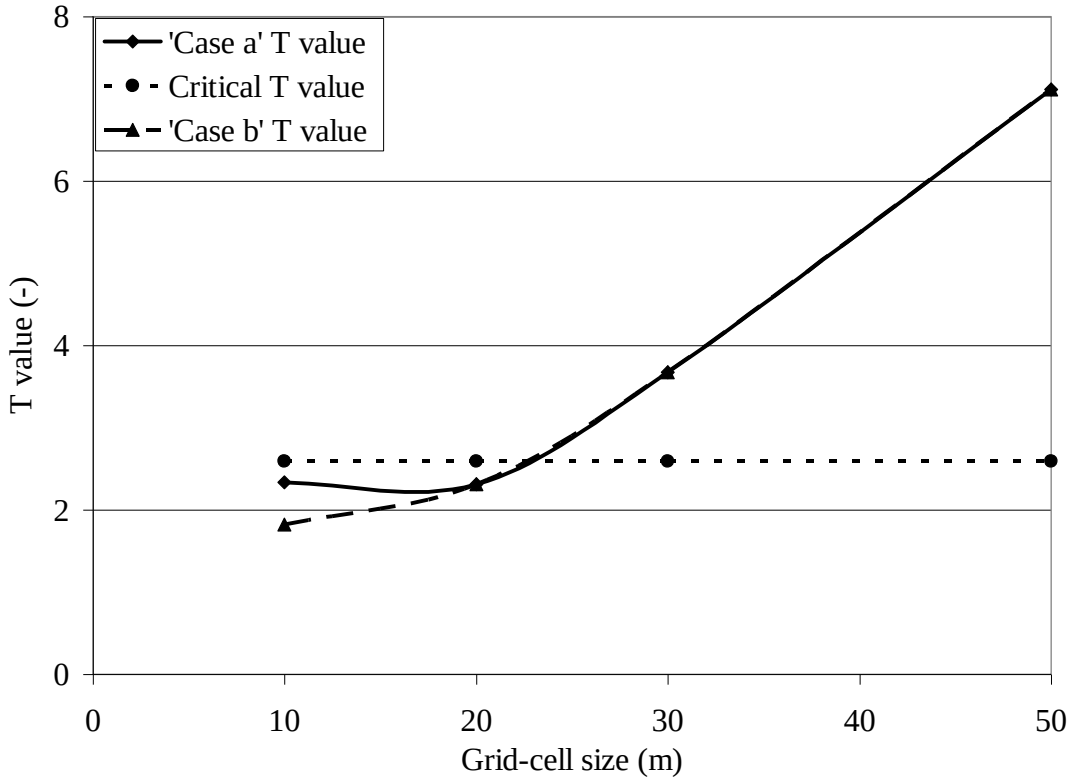

Figure 6.10: Comparison of the T values for the simulated runoff between the 'base case' scenario using the 10 m grid-cell and the post-failure (the 'case a' and 'case b') scenarios for all grid-cell resolutions.

Table 6.7 presents soil erosion and deposition in the post-failure ('case a' and 'case b') scenarios and the results were compared with the 'base case' for all the grid-cell resolutions using both the Hillslope and Flowpath methods. Within a particular DEM resolution level, the Hillslope method predicted consistent post-failure ('case a' and 'case b') sediment yields at the catchment outlet, hillslope and channel compared to the 'base case' scenario. It was also noticed that the sediment yield prediction using the Hillslope method was not affected by the DEM resolution in the post-failure ('case a' and 'case b') scenarios for all grid-cell resolutions. This is related to the sediment yield simulation procedures in the Hillslope method. The Hillslope method simulates the sediment yield using a representative slope profile for a sub-catchment. The length and slope of the profile are derived by weighting all flowpaths in the sub-catchment (Cochrane and Flanagan, 1999). The dominating soil and management of the sub-catchment are lumped in the entire profile. The post-failure patches of the

bare soils were not captured by a representative profile with the Hillslope method. However, the hillslope sediment yield prediction was significantly affected by the grid-cell resolution for the Flowpath method. The Flowpath method predicted significantly higher values of the hillslope sediment yield for ‘case a’ than for the ‘base case’ and ‘case b’.

As previously stated, in the Flowpath method, erosion simulations are done for each flowpath in the catchment. This means all the spatial data, including the locations of post-failure bare soil, are well represented by the method. The Flowpath method predicted slightly higher values of hillslope sediment yield in ‘case b’ than in the ‘base case’ (Table 6.7). As discussed in the previous chapter, the likely reasons for this were the changes in topography in the failure and deposition areas, and increase in the flowpath numbers in the post-failure scenarios. However, the influence of the increase in flowpath numbers in the post-failure (‘case a’ and ‘case b’) scenarios was not valid for the other grid-cell resolutions (i.e. 20, 30 and 50 m). This is because there were no changes in the flowpath numbers in the post-failure scenarios compared to the ‘base case’ for these resolutions. Therefore, the slightly higher prediction of hillslope sediment yields with the Flowpath method in ‘case b’ for the other grid-cells was entirely attributed to the changes in topography due to shallow landslides and soil redistribution.

Table 6.7: Comparison of sediment yields from the catchment outlet, hillslopes and channels, using the Hillslope and Flowpath methods with the 'base case', 'case a' and 'case b' scenarios for the different grid-cell resolutions. Data from 2009 was used for all simulations.

Method	Grid-cell (m)	Scenario	Sediment yield (T)			% catchment area	
			Outlet	Hillslope	Channel	Erosion	Deposition
Hillslope	10	Base case	2863.4	2316.2	547.2	74.9	-
		Case a	2916.5	2366.3	550.2	74.9	-
		Case b	2902.2	2306.0	596.2	74.9	-
Hillslope	20	Base case	2727.2	2354.0	373.2	71.9	-
		Case a	2752.8	2350.5	402.3	71.9	-
		Case b	2752.8	2350.5	402.3	71.9	-
Hillslope	30	Base case	2974.9	3140.1	-165.2*	63.1	-
		Case a	2971.5	3133.9	-162.4*	63.1	-
		Case b	2971.5	3133.9	-162.4*	63.1	-
Hillslope	50	Base case	2689.4	2594.0	95.4	83.6	-
		Case a	2689.5	2594.4	95.1	83.6	-
		Case b	2689.5	2594.4	95.1	83.6	-
Flowpath	10	Base case	NA	119.5	NA	43.9	4.9
		Case a	NA	641.5	NA	46.1	6.5
		Case b	NA	121.0	NA	44.0	4.9
Flowpath	20	Base case	NA	544.3	NA	48.8	3.5
		Case a	NA	1787.2	NA	53.0	4.9
		Case b	NA	544.9	NA	50.7	3.6
Flowpath	30	Base case	NA	1184.5	NA	55.4	2.6
		Case a	NA	4710.7	NA	56.8	3.3
		Case b	NA	1185.7	NA	55.5	2.6
Flowpath	50	Base case	NA	1647.4	NA	62.4	2.6
		Case a	NA	4446.0	NA	63.1	2.8
		Case b	NA	1647.7	NA	62.4	2.6

NA Not Applicable

* The negative sign represents depositional mode

6.5 Summary and conclusions

The GeoWEPP-SLIP model was applied to the Bowenvale catchment using four different (10 m, 20 m, 30 m and 50 m) grid-cell resolutions. Four different components were modelled: (a) runoff and soil erosion in the pre-failure scenario, (b) spatial distribution of shallow landslides and their mobilisation, (c) changes in local topography due to the predicted shallow landslides and their mobilisation, and (d) runoff and soil erosion in post-failure scenarios due to changes in the topography and land-cover following landslide and soil redistribution. The pre- and post-failure soil erosion and sediment yield were modelled using the Flowpath and Hillslope methods. The post-failure scenarios were further categorised into two scenarios: (a) vegetation not re-established (long-term fallow), and (b) re-establishment of vegetation in failure and deposition areas.

The results of this study showed that in general pre- and post-failure soil erosion and runoff predictions at the catchment outlet using the Hillslope method were not significantly changed by input DEM resolution. This implies that a wide range of resolutions can be used for runoff and sediment yield predictions from the catchment outlet.

The sediment yield predictions from only hillslopes for the different resolutions showed that the Hillslope method is consistent regardless of changes in grid-cell resolution. However, hillslope sediment yield predictions with the Flowpath method were influenced by the difference in local slopes, flowpath lengths and size of the catchment. A finer resolution produced substantially lower hillslope sediment yields than a coarser one.

The changes in the local slopes and flowpath lengths as a result of changes in grid-cell resolution affected the soil moisture simulation which altered shallow landslide predictions. Higher soil saturation was obtained due to lower values of the local slopes when using coarser grid-cell resolutions. This resulted in higher landslide potential area and volume. The changes in the DEM resolution altered the spatial distribution pattern of the predicted landslides; decreasing the number of actual landslides captured by the model as resolution became coarser.

The post-failure scenarios sediment yield and runoff at the catchment outlet did not significantly differ from pre-failure scenario sediment yield and runoff when using the Hillslope method. The impact of changes in topography and land-cover due to shallow landslide and soil redistribution modelling was not significant at any resolution. This is because the Hillslope method computes soil erosion using a representative profile for each sub-catchment and the changes in topography and land-cover due to shallow landslides are masked in the profile. The Flowpath method on the other hand predicted significantly higher hillslope sediment yields for all grid-cell resolutions in the post-failure scenarios when vegetation was not re-established. Sediment yield increased with an increase in grid-cell size. This implies that the changes were well captured in the flowpaths passing through the bare soil area. Using the Flowpath method is therefore important for the post-failure soil erosion modelling.

It is therefore suggested that a grid-cell resolution should be chosen according to the simulation needs of the user. If only runoff and or sediment yields from a catchment outlet are needed, it is not necessary to have very fine resolution DEMs. This reduces the cost of creating a high resolution DEM. However, the grid-cell resolution significantly affected the hillslope sediment yields with the Flowpath method. The resolution issue needs to be properly addressed for soil erosion modelling with the method. The study of the interaction between resolution and landslide and soil redistribution prediction is also important. It suggests that the landslide predictions are better when using finer resolution DEMs. The predicted landslides were better matched with the actual landslide scars when a fine grid-cell resolution was used. Therefore, application of a fine grid-cell resolution is recommended for soil moisture, landslide and soil redistribution modelling.

Chapter 7 Summary, Conclusions and Recommendations

This final chapter summarizes the methods developed throughout the thesis and the results obtained from experiments and modelling. The most important conclusions from this thesis together with limitations of the methods and further research are presented.

7.1 Summary

Research was conducted with the objectives of studying water-induced shallow landslides, and soil erosion following shallow landslides. To fulfill the objectives, laboratory and catchment-scale studies on shallow landslides and soil erosion were conducted. A laboratory scale landslide soil erosion flume setup was used to study the shallow landslides and post-failure soil erosion using sandy and silty loess soils. An integrated shallow landslide soil erosion modelling approach was validated using the loess soils experimental results. The approach was extended to a catchment-scale and applied to the Bowenvale research catchment using GIS and different grid-cell resolutions. A summary of specific objectives, methods, and experimental and modeling results are presented in the following sections.

7.1.1 Variation in sediment yields during and after shallow landslides

The first two objectives of this research were: (a) to quantify the impact of shallow landslides on sediment yields, and (b) to study the changes in sediment yields due to changes in local slopes following landslides. Laboratory scale landslide soil erosion experiments were conducted to meet these objectives. A two-sloping experimental flume together with a rainfall simulator was used to trigger shallow landslides and to quantify the sediment yields during failures. Shallow landslides were triggered in two different soils: sandy and fine grained silty loess. A total of 18 experiments (6 in sandy and 12 in loess soils) were conducted in the flume out of which 10 shallow landslides were triggered (6 in sandy and 4 in loess soils). In all experiments, landslide initiation, their retrogressions and slip surface depths were monitored by both direct observations as well as by video camera recordings. Sediment and runoff were collected from the flume outlet every minute during landslides and every 10 minutes before and after landslides. Changes in the soil slope after landslides were recorded.

The sandy soil experimental results revealed that slope failure initiation and retrogressions were influenced by the depth of the soil profiles. The shallower profiles were not only quicker to initiate failures but also more frequent to retrogress than the deeper ones. The initial slip surface depth was also related to the soil profile depths; the initial slip surface depth decreased with the increase in the soil profile depth. Pre-failure sediment discharges were very low and limited to the finer soil particles as would be expected for a sandy soil. However, subsequent variations in the sediment discharge were strongly related to the failure events and their proximity to the outlet. The sediment yields were also affected by the original soil depths; the greater the depth, the higher the sediment yields. Post-failure reductions in sediment discharge were observed and attributed to the post-failure slope stabilisation under continuing rainfall and extensive soil armouring near the flume outlet.

Shallow landslides were triggered in the four of the 12 experiments using silty loess soil. These experimental results showed that peak sediment discharges were observed in response to slope failures and were related to the location of the slope failures, their retrogression, failure volume and the slope gradient of both flume sections; higher peaks were observed if the slope failures occurred closer to the outlet. Failure and transport of materials due to slope failures decreased the slope gradient in the failure area and increased in the deposition area. In active landsliding experiments, post-failure sediment discharge decreased as a function of the evolution of new hillslope after slope failures.

7.1.2 Development of integrated modelling approach

The third objective of the research was to propose and develop an integrated approach for soil erosion, shallow landslide and soil redistribution modelling. The integrated modelling approach integrates a physically-based soil erosion model with a landslide model and a simple rule based soil redistribution model. The modelling approach was validated from the failure and non-failure flume experiments using silty loess soil. It was noticed that the simulated runoff and sediment yields in the pre- and post-failure events were in good agreement with the respective observations in those events. The landslide and soil redistribution models also worked reasonably well in these experiments.

The hillslope 2D version of the integrated modelling approach was extended to a catchment-scale 3D application using GIS which was referred to as GeoWEPP-SLIP model. In the GeoWEPP-SLIP model, the WEPP-GIS extension i.e. GeoWEPP was used for the pre- and post-failure soil erosion and surface runoff modelling; an infinite slope method of the slope stability analysis coupled with the WEPP Hillslope hydrology for landslide prediction, and a simple rule based soil redistribution model to predict the mobilisation. The modelling approach was applied to the Bowenvale research catchment (300 ha) in Christchurch, New Zealand. Soil erosion and runoff were modelled for various simulation (calibration and validation) periods using the Hillslope and Flowpath methods. Landslide modelling was done for the 2009 soil moisture simulation using WEPP in all flowpaths of the catchment. The predicted landslides were compared with the landslide inventories prepared during 2008-2010 field surveys. The application of the model to the Bowenvale showed that the prediction of runoff, sediment yields and landslide distributions were in good agreement with the respective observed values. The Hillslope method predicted consistent values of sediment yield and soil erosion regardless of changes in topography and land-cover in the post-failure scenarios due to shallow landslides and soil redistribution modelling. The Flowpath method, however, was sensitive to the changes in the post-failure scenarios.

7.1.3 Influence of grid-cell resolution

The last aim of the research was to evaluate the GeoWEPP-SLIP model using different input grid-cell resolutions. The model was applied to the Bowenvale research catchment using four different DEM resolutions (10, 20, 30 and 50 m). Results of the study showed that using finer DEM resolution did not significantly change the sediment yield and runoff results between pre- and post-failure scenarios at the catchment outlet using the Hillslope method. However, changes in grid-cell sizes affected the hillslope sediment yield prediction for the Flowpath method; the Flowpath method predicted higher sediment yields at a coarser resolution level. The changes in grid-cell resolution also significantly altered the landslide distribution, area and volume; higher landslide area and volume were predicted using coarser resolutions. Mobilisation of landslide materials also changed with the grid-cell resolution; the deposition volume decreased with an increase in grid-cell size.

7.2 Conclusions

Landslide soil erosion studies and research conducted in the laboratory and catchment presented in this thesis helped to understand the interactions between shallow landslides and soil erosion and resulted in the following conclusions and contributions to science:

Landslide soil erosion flume experiments using sandy soils provided additional data on of mechanisms and conditions leading to water-induced shallow landslides in soil profiles of different depths. These experimental results illustrated actual slope failure initiation and retrogression processes under continued rainfall. The results are important because sediment discharge patterns were related to landslide initiation and retrogression. The results demonstrated how shallow landslide events alter the local slope gradient and long-term soil erosion. Additionally, the results showed that slope failure initiation, retrogressions and sediment discharge during and after slope failures were affected by the original soil profile depths which had not been previously reported in literature.

Studying shallow landslide and soil erosion processes from flume experiments using loess soil provided additional data and information on the effects of soil porosity and soil compaction on pore pressure generation and slope failure initiation. Low soil porosity prohibited the generation of sufficient pore pressure required to trigger slope failures in the first 8 of the 12 experiments. However, these non-failure experimental results were useful to calibrate and validate the integrated model in non-failure events and the sediment yields from these experiments were useful to compare with the sediment yields from the failure ones. The comparisons showed that the post-failure sediment yields were on average about 10% (ranging from about 6 to 12%) less in the failure experiments than in the non-failure experiments. These were mainly due to changes in local slope gradient following landslides. The experimental results were used to successfully evaluate the integrated modelling approach to simulate runoff and soil erosion in both pre- and post-failure events, to predict shallow landslides, and to estimate changes in local slope gradient after shallow landslides.

A unique integrated modelling approach (GeoWEPP-SLIP) was proposed to model soil erosion, shallow landslides and soil redistribution at a catchment-scale using GIS tools. An advantage of the integrated modelling approach is that both the soil erosion and shallow landslide models share the same hydrology, which is based on the WEPP's continuous water balance simulation. The continuous water balance simulation enables landslide predictions over time as soil moisture levels fluctuate due to rainfall, vegetation covers and other parameters. The integrated modelling approach simulates landslides and hillslope soil erosion which are the main sources of sediment supply in mountainous and hilly catchments. A case study application of the model to the Bowenvale catchment showed that the approach may be useful for studying the impact of shallow landslides on long-term sediment yields in hilly and mountainous catchment. The application of GeoWEPP-SLIP to the Bowenvale catchment is intended to demonstrate its predictive ability in terms of soil erosion, runoff and shallow landslides. The results of the integrated modelling approach are promising indicating that the approach may be useful for management applications and decision makings dealing with water-induced hazard (soil erosion and shallow landslides) mitigations.

The study of using different grid-cell resolutions for simulations has resulted in a better understanding of the importance of digital elevation models in modelling landslides and soil erosion with GIS. It also contributed to better understanding of the limitations of practical applications of the GeoWEPP-SLIP modelling approach. The results of the study showed that it is not necessary to use very fine grid-cell resolution for surface runoff and soil erosion modelling at the catchment outlet using the Hillslope method. However, resolution issue needs to be addressed for the hillslope soil erosion and sediment yield simulations using the Flowpath method; results are much improved with finer DEM resolutions. The study also showed that the grid-cell resolution has to be carefully chosen for soil moisture, landslide and soil redistribution modelling. The spatial distribution of the predicted landslides using a finer DEM resolution better matched actual landslide scars than when using a coarser grid-cell resolution.

7.3 Recommendations for further research

The research conducted in this thesis has resulted in new and useful data, which produced results and conclusions on water-induced soil erosion, shallow landslide and soil redistribution processes. However, the original research questions and objectives have in turn raised new questions, for which additional research has to be conducted. Some relevant ideas for additional research are listed below.

7.3.1 Landslide soil erosion studies from flume experiments

In most of the previous laboratory scale landslide studies using sandy soil, shallow landslides were generally triggered in single sloped flumes of about 30° slope (e.g. Iverson et al., 2000; Wang and Sassa, 2003; Lourenco et al., 2006). In the present research, flume experiments were conducted with slopes of 30° in the upper and 10° in the lower flume sections. Although these experiments provided useful data on shallow landslide and soil erosion processes, it is also important to study the processes in other sloping configurations. Changing the flume slopes would provide different results of sediment discharges and sediment yields before, during and after slope failure events. For cohesionless sandy soils, appropriate slopes could range from 25-35° to trigger slope failure in the upper section and 5-15° for deposition in the lower flume sections to study shallow landslide soil erosion processes within a reasonable experimental timeframe. Alternative slope configurations and soil depths could also be studied.

In all loess soil experiments, the soil profile depth was shallow (100 mm). As illustrated in the previous sections and also in Chapter 3, an original soil profile depth is an important parameter which affects slope failure initiation, retrogression, soil redistribution and sediment yields during and after shallow landslides. It is, therefore, imperative to conduct silty soil experiments for deeper profiles and to compare the results with the ones presented in this thesis. Experimentation in deeper soil profiles is however highly labour intensive. Triggering slope failures in fine grained deeper soil profiles within an experimental timeframe requires additional work to achieve soil saturation level required to trigger slope failures. Special set-up is needed to achieve homogenous soil saturation in an entire profile of a deeper soil. Installation of

additional soil moisture sensors would be useful to closely monitor the soil saturation processes.

There has been a considerable amount of research conducted in understanding water-induced shallow landslides using sloping flumes with higher rainfall intensity (e.g. Wang and Sassa; 2001, 2003; Okura et al., 2002; Lourenco et al; 2006). Moderate rainfall intensity was applied in the experiments presented in this thesis. Study of post-failure soil erosion in the higher rainfall intensity is, however, still lacking. It is therefore recommended to conduct further landslide soil erosion experimentations to study soil erosion in both pre- and post-failure periods using higher rainfall intensity because rainfall intensity affects landslide, soil erosion and soil armouring.

In this research, runout distances for silty soil experiments were predicted using a simple rule-based empirical model. In contrast, physically-based models were used for soil erosion and shallow landslide predictions. Further research is therefore sought to use a physically-based runout distance model in the integrated modelling approach. A physically-based runout distance model should be handled carefully because it generally requires a detail investigation on rheological properties such as viscosity, velocity and stresses of the failure materials of the individual slope failures.

7.3.2 Soil erosion shallow landslide modelling using GeoWEPP-SLIP

The landslide modelling of GeoWEPP-SLIP is based on the WEPP's simulation of total soil water content for each flowpath of a catchment. The maximum value of the total soil water content was manually attributed from each flowpath simulated to each grid-cell. Thus, simulating and attributing the maximum value of the total soil water content to each grid-cell of a catchment was extremely time consuming job particularly for a fine grid-cell resolution. It is therefore essential to develop an automated tool that could be used to simulate and attribute the value of the peak soil water content for each grid-cell for a defined simulation period. The automated tool may be developed within the framework of GeoWEPP (WEPP-GIS interface). The tool would first simulate the soil water content, extract peak values of soil water content and then attribute to the respective grid-cells for landslide modelling. The automated tool would reduce the simulation time required in the GeoWEPP-SLIP

model, but using a range of simulated high water content values could also be useful for more detailed studies.

Since only 10 unique management and soil combinations are allowed for a hillslope profile (flowpath in this case) in the WEPP simulation, the total soil water content simulation in each grid-cell of a flowpath was computed in a unique way. In a longer flowpath, the total soil water was attributed to each grid-cell by linearly interpolating the WEPP simulated soil water content. A detail description of the interpolation method was illustrated in Chapter 5. The interpolated total soil water content may not necessarily represent the actual WEPP simulated total soil water content. Further research is therefore needed to increase the maximum allowable management and soil combinations in WEPP. This would help simulate the total soil water content that could be attributed in each grid-cell of longer flowpaths without approximations.

Additional research is also needed on other scale applications under a wide range of landslide scenarios. Validating landslide and soil redistribution could be done by studying in a small scale catchment application where landslides and their mobilisation are frequently observed. Changes in local topography due to landslides and soil redistribution could also be studied from surveyed time series DEMs which may also be used to validate the predicted post-failure topography.

The integrated modelling approach proposed in this thesis covers the modelling of hillslope soil erosion, landslide and soil redistribution. However, the approach does not simulate some other important sediment sources such as road and channel erosion. Additional research is relevant to integrate road and channel erosion models. Modelling road erosion using WEPP could be found in the research of Elliot and Tysdal (1999), Tysdal et al. (1999) and Cochrane et al. (2007a).

When soil is removed and redistributed on hillslopes, it is known that both geotechnical and hydrological behaviour are altered. In the present study, the post-failure soil erosion was evaluated in two scenarios: vegetation not re-established, and vegetation re-established in the failure and deposition areas. It was demonstrated that soil erosion and sediment yields were high in the scenario where vegetation was not re-established due to changes in land-cover resulted in from the landslide and soil

redistribution. Soil erosion was low when the vegetation was fully re-established. The vegetation re-established scenario was based on the assumption that the areas regain their full cover in a short time and thus prevent soil erosion. Further research is required to study changes in soil erosion pattern between vegetation not re-established and vegetation fully re-established scenarios. This would provide data on how the vegetation growth would impact soil erosion and sediment yields in response to time.

The effect of grid-cell resolution on the GeoWEPP-SLIP model was evaluated using four resolutions (10, 20, 30 and 50 m). The study showed that soil erosion, shallow landslide and soil redistribution modelling was significantly affected by the resolution. The observed landslides were better captured at the 10 m resolution level. It may therefore be expected that a resolution finer than 10 m would further improve the simulation of spatial distribution patterns of shallow landslides in comparison to the observed ones. However, to run simulations with the Bowenvale catchment using finer DEM resolutions would require modifications to the current model. Components of the model, such as GeoWEPP, have limitations on the number of flowpath that can be simulated during a model run which are exceeded when using anything equal to or lower than a 5 m grid cell DEM. It is therefore recommended that improvements in the model be made to allow simulations with finer DEM resolutions for similar or larger catchment sizes.

References

Abbott, M.B., Bathurst, J. C., Cunge, J. A., O'Connell, P. E., Rasmussen, J., 1986a. An introduction to the European Hydrological System—Syste`me Hydrologique Europe´en, 'SHE.' 1: History and philosophy of a physically-based, distributed modelling system. Journal of Hydrology, 87(1-2): 45–59.

Abbott, M.B., Bathurst, J.C., Cunge, J.A., O'Connell, P.E., Rasmussen, J., 1986b. An introduction to the European Hydrological System-Systemme Hydrologique Europeen, 'SHE', 2: Structure of a physically-based, distributed modelling system. Journal of Hydrology, 87(1-2): 61–77.

Abernethy, B., Rutherfurd, I.D., 2001. The distribution of strength of riparian tree roots in relation to riverbank reinforcement: soil mechanics and geotechnical controls of channel and hillslope processes. Hydrological Processes, 15: 63-79.

Acharya, G., Smedt, F., Long, N.T., 2006. Assessing landslide hazard in GIS: a case study from Rasuwa, Nepal. Bulletin of Engineering Geology and the Environment, 65: 99-107.

Adams, R., Elliott, S., 2006. Physically based modelling of sediment generation and transport under a large rainfall simulator. Hydrological Processes, 20: 2253-2270.

Aleotti, P., Chowdhury, R., 1999. Landslide hazard assessment: summary review and new perspectives. Bulletin of Engineering Geology and the Environment, 58: 21-44.

Amore, E., Modica, C., Nearing, M.A., Santoro, V.C., 2004. Scale effect in USLE and WEPP application for soil erosion computation from three Sicilian basins. Journal of Hydrology, 293: 100–114.

Anderson, S.A., Sitar, N., 1995. Analysis of rainfall-induced debris flows. Journal of Geotechnical Engineering, ASCE, 121(7): 544–552.

Ascough, J.C., Baffaut, C., Nearing, M.A., Liu, B.Y., 1997. The WEPP watershed model: I. hydrology and erosion. Transactions of the ASAE, 40(4): 921-933.

Barling, D.B., Moore, I.D., Grayson, R.B., 1994. A quasi-dynamic wetness index for characterizing the spatial distribution of zones of surface saturation and soil water content. Water Resources Research, 30(4): 1029–1044.

Bartsch, K.P., Van Miegroet, H., Boettinger, J., Bobrowolski, J.P., 2002. Using empirical erosion models and GIS to determine erosion risk at Camp Williams, Utah. Journal of Soil and Water Conservation, 57(1): 29-37.

Bathurst, J.C., Wicks, J.M., O'Connell, J.A., 1995. The SHE/SHESED basin scale water flow and sediment transport modelling system. In: V.P. Singh (Editor), Computer Models of Watershed Hydrology. Water Resource Publication, Highlands Ranch, Colorodo, USA, pp. 63-94.

Bathurst, J.C., Burton, A., Ward, T.J., 1997. Debris flow run-out and landslide sediment delivery model tests. Journal of Hydraulic Engineering, 123(5): 410–419.

Bathurst, J.C., Moretti, G., El-Hames, A., Moaven-Hashemi, A., Burton, A., 2005. Scenario modelling of basin-scale, shallow landslide sediment yield, Valsassina, Italian Southern Alps. Natural Hazards and Earth System Sciences, 5: 189-202.

Bathurst, J.C., Burton, A., Clarke, B.G., Gallart, F., 2006. Application of the SHETRAN basin-scale, landslide sediment yield model to the Llobregat basin, Spanish Pyrenees. Hydrological Processes, 20: 3119–3138.

Bathurst, J.C., Bovolo, C.I., Cisneros, F., 2010. Modelling the effect of forest cover on shallow landslides at the river basin scale. Ecological Engineering 36: 317–327.

Beasley, D.B., Huggins, L.F., Monke, E.J, 1989. ANSWERS: a model for watershed planning. Transactions of the ASAE, 23(4): 938-944.

Becker, A., Braun, P., 1999. Disaggregation, aggregation and spatial scaling in hydrological modelling. Journal of Hydrology 217, 239-252

Benda, L., Dunne, T., 1997. Stochastic forcing of sediment supply to channel networks from landsliding and debris flow. Water Resources Research, 33: 2849–2863.

Benda, L., Hassan, M.A., Church, M., May, C.L., 2005. Geomorphology of steepland headwaters: the transition from hillslopes and channels. Journal of the American Water Resources Association, 41: 835–851.

Benda, L.E., Cundy, T.W., 1990. Predicting deposition of debris flows in mountain channels. Canadian Geotechnical Journal, 27: 409–417.

Bertolo, P., Wieczorek, G.F., 2005. Calibration of numerical models for small debris flows in Yosemite Valley, California, USA. Natural Hazards and Earth

System Sciences, 5: 993–1001.

Beven, K.J., Kirkby, M.J., 1979. A physically based variable contributing area model of basin hydrology. Hydrological Sciences Bulletin, 24(1): 43-49.

Beven, K.J., Moore, I.D., 1993. Terrain analysis and distributed modelling in hydrology. John Wiley & Sons, New York, 249 pp.

Borga, M., Dalla Fontana, G., Da Ros, D., Marchi, L., 1998. Shallow landslide hazard assessment using a physically based model and digital elevation data. Environmental Geology, 35(2-3): 81–88.

Borga, M., Fontana, G.D., Cazorzi, F., 2002. Analysis of topographic and climatic control on rainfall-triggered shallow landsliding using a quasi-dynamic wetness index. Journal of Hydrology, 268: 56-71.

Brooks, K.N., Ffolliott, P.F., Gregersen, H.M., DeBano, L.F., 1991. Hydrology and the management of watersheds. Iowa State University Press, Ames, Iowa, USA, 392 pp.

Burton, A., Bathurst, J.C., 1998. Physically based modelling of shallow landslide sediment yield at a catchment scale. Environmental Geology, 35(2-3): 89-99.

Cannon, S.H., 2000. Debris-flow response of southern California watersheds recently burned by wildfire. In: G.F. Wieczorec and N.D. Naeser (Editors), Debris Flow Hazards Mitigation: Mechanics, Prediction and Assessment. Balkema, Rotterdam, pp. 45–52.

Casadei, M., Dietrich, W.E., Miller, N.L., 2003. Testing a model for predicting the timing and location of shallow landslide initiation in soil-mantled landscapes. Earth Surface Processes and Landforms, 28: 925-950.

Casagli, N., Dapporto, S., Ibsen, M.L., Tofani, V., Vannocci, P., 2006. Analysis of the landslide triggering mechanism during the storm of 20th–21st November 2000, in Northern Tuscany. Landslides, 3(1): 13-21.

Cernica, J.N., 1995. Geotechnical engineering: soil mechanics. John Wiley & Sons New York, 453 pp.

Charlesworth, P., 2000. Soil water monitoring. CSIRO, Land and Water 104 pp.

Chen, H., Dadson, S., Chi, Y., 2006. Recent rainfall-induced landslides and debris flow in northern Taiwan. Geomorphology, 77: 112-125.

Chen, S., Zhang, Z., Chen, X., Shi, P., 2009. The impact of land use and land cover changes on soil moisture and hydraulic conductivity along the karst hillslopes of southwest China. Environmental Earth Sciences, 59: 811–820.

Chu, S.T., 1978. Infiltration during an unsteady rain. Water Resources Research, 14(3): 461-466.

Claessens, L., Heuvelink, G.B.M., Schoorl, J.M., Veldkamp, A., 2005. DEM resolution effects on shallow landslide hazard and soil redistribution modelling. Earth Surface Processes and Landforms, 30: 461–477.

Claessens, L., Knapen, A., Kitutu, M.G., Poesen, J., Deckers, J.A., 2007. Modelling landslide hazard, soil redistribution and sediment yield of landslides on the Ugandan footslopes of Mount Elgon. Geomorphology, 90: 23-35.

Cochrane, T.A., Flanagan, D.C., 1999. Assessing water erosion in small watersheds using WEPP with GIS and digital elevation models. Journal of Soil and Water Conservation, 54: 678–685.

Cochrane, T.A., 1999. Methodologies for watershed modeling with GIS and DEMs for the parameterization of the WEPP model. Ph.D. Thesis, Purdue University, 198 pp.

Cochrane, T.A., Flanagan, D.C., 2003. Representative hillslope method for applying the WEPP model with DEMs and GIS. Transactions of the ASAE, 46(4): 1041-1049.

Cochrane, T.A., Flanagan, D.C., 2005. Effect of DEM resolution in the runoff and soil loss predictions of the WEPP watershed model. Transactions of the ASAE, 48(1): 109−120.

Cochrane, T.A., Egli, M., Phillips, C., Acharya, G., 2007a. Development of a forest road erosion calculation GIS tool for forest road planning and design. In: L. Oxley and D. Kulasiri (Editors), MODSIM 2007 International Congress on Modelling and Simulation. Modelling and Simulation Society of Australia and New Zealand, Christchurch, New Zealand pp. 1273-1279.

Cochrane, T.A., Jack, G., Weber, P., 2007b. Soil armouring, sediment yield, and acid mine drainage from steep slopes under high intensity rainfall in the west coast of New Zealand, 2007 ASABE Annual Meeting. Paper 072053, Minnesota (USA). ASABE

Corominas, J., 1996. The angle of reach as a mobility index for small and large landslides. Canadian Geotechnical Journal, 33: 260-271.

Corominas, J., 2001. Landslides and climate, In: the proceedings of the 8th international symposium on landslides, Cardiff, UK.

Covert, S.A., Robichaud, P.R., Elliot, W.J., Link, T.E., 2005. Evaluation of runoff

prediction from WEPP-based erosion models for harvested and burned forest watersheds. Transactions of the ASAE, 48(3): 1091−1100.

Crosta, G.B., 2001. Failure and flow development of a complex slide: the 1993 Sesa landslide. Engineering Geology, 59: 173– 199.

Cruden, D.M., Varnes, D. J., 1996. Landslide types and processes. In: A.K. Turner and R.L. Schuster (Editors), Landslides: investigation and mitigation. Transportation Research Board Special Report, Washington D.C., pp. 36-75.

Dai, F., Lee, C.F., Wang, S., 1999. Analysis of rainstorm-induced slide-debris flows on natural terrain of Lantau Island, Hong Kong. Engineering Geology, 51: 279–290.

Dai, F.C., Lee, C.F., 2002. Landslide characteristics and slope instability modeling using GIS, Lantau Island, Hong Kong. Geomorphology, 42: 213-228.

Darboux, F., Huang, C., 2003. An instantaneous-profile laser scanner to measure soil surface microtopography. Soil Science Society of America Journal, 67(1): 92-99.

Day, P.R., 1965. Particle fractionation and particle size analysis. In: C.A. Black (Editor), Methods of Soil Analysis Part I. American Society of Agronomy, Madison.

Delmonaco, G., Leoni, G., Margottini, C., Puglisi, C., Spizzichino, D., 2003. Large scale debris-flow hazard assessment: a geotechnical approach and GIS modelling. Natural Hazards and Earth System Sciences, 3: 443–455.

Deutscher, M.S., Gasmo, J. M., Rahardjo, H., Leong, E. C., 2000. Field measurement of pore-water pressure profile in residual soil slopes of the Bukit Timah granite formation, Singapore, In: the Proceedings of Asian Conference on Unsaturated Soils Balkema, Rotterdam, The Netherlands, pp. 777-782.

Dhakal, A.S., Sidle, R.C., 2003. Long-term modelling of landslides for different forest management practices. Earth Surface Processes and Landforms, 28: 853–868.

Dietrich, W.E., Reiss, R., Hsu, M., Montgomery, D.R., 1995. A process-based model for colluvial soil depth and shallow landsliding using digital elevation data. Hydrological Processes, 9: 383–400.

Dietrich, W.E., Montgomery, D.R., 1998. SHALSTAB: a digital terrain model for mapping shallow landslide potential, http://calm.geo.berkeley.edu/geomorph/shalstab/index.htm Last accessed 10 October 2010.

Doe, W.W., Harmon, R.S., 2001. Introduction to soil erosion and landscape evolution modeling. In: R.S. Harmon and W.W. Doe (Editors), Landscape Erosion and Evolution Modeling. Kluwer Academic / Plenum Publishers, New York, pp. 1-14.

Doten, C.O., Bowling, L.C., Lanini. J.S., Maurer, E.P., Lettenmaier, D.P., 2006. A spatially distributed model for the dynamic prediction of sediment erosion and transport in mountainous forested watersheds. Water Resources Research, 42: W04417, doi:10.1029/2004WR003829.

Eckersley, J.D., 1990. Instrumented laboratory flowslides. Geotechnique, 40(3): 489–502.

Elliot, W.J., Hall, D.E., 1997. Water Erosion Prediction Project (WEPP) Forest Applications. General Technical Report INT-GTR-365. Ogden, UT: USDA Forest Service, Rocky Mountain Research Station.

Elliot, W.J., Tysdal, L. M., 1999. Understanding and reducing erosion from insloping roads. Journal of Forestry, 97(8): 30-34.

Fairfield, J., Leymarie, P., 1991. Drainage networks from grid digital elevation models. Water Resources Research, 27: 709–717.

Ferro, V., 1998. Evaluating overland flow sediment transport capacity. Hydrological Processes, 12: 1895-1910.

Flanagan, D.C., Nearing, M.A., 1995. USDA-Water Erosion Prediction Project: hillslope profile and watershed model documentation. NSERL Report No. 10, USDA-ARS National Soil Erosion Research Laboratory, West Lafayette, IN 47097-1196.

Foster, G.R., 1982. Modelling the erosion processes. In: C.T. Hann (Editor), Hydrologic Modelling of Small Watersheds. ASAE Monograph, pp. 297-380.

Foster, G.R., Huggins, L.F., Meyer, L.D., 1984. A laboratory study of rill hydraulics: II. shear stress relationships. Transactions of the ASAE, 27(3): 797– 804.

Fuchu, D., Lee, C. F., Sijing, W., 1999. Analysis of rainstorm-induced slide-debris flows on natural terrain of Lantau Island, Hong Kong. Engineering Geology, 51: 279–290.

Garbrecht, J., Martz, L.W., 1995. TOPAZ: an automated digital landscape analysis tool for topographic evaluation, drainage identification, watershed segmentation and subcatchment parameterization: overview, ARS-NAWQL 95-1. USDA-ARS, Durant, Oklahoma.

Gasmo, J., Hritzuk, K. J., Rahardjo, H., Leong, E. C., 1999. Instrumentation of an unsaturated residual soil slope. Geotechnical Testing Journal 22(2): 128-137.

Godt, J.W., Baum, R.L., Savage, W.Z., Salciarini, D., Schulz, W.H., Harp, E.L., 2008. Transient deterministic shallow landslide modeling: Requirements for susceptibility and hazard assessments in a GIS framework. Engineering Geology, 102: 214-226.

Goldin, A., 1987. Reassessing the use of loss-on-ignition for estimating organic matter content in noncalcareous soils. Communications in soil science and plant analysis, 18(10): 1111-1116.

Goodchild, M.F., Parks, B.O., Steyaert, L.T., 1993. Environmental modeling with GIS. Oxford University Press, New York, 488 pp.

Gorsevski, P.V., Gessler, P.E., Boll, J., Elliot, W.M., Foltz, R.B., 2006. Spatially and temporally distributed modeling of landslide susceptibility. Geomorphology, 80: 178–198.

Graham, J., 1984. Methods of stability analysis. In: D. Brunsden and D.B. Prior (Editors), Slope Instability. Wiley & Sons, New York, pp. 171-21 5.

Green, W.H., Ampt, G. A., 1911. Studies on soil physics: 1. the flow of air and water through soil. Journal of Agricultural Science, 4: 1–24.

Greenway, D.R., 1987. Vegetation and slope stability. In: M.G. Anderson and K.S. Richards (Editors), Slope Stability: Geotechnical, Engineering and Geomorphology. John Wiley & Sons pp. 187-230.

Hungr, O., 1995. A model for the runout analysis of rapid flow slides, debris flows, and avalanches. Canadian Geotechnical Journal, 32: 610-623.

Hungr, O., Evans, S.G., Bovis, M.J., Hutchinson, J.N., 2001. A review of the classification of landslides of the flow type. Environmental and Engineering Geoscience, 7: 221-238.

Hunter, G., Fell, R., 2003. Travel distance angle for “rapid” landslides in constructed and natural soil slopes. Canadian Geotechnical Journal, 40: 1123-1141.

Hutchinson, M.F., 1989. A new procedure for gridding elevation and stream line data with automatic removal of spurious pits. Journal of Hydrology, 106: 211–232.

Iverson, R.M., LaHusen, R.G., 1989. Dynamic pore-pressure fluctuations in rapidly shearing granular materials. Science, 246: 796–799.

Iverson, R.M., Reid, M.E., LaHusen, R.G., 1997. Debris-flow mobilization from landslides. Annual Review of Earth Planetary Sciences, 25: 85-138.

Iverson, R.M., 1997. The physics of debris flows. Reviews of Geophysics, 35: 245–296.

Iverson, R.M., Reid, M.E., Iverson, N.R., LaHusen, R.G., Logan, M., Mann, J.E., Brien, D.L., 2000. Acute sensitivity of landslide rates to initial soil porosity. Science, 290: 513-516.

Iverson, R.M., 2005. Regulation of landslide motion by dilatancy and pore pressure feedback. Journal of Geophysical Research, 110, F02015, doi:10.1029/2004JF000268.

Jenson, S.K., Domingue, J.O., 1988. Extracting topographic structure from digital elevation data for geographic information system analysis. Photogrammetric Engineering and Remote Sensing, 54(11): 1593-1600.

Johnson, A.C., Swanston, D.N., McGee, K.E., 2000. Landslide initiation, runout, and deposition within clearcuts and old-growth forests of Alaska. Journal of the American Water Resources Association, 36(1): 17-30.

Johnson, A.M., Rodine, J.R., 1984. Debris flow. In: D. Brunsden and D.B. Prior (Editors), Slope Instability. Wiley New York, pp. 257-361.

Johnson, K.A., Sitar, N., 1990. Hydrologic conditions leading to debris flow initiation. Canadian Geotechnical Journal, 27(6): 789–801.

Kandel, D.D., Western, A.W., Grayson, R.B., Turral, H.N., 2004. Process parameterization and temporal scaling in surface runoff and erosion modelling. Hydrological Processes, 18: 1423–1446.

Kinnell, P.I.A., Risse, L.M., 1998. USLE-M: Empirical modelling rainfall erosion through runoff and sediment concentration. Soil Science Society of America Journal, 62: 1667-1672.

Korup, O., McSaveney, M.J., Davies, T.R.H., 2004. Sediment generation and delivery from large historic landslides in the Southern Alps, New Zealand. Geomorphology, 61: 189-207.

Lacerda, W.A., 2007. Landslide initiation in saprolite and colluvium in southern Brazil: field and laboratory observations. Geomorphology, 87(3): 104-119.

Lambe, T.W., Whitman, R.V., 1979. Soil mechanics, SI version. John Wiley & Sons, Chichester, 553 pp.

Lan, H.X., Lee, C.F., Zhou, C.H., Martin, C.D., 2005. Dynamic characteristics analysis of shallow landslides in response to rainfall event using GIS. Environmental Geology, 47: 254–267.

Larsen, M.C., Wieczorek, G.F., Eaton, L.S., Torres-Sierra, H.T., 2000. The Venezuela landslide and flash flood disaster of December 1999, In: the Proceedings of the Second Plinius Conference on Mediterranean Storms. European Geophysical Society, Siena, Italy, pp. 519–529.

Lee, K.T., Ho, J., 2007. Prediction of landslide occurrence based on slope-instability analysis and hydrological model simulation. Journal of Hydrology, 375: 489-497.

Legros, F., 2002. The mobility of long-runout landslides. Geomorphology, 63: 301–331.

Lenzi, M.A., Marchi, L., 2000. Suspended sediment load during floods in a small stream of the Dolomites (northeastern Italy). Catena, 39: 267-282.

Löffler-Mang, M., Joss, J., 2000. An optical disdrometer for measuring size and velocity of hydrometeors. Journal of Atmospheric and Oceanic Technology, 17: 130-139.

Lourenco, S.D.N., Sassa, K., Fukuoka, H., 2006. Failure process and hydrologic response of a two layer physical model: implications for rainfall-induced landslides. Geomorphology, 73: 115-130.

Malet, J.P., Laigle, D., Remaître, A., Maquaire, O., 2005. Triggering conditions and mobility of debris flows associated to complex earthflows. Geomorphology, 66: 215-235.

Martin, Y., Rood, K., Schwab, J.W., Church, M., 2002. Sediment transfer by shallow landsliding in the Queen Charlotte Islands, British Columbia. Canadian Journal of Earth Sciences, 39(2): 189-205.

Martz, L.W., Garbrecht, J., 1992. Numerical definition of drainage network and subcatchment areas from digital elevation models. Computers and Geoscience, 18(6): 747-761.

Meadows, D.G., Young, M.H., McDonald, E.V., 2005. A laboratory method for determining the unsaturated hydraulic properties of soil peds. Soil Science Society of America Journal, 69(3): 807-815.

Mein, R.G., Larson, C.L., 1973. Modeling infiltration during a steady rain. Water Resources Research, 9(2): 384-394.

Mellerowicz, K.T., Rees, H.W., Chow, T.L., Ghanem, I., 1994. Soil conservation planning at the watershed level using the Universal Soil Loss Equation with GIS and micorocomputer technologies: a case study. Journal of Soil and Water

Conservation, 49(2): 194-200.

Mitasova, H., Hofierka, J., Zlocha, M., Iverson, L.R., 1996. Modeling topographic potential for erosion and deposition using GIS. International Journal of Geographical Information Science, 10(5): 629-641.

Monteith, J.L., 1965. Evaporation and environment, In: Proceedings of the 19th Symposium of the Society for Experimental Biology. Cambridge University Press, New York, pp. 205–233.

Montgomery, D.R., Dietrich, W.E., 1994. A physically based model for the topographic control on shallow landsliding. Water Resources Research, 30: 1153-1171.

Montgomery, D.R., Sullivan, K., Greenberg, H.M., 1998. Regional test of a model for shallow landsliding. Hydrological Processes, 12(6): 943–955.

Moore, I.D., Grayson, R.B., Ladson, A.R., 1991. Digital terrain modelling: a review of hydrological, geomorphological, and biological applications. Hydrological Processes, 5(1): 3-30.

Morgan, R.P.C., Rickson, R.J., 1995. Slope stabilization and erosion control: a bioengineering approach. E&FN Spon, London, 274 pp.

Moriwaki, H., Inokuchi, T., Hattanji, T., Sassa, K., Ochiai, H., Wang, G., 2004. Failure processes in a full-scale landslide experiment using a rainfall simulator. Landslides, 1: 277-288.

Mukhlisin, M., Kosugi, K., Satofuka, Y., Mizuyama, T., 2006. Effects of soil porosity on slope stability and debris flow runout at a weathered granitic hillslope. Vadose Zone Journal, 5: 283-295.

Nash, J.E., Sutcliffe, J.V., 1970. River flow forecasting through conceptual models. Part 1. A discussion of principles. Journal of Hydrology, 10(3): 282-290.

Nearing, M.A., Page, D.I., Simanton, J.R., Lane, L.J., 1989. Determining erodibility parameters from rangeland field data for a process-based erosion model. Transactions of the ASAE, 32(3): 919–924.

Nearing, M.A., Parker, S.C., 1994. Detachment of soil by flowing water under turbulent and laminar conditions. Soil Science Society of America Journal, 58: 1612-1614.

Nearing, M.A., 1998. Why soil erosion models over-predict small losses and under-predict large soil losses. Catena, 32: 15-22.

Nearing, M.A., Govers, G., Norton, L.D., 1999. Variability in soil erosion data from

replicated plots. Soil Science Society of America Journal, 63(6): 1829–1835.

Nicks, A.D., Lane, L.J., Gander, G.A, 1995. Weather generator. In: D.C. Flanagan and M.A. Nearing (Editors), USDA-Water Erosion Prediction Project Hillslope Profile and Watershed Model Documentation, NSERL Report No. 10. USDA-ARS National Soil Erosion Research Laboratory, West Lafayette, IN.

Norton, L.D., Brown, L.C., 1992. Time-effect on water erosion for ridge tillage. Transactions of the ASAE, 35(2): 473-478.

O'Callaghan, J.F., Mark, D.M., 1984. The extraction of drainage networks from digital elevation data. Computer Vision, Graphics, and Image Processing, 28(3): 323-344.

O'Loughlin, E.M., 1986. Prediction of surface saturation zones in natural catchments by topographic analysis. Water Resources Research, 22: 794-804.

O'Brien, J.S., Julien, P.Y., Fullerton, W.T., 1993. Two-dimensional water flood and mudflow simulation. Journal of Hydraulic Engineering, 119(2): 244-261.

Okura, Y., Kitahara, H., Ochiai, H., Sammori, T., Kawanami, A., 2002. Landslide fluidization process by flume experiments. Engineering Geology, 66: 65-78.

Olivares, L., Damiano, E., 2007. Postfailure mechanics of landslides: laboratory investigation of flowslides in Pyroclastic soils. Journal of Geotechnical and Geoenvironmental Engineering, 133(1): 51-62.

Onstad, C.A., 1984. Depression storage on tilled soil surfaces. Transactions of the ASAE, 27(3): 729-732.

Oropeza-Mota, J.L., Larose, M., Norton, L.D., 2004. Testing the applicability of the WEPP model for predicting soil loss in tropical hillside lands in the Tuxtlas, Veracruz, Mexico, In: the Proceedings of ASA-CSSA-SSSA Seattle, WA.

Pack, R.T., Tarboton, D.G., Goodwin, C.N., 2001. Assessing terrain stability in a GIS using SINMAP, 15th annual GIS conference, Vancouver, British Columbia, pp. 19-22.

Pandey, A., Chowdary, V.M., Mal, B.C., Billib, M., 2009. Application of the WEPP model for prioritization and evaluation of best management practices in an Indian watershed. Hydrological Processes, 23: 2997–3005.

Pathak, S., Nilsen, B., 2004. Probabilistic rock slope stability analysis for Himalayan condition. Bulletin of Engineering Geology and the Environment, 63: 25–32.

Pieri, L., Bittelli, M., Wu, J.Q., Dun, S., Flanagan, D.C., Pisa, P.R., Ventura, F.,

Salvatorelli, F., 2007. Using the Water Erosion Prediction Project (WEPP) model to simulate field-observed runoff and erosion in the Apennines mountain range, Italy. Journal of Hydrology, 336(84-97).

Preston, N.J., Crozier, M.J., 1999. Resistance to shallow landslide failure through root-derived cohesion in east coast hilly country soils, North Island, New Zealand. Earth Surface Processes and Landforms, 24: 665-675.

Quinn, P., Beven, K., Chevallier, P., Planchon, O., 1991. The prediction of hillslope flow paths for distributed hydrological modelling using digital terrain models. Hydrological Processes, 5: 59–79.

Ran, J., He, S., Cao, J., Xiong, Z., Chen, H., 2002. Study on preserving benefit of water and soil in subtropical karst forest area: a case study in Maolan National Karst Forest Reserve, Libo, Guizhou. Journal of Soil and Water Conservation, 16(5): 92–95.

Renard, K.G., Foster, G.R., Weesies, G.A., McCool, D.K., Yoder, D.C., 1997. Predicting soil erosion by water: a guide to conservation planning with the revised universal soil loss equation (RUSLE), U.S. Department of Agriculture, Agricultural Handbook No. 703.

Renschler, C.S., 2003. Designing geo-spatial interfaces to scale process models: the GeoWEPP approach. Hydrological Processes, 17: 1005-1017.

Revellino, P., Hungr, O., Guadagno, F.M., Evans, S.G., 2004. Velocity and runout simulation of destructive debris flows and debris avalanches in pyroclastic deposits, Campania region, Italy. Environmental Geology, 45: 295-311.

Rickenmann, D., 1999. Empirical relationships for debris flows. Natural Hazards, 19: 47-77.

Ries, J.B., 2000. The landslide in the Surma Khola Valley, High Mountain Region of the Central Himalaya in Nepal. Physics and Chemistry of the Earth: Part B. Hydrology Oceans and Atmosphere, 25: 51– 57.

Risse, L.M., Nearing, M.A., Nicks, A.D., Laflen, J.M., 1993. Error assessment in the universal soil loss equation. Soil Science Society of America Journal, 57(3): 825-833.

Rosso, R., Rulli, M.C., Vannucchi, G., 2006. A physically based model for the hydrologic control on shallow landsliding. Water Resources Research, 42: doi:10.1029/2005WR00436.

Ruttimann, M., Schaub, D., Prasuhn, V., Ruegg, W., 1995. Measurement of runoff

and soil erosion on regularly cultivated fields in Switzerland-some critical considerations. Catena, 25: 127-139.

Saavedra, C., 2005. Estimating spatial patterns of soil erosion and deposition in the Andean region using geo-information techniques a case study in Cochabamba, Bolivia. Ph.D. Thesis, Wageningen University, Enschede, The Netherlands.

Sanderson, F., Bakkehøi, S., Hestenes, E., Lied, K., 1996. The influence of meteorological factors on the initiation of debris flows, rockfalls, rockslides and rockmass stability, In: the proceedings of 7th international symposium on landslides, Rotterdam, pp. 97-114.

Sassa, K., 1984. The mechanism starting liquefied landslides and debris flows, In: the Proceedings of 4th International Symposium on Landslides, Toronto, Canada, pp. 349–354.

Sassa, K., 2000. Mechanism of flows in granular soils, In: the Proceedings of GeoEng2000, Melbourne, pp. 1671– 1702.

Saulnier, G., Obled, C., Beven, K., 1997. Analytical compensation between DTM grid resolution and effective values of saturated hydraulic conductivity within the TOPMODEL framework. Hydrological Processes, 11: 1331-1346.

Schoorl, J.M., Sonneveld, M.P.W., Veldkamp, A., 2000. Three dimensional landscape process modeling: the effect of DEM resolution. Earth Surface Processes and Landforms, 25: 1025–1034.

Schuerch, P., Densmore, A.L., McArdell, B.W., Molnar, P., 2006. The influence of landsliding on sediment supply and channel change in a steep mountain catchment. Geomorphology, 78: 222-235.

Schwab, M., Rieke-Zapp, D., Schneider, H., Liniger, M., Schlunegger, F., 2008. Landsliding and sediment flux in the Central Swiss Alps: a photogrammetric study of the Schimbrig landslide, Entlebuch. Geomorphology, 97: 392-406.

Scull, P., Franklin, J., Chadwick, O.A., McArthur, D., 2003. Predictive soil mapping: a review. Progress in Physical Geography, 27(2): 171-197.

Shahgholi, M., Fakher, A., Jones, C.J.F.P., 2001. Horizontal slice method of analysis. Geotechnique, 51(10): 881-885.

Sharmeen, S., Willgoose, G.R., 2007. A one-dimensional model for simulating armouring and erosion on hillslopes: 2. Long term erosion and armouring predictions for two contrasting mine spoils. Earth Surface Processes and Landforms, 32: 1437–1453.

Shrestha, R., Tachikaw, Y., Takar, K., 2006. Input data resolution analysis for distributed hydrological modeling. Journal of Hydrology, 319: 36–50.

Sidle, R.C., Pearce, A.J., O'Loughlin, C.L., 1985. Hillslope stability and land use. Water Resources Monograph Series 11, American Geophysical Union

Sidle, R.C., 1991. A conceptual model of changes in root cohesion in response to vegetation management. Journal of Environmental Quality, 20: 43–52.

Sidle, R.C., Ochiai, H., 2006. Landslides: processes, prediction, and land use. American Geophysical Union, Washington DC, 312 pp.

Sivapalan, M., Jothityangkoon, C., Menabde, M., 2002. Linearity and nonlinearity of basin response as a function of scale: discussion of alternative definitions. Water Resources Research, 38(2): doi:10.1029/2001WR000482

Skempton, A.W., DeLory, F.A., 1957. Stability of natural slopes in London clay. ASCE Journal 2: 378-381.

Skidmore, A.K., Ryan, P.J., Dawes, W., Short, D., O'Loughlin, E.M., 1991. Use of an expert system to map forest soils from a geographical information system. International Journal of Geographical Information Science, 5: 431-445.

Sloan, P.G., Moore, I.D., 1984. Modeling subsurface stormflow on steeply sloping forested watersheds. Water Resources Research, 20: 1815-1822.

Smith, R.E., Goodrich, D.C., Woolhiser, D.A., Unkrich, C.L., 1995. KINEROS: a kinematic runoff and erosion model. In: V.P. Singh (Editor), Computer Models of Watershed Hydrology. Water Resources Publications, pp. 697-732.

Soil Survey Staff, 1998. Keys to Soil Taxonomy. 8th ed. USDA-NRCS, Washington, DC.

Spence, K.J., Guymer, I., 1997. Small-scale laboratory flowslides. Geotechnique, 75(5): 915-932.

Squier, L.R., Harvey, A.F., 2000. Two debris flows in Coast Range, Oregon, USA: logging and public policy impacts. In: G.F. Wieczorec and N.D. Naeser (Editors), Debris Flow Hazards Mitigation: Mechanics, Prediction and Assessment. Balkema, Rotterdam, pp. 127– 138.

Sumner, M.E., Miller, W.P., 1996. Cation exchange capacity and exchange coefficients. In: A.L. Sparks (Editor), Methods of Soil Analysis. Part 3. Chemical Methods. American Society of Argon. Madison. Willy International, pp. 1201-1230.

Sun, H., Cornish, P.S., Daniell, T.M., 2001. Turbidity-based erosion estimation in a

catchment in South Australia. Journal of Hydrology, 253: 227-238.

Süzen, M.L., Doyuran, V., 2004. A comparison of the GIS based landslide susceptibility assessment methods: multivariate versus bivariate. Environmental Geology, 45: 665–679.

Takahashi, T., 1991. Debris-Flow, Balkema, Rotterdam.

Tarboton, D.G., Bras, R.L., Rodriguez-Iturbe, I., 1991. On the extraction of channel networks from digital elevation data. Hydrological Processes, 5(1): 81-100.

Terlien, M.T.J., 1997. Hydrological landslide triggering in ash-covered slopes of Manizales (Colombia). Geomorphology, 20: 165-175.

Terlien, M.T.J., 1998. The determination of statistical and deterministic hydrological landslide-triggering thresholds. Environmental Geology, 35(2-3): 124-130.

Thieken, A.H., Lucke, A., Diekkrueger, B., Richter, O., 1999. Scaling input data by GIS for hydrological modelling. Hydrological Processes, 13: 611-630.

Thompson, J.A., Bell, J.C., Butler, C.A., 2001. Digital elevation model resolution: effects on terrain attribute calculation and quantitative soil-landscape modelling. Geoderma, 100(1-2): 67-89.

Tiwari, A.K., Risse, L.M., Nearing, M.A., 2000. Evaluation of WEPP and its comparison with USLE and RUSLE. Transactions of the ASAE, 43(5): 1129-1135.

Tofani, V., Dapporto, S., Vannocci, P., Casagli, N., 2005. Analysis of infiltration, seepage processes and slope instability mechanisms during the November 2000 storm event in Tuscany. Advances in Geosciences, 2: 301–304.

Tohari, A., Nishigaki, M., Komatsu, M., 2007. Laboratory rainfall-induced slope failure with moisture content measurement. Journal of Geotechnical and Geoenvironmental Engineering, 133(5): 575-587.

Trangmar, B.B., 1998. Soil Map of the Port Hills, Canterbury, New Zealand. Landcare Research Map.

Tysdal, L.M., Elliot, W.J., Luce, C.H., Black, T.A., 1999. Modeling erosion from insloping low-volume roads with WEPP watershed model, Seventh International Conference on Low-Volume Roads, Baton Rouge, Louisiana. Transportation Research Record.

Van De Wiel, M.J., Darby, S.E., 2007. A new model to analyse the impact of woody riparian vegetation on the geotechnical stability of riverbanks. Earth Surface Processes and Landforms, 32: 2185–2198.

Van Rompaey, A.J.J., Krasa, J., Dostal, T., Govers, G., 2003. Modelling sediment supply to rivers and reservoirs in Eastern Europe during and after collectivisation period. Hydrobiologia, 494: 169–176.

Van Westen, C.J., Terlien, M.T.J., 1996. An approach towards deterministic landslide hazard analysis in GIS: a case study from Manizales (Colombia). Earth Surface Processes and Landforms, 21: 853–868.

Van Westen, C.J., 2000. The modelling of landslide hazards using GIS. Surveys in Geophysics, 21: 241-155.

Vanacker, V., Vanderschaeghe, M., Govers, G., Willems, E., Poesen, J., Deckers, J., De Bievere, B., 2003. Linking hydrological, infinite slope stability and land-use change models through GIS for assessing the impact of deforestation on slope stability in high Andean watersheds. Geomorphology, 52: 299–315.

Vanacker, V., Molina, A., Govers, G., Poesen, J., Deckers, J., 2007. Spatial variation of suspended sediment concentrations in a tropical Andean river system: The Paute River, southern Ecuador. Geomorphology, 87: 53-67.

Vandre, B.C., 1985. Rudd creek debris flow. In: D.S. Bowles (Editor), Delineation of Landslide, Flash Flood, and Debris Flow Hazards in Utah. General Series Report. Utah Water Research Laboratory, Utah State University, Logan, Utah, pp. 117–131.

Varnes, D.J., 1978. Slope movement types and process. In: R.L. Schuster and R.J. Krizek (Editors), Landslides: Analysis and Control-Transportation Research Board, Special Report. National Research Council, Washington D.C., pp. 11–33.

Vázquez, R.F., Feyen L., Feyen J., Refsgaard, J.C., 2002. Effect of grid size on effective parameters and model performance of the MIKE-SHE code. Hydrological Processes, 16: 355–372.

Verburg, P.H., Soepboer, W., Veldkamp, A., Limpiada, R., Espaldon, V., Mastura, S.S.A., 2002. Modeling the spatial dynamics of regional land use: the CLUE-S model. Environmental Management, 30(3): 391–405.

Vieux, B.E., 1991. Geographic information systems and non-point source water quality and quantity modelling Hydrological Processes, 5(1): 101-113.

Wang, C., Esaki, T., Xie, M., Qiu, C., 2006. Landslide and debris-flow hazard analysis and prediction using GIS in Minamata–Hougawachi area, Japan. Environmental Geology, 51: 91–102.

Wang, G., Sassa, K., 2001. Factors affecting rainfall-induced flowslides in laboratory flume tests. Geotechnique, 51(7): 587-599.

Wang, G., Sassa, K., 2003. Pore-pressure generation and movement of rainfall-induced landslides: effects of grain size and fine-particle content. Engineering Geology, 69: 109-125.

Ward, T.J., Li, R.M., Simons, D.B., 1981. Use of a mathematical model for estimating potential landslide sites in steep forested drainage basins. International Association of Hydrological Science Publication, 132: 21–41.

Wendt, R.C., Alberts, E.E., Hjelmfelt A.T., 1986. Variability of runoff and soil loss from fallow experimental plots. Soil Science Society of America Journal, 50(3): 730-736.

Weyman, D.R., 1973. Measurement of the downslope flow of water in a soil. Journal of Hydrology, 20(3-4): 267-288.

Wicks, J.M., Bathurst, J.C., Johnson, C.W., 1992. Calibrating SHE soil-erosion model for different land covers. Journal of Irrigation and Drainage Engineering, 118(5): 708-723.

Wicks, J.M., Bathurst, J.C., 1996. SHESED: a physically based, distributed erosion and sediment yield component for the SHE hydrological modelling system. Journal of Hydrology, 175(1-4): 213-238.

Wieczorek, G.F., 1987. Effect of rainfall intensity and duration on debris flows in central Santa Cruz Mountains, California. Geological Society of America, Review in Engineering Geology, 7: 93-104.

Williams, J.R., 1975. Sediment routing for agricultural watersheds. Journal of the American Water Resources Association, 11(5): 965–974.

Willmott, C.J., 1981. On the validation of models. Physical Geography, 2: 184–194.

Wilson, J.P., Repetto, P.L., Snyder, R.D., 2000. Effect of data source, grid resolution and flow-routing method on computed topographic attributes. In: J.P. Wilson and J.C. Gallant (Editors), Terrain analysis: principles and applications. John Wiley & Sons, New York, USA, pp. 133-161.

Wischmeier, W.H., Smith, D.D., 1978. Predicting rainfall erosion losses - a guide to conservation planning, U.S. Department of Agriculture, Agricultural Handbook No. 537.

Wise, S., 2000. Assessing the quality for hydrological applications of digital elevation models derived from contours. Hydrological Processes, 14: 1909-1929.

Wolock, D.M., Price, C.V., 1994. Effects of digital elevation model map scale and data resolution on a topography-based watershed model. Water Resources Research, 30(11): 3041-3052.

Woolhiser, D.A., Smith, R.E., Goodrich, D.C., 1990. KINEROS: a kinematic runoff and erosion model: documentation and user manual, USDA Agricultural Research Service ARS-77.

Wu, W., Sidle, R.C., 1995. A distributed slope stability model for steep forested basins. Water Resources Research, 13: 2097–2110.

Xie, M., Esaki, T., Zhou, G., Mitani, Y., 2003. Geographic information systems-based three-dimensional critical slope stability analysis and landslide hazard assessment. Journal of Geotechnical and Geoenvironmental Engineering, 129(12): 1109–1118.

Yalin, M.S., 1963. An expression for bed-load transportation. Journal of Hydraulics Division, ASCE, 98: 221-250.

Yeakley, J.A., Swank, W.T., Swift, L.W., Hornberger, G.M., Shugart, H.H., 1998. Soil moisture gradients and controls on a southern Appalachian hillslope from drought through recharge. Hydrology & Earth System Sciences, 2(1): 41-49.

Young, R.A., Onstad, C.A., Bosch, D.D., Anderson, W.P., 1989. AGNPS: a non point-source pollution model for evaluating agricultural watersheds. Journal of Soil and Water Conservation, 44(2): 168-173.

Yu, B., Rosewell, C.J., 2001. Evaluation of WEPP for runoff and soil loss prediction at Gunnedah, NSW, Australia. Australian Journal of Soil Research, 39: 1131-1145.

Zeleke, G., Winter, T., Flanagan, D., 1999. BPCDG: breakpoint climate data generator for WEPP using observed climate standard weather data sets, http://topsoil.nserl.purdue.edu/nserlweb/weppmain/BPCDG.html Last accessed 10 October 2010.

Zevenbergen, L.W., Thorne, C.R., 1987. Quantitative analysis of land surface topography. Earth Surface Processes and Landforms, 12: 47-56.

Zhang, J.X., Wu, J.Q., Chang, K., Elliot, W.J., Dun, S., 2009. Effects of DEM source and resolution on WEPP hydrologic and erosion simulation: a case study of two forest watersheds in northern Idaho. Transactions of the ASAEB, 52(2): 447-457.

Zhang, L., O'Neill, A.L., Lacey, S., 1996a. Modelling approaches to the prediction of

soil erosion in catchments. Environmental Software, 11(1-3): 123-133.

Zhang, W., Montgomery, D.R., 1994. Digital elevation model grid size, landscape representation, and hydrologic simulations. Water Resources Research, 30(4): 1019-1028.

Zhang, X.C., Nearing, M.A., Risse, L.M., McGregor, K.C., 1996. Evaluation of WEPP runoff and soil loss predictions using natural runoff plot data. Transactions of the ASAE, 39: 855-864.